

Fire-Induced Spalling Modeling of High-Performance Concrete

Proefschrift

ter verkrijging van de graad van doctor
aan de Technische Universiteit Delft,
op gezag van de Rector Magnificus prof. ir. K.C.A.M. Luyben,
voorzitter van het College voor Promoties,
in het openbaar te verdedigen op dinsdag 24 april 2012 om 10.00 uur

door

Jie ZHAO

Master of Science aan de Beijing University of Technology, P. R. China
geboren te Harbin, Heilongjiang Province, P. R. China

Dit proefschrift is goedgekeurd door de promotor:
Prof. dr. ir. K. van Breugel

Samenstelling promotiecommissie:

| | |
|------------------------------|---|
| Rector Magnificus | voorzitter |
| Prof. dr. ir. K. van Breugel | Technische Universiteit Delft, promotor |
| Prof. dr. ir. J. G. Rots | Technische Universiteit Delft |
| Prof. dr. ir. J. J. Zheng | Zhejiang University of technology, P. R. China |
| Prof. dr. ir. G. F. Peng | Beijing Jiaotong University, P. R. China |
| Prof. dr. ir. F. Dehn | Leipzig Institute for Materials Research and Testing, Germany |
| Dr. ir. E. A. B. Koenders | Technische Universiteit Delft |
| Dr. ir. L. Pel | Technische Universiteit Eindhoven |
| Prof. dr. ir. P. C. Rem | Technische Universiteit Delft, reservelid |

ISBN: 978-90-9026717-3

Keywords: High-performance concrete; Fire spalling; Modeling

Printed by Haveka BV, the Netherlands

Cover design: Haveka BV and Jie Zhao

Copyright © 2012 by Jie Zhao

All rights reserved. No part of the material protected by this copyright notice may be reproduced or utilized in any form or by any means, electronic or mechanical, including photocopying, recording or by any information storage and retrieval system, without written permission from the author.

To my beloved family

Acknowledgements

The research project reported in this thesis was sponsored by China Scholarship Council (CSC) and Delft University of Technology (TU Delft). The research was conducted in the Section of Materials and Environment at the Faculty of Civil Engineering and Geosciences of TU Delft. CSC and TU Delft are gratefully acknowledged for the financial support and the opportunity offered to me for pursuing a Ph.D. degree.

I would like to express my sincere thanks to my promoter and supervisor, Prof. dr. ir. Klaas van Breugel, for his support, guidance, and encouragement throughout the whole course of this study. He taught me to be patient, be logic, and pay more attention to the details. I wish to thank Dr. Zhan Qi Guo, who gave me a lot of help and technical support at the starting stage of this project. I would like to express my sincere gratitude to Prof. Gai Fei Peng of my home university, Beijing Jiaotong University, and Prof. Jian Jun Zheng of Zhejiang University of Technology for their valuable discussions, suggestions, guidance, support, and encouragement.

I wish to thank my present and former colleagues, Ayda Agar Ozbek, Lupita Sierra Beltran, Virginie Wiktor, Ying Wang, Nguyen Van Tuan, Senot Sangadji, Jongsuk Lee, Hao Huang, Farhad Pargar, Chun Ping Gu, Hua Dong, Jun Feng Su, Albert Soto Masip, Neven Ukrainczyk, Trong Quyen Phung, and Zhi Wei Qian, for their help, technical and funny discussions, amusing talks, encouragement, and support. Their friendship made my journey to finishing my study easier and my daily life rich and colorful. I would like to express my thanks to Dennis and Erik for the translation of the summary. I wish to thank Dr. Guang Ye, Jian Zhou, and their wives for their kindness and nice invitations. I would like to say tanks to my friends, Beibei Hu, Shun Chen, Wei Zheng, Ziru Li, Yan Wei. We were from the same cooperation project and came to the Netherlands together. We shared our joy, happiness, stress, and depression together. I wish to thank Mr. Cees Timmers and Ms. Franca Post of the central liaison office at TU Delft (CICAT) for their management support and help. I would like to express my thanks to my landlord, Jan and Elly, for offering me a nice apartment and their friendship and kindness.

I'm grateful to my home university, Beijing Jiaotong University, for allowing me to pursue my Ph.D. degree abroad. I wish to thank my boss and my colleagues in my home university, for their support and encouragement.

Last but not least, I would like to express my thanks to my parents, my parents in law, and my beloved family for their continuous support and encouragement during the research. Without their support, my thesis could never have been completed.

Jie Zhao
Delft, April 2012

Table of contents

| | |
|---|-----------|
| List of symbols | iii |
| List of abbreviations | ix |
| Chapter 1 General introduction..... | 1 |
| 1.1 Development of high-performance concrete | 1 |
| 1.2 Fire risk..... | 1 |
| 1.3 Fire damage | 3 |
| 1.4 Current state of spalling modeling | 4 |
| 1.5 Scope and objectives of this study | 4 |
| 1.6 Research strategy of this study | 5 |
| 1.7 Outline of this thesis..... | 5 |
| Chapter 2 General literature review | 9 |
| 2.1 Experimental study on fire damage..... | 9 |
| 2.2 Fire damage modeling - state of art..... | 13 |
| 2.3 Modeling evaluation and conclusions | 17 |
| Chapter 3 Temperature field determination | 19 |
| 3.1 Introduction | 19 |
| 3.2 Temperature field determination | 19 |
| 3.3 One-way coupling of thermo-to-mechanical analysis..... | 23 |
| 3.4 Application | 23 |
| 3.5 Summary | 24 |
| Chapter 4 Thermal decomposition prediction of hardened cement paste..... | 25 |
| 4.1 Introduction and literature review | 25 |
| 4.2 Decomposition prediction of hardened cement paste..... | 26 |
| 4.3 Volume fraction evolution of various constituents | 31 |
| 4.4 Experimental verification of numerical method..... | 33 |
| 4.5 Analysis of heating rate effect on thermal decomposition..... | 36 |
| 4.6 Summary and conclusions..... | 39 |
| Chapter 5 Vapor pressure analysis..... | 41 |
| 5.1 Introduction and literature review | 41 |
| 5.2 Vapor pressure determination | 42 |
| 5.3 Mechanical modeling of vapor pressure | 45 |
| 5.4 Example of vapor pressure determination..... | 48 |

| | | |
|------------------|---|------------|
| 5.5 | Summary | 48 |
| Chapter 6 | Moisture transport analysis | 49 |
| 6.1 | Introduction | 49 |
| 6.2 | Governing equation of moisture transport..... | 50 |
| 6.3 | Permeability determination | 51 |
| 6.4 | Numerical solution of moisture transport..... | 57 |
| 6.5 | Application | 58 |
| 6.6 | Summary | 59 |
| Chapter 7 | Thermo-poro mechanical analysis..... | 61 |
| 7.1 | Introduction and literature review | 61 |
| 7.2 | Basic equations of elastic thermo-poro mechanical analysis | 62 |
| 7.3 | Non-linear mechanical analysis..... | 64 |
| 7.4 | Numerical solution of two-dimensional problem..... | 68 |
| 7.5 | Thermal variation of elastic modulus | 71 |
| 7.6 | Verification of elastic modulus prediction | 72 |
| 7.7 | Summary | 73 |
| Chapter 8 | Numerical investigation of spalling of heated concrete | 75 |
| 8.1 | Introduction | 75 |
| 8.2 | Numerical model description | 76 |
| 8.3 | Determination of material parameters | 77 |
| 8.4 | Temperature field analysis | 81 |
| 8.5 | Thermal decomposition analysis | 82 |
| 8.6 | Moisture transport and vapor pressure analysis | 84 |
| 8.7 | Analysis of thermal reduction of elastic modulus | 99 |
| 8.8 | Thermo-poro mechanical damage analysis of heated concretes | 100 |
| 8.9 | Summary and conclusions..... | 119 |
| Chapter 9 | Conclusions and prospects | 123 |
| 9.1 | Specific features | 123 |
| 9.2 | Conclusions | 124 |
| 9.3 | Prospects..... | 125 |
| References | | 127 |
| Summary | | 135 |
| Samenvatting | | 137 |

List of symbols

Roman lower case letters

| | | |
|------------------|-------------|---|
| a | [-] | Conversion degree |
| b | [bar] | Klinkenberg constant |
| c | [J/(kg·°C)] | Specific heat |
| d_c | [m] | Critical pore diameter |
| f | [Pa/m] | Body force |
| f_{agg} | [-] | Volume fraction of aggregates in concrete |
| f_{AL}^0 | [-] | Initial volume fraction of hydrated aluminates |
| f_{AL}^{PP} | [-] | Porosity of decomposition product of hydrated aluminates |
| f_{AL}^r | [-] | Volume fraction of residual undecomposed hydrated aluminates |
| f_{AL}^{SP} | [-] | Volume fraction of solid decomposition product of hydrated aluminates |
| f_{AL}^w | [-] | Volume fraction of water decomposed from hydrated aluminates |
| f_c | [MPa] | Compressive strength |
| f_{cap} | [-] | Capillary porosity of hardened cement paste |
| f_{cap}^0 | [-] | Initial volume fraction of capillary pores |
| f_{cap}^1 | [-] | Volume fraction of capillary pores at complete decomposition of hardened cement paste |
| f_{cap}^{AL} | [-] | Capillary porosity at complete decomposition of hydrated aluminates |
| f_{cap}^{CH} | [-] | Capillary porosity at complete decomposition of CH |
| f_{cap}^{con} | [-] | Capillary porosity of concrete |
| f_{cap}^{CSH} | [-] | Capillary porosity at complete decomposition of C-S-H |
| f_{cap}^{test} | [-] | Test result of volume fraction of capillary pores |
| f_{CH}^0 | [-] | Initial volume fraction of CH |
| f_{CH}^{PP} | [-] | Porosity of decomposition product of CH |
| f_{CH}^r | [-] | Volume fraction of residual undecomposed CH |
| f_{CH}^{SP} | [-] | Volume fraction of solid decomposition product of CH |
| f_{CH}^w | [-] | Volume fraction of water decomposed from CH |
| f_{CSH}^0 | [-] | Initial volume fraction of conventional C-S-H |
| f_{CSH}^{0s} | [-] | Initial volume fraction of solid C-S-H |
| f_{CSH}^{cap} | [-] | Volume fraction of additional capillary pores due to |

| | | |
|------------------|--------------------------|--|
| | | decomposition of C-S-H gel |
| f_{CSH}^{gelp} | [-] | Volume fraction of gel pores in conventional C-S-H gel |
| f_{CSH}^{pp} | [-] | Porosity of decomposition product of conventional C-S-H |
| f_{CSH}^r | [-] | Volume fraction of residual undecomposed C-S-H |
| f_{CSH}^s | [-] | Initial volume fraction of solid conventional C-S-H |
| f_{CSH}^{sp} | [-] | Volume fraction of solid decomposition product of C-S-H |
| f_{CSH}^w | [-] | Volume fraction of water decomposed from C-S-H |
| f_{dehy}^w | [-] | Volume fraction of water released from decomposition in matrix |
| f_{gel} | [-] | Volume fraction of cement gel |
| f_{gel}^{AL} | [-] | Volume fraction of hydrated aluminates in cement gel |
| f_{gel}^{CH} | [-] | Volume fraction of CH in cement gel |
| f_{gel}^{CSH} | [-] | Volume fraction of conventional C-S-H in cement gel |
| f_h | [-] | Volume fraction of high-permeable phase |
| f_{hc} | [-] | Critical volume fraction of high permeable phase |
| f_{hcp} | [-] | Volume fraction of hcp in concrete |
| f_{in} | [-] | Volume fraction of inclusion phase |
| f_{pCSH}^0 | [-] | Initial volume fraction of pozzolanic C-S-H |
| f_{pCSH}^{pp} | [-] | Porosity of decomposition product of pozzolanic C-S-H |
| f_{pCSH}^r | [-] | Volume fraction of residual undecomposed pozzolanic C-S-H |
| f_{pCSH}^s | [-] | Initial volume fraction of solid pozzolanic C-S-H |
| f_t | [-] | Tensile strength |
| f_{unhyC} | [-] | Volume fraction of unhydrated cement |
| f_{unhySF} | [-] | Volume fraction of unhydrated silica fume |
| h_c | [W/(m ² ·°C)] | Convective heat transfer coefficient |
| k | [kg/(m·Pa·s)] | Mass permeability of hardened cement paste |
| k' | [m ²] | Intrinsic permeability |
| k'_g | [m ²] | Intrinsic permeability to gas |
| k_h | [m ²] | Permeability of high-permeable phase |
| k_l | [m ²] | Permeability of low permeable phase |
| k'_l | [m ²] | Intrinsic permeability to liquid |
| k_r | [-] | Coefficient of reaction rate |
| k_{rg} | [-] | Relative permeability coefficient |
| k_{tr} | [-] | Transient creep coefficient |
| m | [kg/s] | Net mass flow in unit time |
| \dot{m}_{dh} | [kg/(m ³ ·s)] | Moisture source from thermal decomposition |
| m_m | [kg] | Mass of moisture |
| n | [-] | Number of nodes of element |
| n_{AL}^w | [mol] | Water decomposed from per mole of hydrated aluminates |
| n_{CH}^w | [mol] | Water decomposed from per mole of CH |
| n_{CSH}^w | [mol] | Water decomposed from per mole of C-S-H |
| ne | [-] | Number of elements |
| p | [Pa] | Vapor pressure |
| p' | [Pa] | Constrained force intensity |
| p_{AL} | [-] | Porosity of aluminates |
| p_{C2S} | [-] | Porosity of C ₂ S |
| p_{CaO} | [-] | Porosity of CaO |
| p_e | [Pa] | Effective vapor pressure |

| | | |
|------------|--------------------------|--|
| p_i^e | [Pa] | Element nodal unknowns of vapor pressure |
| p_{test} | [-] | Test result of porosity |
| q | [W/m ²] | Heat flux |
| q' | [kg/(m ² ·s)] | Mass flux |
| t | [s] | Time |
| u | [m] | Displacement |
| u^e | [m] | Element nodal displacement |
| ν | [-] | Drained Poisson's ratio |
| ν_c | [-] | Poisson's ratio of undamaged material |

Roman capital letters

| | | |
|------------|--------------------|---|
| A | [s ⁻¹] | Pre-exponential or frequency factor |
| A_e | [m ²] | Element surface area |
| A_r | [m ²] | Surface area of radiation |
| E | [Pa] | Elastic modulus |
| E_a | [kJ/mol] | Activation energy |
| E_c | [Pa] | Elastic modulus of undamaged material |
| E_{cr} | [Pa] | Elastic modulus of crack |
| G | [Pa] | Drained shear modulus |
| G_m | [Pa] | Shear modulus of matrix |
| H | [Pa] | Biot coefficient |
| H_1 | [Pa] | Specific storages coefficient of fluid due to applied stress |
| I_c | [J] | Elastic strain energy |
| K | [Pa] | Drained bulk modulus |
| K_e | [Pa] | Effective bulk modulus |
| K_{in} | [Pa] | Bulk modulus of inclusion |
| K_m | [Pa] | Bulk modulus of matrix |
| R | [kJ/(kmol·K)] | Universal gas constant (=8.314) |
| R_0 | [-] | Standard transformation matrix |
| R_1 | [Pa] | Specific storages coefficient of fluid due to applied pore pressure |
| R_Ω | [-] | Residual of spatial domain |
| R_Γ | [-] | Residual of boundary |
| S | [-] | Replacement of cement by mass with silica fume |
| S_d | [-] | Moisture content (or moisture saturation degree) |
| S_d^0 | [-] | Initial moisture content (or moisture saturation degree) |
| S_w | [-] | Liquid water saturation degree |
| T | [K] | Temperature |
| T^e | [K] | Element nodal temperature |
| M_i | [kg/mol] | Mole mass of i |
| M_w | [kg/mol] | Mole mass of water |
| N_i | [-] | Shape functions |
| U_e | [J] | Element total potential strain energy |
| U_{te} | [J] | Element strain energy |
| V_0 | [m ³] | Bulk volume of cement paste |
| V_l | [m ³] | Volume of liquid phase in capillary pores |

| | | |
|-------|---------|--|
| V_m | $[m^3]$ | Volume of moisture |
| V_v | $[m^3]$ | Volume of vapor phase in capillary pores |

Greek letters

| | | |
|----------------------|---------------------------|---|
| α | [-] | Damage variable |
| α_b | [-] | Biot-Willis coefficient |
| α_c | [-] | Degree of hydration of cement |
| α_p | [-] | Coefficient of equivalent expansion of vapor pressure |
| α_s | [-] | Degree of hydration of silica fume |
| α_t^e | $[^{\circ}C^{-1}]$ | Coefficient of effective thermal expansion |
| β | [-] | Thermal decomposition degree of hardened cement paste |
| γ | [-] | Shear retention factor |
| δ_{ij} | [-] | Kronecker delta (if i equals j , $\delta_{ij}=1$, else $\delta_{ij}=0$) |
| ε | [-] | Total strain |
| ε' | [-] | Effective strain(=total strain-effective thermal strain) |
| ε_0 | [-] | Initial strain |
| ε_{0v} | [-] | Potential volume strain |
| ε_{bcp} | [-] | Basic creep |
| ε_{ccp} | [-] | Microcracking induced strain of free expansion |
| ε_{con} | [-] | Elastic strain of concrete |
| ε_{cp} | [-] | Total creep strain |
| ε_{cr} | [-] | Crack strain |
| ε_{cr}'' | [-] | Stress free crack strain |
| ε_e | [-] | Strain at peak stress under uniaxial tension |
| ε_{mcp} | [-] | Material degradation induced creep strain |
| ε_{th} | [-] | Free thermal strain |
| ε_r | [-] | Emissivity of thermal radiation |
| ε_{th}^e | [-] | Effective thermal strain |
| ε_{tr} | [-] | Transient creep |
| ζ | [-] | Increment of fluid content |
| η | $[N \cdot s/m^2]$ | Dynamic viscosity |
| κ | [-] | history dependent damage parameter |
| λ | $[W/(m \cdot ^{\circ}C)]$ | Thermal conductivity |
| μ | [-] | Strain softening parameter |
| ρ | $[kg/m^3]$ | Mass density |
| ρ_c | $[kg/m^3]$ | Density of cement |
| ρ_{hcp} | $[kg/m^3]$ | Density of hardened cement paste |
| ρ_{SF} | $[kg/m^3]$ | Density of silica fume |
| ρ_v | $[kg/m^3]$ | Mass density of vapor |
| ρ_w | $[kg/m^3]$ | Mass density of water |
| σ | [Pa] | Stress |
| σ^e | [Pa] | Effective stress |
| σ_r | $[W/(m^2 \cdot K^4)]$ | Stefan-Boltzmann constant |
| $\dot{\phi}$ | $[W/m^3]$ | Internal heat generating rate |
| ν | $[m^3/kg]$ | Specific volume |
| ω_j | [-] | Weighting function |

| | | |
|----------|-----|---------------------------|
| Γ | [-] | Boundary |
| Ω | [-] | Spatial domain of element |
| Φ | [W] | Radiation heat |

Matrices and vectors

| | |
|---------------|--|
| $[B]$ | Geometric matrix |
| $[C]$ | Heat capacity matrix |
| $[D]$ | Elastic matrix |
| $[K]$ | Heat conductivity matrix |
| $[K']$ | Mass capacity matrix |
| $[K'']$ | Mass transport matrix |
| $[K_1]$ | Stiffness matrix |
| $\{F'\}$ | Mass transport right-hand vector |
| $\{F_1\}$ | Mechanical analysis right-hand vector |
| $\{p\}$ | Vapor pressure vector |
| $\{\dot{p}\}$ | Time derivative of vapor pressure vector |
| $\{P\}$ | Thermal right-hand vector |
| $\{T\}$ | Temperature vector |
| $\{\dot{T}\}$ | Time derivative of temperature vector |
| $\{u\}$ | Displacement vector |

List of abbreviations

| | |
|-------------------|--|
| AFt | Ettringite |
| CH | Calcium hydroxide |
| C ₂ S | Dicalcium silicate 2CaO·SiO ₂ |
| C ₃ A | Tricalcium aluminate 3CaO·Al ₂ O ₃ |
| C ₃ S | Tricalcium silicate 3CaO·SiO ₂ |
| C ₄ AF | Calcium ferroaluminate 4CaO·Al ₂ O ₃ ·Fe ₂ O ₃ |
| C-S-H | Calcium silicate hydrates |
| FEM | Finite element method |
| HPC | High performance concrete |
| HSC | High strength concrete |
| ITZ | Interfacial transition zone |
| LITS | Load-induced thermal strain |
| MIP | Mercury intrusion porosimetry |
| NMR | Nuclear magnetic resonance |
| NSC | Normal strength concrete |
| OPC | Ordinary Portland cement |
| SF | Silica fume |
| <i>w/b</i> | Water to binder ratio |
| <i>w/c</i> | Water to cement ratio |

Chapter 1

General introduction

1.1 Development of high-performance concrete

Nowadays, high-performance concrete (HPC), as it can satisfy the expectations for excellent mechanical properties and a long service life, is increasingly applied in various structures, such as bridges, tunnels, high-rise buildings, and large-span infrastructures. The history of HPC can be traced back to the early 1980s and it has been extensively developed since 1990. In the fabrication, water reducing agents and fine mineral admixtures are usually added, leading to denser concrete with high strength and better durability compared with normal-strength concrete (NSC). Due to its high strength, structural elements of HPC are relatively light and slender, which offers significant economic, architectural, and structural advantages over conventional concrete. It can also result in a better use and conservation of our limited natural resources and relatively mitigate the environmental damage of concrete production. The broadly accepted definition of HPC (with high strength) is the concrete with compressive strength more than 60 MPa, elastic modulus higher than 40 GPa, current flow in a 6-hour chloride permeability test less than 500 coulombs, 90 day drying shrinkage less than 0.04%, and slump greater than 200 mm for fresh concrete [Aitcin, 1998; Feng, 1992].

1.2 Fire risk

Regarding the fire resistance, generally speaking, concrete has much better fire resistance capacity than other materials, such as steel, and it always provides a cover to protect reinforcement. However, from the evidence of fire accidents that have happened in reality, it has been found that HPC underwent drastic damage under fire conditions and its fire resistance capacity is much lower than NSC. For example, on 18th November, 1996, a fire occurred in the Channel Tunnel connecting England with France. Along a 50-metre length of the tunnel, the 0.4-meter thick tunnel lining was reduced to a mean depth of 0.17 meters, with the thinnest area being 0.02 meters (Fig. 1.1 (a)). Although nobody was killed during the accident, with the spalled concrete falling from above, it was quite dangerous for firefighters to extinguish the fire [Colombo, 2001]. Other fire accidents also caused severe damage to HPC structures along with economic losses and even human consequences, such as the fire in the Mont Blanc Tunnel connecting France with Italy in 1999 (Fig. 1.1 (b)) and the Tauern Tunnel fire in Austria in 1999. Fire can cause damage to NSC as well, such as the collapse of an eight-story concrete building in Hengyang city in China in 2003 and the partial collapse of the architecture building in Delft University of Technology in the Netherlands in 2008 (Fig. 1.2). It is conceivable that if the two buildings were made of HPC, the loss could be even greater due to the lower fire resistance capacity of HPC.

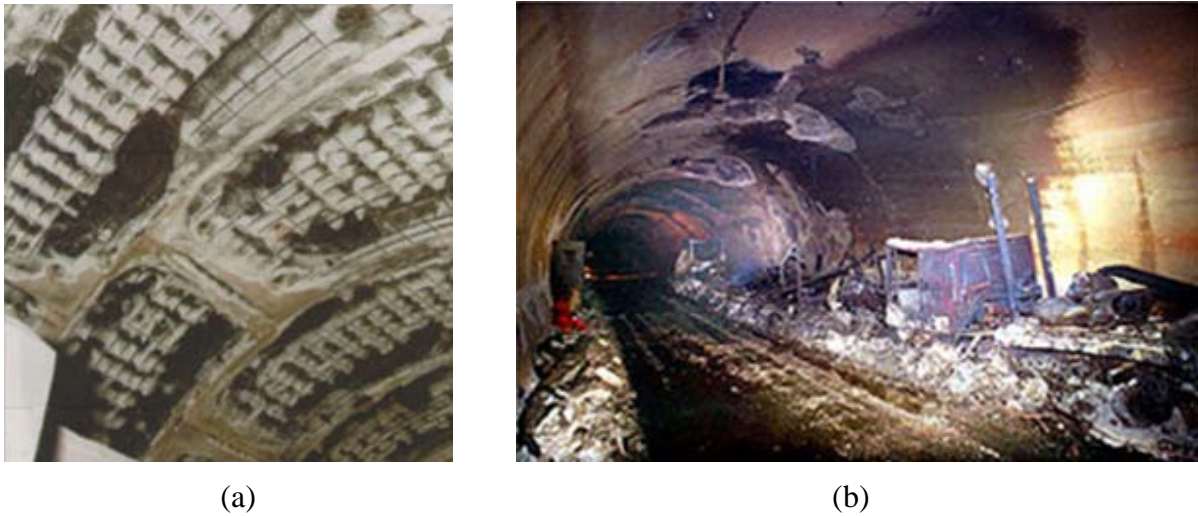


Fig. 1.1 Fire damage to concrete of Channel Tunnel (a) and Mont Blanc Tunnel (b).



Fig. 1.2 Architecture building before (a) and after (b) fire in Delft University of Technology.

The aforementioned fire disasters of HPC structures have clearly shown that HPC is not perfect; it has some shortcomings, i.e., when exposed to elevated temperatures, it can fail in brittle or even violent manners (explosive spalling) and its relative damage extent is higher than that of NSC [Peng, 2000]. Also laboratory experiments have evidenced the large damage to HPC when exposed to high temperatures (Fig. 1.3).



(a) HPC-70 with 100% moisture content



(b) HPC-110 with 88% moisture content



(c) HPC-120 with 100% moisture content

Fig. 1.3 Explosive spalling of unloaded 100 mm HPC cubes with different moisture contents under fire condition (The temperature range of spalling occurrence was 480 to 510 °C and the heating duration was around three minutes) [Peng, 2000].

1.3 Fire damage

1.3.1 Fire damage categories

In general, fire damage to concrete can be classified into two categories: the mechanical damage and the chemical damage. The chemical damage is caused by the dehydration and decomposition of hardened cement paste and the transformation and decomposition of aggregates, which is reflected in the variation of material properties, such as the elastic modulus, the strength, and the permeability. The mechanical damage, which is in the form of cracking or even spalling, is due to the thermal stress induced by the temperature gradient, the vapor pressure, and the volume expansion mismatch between aggregates and matrix.

1.3.2 Spalling

Among those damages, spalling is the most detrimental to concrete structures as it can cause direct exposure of steel reinforcement to fire, resulting in failure of concrete elements. The term 'spalling' is used to describe the separation of a portion of concrete from a structural element or a specimen. It can be either a progressive and non-explosive separation of the surface layer [Sanjayan and Stocks, 1993; Mindeguia et al., 2010], or a sudden and violent/explosive concrete disintegration accompanied by the release of a large amount of energy which projects the broken concrete fragments with high velocity without any warning

[Peng, 2000; Phan and Carino, 2002; Noumowe et al., 2009]. Explosive spalling shows a much higher probability in HPC than in NSC. It has also been found that spalling is closely related to the heating rate. The higher the heating rate is, the higher the risk of spalling is [Hertz, 1992; Chan et al., 1999; Kalifa et al., 2000].

1.3.3 Spalling hypotheses

Two hypotheses have been proposed to explain spalling: the vapor pressure mechanism [Anderberg, 1997; Peng, 2000] and the temperature gradient induced thermal stress mechanism [Bažant, 1997; Ulm et al., 1999a, 1999b]. The first hypothesis supposes that heating produces water vapor in concrete and as the permeability of HPC is low, which limits the ability of vapor to escape, a build-up of vapor pressure results. When heating continues, the vapor pressure increases until the internal stresses/energy becomes very high, resulting in sudden and explosive spalling. The second hypothesis is based on the fact that heating causes the thermal expansion of concrete. For different parts of concrete, the expansion is different. Due to the incompatibility of volume changes, thermal stresses are induced, causing a sudden failure (spalling) of the solid together with the release of the potential energy. Another possible explanation of spalling is the combination of the two hypotheses [Bažant, 1997; Phan and Carino, 2002; Noumowe et al., 2009]. The detailed discussion on spalling hypotheses is shown in Chapter 2.

1.4 Current state of spalling modeling

Since HPC is prone to spalling under fire conditions, the question is how to prevent spalling and hence minimize the shortcomings of HPC. To achieve this goal, first, the mechanism of spalling should be understood. To this end, considerable experimental and modeling work has been conducted by researchers (Chapter 2 Literature review). With regard to the modeling, in most of the existing models, the spalling phenomenon is analyzed at the macro-level, where concrete is treated as a homogeneous material, the material properties are expressed as a function of temperature, and the equation of ideal gas is usually adopted for the determination of the vapor pressure generated in concrete. The following modeling aspects are still inadequate:

- The meso-level spalling analysis.
- The heating history-based thermal decomposition prediction of hardened cement paste.
- The precise prediction of vapor pressure.
- The heating history-based prediction of material properties.
- The quantitative investigation of the mechanism of spalling.
- The energy-based analysis of spalling.

In view of the current state of the analysis of spalling, the scope, the objectives, and the strategy of this study are shown below.

1.5 Scope and objectives of this study

A meso-level numerical model is proposed in this thesis to analyze the fire spalling of HPC in a quantitative manner. The results of this study can provide a guidance and reference to

engineers and researchers for working out measures to prevent HPC from spalling and to designers for designing HPC structures with high fire resistance capacity. The main objectives of this study are as follows:

- As the spalling mechanism of heated HPC is still not clear and the quantitative analysis is still inadequate, the first objective of this study is to investigate the spalling mechanism in a quantitative manner.
- In view of the fact that the heating history effect on the material properties hasn't been considered in the existing models, the second objective of this study is to propose a heating history-based material property prediction model to investigate the spalling mechanism as accurately as possible.
- The third objective of this study is to quantitatively study the influencing factors of spalling, such as the moisture content and the heating rate.

1.6 Research strategy of this study

In this thesis, the following aspects are considered in the fire spalling study:

- The thermal decomposition of hardened cement paste.
- The vapor pressure.
- The moisture migration.
- The thermal decomposition-induced variation in material properties, such as the permeability and the elastic modulus.
- The non-linear mechanical behavior of the material.

The following factors are not considered:

- The drying shrinkage of hardened cement paste.
- The time-dependent/basic creep of heated hardened cement paste.
- The hydration of the residue unhydrated cement.
- The effect of vapor pressure on the decomposition kinetics of hardened cement paste.

The drying shrinkage and the time-dependent/basic creep (Chapter 2) of hardened cement paste are assumed to have little effect on fire spalling since it has been found that fire spalling mainly occurs in the first several minutes of heating [Sanjayan and Stocks, 1993; Peng, 2000; Pereira et al., 2011]. The load-induced/transient thermal creep (Chapter 2) is, however, accounted for in the mechanical analysis (Chapter 7). The hydration of the residue unhydrated cement and the effect of vapor pressure on the decomposition kinetics of hardened cement paste are assumed negligible.

1.7 Outline of this thesis

This thesis consists of nine chapters. In Chapters 3 through 7, five different modeling parts of fire spalling are proposed and described. In Chapter 8, the five modeling parts are synthesized and implemented for a meso-level study of spalling. The conclusions and the prospects of the study are in Chapter 9 (Fig. 1.4):

Chapter 1 is the general introduction. The background, the objectives, and the scope of this study are presented.

Chapter 2 is the literature review. The state of the art of fire damage modeling of HPC is reviewed based on a literature survey.

Chapter 3 deals with the temperature field determination. In this chapter, the numerical solution of the transient temperature field is presented. The thermo-mechanical coupling phenomenon is discussed.

Chapter 4 is about the thermal decomposition prediction of hardened cement paste. Based on the kinetic and stoichiometric analysis, the decomposition and the volume evolution of various constituents in hardened cement paste are predicted according to the heating history.

Chapter 5 presents the vapor pressure analysis. The analysis consists of two parts: the determination of vapor pressure and the analysis of the mechanical effect of vapor pressure. The vapor pressure determination is based on the application of steam tables and the analysis of the mechanical effect of vapor pressure is based on the theory of poroelasticity. The coupling phenomenon between solid and vapor is also discussed.

Chapter 6 deals with the moisture transport. The moisture migration driven by the vapor pressure gradient is analyzed. In the analysis, the evolution of the permeability of matrix with the heating process is predicted and the effects of the slip-flow and the liquid water saturation degree on the permeability are considered. The governing equation of the moisture transport is obtained according to the mass conservation principle and is solved numerically.

Chapter 7 focuses on the mechanical analysis. The fixed anisotropic smeared crack concept is employed to analyze the non-linear thermo-poro mechanical behavior of heated concrete. Both the thermal load and the load of vapor pressure are considered. The transient creep is also accounted for in the constitutive relation. A numerical method for the prediction of the decrease of elastic modulus of hardened cement paste induced by thermal decomposition is proposed.

Chapter 8 shows the spalling investigation. In this chapter, all modeling parts presented in the previous chapters are integrated to analyze the spalling phenomenon of heated concrete on a meso-level. To quantitatively study the spalling mechanism, the thermo-chemo-hydro-mechanical behavior of both HPC and NSC with different moisture contents under two heating conditions, i.e., fast heating (ISO 834 fire) and slow heating, is investigated. The mechanical failure is also analyzed from the energy perspective.

Chapter 9 consists of conclusions and prospects. Some remarks and future developments are presented.

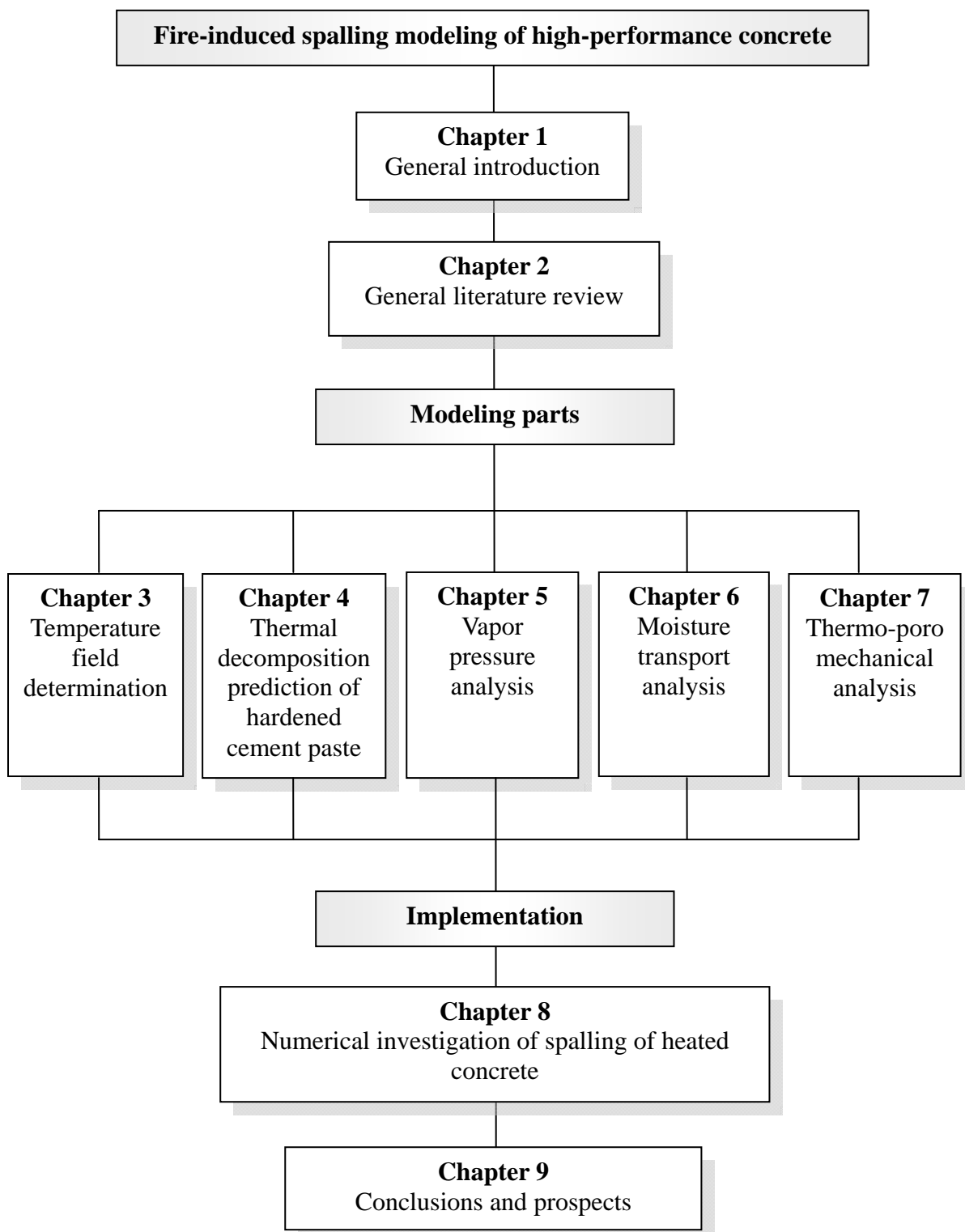


Fig. 1.4 Outline of thesis

Chapter 2

General literature review

HPC will undergo thermo-mechanical degradation or even explosive spalling under high temperature conditions, such as fire, and the safety of concrete structures will be endangered. To investigate the damage mechanism and to prevent concrete from spalling, much experimental and modeling work has been conducted in the past. A brief review is presented in this chapter.

2.1 Experimental study on fire damage

With regard to spalling, Hertz [1992] investigated the influence of silica fume on spalling. It was found that dense concrete was more likely to spall and the risk of explosive spalling increased with the increase of moisture content, the decrease of permeability, the decrease of tensile strength, and the increase of heating rate. Anderberg [1997] also found that the lower the heating rate was, the lower the risk of spalling. Sanjayan and Stocks [1993] studied the fire spalling of reinforced concrete slabs and observed that HSC was more prone to spalling than NSC under fire loads and the spalling generally occurred in the early stage of fire. Phan and Carino [2002] conducted spalling tests on cylinder specimens of high-strength concrete. The heating rate of the furnace was 5 °C/min. In the unstressed test, when spalling occurred, the measured surface temperature of the specimens was in the range of 280 °C to 320 °C after heating for about 2 hours. It was concluded from the test results that the vapor pressure was the primary cause for spalling and the thermal stress induced by temperature gradient was secondary. Peng [2000] experimentally investigated the relationship of the concrete strength, the moisture content, and the spalling probability. The test results showed that the higher the concrete strength and the moisture content, the higher the spalling probability. The temperature range of spalling occurrence was 480 °C to 510 °C and the heating duration was around three minutes. Noumowe et al. [2009] studied the high-temperature behavior of lightweight aggregate concrete. The heating rate of the oven was 1 °C/min. After heating for more than 10 hours, explosive spalling occurred when the temperature at the surface of the specimens was between 290 °C and 430 °C.

From the reported test results of spalling, it can be seen that vapor pressure is supposed playing an important role in spalling. To investigate the vapor pressure in heated concrete, Consolazio et al. [1998] measured both the transient temperature and vapor pressure in mortar subjected to radiant heating. The measured peak value of the vapor pressure was around 3 MPa. No spalling happened in the test. Kalifa et al. [2000] experimentally recorded the vapor pressure in concrete exposed to radiant heating. The highest value of the vapor pressure was less than 4 MPa and the peak moved inward with the heating process. The saturation front

(moisture clog) was also observed. Mindeguia et al. [2010] conducted a similar test to Kalifa's and got the similar results.

In addition to spalling, concrete will experience material degradation, such as the decrease of the elastic modulus and the strength. The effect of high temperatures on the mechanical properties of concrete was investigated by many researchers [Schneider, 1998; Phan and Carino, 1998; Peng, 2000; Kodur et al., 2008b; Husem, 2006; Youssef and Moftah, 2007; Behnood and Ziari, 2008]. The test methods used can be classified into three categories:

- Stressed. In the stressed test, a load is applied to the specimen prior to and during the heating. The mechanical test is carried out when the specimen is hot. This test method simulates the real situation of heated structural elements. However, the tests of this method are rarely found in the literature.
- Unstressed. In the unstressed test, the specimen is heated without preload and tested hot.
- Unstressed residual. In the unstressed residual test, the specimen is also heated without preload, but tested when it is cooled to room temperature.

The decreases of the compressive strength and the elastic modulus of concrete under unstressed and unstressed residual test conditions are respectively shown in Fig. 2.1 and Fig. 2.2, which were summarized by Phan and Carino [1998].

Phan and Carino [1998] concluded that the degradation of HSC with respect to temperature was different from that of NSC. "The differences are more pronounced in the temperature range between 25 °C and approximately 400 °C, where higher-strength concretes have higher rates of strength loss than lower-strength concretes. These differences become less significant at temperatures above 400 °C. Compressive strengths of HSC at 800 °C decrease to approximately 30% of the original room-temperature strengths. A temperature of 300 °C marks the beginning of higher rate of decrease in modulus of elasticity for all concretes." Phan and Carino also pointed out that "current design recommendations for compressive strength and modulus of elasticity of fire-exposed concretes are more relevant to NSC than HSC. The Eurocode and CEB design curves have questionable application to HSC".

From a microscopic point of view, microstructure damage induced by thermal decomposition of constituents in hardened cement paste occurs when concrete is exposed to elevated temperatures. The coarsening effect of high temperature on hardened cement paste were verified experimentally by Lin et al. [1996], Luo et al. [2000], Liu [2006], Caré [2008], Peng and Huang [2008], and Fares et al. [2010]. It has been found that ettringite (AFt) and CH start to decompose at 70 °C and 430 °C, respectively, and the chemical-bound water in C-S-H gel is gradually released once the temperature exceeds 600 °C [Shimada and Young, 2001; Pourchez et al., 2006; Zelić et al., 2002; Peng and Huang, 2008; Lin et al., 1996]. The decomposition kinetics of hardened cement paste was investigated by Peng and Huang [2008]. It was found that the decomposition degree was closely related to the heating temperature and the heating duration. The kinetics equation of C-S-H decomposition was also formulated in their study.

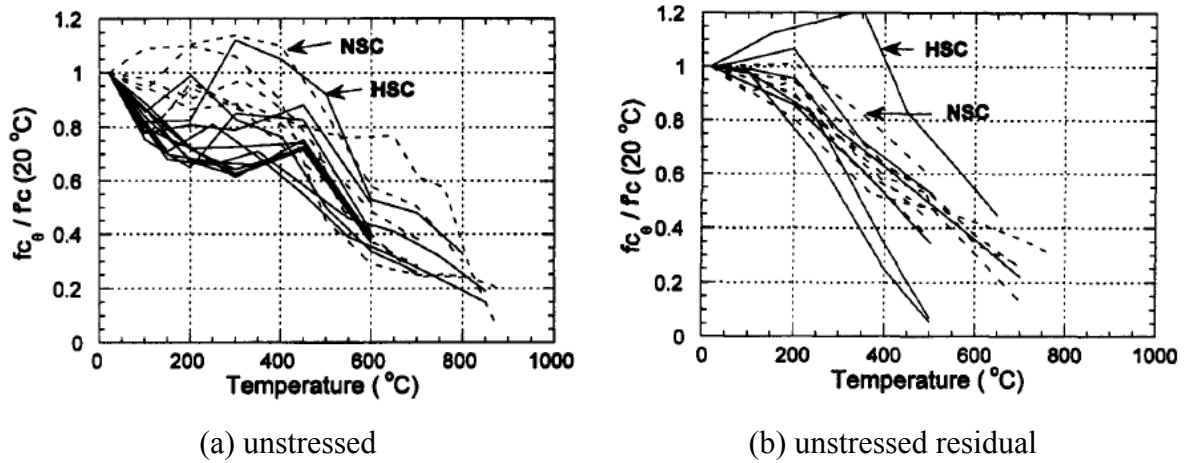


Fig. 2.1 Compressive strength vs. temperature by (a) unstressed and (b) unstressed residual tests [Phan and Carino, 1998].

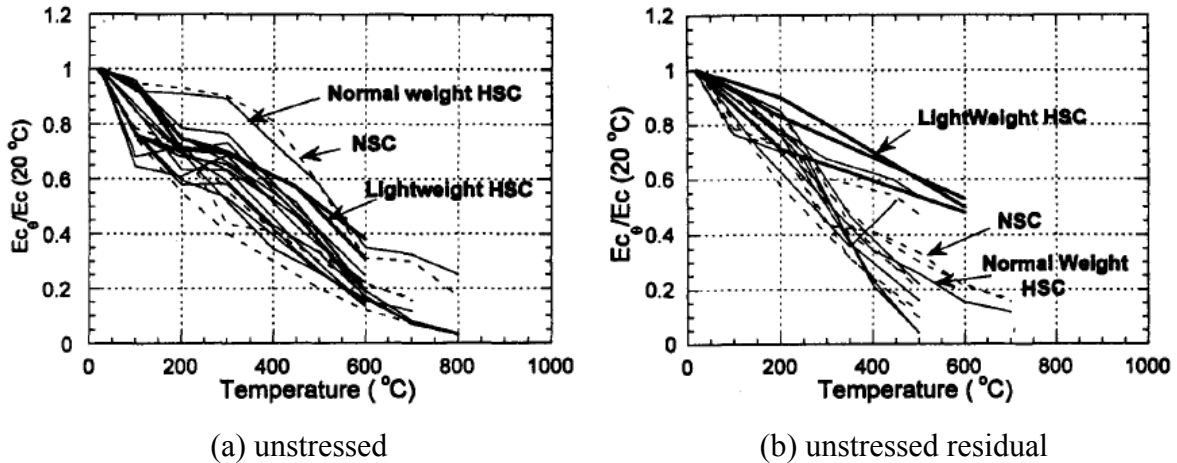
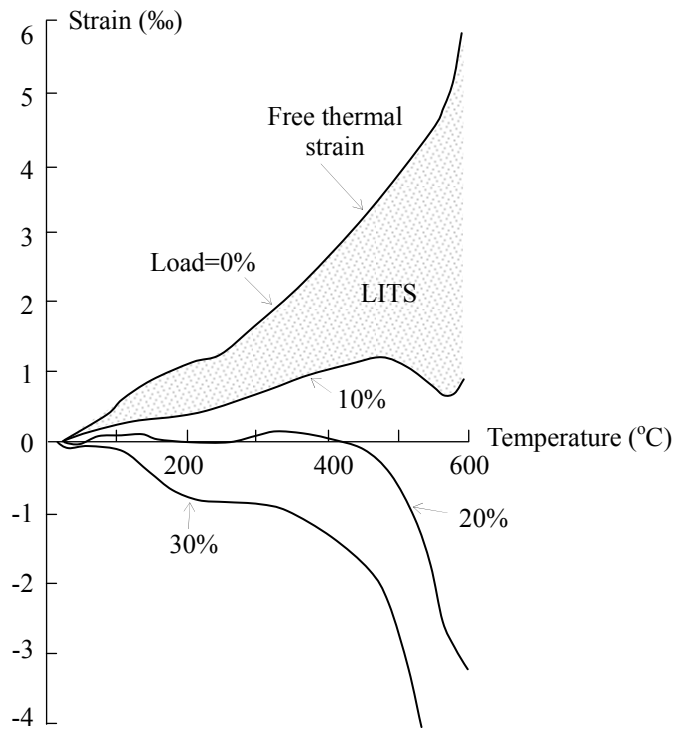


Fig. 2.2 Elastic modulus vs. temperature by (a) unstressed and (b) unstressed residual tests [Phan and Carino, 1998].

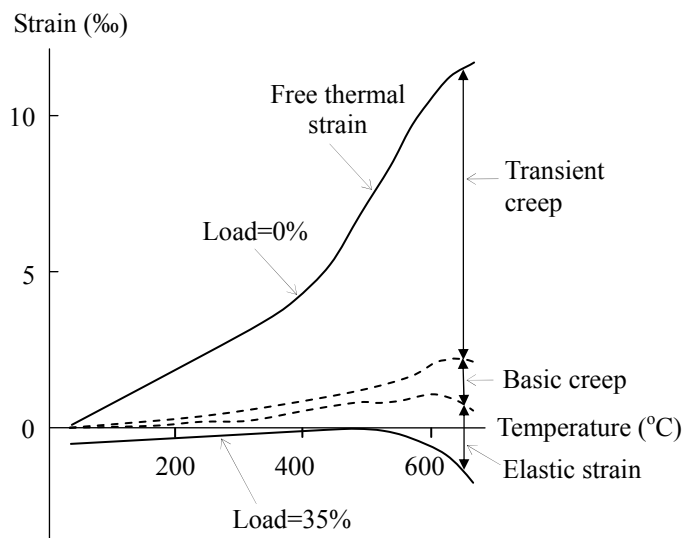
For creep of heated NSC, Anderberg and Thelanderson [1976] and Khoury et al. [1985] experimentally investigated the thermal strain of concretes under different loads (Fig. 2.3). It was found that big differences exist between the thermal strain without load (free thermal strain) and that under load. The difference was referred to as the load-induced thermal strain (LITS), which comprised transient creep, basic creep, and elastic strain (Fig. 2.3 (b)). For the transient creep, Anderberg and Thelanderson [1976] proposed an expression according to the test results as

$$\varepsilon_{tr} = -k_{tr} \frac{\sigma}{f_c} \cdot \varepsilon_{th} \tag{2.1}$$

where σ/f_c is the stress to strength ratio, k_{tr} is a coefficient, which ranges from 1.8 to 2.35, and ε_{th} is the free thermal strain. Schrefler et al. [2002] pointed out that for stress analysis of heated concrete, the transient creep or LITS should be taken into account, otherwise the results would be erroneous.



(a) Experimental results of load-induced thermal strain at heating rate of 1.0 °C/min [Khoury et al, 1985].



(b) Components of load-induced thermal strain at heating rate of 5 °C/min [Anderberg and Thelanderson, 1976].

Fig. 2.3 Transient creep of heated concrete.

2.2 Fire damage modeling - state of art

To reveal the fire damage mechanisms of concrete and to theoretically quantify and predict the degree of damage, considerable modeling work has been conducted. The fire damage modeling concerns several aspects: the temperature field determination, the vapor pressure modeling, the moisture transport analysis, the mechanical modeling, and the material degradation prediction. Four types of models exist so far:

- The material degradation modeling.
- The heat and moisture transport modeling.
- The structural level fire damage modeling.
- The spalling modeling.

2.2.1 Material degradation modeling

Regarding to the material degradation modeling, Tsai et al. [2005] worked out a model to predict the residual strength of heated concrete. In the model, the residual strength was empirically formulated as a function of the heating temperature and the exposure duration. Chiang et al. [2005] and Tanyildizi and Çevik [2010] used the artificial neural network and the empirical genetic-programming method, respectively, to get better fits to the experimental data for predicting the residual strength of concrete. Knaack et al. [2010] proposed a temperature-dependent expression of the compressive strength of concrete based on the curve fitting of the tests results. Ulm et al. [1999a] modeled the dehydration and its effects on material properties macroscopically. The dehydration was considered as an inverse process of hydration. An inverse linear relation between dehydration degree and the relative elastic modulus was assumed. Grondin et al. [2007] used a multi-scale (from meso-level to macro-level) model to predict the LITS under different loading and uniform temperature conditions. It was assumed that LITS was mainly attributed to the decrease of mechanical material properties, which was caused by the combination of the compressive load and the volume mismatch between matrix and aggregates. The isotropic damage model was employed to model the mechanical damage. The macro-level material properties were obtained by volume weighted averaging the properties of matrix and aggregate. The vapor pressure and the thermal gradient induced damage were not taken into account in the model.

2.2.2 Heat and moisture transport modeling

For the heat and moisture transport modeling, FEM is widely used for getting the numerical solution of the temperature and moisture distribution. The governing equation of heat transport can be derived from the law of energy conservation (the first law of thermodynamics) and Fourier's law of heat conduction. According to the law of mass conservation and Darcy's law and/or Fick's law, the governing equation of moisture transport can be obtained. Tenchev et al. [2001a, 2001b] used a coupled model to simulate the heat and moisture transport in a heated concrete wall. The latent heat of dehydration and vaporization was considered. The gaseous phase was assumed as an ideal gas. The volume fractions of the liquid phase and the gas phase were determined by using the sorption isotherm curves proposed by Bažant and Thonguthai [1978]. The amount of dehydrated water was expressed as a function of temperature following the model proposed by Bažant and Kaplan [1996]. The porosity was taken as temperature dependent and the permeability was taken as a function of the

temperature-induced increase of the cross section of the pores. In the models of Khoury et al. [2002] and Gawin et al. [2002, 2003], the permeability was expressed as a function of the temperature, the pore pressure, and the degree of the thermo-mechanical damage. Li et al. [2006] followed Gawin's model, but took the desalination process into account. The permeability of the model of Majumdar et al. [1995, 1997] was obtained by curve fitting of the experimental data. Consolazio et al. [1998] modeled the moisture transport in saturated mortar subjected to radiant heating. The boundary condition and the thermal material properties were modeled. However, the coarsening effect induced by the thermal decomposition of hardened cement paste was not considered. Chung et al. [2005, 2006] modeled the moisture transport in heated reinforced concrete. The transport of the gas phase and the liquid phase was modeled. The gas phase slip-flow [Klinkenberg, 1941] was considered. The influence of high temperatures on the permeability was, however, not considered and neither damage nor spalling was predicted. Benes and Mayer [2008] proposed a one dimensional model to analyze the temperature field, the moisture transport, and the vapor pressure in heated concrete. The material properties were taken as temperature dependent. The vapor phase was assumed as an ideal gas. Pont et al. [2011] presented a thermo-hydro model to determine the temperature and gas pressure fields in heated concrete. The vapor pressure was determined according to the ideal gas law and the material properties were temperature dependent.

2.2.3 Structural level fire damage modeling

Since the thermal behavior of each component affects the safety of a whole concrete structure, a number of structure-level analyses can be found in the literature. Hurst and Ahmed [1998] worked out a model to predict the thermal response of concrete slabs. In the model, the moisture migration and the vapor pressure, which followed the ideal gas law, were considered. The mechanical analysis, however, was lacking in the model. Huang et al. [1999, 2003a, 2003b] used an anisotropic layered damage model to model the membrane action of concrete slabs under fire conditions. The material properties were temperature dependent. Huang [2010] artificially introduced spalling into the structural mechanical analysis of slabs by using a 'void surface layer' of certain depth with zero mechanical strength and stiffness. Three cases of different depths of spalling were studied. From the numerical results, it was concluded that the membrane force in the slab could reduce the impact of spalling on the fire resistance of heated slabs. Zha [2003] simulated the fire resistance of columns and beams. The material properties were temperature dependent. The simulation results showed that the fire resistance of those elements could be increased by increasing the thickness of the concrete cover and the amount of reinforcement used. Lim et al. [2004] and Usmani and Cameron [2004] modeled the fire response of reinforced concrete slabs. The results showed that two-way slabs had better fire resistance capacity than one-way slabs because of the tensile-membrane effect. Schrefler et al. [2002], Khoury et al. [2002], Gawin et al. [2003], and Pont et al. [2005a] modeled the fire damage to structural elements. Schrefler et al. and Khoury et al. studied tunnel linings, Gawin et al. investigated a one-side heated wall, and Pont et al. modeled a 1.5-meter high hollow cylinder. The common features of their models are:

- The isotropic damage model was employed.
- The gas phase was treated as an ideal gas.
- The material properties were taken as temperature dependent.

The output of their models was the distribution of the damage degree in concrete elements.

Spalling was, however, not predicted. Bratina et al. [2007] and Kodur et al. [2008a, 2008b, 2009] modeled the fire resistance of concrete beams. In their models, the material properties were temperature dependent and were obtained from either the Eurocode or the ASCE Manual. The relationship between the bending moment and the curvature was analyzed to study the failure of the beam. In Kodur's model, spalling was predicted by simple descriptive assumptions. Caldas et al. [2010] investigated the interaction diagrams for the cross-section analysis and design of reinforced concrete elements under fire conditions. The material properties were taken from the Eurocode. Terro [1998] investigated the effect of thermal creep on the structural behavior of heated concrete elements. In the model, the total strain comprised free thermal strain and LITS. The free thermal strain was assumed linearly related to the content of aggregate and the base value was obtained from the test results of heated concrete with 65% aggregate content. The LITS was taken as linearly proportional to the stress level and the base value was taken from the empirical expression of heated concrete stressed with 30% the compressive strength. The modeling results showed that the thermal creep had little effect on the structural behavior of heated slabs, but had tremendous effect on the deformation of heated columns. Sadaoui and Khennane [2009] modeled the transient thermal creep of reinforced concrete columns. Two cases were studied: in the first case, the transient creep was considered explicitly as an additional component of the total strain and the expression of the creep proposed by Anderberg and Thelanderson [1976] was used; in the second case, the transient creep was considered implicitly through the variation of material properties recommended in the Eurocode. It was found that the results in the second case deviated much from the test results because of the double counts of the transient creep in both the elastic modulus and the ultimate strain. Ali et al. [2010] studied the fire behavior of HSC columns under different loads. In the model, the material properties were also taken from the Eurocode. The anisotropic damage model was employed. The vapor pressure was not considered and spalling was not predicted.

2.2.4 Spalling modeling

As spalling is the most detrimental damage to HPC, considerable spalling modeling work can be found in the literature. In the vapor pressure build-up mechanism of spalling (Chapter 1), a theory of moisture-clog spalling (Fig. 2.4) has been proposed [Bažant, 1997; Consolazio et al., 1998; Kalifa et al., 2000]. During thermal loading, the vapor migrates along the pressure gradient both outward to the atmosphere and inward to the lower temperature region. The inward migration will be impeded when a complete saturated layer/front is formed by condensation. Thus, the vapor can only escape outwardly. If the permeability is low, high vapor pressure will build up because of the high moisture content of the saturated layer and spalling may occur when the pressure reaches a certain value. The moisture clog phenomenon has been verified by van der Heijden [2011] using the nuclear magnetic resonance (NMR) test. However, no quantitative experimental or numerical evidences of moisture-clog spalling could be found so far in the literature.

Bažant [1997] stated that the vapor pressure could only trigger the happening of explosive spalling and the thermal stress induced potential energy might play a dominant role in explosive spalling as shown in Fig. 2.5 (a). The quantitative analysis was, however, lacking. Ulm et al. [1999] developed a chemo-plastic model to analyze the fire spalling of concrete rings of the Channel Tunnel (Chunnel). The plastic strain was used as an indicator for approximately evaluating the spalling depth in the concrete rings. It was concluded that

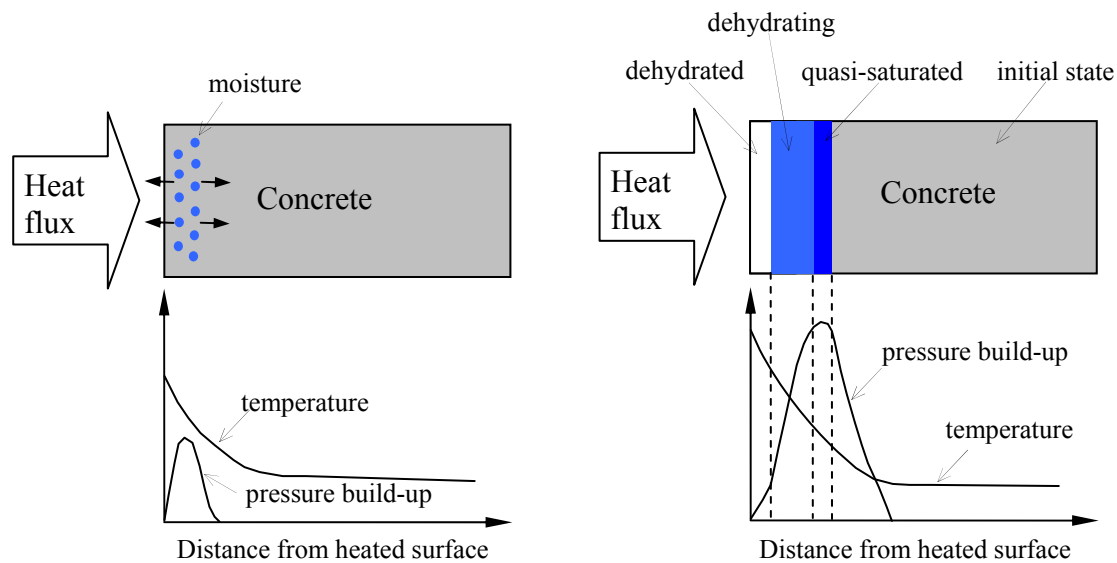


Fig. 2.4 Schematic illustration of moisture-clog and build-up vapor pressure.

spalling was caused by the restrained thermal dilatation induced compressive stress. The vapor pressure was, however, not considered. Bentz [2000] investigated the percolation of the interfacial transition zones (ITZ) and suggested that, by adding polypropylene fibers of 20 mm in length and 0.25 mm in diameter, the percolation route could be formed for vapor to escape and thus spalling could be prevented. Ichikawa and England [2004] used a one-dimensional model to simulate the spalling of the concrete wall of a nuclear reactor containment vessel. The vapor pressure was calculated using a set of formulated equations. Spalling was assumed to occur when the vapor pressure induced tensile stress exceeded the tensile strength of concrete. The thermal decomposition induced material degradation was not considered. Gawin et al. [2006] used a fully coupled model, where the gas pressure, the capillary pressure, the temperature, and the stress/strain were coupled together, to describe the concrete thermo-mechanical behavior. The vapor pressure was predicted using the ideal gas equation. The isotropic damage model proposed by Mazars [1989] was applied for the mechanical damage assessment. Spalling wasn't predicted directly. Instead, four spalling indices based on different failure modes, i.e., the shear failure (Fig. 2.5 (a)), the buckling failure (Fig. 2.5 (b)), the simplified fracture failure (Fig. 2.5 (c)), and the integrative failure, were used for the prediction. Dwaikat and Kodur [2009] proposed a one-dimensional model to predict the fire spalling of concrete elements. The spalling was assumed to occur when the calculated vapor pressure exceeded the temperature-dependent tensile strength of concrete. The vapor pressure was predicted by the use of the ideal gas equation. The moisture transport was analyzed and the expression of the evolution of permeability developed by Gawin et al. [1999] was used. The mass of water in concrete was predicted as a function of the pore pressure and the temperature using the semi-empirical expression of sorption isotherms developed by Bažant [1978]. De Moraes et al. [2010] proposed a model for the spalling of small specimens. In the model, the vapor pressure and the moisture transport were considered. The linear isotropic elastic law and the elasto-plastic law were used for the mechanical analysis. It was inferred that spalling was attributed to the superposition of the effects of vapor pressure and the thermal dilatation. The material properties were taken as temperature dependent. Although small specimens were analyzed, the aggregate and matrix were not treated distinctively, i.e., concrete was treated as homogenous. Thus, the local effect of vapor pressure and the volume mismatch between aggregates and matrix were not accounted for.

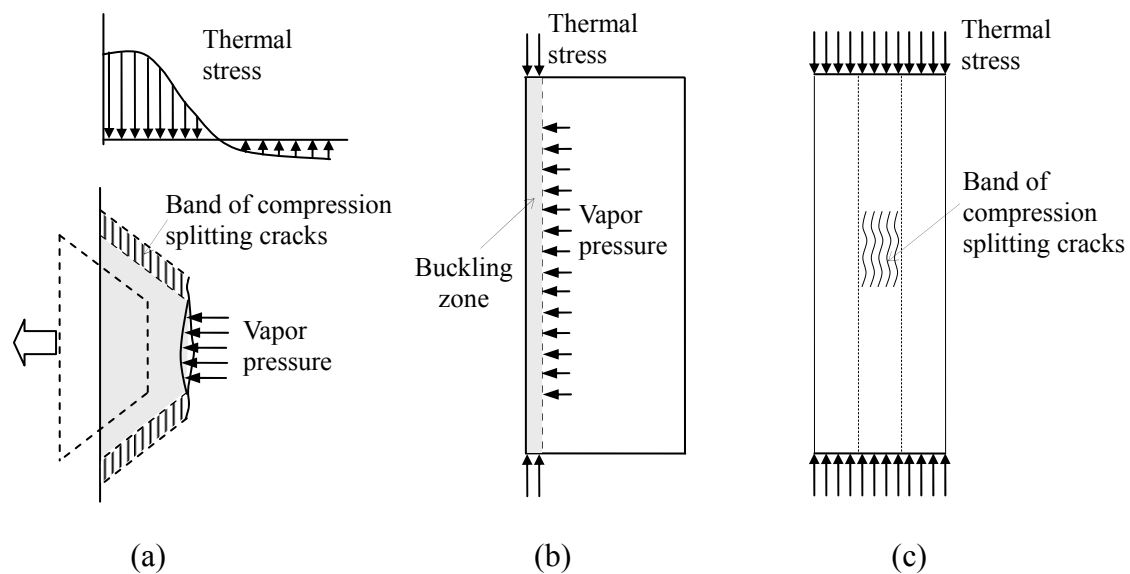


Fig. 2.5 Possible mechanisms of explosive thermal spalling: (a) pressure shear model, (b) buckling model, and (c) compression splitting cracking model.

The afore mentioned models analyzed the spalling phenomenon at the macro-level, where concrete was treated as a homogeneous material. Few meso-level studies can be found in the literature. Tenchev and Purnell [2005] investigated spalling on an arithmetic parallel averaged meso-level. In the model, equal strains and different stresses were assumed. The macroscopic stresses and the stiffness matrix were obtained by weighted averaging those of mortar and aggregate. The volume fractions of both mortar and aggregate were equal to 0.5. The isotropic damage model was used for the mechanical analysis. It was concluded that the plane of spalling was parallel to the main compressive stress because of the tensile transverse stress induced by the compressive stress. The material properties were temperature dependent. The ideal gas equation was used for the determination of vapor pressure. Fu et al. [2004a, 2004b, 2007] used a mesoscopic thermal-elastic damage model to investigate both the temperature gradient and the thermal volume mismatch induced cracks in heated concrete. The material was treated as brittle elastic. The material properties were temperature dependent. Although the crack pattern was simulated, spalling was not predicted and vapor pressure was not considered. Gawin et al. [2004], Pont et al. [2005a], and Li et al. [2006] modeled the fire damage of small specimens. However, the specimens were still treated as homogenous and spalling wasn't predicted.

2.3 Modeling evaluation and conclusions

Fire spalling of concrete is a complex phenomenon. The complexity stems from the coupled thermo-chemo-hydro-mechanical reaction of concrete to the elevated temperatures and from the reaction itself. Several aspects need to be incorporated in the damage analysis: the temperature field, the thermal decomposition of hardened cement paste, the vapor pressure, the moisture transport, the material degradation, and the mechanical damage. From the above literature survey, it can be seen that, so far, none of the existing models works well for analyzing the spalling phenomenon of heated concrete. The following modeling aspects are still inadequate:

- The study of the mechanism of fire spalling and the heating rate effect on spalling. The fire spalling mechanism is still not quantitatively explained and the heating rate effect study is also lacking.
- The meso-level spalling analysis. In most of the existing models, spalling is analyzed at the macro-level, where the concrete is treated as a homogenous material. Some details are, therefore, missing for the spalling investigation, such as the aggregate influence on the moisture transport, the decomposition of the matrix, the damage induced by the volume mismatch between aggregates and the matrix, the vapor pressure effect on the stress/strain field, etc.
- The prediction of the thermal decomposition of hardened cement paste. Since the microstructural evolution of matrix depends on the thermal decomposition and the properties of materials are closely related to the microstructure, it is of fundamental importance to appropriately evaluate the decomposition in the fire spalling analysis. However, there is no such a model available in the literature.
- The heating history-based prediction of material properties. In most existing models, material properties are taken as temperature dependent according to the experimental results. In the experiments, usually the heating rate is low and the heating duration is long to insure a uniform temperature distribution in specimens. Thus, a significant drying shrinkage of the matrix can be induced and the material properties are affected markedly. As fire spalling occurs in the first several minutes of heating, the shrinkage effect is negligibly small. The actual material properties under the fire condition can be much different from the temperature-dependent ones.
- The prediction of vapor pressure using steam tables. The ideal gas equation is usually adopted for the determination of vapor pressure in existing models. However, when the moisture saturation degree is high, water vapor behaves much differently from ideal gases, resulting in a large deviation. Therefore, when the steam table is used, better predictions can be expected.

In this thesis, the fire spalling phenomenon of concrete is investigated on a meso-level. In the analysis, the permeability and the elastic modulus of the matrix are predicted based on the thermal decomposition analysis. The decomposition of the matrix is predicted as a function of the heating history. The vapor pressure is determined by the use of steam tables. The moisture transport and the non-linear mechanical analyses are conducted. The fire spalling mechanism is investigated in a quantitative manner and the heating rate effect on spalling is also studied. The outline of this thesis is shown in Fig. 1.4.

Chapter 3

Temperature field determination

3.1 Introduction

In heated concrete, the complex thermo-hydro-mechanical reaction stems from the high temperature. It is, therefore, essential to predict the temperature field evolution for the spalling analysis. This modeling part is described and discussed in this chapter. The implementation for spalling analysis is shown in Chapter 8 (Fig. 3.1). In the modeling, the governing equation of the temperature field is presented. The FEM is applied for getting the solution. The thermo-mechanical coupling phenomenon is also discussed.

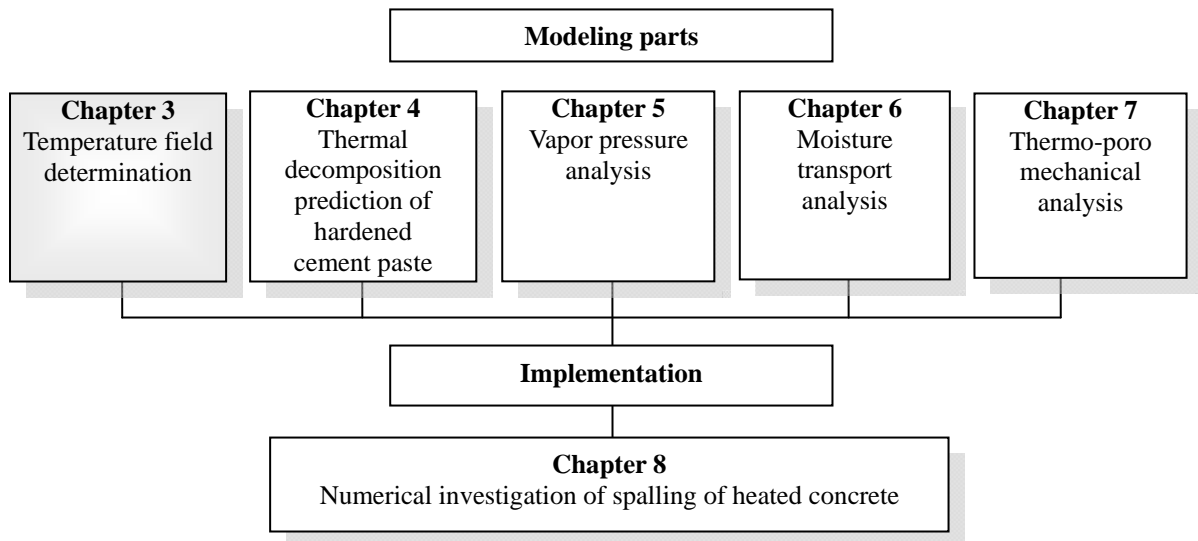


Fig. 3.1 Modeling parts of fire spalling analysis.

3.2 Temperature field determination

3.2.1 Fourier's law of heat conduction

It is well-known that, in a solid, heat conducts from the high to low temperature region, which can be described by Fourier's law as

$$q_i = -\lambda_i \frac{\partial T}{\partial x_i} \quad (3.1)$$

where T is the temperature, λ is the thermal conductivity, and q is the heat flux. The minus sign indicates that heat flows in the direction of decreasing temperature.

3.2.2 Governing equation of temperature field

Under a certain heating condition, the temperature field in a solid can be described by a differential equation (Eq. 3.2) deduced from the principle of energy conservation (the first law of thermodynamics) and Fourier's law.

$$\rho c \dot{T} = \frac{\partial}{\partial x_i} \left(\lambda_i \frac{\partial T}{\partial x_i} \right) + \dot{\phi} \quad (3.2)$$

where ρ is the mass density, c is the specific heat, $\dot{\phi}$ is the internal heat source, and \dot{T} is the time derivative of temperature.

3.2.3 Initial and boundary conditions

To solve Eq. 3.2, the initial and boundary conditions need to be specified. The initial condition is the temperature distribution in the solid before the start of heating. The boundary condition is the thermal interaction between the solid and the surroundings. The boundary condition can be classified into three types (Fig. 3.2):

(1) Specified boundary temperature. The boundary temperature is given, which can be uniform or vary along the boundary locations and/or with time. This condition can be mathematically expressed as

$$T|_{\Gamma} = T(x, y, z, t) \quad (3.3a)$$

with Γ being the boundary where the temperature is specified to be $T(x, y, z, t)$.

(2) Specified heat flux. By using Fourier's law, the mathematical formulation of the heat flux across the boundary surface can be described as

$$q_n|_{\Gamma} = -\lambda \frac{\partial T}{\partial n}|_{\Gamma} = q(x, y, z, t) \quad (3.3b)$$

where $\partial/\partial n$ is the differentiation along the outward normal to the boundary surface. Radiation belongs to this type of boundary condition. The heat flux can be derived from the following equation,

$$\Phi = \varepsilon_r A_r \sigma_r (T_1^4 - T_2^4) \quad (3.3b1)$$

where Φ is the radiation heat, σ_r is the Stefan-Boltzmann constant, ε_r is the emissivity, A_r is the surface area, and the subscripts 1 and 2 indicate the two bodies of radiation.

(3) Convection condition. When heat is transferred by the convection of the ambient gas, the boundary condition can be specified as

$$-\lambda \frac{\partial T}{\partial n} \Big|_{\Gamma} = h_c (T_{\Gamma} - T_f) \tag{3.3c}$$

where h_c is the convective heat transfer coefficient between the gas and the boundary of the solid.

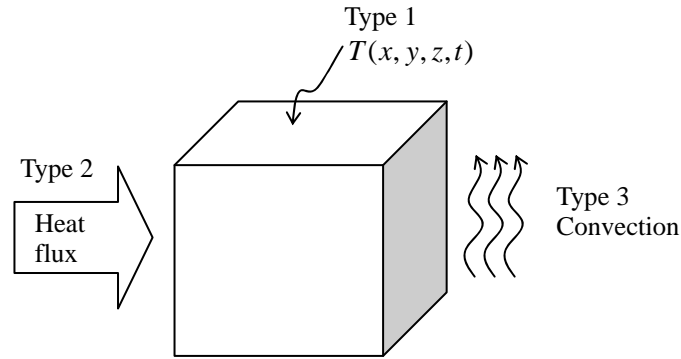


Fig. 3.2 Schematic illustration of three types of thermal boundary conditions of a solid.

3.2.4 Numerical solution of temperature field

The FEM is used for the determination of temperature field. The Galerkin weighted-residual scheme is applied [Zienkiewicz and Taylor, 2000]. By discretizing the domain into a number of finite elements, the approximate value of temperature in each element can be expressed in terms of nodal temperatures using the interpolation polynomial shape functions, N_i

$$T = \sum_{i=1}^n N_i T_i^e \tag{3.4}$$

where T_i^e is the element nodal temperature, n is the number of nodes of the element (Fig. 3.3).

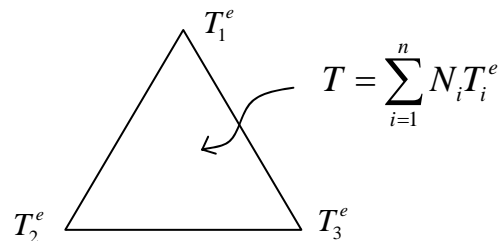


Fig. 3.3 Illustration of temperature field expressed by nodal temperatures in 2D three-node triangular element.

By substituting Eq. 3.4 into the governing equation and the boundary condition (Eq. 3.2 and Eq. 3.3), the residuals are obtained

$$R_{\Omega} = \frac{\partial}{\partial x_i} \left(\lambda \frac{\partial T}{\partial x_i} \right) - \rho c \frac{\partial T}{\partial t} \quad (3.5a)$$

$$R_{\Gamma_2} = \lambda \frac{\partial T}{\partial x_i} n_i - q \quad (3.5b)$$

$$R_{\Gamma_3} = \lambda \frac{\partial T}{\partial x_i} n_i - h_c (T_f - T_{\Gamma}) \quad (3.5c)$$

For three-node triangular element, by applying the Galerkin method, the following equation is obtained

$$\int_{\Omega} \omega_1 R_{\Omega} d\Omega + \int_{\Gamma_2} \omega_2 R_{\Gamma_2} d\Gamma + \int_{\Gamma_3} \omega_3 R_{\Gamma_3} d\Gamma = 0 \quad (3.6)$$

with

$$\omega_1 = N_i \quad (i = 1, 2, 3) \quad (3.6a)$$

$$\omega_2 = \omega_3 = -N_i \quad (i = 1, 2, 3) \quad (3.6b)$$

where Ω denotes the 2D domain of element, Γ_2 and Γ_3 are the boundary subjected to the second and third type boundary conditions. Integrating Eq. 3.6 by parts and summing up for all the elements yields

$$[C]\{\dot{T}\} + [K]\{T\} = \{P\} \quad (3.7)$$

with

$$[C] = \sum_e \int_{\Omega_e} \rho c N_i N_j d\Omega \quad (3.7a)$$

$$[K] = \sum_e \int_{\Omega_e} \lambda_i \frac{\partial N_i}{\partial x_l} \frac{\partial N_j}{\partial x_l} d\Omega + \sum_e \int_{\Gamma_3^e} h N_i N_j d\Gamma \quad (3.7b)$$

$$\{P\} = \sum_e \int_{\Omega^e} N_i \dot{\phi} d\Omega + \sum_e \int_{\Gamma_2^e} q N_i d\Gamma + \sum_e \int_{\Gamma_3^e} h T_f N_i d\Gamma \quad (3.7c)$$

As the time derivative of temperature presents in Eq. 3.7, the discretization of the time domain is needed. By applying the backward difference method, Eq. 3.7 can be expressed as

$$\left([K] + \frac{[C]}{\Delta t} \right) \{T_t\} = \{P_t\} + \frac{[C]}{\Delta t} \{T_{t-\Delta t}\} \quad (3.8)$$

where Δt is the given time interval. Thus, the temperature distribution at each time step can be obtained by solving Eq. 3.8.

3.3 One-way coupling of thermo-to-mechanical analysis

According to the thermomechanics, in a heated solid, a coupling phenomenon exists, i.e. the thermo-to-mechanical and vice versa. The thermo-to-mechanical is that the volume change induced by temperature change causes thermal stress in the solid; the mechanical-to-thermo is that an equivalent internal heat source (or sink) resulting from the mechanical loads influences the temperature development [Hsu, 1986]. For fully coupled analysis, the temperature field and the stress/strain field need to be solved simultaneously and unsymmetrical stiffness matrices are usually resulted. Regarding to the thermo-mechanical behavior of concrete, since the deformation of the solid is rather small and the resulting mechanical-to-thermo effect is also negligibly small, the one-way coupling of thermo-to-mechanical is considered in this thesis. As the temperature field is independent of the stress field in the one-way coupling, the analysis is mathematically simplified.

3.4 Application

The meso-level fire spalling analysis in this thesis is based on the experiments conducted by Peng [2000] (Chapter 8). The 100 mm concrete cube is modeled as a 2D two-phase (aggregate and matrix) composite. Three-node triangular elements are used for the discretization. In the temperature field prediction, the first type of boundary condition is used and the imposed surface temperature follows the standard heating curve recommended in ISO 834 [1999] as shown in Fig. 3.4. The heat sink induced by the thermal decomposition and the vaporization of free water in concrete is assumed negligibly small. The thermal material properties are taken as constant. The predicted evolution of temperature is compared with the test results [Peng, 2000] in Fig. 3.5/Fig. 8.5. It can be seen that the predicted results are in good agreement with the measured ones. The detailed description is shown in Chapter 8.

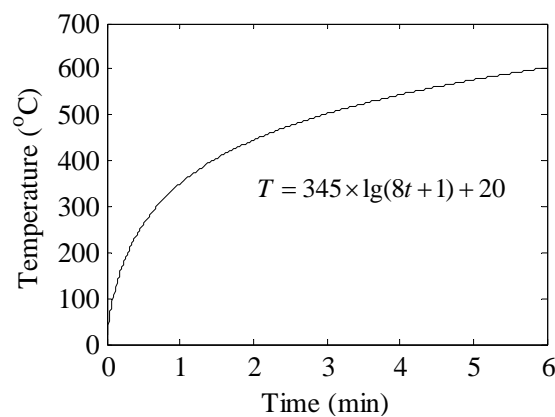


Fig. 3.4 Heating curve of ISO 834 fire [1999].

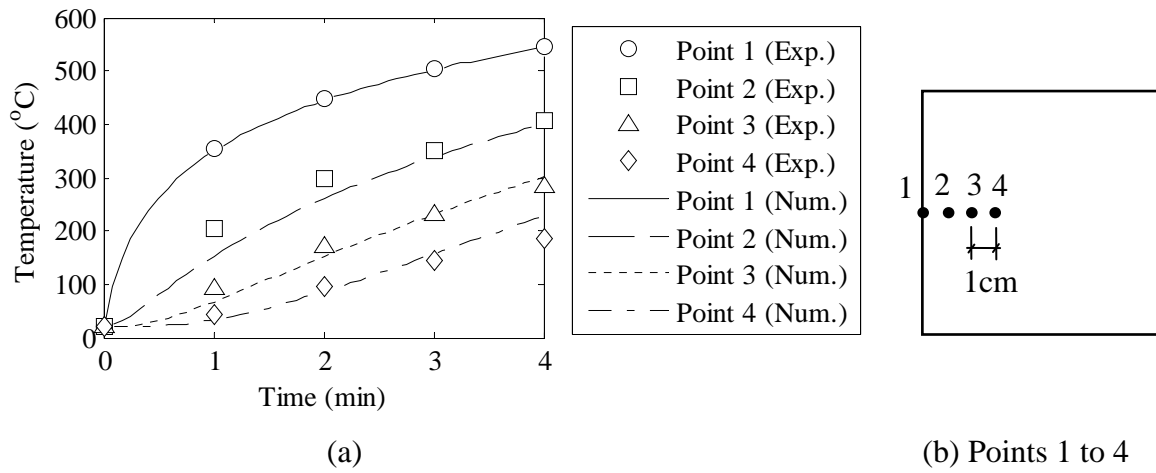


Fig. 3.5 Comparison of measured and predicted temperature evolution in a concrete cube.

3.5 Summary

In this chapter, the governing equation of the temperature field derived from Fourier’s law of heat conduction and the first law of thermodynamics has been presented. The FEM and the Galerkin weighted residual scheme have been applied for obtaining the numerical solution. The one-way coupling of thermo-to-mechanical has been discussed. The prediction of the evolution of the temperature field in heated concrete cubes is shown in Chapter 8.

Chapter 4

Thermal decomposition prediction of hardened cement paste

4.1 Introduction and literature review

When exposed to elevated temperatures, hardened cement paste will undergo decomposition, resulting in thermal damage of concrete. To better understand the thermal damage mechanism, it is essential to investigate the whole decomposition process (Fig. 4.1). It has been experimentally verified that ettringite (AFt) and CH start to decompose at 70 °C and 430 °C, respectively, and the chemical-bound water in C-S-H gel is gradually released once the temperature exceeds 600 °C [Shimada and Young, 2001; Pourchez et al., 2006; Zelić et al., 2002; Peng and Huang, 2008; Lin et al., 1996]. Due to the decomposition, the content of various constituents in hardened cement paste will change (Fig. 4.2), resulting in the variation of material properties. As it has been mentioned in Chapter 1, the thermal damage, such as spalling, is closely related to the heating rate. From a chemical decomposition point of view, the kinetics of decomposition plays an important role in the resulting damage. Therefore, incorporating the kinetics into the thermal damage analysis is of fundamental importance for a better understanding of the damage mechanism. However, such an analysis is seldom reported in the literature (Chapter 2). In most existing models, the material properties are simply expressed as a function of temperature [Khoury et al., 2002; Gawin et al., 2002, 2003; Tenchev and Purnell, 2005; Pont et al., 2011; Lee et al., 2009]. The results of those models may be more convincing if the decomposition kinetics/heating rate had been considered.

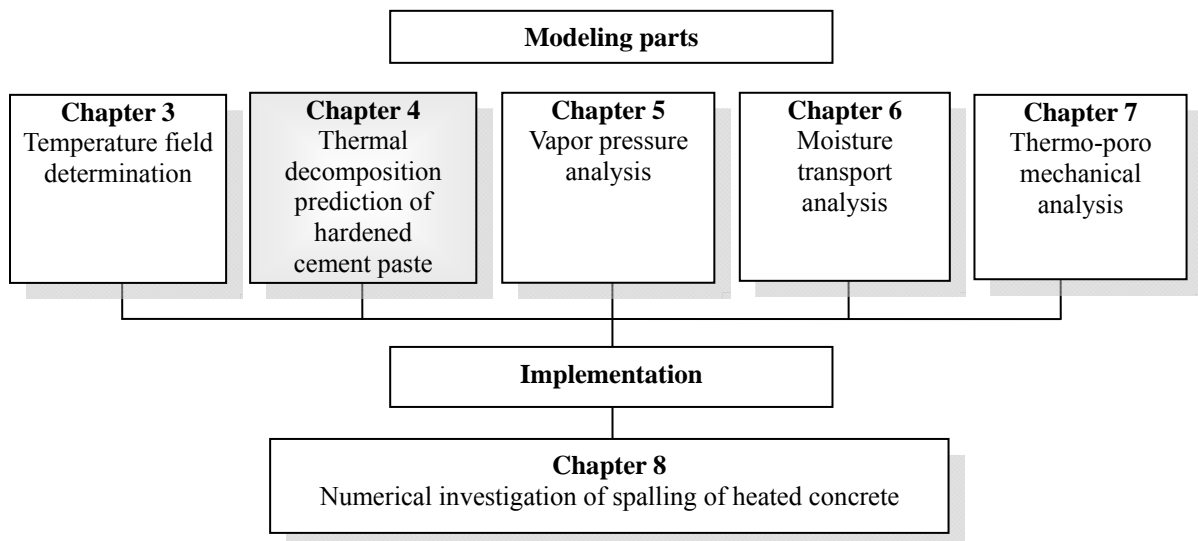


Fig. 4.1 Modeling parts of fire spalling analysis.

$$f_{gel} = \frac{0.68\alpha_c}{w/c + 0.32} \quad (4.2)$$

where α_c is the degree of hydration of cement and w/c is the water-to-cement ratio. If a mass fraction S of cement is replaced by silica fume and the degree of hydration of silica fume is taken as zero firstly, f_{unhyC} and f_{gel} can be modified as

$$f_{unhyC} = \frac{0.32(1-\alpha_c)(1-S)}{w/c + 0.32(1-S) + S/\rho_{SF}} \quad (4.3)$$

$$f_{gel} = \frac{0.68\alpha_c(1-S)}{w/c + 0.32(1-S) + S/\rho_{SF}} \quad (4.4)$$

where ρ_{SF} is the density of silica fume and w/c is converted into the water to binder ratio.

According to Bentz and Garboczi [1991], each volume unit of C_3S produces 1.7 volume units of C-S-H and 0.61 volume units of CH; each volume unit of C_2S produces 2.39 volume units of C-S-H and 0.191 volume units of CH; and each volume unit of C_3A produces 1.69 volume units of hydrated aluminates. The density of C_3S , C_2S , C_3A , and C_4AF are 3.25, 3.28, 3.04, and 3.77 g/cm³, respectively. In addition, it is assumed in this thesis that each volume unit of C_4AF produces the same amount of hydration product as C_3A . Therefore, with those parameters, the volume fraction of CH (f_{gel}^{CH}), hydrated aluminates (f_{gel}^{AL}), and C-S-H (f_{gel}^{CSH}) in the hydration product of cement can be calculated.

When silica fume is added for HPC, the pozzolanic reaction can be expressed as [Bentz et al., 2000]



where the numbers below each reactant indicate the volume stoichiometries. Thus, the initial volume fractions of pozzolanic C-S-H (f_{pCSH}^0), CH (f_{CH}^0), unhydrated silica fume (f_{unhySF}), conventional C-S-H (f_{CSH}^0), hydrated aluminates (f_{AL}^0), and capillary pores (f_{cap}^0) can be estimated for a given degree of hydration of silica fume α_s as follows

$$f_{pCSH}^0 = \frac{3.77S\alpha_s / \rho_{SF}}{w/c + 0.32(1-S) + S / \rho_{SF}} \quad (4.6)$$

$$f_{CH}^0 = f_{gel} \cdot f_{gel}^{CH} - \frac{1.35S\alpha_s / \rho_{SF}}{w/c + 0.32(1-S) + S / \rho_{SF}} \quad (4.7)$$

$$f_{unhySF} = \frac{S(1-\alpha_s) / \rho_{SF}}{w/c + 0.32(1-S) + S / \rho_{SF}} \quad (4.8)$$

$$f_{CSH}^0 = f_{gel} \cdot f_{gel}^{CSH} \quad (4.9)$$

$$f_{AL}^0 = f_{gel} \cdot f_{gel}^{AL} \quad (4.10)$$

$$f_{cap}^0 = 1 - (f_{CSH}^0 + f_{pCSH}^0 + f_{CH}^0 + f_{AL}^0 + f_{unhyC} + f_{unhySF}) \quad (4.11)$$

It should be pointed out that, since the volume fractions of all the constituents in hardened cement paste are determined by the hydration degree of cement and silica fume, once the hydration degree of silica fume and the capillary porosity are known, the hydration degree of cement can be obtained by solving Eq. 4.11. The volume fraction evolution of constituents in hardened cement paste with the hydration of cement and SF is schematically shown in Fig. 4.3.

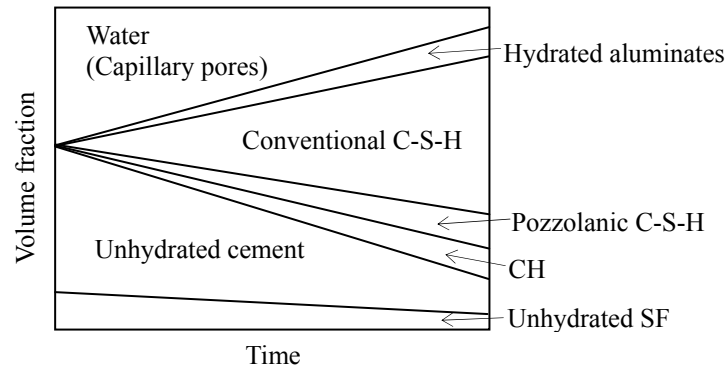


Fig. 4.3 Schematic illustration of volume fraction evolution of constituents in hardened cement paste with hydration of cement and SF.

4.2.2 Decomposition kinetics determination of hardened cement paste

In solids, water can be bound in different ways. In hydroxides, water is strongly held in the form of constituent hydroxyl ions. In hydrates, water molecules are combined either as individual units, or in the form of ligands coordinated to a particular ion. Elevated temperatures can result in bond redistribution and release of water molecules. Thermal decomposition of hardened cement paste belongs to the category of heterogeneous reactions, where the boundary surface and the region with defects in the reactant is more sensitive to chemical changes than that in the bulk of the reactant. Reaction kinetics deals with the rate of chemical transformations, which generally increases markedly with the increase of temperature. It has been shown that the rate coefficient almost invariably fits the Arrhenius equation [Galwey and Brown, 1999]

$$k_r = A \cdot \exp(-E_a/RT) \quad (4.12)$$

where A is the pre-exponential or frequency factor, E_a is the activation energy which represents the energy barrier that must be surmounted during the bond redistribution, R is the universal gas constant (8.314 kJ/(kmol·K)), and T is the temperature. Thus, the kinetics equation can be expressed as [Galwey and Brown, 1999]:

$$\frac{da}{dt} = A \cdot \exp(-E_a/RT) \cdot f(a) \quad (4.13)$$

where a is the conversion degree and $f(a)$ is a kinetic expression.

- **CH** For CH decomposition, Zelić et al. [2002] investigated the kinetics by means of differential scanning calorimetry under non-isothermal conditions. They concluded that CH starts to decompose at 430 °C, the activation energy is $E_a=127$ kJ/mol, the pre-exponential factor is $A=7.58 \times 10^6$ s⁻¹, and the kinetic expression follows a power law, i.e.

$$f(a) = 2a^{1/2} \quad (4.14)$$

The rate equation is valid for conversion degrees between 0.004 to 0.554 and can be written as

$$\frac{da}{dt} = 1.516 \times 10^7 \exp(-1.527 \times 10^4 / T) \cdot a^{1/2} \quad (4.15)$$

It was found that the curve of the conversion rate against the conversion degree is mirror-symmetric with respect to the conversion degree of 0.5 (Fig. 4.4) [Zelić et al., 2002]. At different conversion degrees, the conversion rate as a function of temperature is plotted in Fig. 4.5 (a).

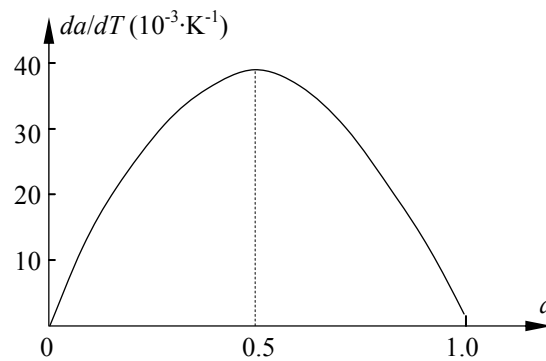


Fig. 4.4 Experimental results of decomposition rate of CH as a function of conversion degree at heating rate of 20 °C/min of Zelić et al. [2002].

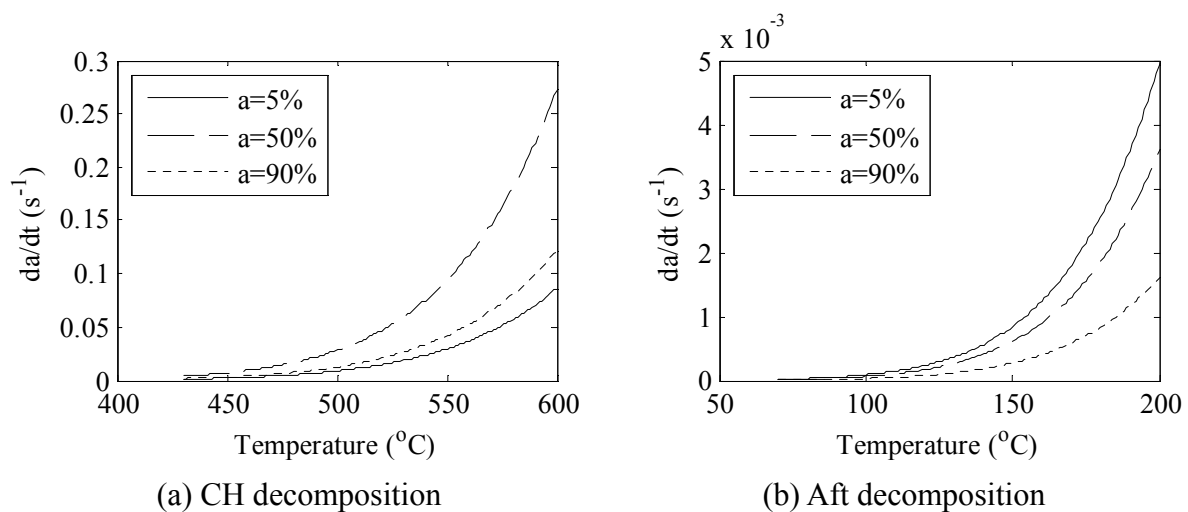


Fig. 4.5 Conversion rate of (a) CH and (b) Aft as a function of temperature at different conversion degrees.

- **AFt** For AFt decomposition, the activation energy is $E_a=59$ kJ/mol, the pre-exponential factor is $A=1.0 \times 10^{-6} \text{ min}^{-1}$ ($1.66 \times 10^4 \text{ s}^{-1}$), and the kinetic expression is as follows [Pourchez et al., 2006; Yang et al., 2007]

$$f(a) = (1 - a)^{1/2} \quad (4.16)$$

It was shown that AFt starts to decompose at 70°C . The conversion rate equation can be written as

$$\frac{da}{dt} = 1.66 \times 10^4 \exp(-7.096 \times 10^3/T) \cdot (1 - a)^{1/2} \quad (4.17)$$

At different conversion degrees, the conversion rate as a function of temperature is plotted in Fig. 4.5 (b). As few tests have been conducted on other aluminates, it is assumed in this thesis that their decomposition kinetics follows that of AFt.

- **C-S-H** For C-S-H decomposition, the kinetics is derived from the experimental results of Peng and Huang [2008]. In their experiment, the residual amount of C-S-H was measured as a function of exposure duration under three target temperatures, i.e., 600°C , 700°C , and 800°C . Based on the experimental results, the residual amount of C-S-H was expressed in terms of exposure duration as follows (Fig. 4.6) [Peng and Huang, 2008]

$$\frac{\Delta y}{y_0} = \begin{cases} -1.0 \times 10^{-6} t^3 + 0.0013 t^2 - 0.36 t + 97.72, & \text{for } T = 600^\circ\text{C} \\ -2.0 \times 10^{-6} t^3 + 0.002 t^2 - 0.67 t + 100.61, & \text{for } T = 700^\circ\text{C} \\ -2.0 \times 10^{-8} t^5 + 8.0 \times 10^{-6} t^4 - 0.0015 t^3 + 0.13 t^2 - 5.47 t + 99.82, & \text{for } T = 800^\circ\text{C} \end{cases} \quad (4.18)$$

where Δy and y_0 are the residual and original amount of C-S-H, respectively and t is time in minute. Derivation of Eq. 4.18 with respect to time yields Eq. 4.19. The decomposition rate at certain conversion degree and temperature can then be obtained by interpolation. The initial decomposition temperature is taken as 600°C .

$$\frac{d\alpha}{dt} = \begin{cases} 3 \times 10^{-6} t^2 - 0.0026 t + 0.36, & \text{for } T = 600^\circ\text{C} \\ 6.0 \times 10^{-6} t^2 - 0.004 t + 0.67, & \text{for } T = 700^\circ\text{C} \\ 1.0 \times 10^{-7} t^4 - 3.2 \times 10^{-5} t^3 + 0.0045 t^2 - 0.26 t + 5.47, & \text{for } T = 800^\circ\text{C} \end{cases} \quad (4.19)$$

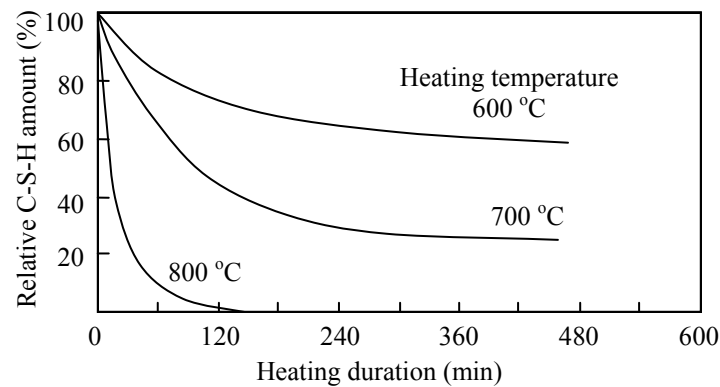


Fig. 4.6 Relative C-S-H amount as a function of exposure duration under different temperatures [Peng and Huang, 2008].

4.3 Volume fraction evolution of various constituents

Owing to thermal decomposition, the volume fractions of capillary pores, residual constituents, and decomposition products in hardened cement paste vary with the conversion degree, which can be determined through stoichiometric analysis as shown below.

4.3.1 Volume fraction of capillary pores

The volume of water decomposed from the reactants is regarded as additional pores and the volume fraction f_i^w can be calculated as follows

$$f_i^w = f_i^0 a_i n_i^w \frac{\rho_i / M_i}{\rho_w / M_w} \quad (4.20)$$

where f_i^0 is the initial volume fraction of reactant i ($i=CH, AL, \text{ or } C-S-H$), n_i^w denotes the amount of water in mole decomposed per mole of reactant i , ρ_w and M_w are the density and molar mass of water, and ρ_i and M_i are the density and molar mass of reactant i .

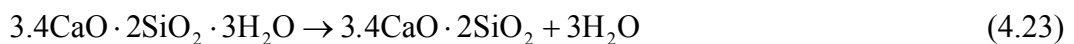
- **CH** For CH decomposition, $n_{CH}^w = 1.0$, $\rho_{CH} = 2.24 \text{ g/cm}^3$, $M_{CH} = 74 \text{ g/mol}$, and the decomposition equation can be expressed as



- **AFt** For AFt, the empirical chemical formula is $3\text{CaO} \cdot \text{Al}_2\text{O}_3 \cdot 3\text{CaSO}_4 \cdot 32\text{H}_2\text{O}$ [Shimada and Young, 2001]. It was shown that the decomposition product of AFt is called meta-ettringite, which contains 10-13 H_2O molecules per formula unit [Shimada and Young, 2001; Pourchez et al., 2006]. Thus, $n_{AFt}^w = 20$, $\rho_{AFt} = 1.8 \text{ g/cm}^3$, $M_{AFt} = 1255 \text{ g/mol}$, and the decomposition equation can be written as



- **C-S-H** Since conventional cement gel and pozzolanic C-S-H contain 28% and 19% gel pores, respectively [Hansen, 1986; Bentz et al., 2000], f_i^0 ($i = CSH$) in Eq. 4.20 should be replaced with the volume fraction of solid C-S-H, f_{CSH}^{0s} . The chemical formula of conventional solid C-S-H is $\text{C}_{3.4}\text{S}_2\text{H}_3$ [Tennis and Jennings, 2000]. According to the experimental results [Lin et al., 1996; Peng and Huang, 2008], the main product of C-S-H decomposition is C_nS . Thus, $n_{CSH}^w = 3.0$ and the decomposition equation for $\text{C}_{3.4}\text{S}_2\text{H}_3$ is expressed as



In addition, for solid C-S-H, $\rho_{CSH} = 1.75 \text{ g/cm}^3$, $M_{CSH} = 365 \text{ g/mol}$ [Tennis and Jennings, 2000]. It is assumed in this thesis that the parameters of C-S-H, n_{CSH}^w , ρ_{CSH} , M_{CSH} , and the conversion degree in Eq. 4.20 take the same values for both conventional and pozzolanic for the whole decomposition process. The initial volume fraction of the solid part in conventional C-S-H, f_{CSH}^s , equals

$$f_{CSH}^s = (1 - f_{CSH}^{gelp})f_{CSH}^0 \quad (4.24)$$

and in pozzolanic C-S-H, f_{pCSH}^s , is

$$f_{pCSH}^s = (1 - 0.19)f_{pCSH}^0 \quad (4.25)$$

where f_{CSH}^{gelp} is the volume fraction of gel pores in conventional C-S-H and given by

$$f_{CSH}^{gelp} = 0.28 / f_{gel}^{CSH} \quad (4.26)$$

Thus, the total initial volume fraction of solid C-S-H is equal to

$$f_{CSH}^{0s} = f_{CSH}^s + f_{pCSH}^s \quad (4.27)$$

Substitution of Eq. 4.27 into Eq. 4.20 yields the volume fraction of additional pores due to the decomposition of the solid C-S-H. Gel pores reside in C-S-H and it is assumed that gel pore water can only be released together with the decomposition of C-S-H for short-time heating. By converting gel pores into capillary pores with the decomposition of C-S-H, the volume fraction of additional capillary pores due to the decomposition of C-S-H is equal to

$$f_{CSH}^{cap} = f_{CSH}^w + f_{CSH}^s a_{CSH} \frac{f_{CSH}^{gelp}}{1 - f_{CSH}^{gelp}} + f_{pCSH}^s a_{CSH} \frac{0.19}{1 - 0.19} \quad (4.28)$$

Thus, the total volume fraction of capillary pores is given by

$$f_{cap} = f_{cap}^0 + f_{CH}^w + f_{AFt}^w + f_{CSH}^{cap} \quad (4.29)$$

The decomposition degree β of hardened cement paste is defined as

$$\beta = \frac{f_{cap} - f_{cap}^0}{f_{cap}^1 - f_{cap}^0} \quad (4.30)$$

where f_{cap}^1 is the volume fraction of capillary pores at the complete decomposition of hardened cement paste (Fig. 4.7).

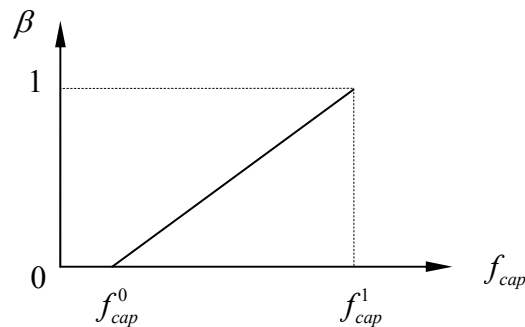


Fig. 4.7 Decomposition degree β versus volume fraction of capillary pores f_{cap} of hardened cement paste.

4.3.2 Volume fractions of residual constituents and decomposition products

The volume fractions of residual CH (f_{CH}^r), hydrated aluminates (f_{AL}^r), conventional C-S-H (f_{CSH}^r), and pozzolanic C-S-H (f_{pCSH}^r) in hardened cement paste are determined as follows

$$f_{CH}^r = (1 - a_{CH})f_{CH}^0 \quad (4.31a)$$

$$f_{AL}^r = (1 - a_{AFt})f_{AL}^0 \quad (4.31b)$$

$$f_{CSH}^r = (1 - a_{CSH})f_{CSH}^s / (1 - f_{CSH}^{gelp}) \quad (4.31c)$$

$$f_{pCSH}^r = (1 - a_{CSH})f_{pCSH}^s / (1 - 0.19) \quad (4.31d)$$

The volume fractions of solid decomposition products of CH (f_{CH}^{sp}), hydrated aluminates (f_{AL}^{sp}), and C-S-H (f_{CSH}^{sp}) are given by

$$f_{CH}^{sp} = f_{CH}^0 a_{CH} - f_{CH}^w \quad (4.32a)$$

$$f_{AL}^{sp} = f_{AL}^0 a_{AFt} - f_{AFt}^w \quad (4.32b)$$

$$f_{CSH}^{sp} = f_{CSH}^{0s} a_{CSH} - f_{CSH}^w \quad (4.32c)$$

The volume fractions of various constituents in decomposed hardened cement paste are schematically shown in Fig. 4.2. The porosity of the decomposition products of hydrated aluminates (f_{AL}^{pp}), CH (f_{CH}^{pp}), conventional C-S-H (f_{CSH}^{pp}), and pozzolanic C-S-H (f_{pCSH}^{pp}) can be calculated as

$$f_{AL}^{pp} = n_{AL}^w \frac{\rho_{AL} / M_{AL}}{\rho_w / M_w} = 0.52 \quad (4.33a)$$

$$f_{CH}^{pp} = n_{CH}^w \frac{\rho_{CH} / M_{CH}}{\rho_w / M_w} = 0.54 \quad (4.33b)$$

$$f_{CSH}^{pp} = n_{CSH}^w \frac{\rho_{CSH} / M_{CSH}}{\rho_w / M_w} + 0.28 / f_{gel}^{CSH} = 0.58 \quad (\text{if } f_{gel}^{CSH} = 0.65) \quad (4.33c)$$

$$f_{pCSH}^{pp} = n_{pCSH}^w \frac{\rho_{pCSH} / M_{pCSH}}{\rho_w / M_w} + 0.19 = 0.40 \quad (4.33d)$$

4.4 Experimental verification of numerical method

The proposed decomposition method will be verified by comparing the predicted porosity evolution in hardened cement paste with three sets of experimental data published in the literature: Piasta et al. [1984], Komonen and Penttala [2003], and Biolzi et al. [2008].

- Experiment of Piasta et al.

The first set of experimental data is taken from Piasta et al. [1984]. In their experiment, an ordinary Portland cement (OPC-375) with composition of C_3S -63.2%, C_2S -15.4%, C_3A -9.9%, and C_4AF -8.0% by mass was used. The water-to-cement ratio was 0.4. After 28-day curing at room temperature, the samples of hardened cement paste were exposed to high temperatures ranging from 20 to 800 °C with an interval of 100 °C. The exposure duration of each target temperature was 3 hours. The heating curve is shown in Fig. 4.8 (a). After natural cooling, the porosity in cm^3/g was measured by porosimetric analysis. For the sake of comparison, the porosity is converted into the volume fraction by

$$f_{cap}^{test} = p_{test} \rho_{hcp} \quad (4.34)$$

where f_{cap}^{test} is the converted volume fraction of capillary pores, p_{test} is the measured porosity in cm^3/g , and ρ_{hcp} is the density of hardened cement paste and approximately given by Eq. 4.35. The experimental results are shown in Fig. 4.8 (b).

$$\rho_{hcp} = \frac{(1 + w/c)\rho_c}{1 + (w/c)\rho_c / \rho_w} \quad (4.35)$$

From the chemical composition of the used cement, the volume fractions of C-S-H, CH, and hydrated aluminates in cement gel are calculated as 66.96%, 19.29%, and 13.75%, respectively. Substitution of the measured porosity at 20 °C into Eq. 4.11 yields the degree of hydration, i.e., 71.7%. With these parameters known, the volume fraction evolution of capillary pores can be determined using the numerical method proposed in this chapter. The results are compared with the experimental data in Fig. 4.8 (b). It can be seen from Fig. 4.8 (b) that the numerical results are in good agreement with the experimental results except at 800 °C, where the relatively small experimental value could be caused by the sintering effect [Piasta et al., 1984].

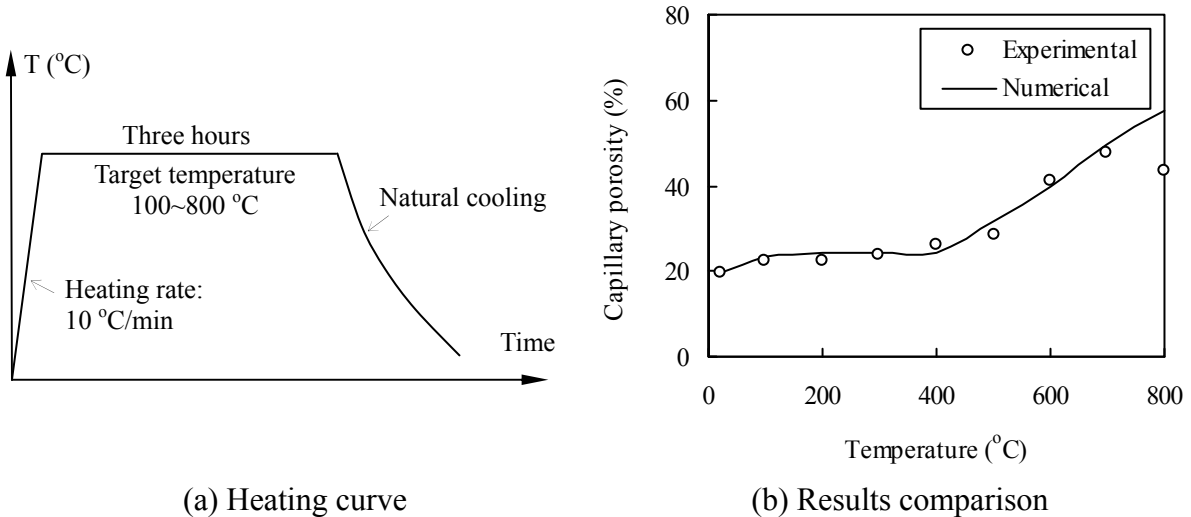


Fig. 4.8 Heating curve and comparison between numerical results and experimental results of heated hardened cement paste of Piasta et al. [1984].

- Experiment of Komonen and Penttala

The second set of experimental data is taken from Komonen and Penttala [2003]. In their experiment, an ordinary Portland cement CEM I 42.5 R was used. The water-to-cement ratio of was 0.32. The target temperatures for porosity measurement were 20, 50, 75, 100, 120, 150, 200, 300, 400, 440, 520, 600, 700, 800, and 1000 °C. The heating rate was 4 °C/min. When the target temperature was reached, the temperature was kept constant for 60 minutes (Fig. 4.9 (a)). The specimens of hardened cement paste were then cooled down to the ambient temperature at a rate of 4 °C/min and the porosity was measured by the mercury intrusion porosimetry (MIP) test.

From the chemical composition of the used cement, the volume fractions of C-S-H, CH, and hydrated aluminates in cement gel are calculated as 66.91%, 18.69%, and 14.39%, respectively. Using the measured porosity at 20 °C, the degree of hydration can be obtained from Eq. 4.11, i.e., 56.9%. With these parameters known, the volume fraction evolution of capillary pores can be determined. The results are shown in Fig. 4.9 (b), together with the experimental results. The average relative error between them is equal to 7.1%. It can be concluded that the numerical results are in good agreement with the experimental results.

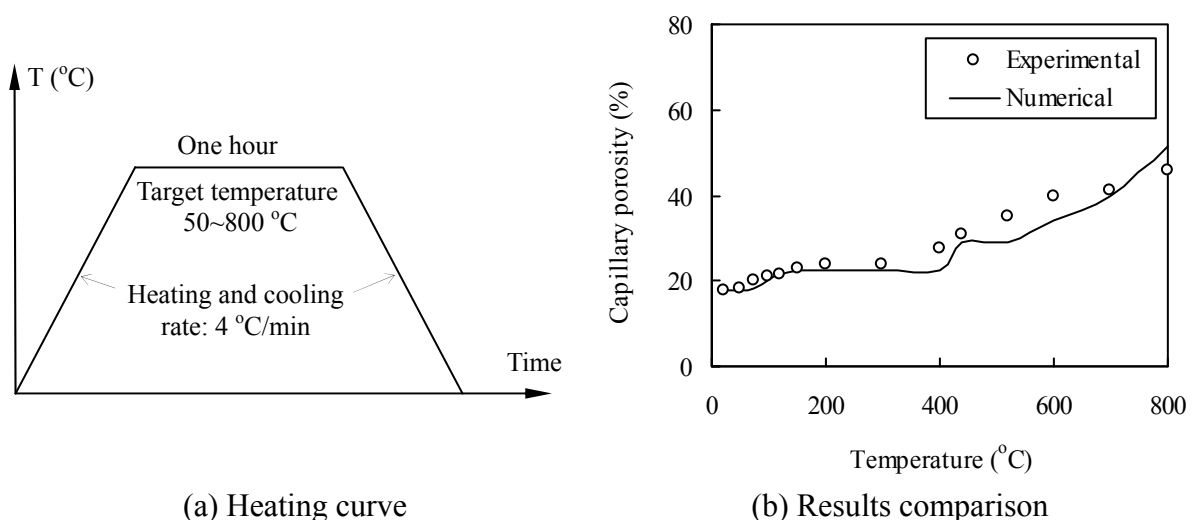


Fig. 4.9 Heating curve and comparison between numerical results and experimental results of heated hardened cement paste of Komonen and Penttala [2003].

- Experiment of Biolzi et al.

The third set of experimental data is taken from Biolzi et al. [2008]. In their experiment, for making HPC, a Portland cement CEM I 52.5 R was used and 10% cement by mass was replaced by silica fume. The water-to-binder ratio was 0.22. Quartz aggregates with a maximum diameter of 3 mm were used. The aggregate-to-binder ratio was 2.0. The specimens were cured for 28 days before testing. The target temperatures were 20, 250, 500, and 750 °C. The heating rate was 1 °C/min and the exposure duration at each target temperature was 2 hours (Fig. 4.10 (a)). After the specimens were cooled down to the ambient temperature at a rate of 0.5 °C/min, the porosity was measured by MIP tests. Since the porosity in aggregates is negligibly small, the porosity in concrete f_{cap}^{con} can be converted into the porosity in hardened

cement paste f_{cap} by

$$f_{cap} = f_{cap}^{con} \left(1 + \frac{f_{agg}}{f_{hcp}} \right) \quad (4.36)$$

where f_{agg} and f_{hcp} are the volume fractions of aggregate and hardened cement paste, respectively.

According to the experimental results of Lu et al. [1993], the degree of hydration of silica fume is taken as 40%. From the chemical composition of the used cement and the measured porosity of hardened cement paste at 20 °C, the volume fractions of C-S-H, CH, and hydrated aluminates in cement gel are calculated as 65.87%, 19.89%, and 14.24%, respectively, and the hydration degree of cement is obtained as 38.5%. Thus, the volume fraction evolution of capillary pores in hardened cement paste can be calculated as shown in Fig. 4.10 (b). It can be seen that the numerical results are in good agreement with the experimental results.

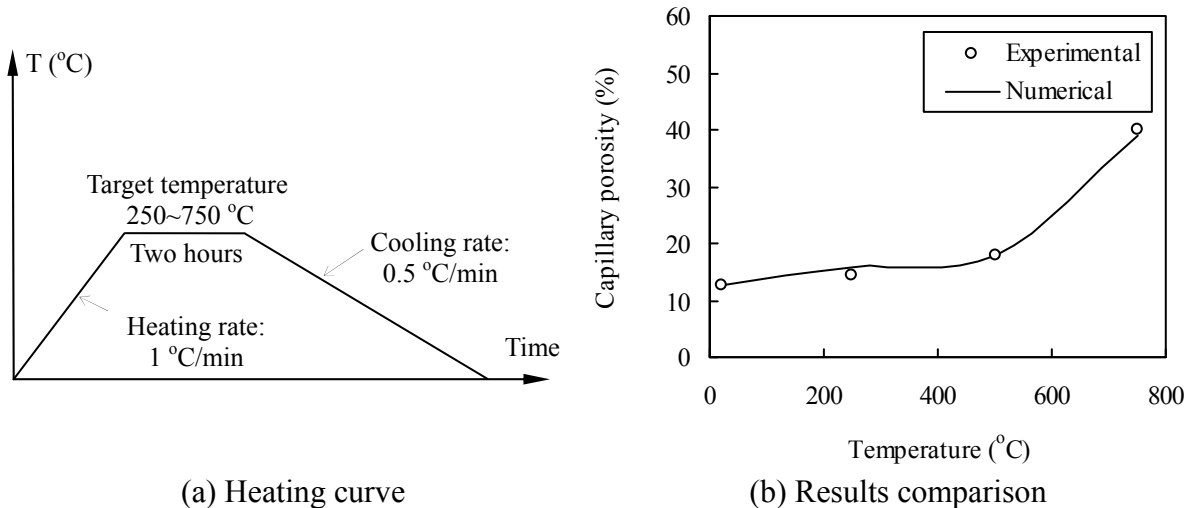


Fig. 4.10 Heating curve and comparison between numerical results and experimental results of Biolzi et al. [2008].

4.5 Analysis of heating rate effect on thermal decomposition

To evaluate the heating rate effect on the decomposition of hardened cement paste, an ordinary Portland cement (OPC 52.5) with chemical composition of C_3S -55.8%, C_2S -15.8%, C_3A -9.2%, and C_4AF -9.1% by mass is considered. The corresponding volume fractions of C-S-H, CH, and hydrated aluminates in cement gel are 66.41%, 18.59%, and 15.0%, respectively. Ten percent cement by mass is replaced by silica fume with a density of 2.2 g/cm³. The water-to-binder ratio is 0.26. The degrees of hydration of cement and silica fume at the curing age of 28 days are 50% and 40%, respectively [Parrot and Killoh, 1984; Lu et al., 1993]. Thus, the initial volume fractions of conventional C-S-H, pozzolanic C-S-H, CH, hydrated aluminates, unhydrated cement, unhydrated silica fume, and capillary pores are calculated as 34.24%, 11.55%, 5.45%, 7.73%, 24.26%, 4.60%, and 12.16%, respectively. The decompositions at four heating rates, i.e., 1 °C/min, 5 °C/min, 10 °C/min, and the standard heating curve recommended in ISO 834 [1999] shown in Fig. 4.11 are investigated.

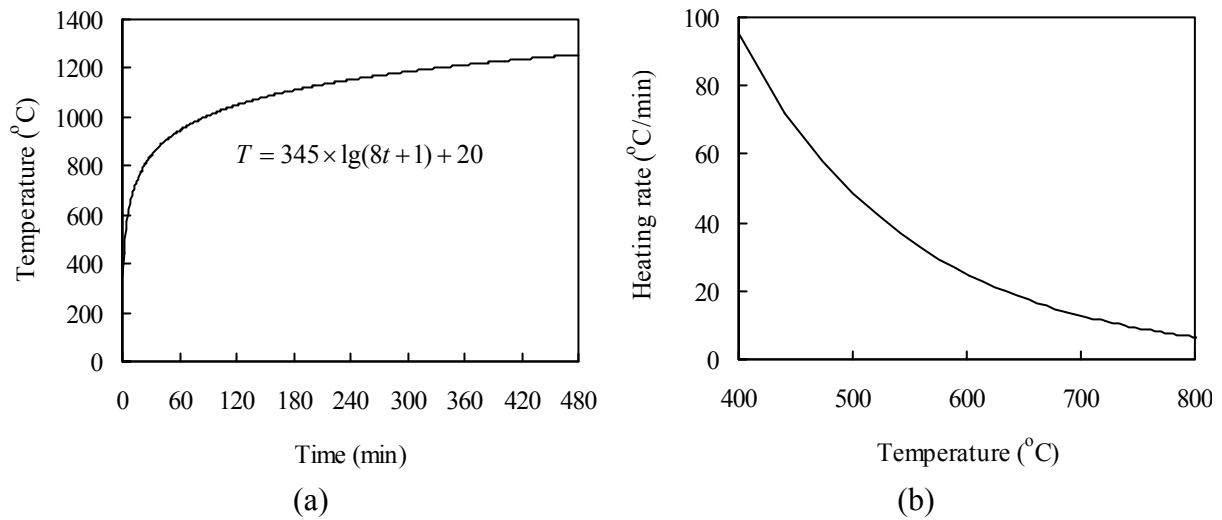


Fig. 4.11 Heating curve (a) and heating rate (b) of ISO 834 fire [1999].

The conversion degrees of hydrated aluminates, CH, and C-S-H are plotted against temperature in Fig. 4.12, Fig. 4.13, and Fig. 4.14, respectively. It can be seen from these figures that the heating rate exerts a remarkable influence on the decomposition of hardened cement paste. When the heating rate increases from low to high, the temperature of complete decomposition of hydrated aluminates and CH increase from 162 °C to 325 °C and from 443 °C to 519 °C, respectively. At 800 °C, C-S-H decomposes completely under the heating rate of 1 °C/min. Under the heating rate of 10 °C/min or exposed to ISO 834 fire, however, the decomposition ratio is only about 33%.

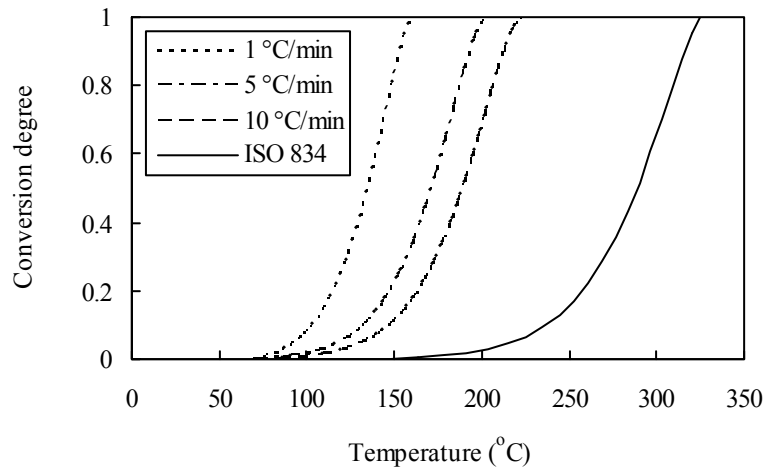


Fig. 4.12 Decomposition of hydrated aluminates under different heating rates.

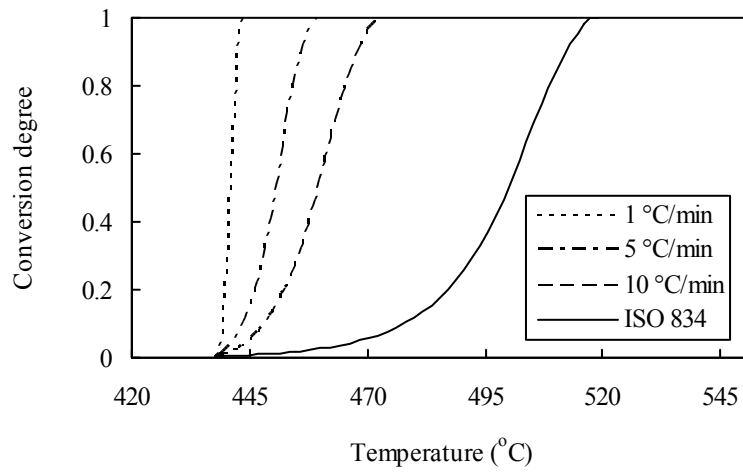


Fig. 4.13 Decomposition of CH under different heating rates.

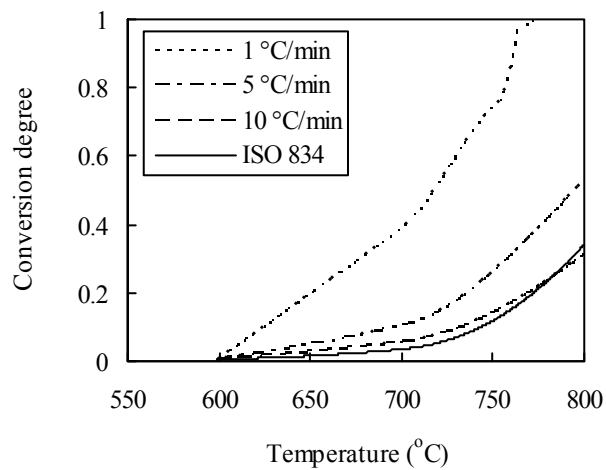


Fig. 4.14 Decomposition of C-S-H under different heating rates.

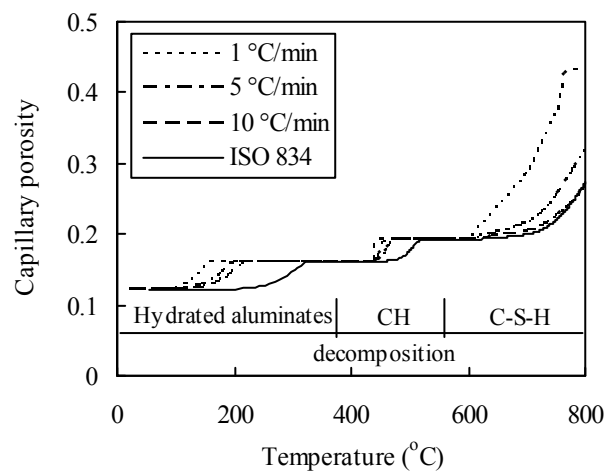


Fig. 4.15 Capillary porosity evolution under different heating rates.

The volume fraction evolution of capillary pores under different heating rates is shown in Fig. 4.15. It can be seen from Fig. 4.15 that the heating rate exerts a remarkable effect on the evolution of capillary porosity. The lower the heating rate, the faster the development of the capillary porosity with respect to the heating temperature. Thus, the corresponding material properties, the release of water from decomposition, the escape of water vapor, and the development of vapor pressure will be totally different.

4.6 Summary and conclusions

A numerical method has been presented for the prediction of thermal decomposition of hardened cement paste. By analyzing the kinetics of decomposition, the volume fraction evolution of various constituents in hardened cement paste has been estimated and the whole thermal decomposition process has been traced. After the proposed numerical method has been verified by comparing the numerical prediction with three sets of experimental data obtained from the literature, the effect of the heating rate on the thermal decomposition of hardened cement paste has been evaluated in a quantitative manner. Based on the numerical results (Fig. 4.15), it has been learned that the higher the heating rate, the slower the increase of capillary porosity with respect to the heating temperature. Therefore, it can be concluded that incorporating the heating rate into the thermal damage analysis of heated concrete is of great importance.

In the proposed method, the influence of vapor pressure on the decomposition kinetics and the hydration of residual unhydrated cement under high temperature conditions have been assumed negligible. The drying shrinkage of hardened cement paste under short time heating has also been assumed negligible. The predictions of the permeability and the elastic modulus of hardened cement paste based on the thermal decomposition analysis will be shown in Chapters 6 and 7, respectively. Both the coarsening effect of decomposition on the pore system and the moisture released from the decomposition are considered in the vapor pressure determination in Chapter 5. An integrated spalling analysis incorporating the thermal decomposition analysis, the vapor pressure determination, the moisture transport prediction, and the mechanical analysis is shown in Chapter 8.

Chapter 5

Vapor pressure analysis

5.1 Introduction and literature review

Since vapor pressure is supposed to play a dominant role in fire spalling (Chapter 1), the vapor pressure analysis is an important modeling part in the fire spalling investigation of HPC (Fig. 5.1). Two aspects need to be considered in the analysis: the determination of vapor pressure and the mechanical effect analysis of vapor pressure. As already mentioned in Chapter 2, in the existing spalling models, the water vapor is usually assumed to be an ideal gas and the ideal gas law is usually applied for the determination of its value [Bažant, 1978; Majumdar et al., 1995, 1997; Majorana et al., 1998; Schrefler et al., 2002; Khoury et al., 2002; Mounajed, 2004; Tenchev and Purnell, 2005; Pont et al., 2005a; Li et al., 2006; Gawin et al., 2006; Benes and Mayer, 2008; Dwaikat and Kodur, 2009; Pont et al., 2010]. However, Kalifa et al. [2000] experimentally verified that, in heated concrete, the gas phase doesn't follow the ideal gas law. Bažant [1978] and Gawin et al. [2003] also found that, when the ideal gas law was employed, either the corresponding water content or the density of water vapor differed significantly from the test results and satisfactory fits of the test data could not be achieved. The reason for this is that, from a microscopic point of view, the ideal gas itself adheres to several idealizations: the volume of the gas molecules is negligible compared with the volume occupied by the gas; the molecules are in random motion; no forces act on the gas molecules except during collisions [Moran and Shapiro, 2008]. However, when the moisture content of

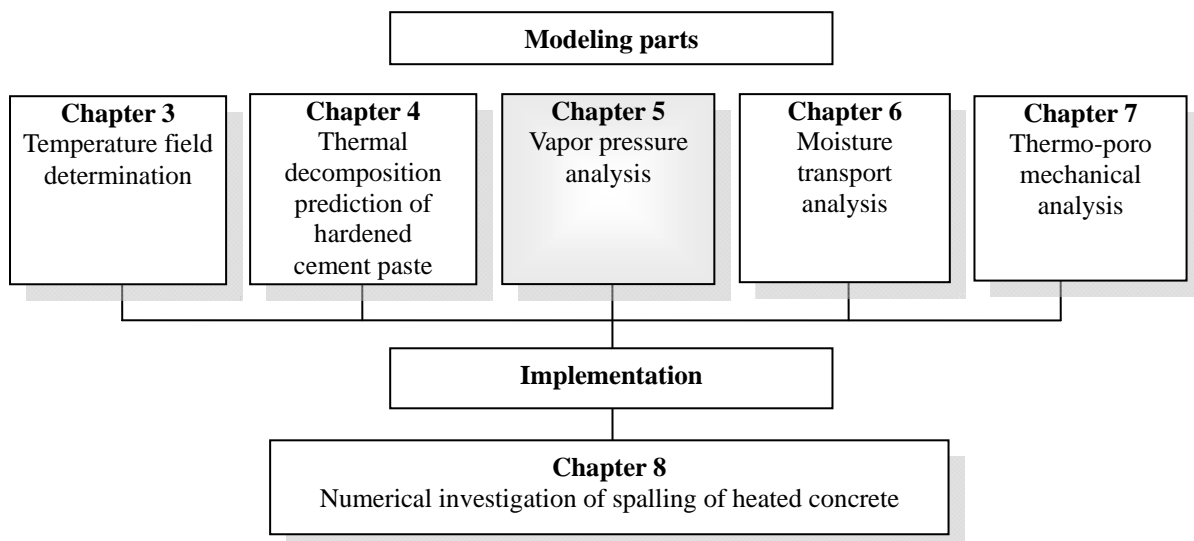


Fig. 5.1 Modeling parts of fire spalling analysis.

concrete is high, the volume of molecules of water vapor is not negligible. To remedy, Bažant [1978] worked out a semi-empirical expression of sorption isotherms to determine the free water content in concrete as a function of the relative pore pressure and temperature. In Gawin's model [2003], the density of water vapor in the temperature range close to the critical point (374.15 °C) was empirically modified as a function of temperature. In this thesis, steam tables, which describe the real state of water vapor, are used for the determination of vapor pressure. The effects of the thermal decomposition (Chapter 4) and the vapor pressure gradient induced moisture migration (Chapter 6) are taken into account in the calculation.

In addition to the determination of vapor pressure, the mechanical effect of vapor pressure on stress and strain fields in heated concrete should be modeled. Majumdar and Marchertas [1997] incorporated the vapor pressure in the stress analysis by applying an equivalent surface load on the sides of the 2D finite elements. Ichikawa and England [2004] used a simplified model to calculate the tensile stress as a function of the pore volume and the vapor pressure. Then the tensile stress was compared with the tensile strength of concrete to determine the tensile failure caused by vapor pressure. Tenchev and Purnell [2005] applied a body force equal to the vapor pressure gradient in the stress field analysis. Dwaikat and Kodur [2009] tried to correlate the vapor pressure with the temperature-dependent tensile strength of concrete to determine the possibility of tensile fracture. In this thesis, the analysis of the mechanical effect of vapor pressure on fire spalling is based on the theory of poroelasticity. The parameter needed in the poro-mechanical analysis, i.e., the Biot modulus [Biot, 1941], is determined by an equivalent expansion method proposed in this thesis. The mechanical coupling between fluid and solid is also discussed. The implementation of vapor pressure modeling for spalling analysis is shown in Chapter 8.

5.2 Vapor pressure determination

5.2.1 Water type in concrete

In general, three different states of water (although the distinction is not absolute) exist in hardened cement paste: chemically bound water, physically adsorbed water, and free water. The chemically bound water, which is also termed non-evaporable water, combines with the components of cement clinker to form hydration products. The physically adsorbed water is adsorbed at the surface of solid particles. This part of water occupies the gel pores and the surface layer of capillary pores and is attracted by the surface force of solid. The rest of water is free water existing in the capillary pores, if any is still available. The nominal diameter of gel pores is around 3 nm and that of capillary pores is one or two orders of magnitude larger [Hansen, 1986; Neville, 1995]. Upon heating, the chemically bound water will be released and turn into free water by the thermal decomposition of hydration products (Chapter 4).

5.2.2 Phase changing of water on heating

The term “phase” refers to a quantity of matter that is homogeneous in both chemical composition and physical structure. For a single-phase system, the state is fixed by any two of the three state properties, i.e., pressure, specific volume, and temperature. When water is heated under certain pressure, a phase transition (vaporization) from water to water vapor will happen at a certain temperature as shown in Fig. 5.2. In this figure, the areas labeled liquid-vapor is a two-phase region, where water and vapor coexist in equilibrium and are

called saturated water and saturated vapor. Within the two-phase region, the pressure and the temperature are dependent on one another and the state can only be described by the specific volume and either the pressure or the temperature. The point at the top of the two-phase region is called critical point and the corresponding state parameters are called critical parameters. The critical temperature is the maximum temperature at which the liquid and vapor can coexist. When the state of a liquid reaches the critical point, the distinction between vapor and liquid dose no longer exist. For water, the critical temperature and pressure are 374.15 °C and 22.09 MPa, respectively. When liquid water is fully vaporized, the vapor phase on further heating is called superheated vapor/steam. Steam tables (tables of saturated water and superheated steam), which describe the real state of heated water and vapor, can be used for retrieving the state data. Examples of steams tables are shown in Table 5.1 and Table 5.2 [Moran and Shapiro, 2008].

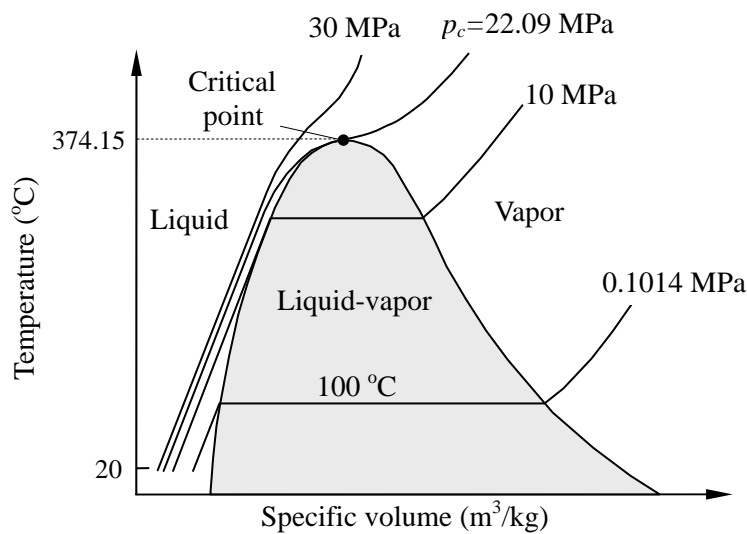


Fig. 5.2 Sketch of temperature-specific volume relation of water (not to scale) [Moran and Shapiro, 2008].

Table 5.1 Example of table of saturated water

| T (°C) | Pressure (MPa) | Specific volume (m ³ /kg) | |
|--------|----------------|--------------------------------------|-----------------|
| | | Saturated water | Saturated vapor |
| 300 | 8.581 | 1.4036×10 ⁻³ | 0.02167 |
| 320 | 11.27 | 1.4988×10 ⁻³ | 0.01549 |
| 340 | 14.59 | 1.6379×10 ⁻³ | 0.01080 |
| 360 | 18.65 | 1.8925×10 ⁻³ | 0.006945 |
| 374.14 | 22.09 | 3.155×10 ⁻³ | 0.003155 |

Table 5.2 Example of table of superheated steam

| T (°C) | Specific volume (m ³ /kg) | | | | |
|--------|--------------------------------------|------------|------------|------------|------------|
| | P=8.0 MPa | P=10.0 MPa | P=12.0 MPa | P=14.0 MPa | P=16.0 MPa |
| 360 | 0.03089 | 0.02331 | 0.01811 | 0.01422 | 0.01105 |
| 400 | 0.03432 | 0.02641 | 0.02108 | 0.01722 | 0.01426 |
| 440 | 0.03742 | 0.02911 | 0.02355 | 0.01954 | 0.01652 |
| 480 | 0.04034 | 0.03160 | 0.02576 | 0.02157 | 0.01842 |

5.2.3 Vapor pressure determination

When exposed to high temperatures, the vapor phase in concrete will be either saturated vapor or superheated steam. The steam tables are used for the vapor pressure determination in this thesis. In the vapor pressure determination, only free water in the capillary pores is considered and the effect of the adsorbed water in gel pores is ignored in view of the fact that, since the size of gel pore is less than ten water molecules and the water is strongly adsorbed, the water phase in gel pores can not be considered as a bulk water phase, but as structured water [Feldman, 1972; Bažant et al., 1978; Ulm et al., 2004; Ghabezloo et al., 2009]. The same assumption is also made by Bažant et al. [1978], Ulm et al. [2004], and Ghabezloo et al. [2009]. As temperature and specific volume can be regarded as independent variables, the pressure can be determined as a function of those two. To calculate the specific volume of the moisture, first, the definition of the moisture content (or the moisture saturation degree), S_d , is specified in Eq. 5.1a, that is, the percentage of the pore space filled with water converted from the whole moisture (vapor phase is also converted into water). Another definition of the water saturation degree, S_w , which is used later, is also specified here in Eq. 5.1b.

$$S_d = \frac{V_l + V_v \cdot \rho_v / \rho_w}{f_{cap} \cdot V_0} \quad (5.1a)$$

$$S_w = \frac{V_l}{f_{cap} \cdot V_0} \quad (5.1b)$$

where V_l and V_v are the volume of the liquid phase and the vapor phase in the capillary pores, respectively, f_{cap} is the capillary porosity, V_0 is the bulk volume of cement paste, and ρ_w and ρ_v are the mass density of water and vapor, respectively. At certain temperature, the specific volume of moisture can be calculated as follows

$$\nu = \frac{V_m}{m_m} = \frac{f_{cap} \cdot V_0}{f_{cap} \cdot V_0 \rho_w S_d} = \frac{1}{\rho_w S_d} \quad (5.1)$$

where V_m and m_m are the volume and mass of the moisture, respectively. When the temperature and the specific volume of moisture are known at certain moment of heating, the pressure can be obtained from the steam tables and also the water saturation degree can be determined. In the specific volume determination of the moisture in the capillary pores, the coarsening of the pore system induced by the thermal decomposition and the moisture released from the thermal decomposition are accounted for (Chapter 4). It should be mentioned that the energy needed for the phase transition (vaporization) is not considered explicitly in the analysis and the influence of the energy on the temperature field evolution is assumed negligible (Chapter 3).

As concrete is a porous medium, the build-up vapor pressure in heated concrete is coupled with the moisture transport, that is, the build-up vapor pressure is the driving force for the moisture transport and, in return, the moisture transport influences the vapor pressure build-up. The coupling makes both the vapor pressure build-up and the moisture transport non-linear. To deal with this complex phenomenon, in this thesis, a simplified method is employed, i.e., the so-called “staggered way” [Zienkiewicz and Taylor, 2000]. That is, in the calculation, the

time scale is divided into several time steps. In each time step, first, the vapor pressure is determined. Then, the moisture transport is analyzed. After the moisture transport, the vapor pressure is calculated again for the next time step and the moisture transport is also analyzed again. For each time step, the temperature, the thermal decomposition, and the mechanical damage are analyzed and the material properties of heated concrete are updated as well. Although only approximate results can be obtained from this numerical method, when the size of the element and the time step are small enough, a good approximation can be got [Zienkiewicz and Taylor, 2000].

Owing to the lack of the experimental data, the highest value that the vapor pressure can reach in heated concrete is assumed to be 35 MPa because, beyond 35 MPa, the magnitude of vapor pressure is too sensitive to the specific volume of moisture, that is, a tiny change in the specific volume of moisture will induce a tremendous increase in vapor pressure [Meyer et al., 1967]. It is assumed that the vapor pressure in heated concrete is not that sensitive.

5.3 Mechanical modeling of vapor pressure

The effect of vapor pressure on the stress and strain field in concrete is incorporated into the mechanical analysis (Chapter 7). As concrete can be treated as a porous medium due to the presence of gel pores and capillary pores, the theory of poromechanics is applied. The general theory of poroelasticity was formulated by Biot [1941] and applied originally to geomechanics and hydrogeology.

5.3.1 Theory of poroelasticity

For an isotropic fluid-filled porous medium, such as soil and/or rock system (Fig. 5.3 (a)), Biot's theory [Biot, 1941] consists of two linear constitutive equations:

$$\varepsilon = \frac{\sigma}{K} + \frac{p}{H} \quad (5.2)$$

$$\zeta = \frac{\sigma}{H_1} + \frac{p}{R_1} \quad (5.3)$$

where σ is the hydrostatic pressure, p is the fluid pressure, ε is the volumetric strain, ζ is the increment of fluid content, K is the drained bulk modulus and the coefficient $1/K$ is called the compressibility under drained condition, $1/H$ is the Biot modulus, which is the specific volumetric strain caused by the pore pressure while the applied stress is held constant, and $1/H_1$ and $1/R_1$ are specific storages of fluid due to the applied stress and pore pressure, respectively. The coefficient $1/H_1$ is equal to $1/H$ [Biot, 1941]. The parameter, K/H , is called the Biot-Willis coefficient. The first constitutive equation states that the changes in applied stress and pore pressure produce a fractional volume change. The second constitutive equation describes that the changes in applied stress and pore pressure require fluid to be added to or removed from the porous medium. Although Biot's theory is originally used in geomechanics and hydrogeology for analyzing the soil and/or rock system [Biot, 1941], the constitutive equations of the theory can be adopted for the poro-mechanical analysis of heated concrete (Fig. 5.3).

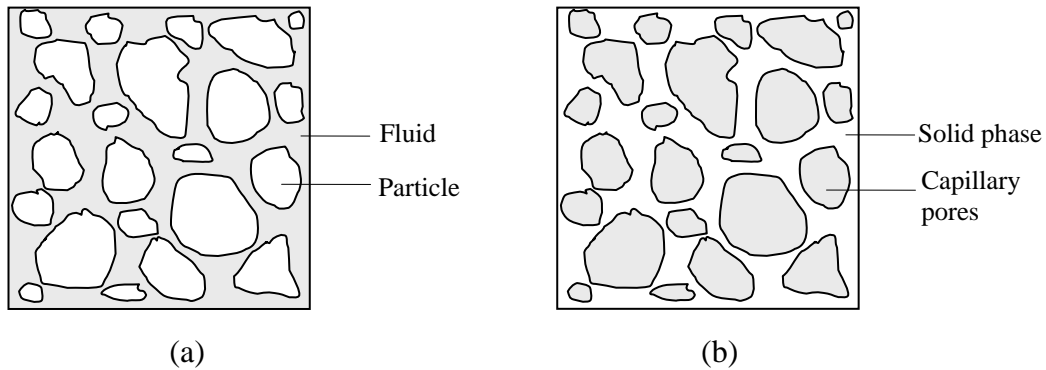


Fig. 5.3 Fluid filled porous medium: (a) Soil and/or rock system; (b) Hardened cement paste.

5.3.2 One-way coupling of fluid-to-solid analysis

According to the poro-mechanical theory [Biot, 1941; Coussy, 2004], two coupling phenomena reflect the poroelastic behavior of a porous medium: the solid-to-fluid coupling and the fluid-to-solid coupling. The first coupling occurs when the applied stress change causes a fluid pressure or fluid storage change. The second one concerns the change in fluid pressure or fluid storage produces a change in the volume of the porous medium. The extent of the solid-to-fluid coupling depends on the compressibilities of the solid skeleton and the pore fluid. Since the solid skeleton of concrete is much more incompressible compared to the water vapor, the solid-to-fluid coupling can be negligible. The one-way coupling mathematically simplifies the analysis as the fluid-flow problem can be solved independently of the stress field.

The generalized linear elastic constitutive relation incorporating the one-way coupling of the fluid-to-solid and the thermal expansion is as follows [Biot, 1941; Coussy, 2004]:

$$\varepsilon_{ij} = \frac{1}{2G} \left[\sigma_{ij} - \frac{\nu}{1+\nu} \sigma_{kk} \delta_{ij} \right] + \frac{1}{3H} p \delta_{ij} + \varepsilon_{th}^e \delta_{ij} \quad (5.4)$$

where ν is drained Poisson's ratio, G is the drained shear modulus, p is the pore pressure, δ_{ij} is the Kronecker delta (if i equals j , $\delta_{ij}=1$, else $\delta_{ij}=0$), and ε_{th}^e is the effective thermal strain (Chapter 7).

5.3.3 Determination of Biot modulus

For a soil or/and rock system, the Biot modulus, $1/H$, can be determined through unjacketed experiments (Fig. 5.4). In the unjacketed test, a sample of volume V is immersed in a confining fluid with pressure of P_c . The confining fluid permeates the pore spaces throughout the interior of the sample. Then by measuring the unjacketed compressibility, the Biot modulus can be calculated [Berryman, 1992]. However, in the case of concrete, especially HPC, although it can be treated as a porous medium, the pore structure is much different from that of the soil and/or rock system (Fig. 5.3). For the latter, most of the pores are connected and only the connected pores are of concern for geomechanics and hydrogeology. For the former, since the permeability is very low and most of the pores are isolated compared with the latter, it is difficult to determine the Biot modulus by the unjacketed test. In this thesis, an

equivalent expansion method is proposed for the determination of the Biot modulus as shown Fig. 5.5.

In Fig. 5.5, a cube of hardened cement paste or mortar is fully constrained. As the cube is isotropic and the pores are evenly distributed in the matrix, when the pore pressure increases from zero to p , according to the static equilibrium, the constrained force intensity, p' , is equal to

$$p' = -p \cdot f_{cap} \tag{5.5}$$

where f_{cap} is the capillary porosity. The potential volume strain, ε_{0v} , caused by pore pressure can then be calculated as

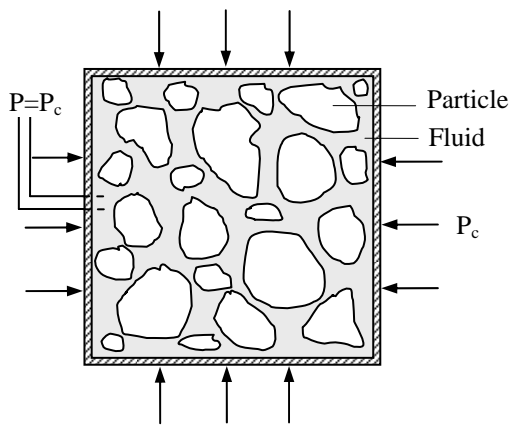


Fig. 5.4 Schematic illustration of unjacketed test.

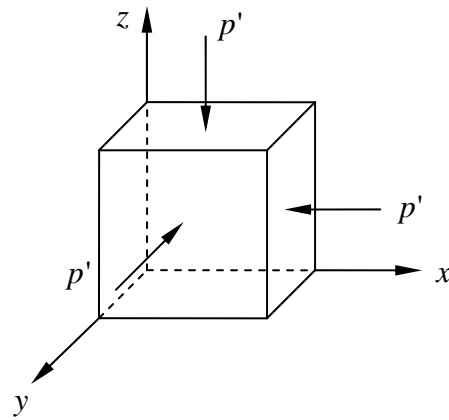


Fig. 5.5 Fully constrained cube of hardened cement paste or mortar.

$$\varepsilon_{0v} = -\frac{3(1-2\nu)}{E} p' \tag{5.6}$$

Thus, the Biot modulus, $1/H$, and the Biot-Willis coefficient, α_b , can be obtained respectively as follows

$$\frac{1}{H} = \frac{3(1-2\nu) \cdot f_{cap}}{E} \tag{5.7}$$

$$\alpha_b = \frac{K}{H} = f_{cap} \tag{5.8}$$

5.3.4 Effective stress determination

From Eq. 5.4, it can be seen that the bulk elastic volume change is governed by the combination of stress and pore pressure, which is called effective stress and expressed as [Coussy, 2004]

$$\sigma_{ij}^e = \sigma_{ij} + \alpha_b \cdot p \delta_{ij} \tag{5.9}$$

Substitution of Eq. 5.8 into Eq. 5.9 yields

$$\sigma_{ij}^e = \sigma_{ij} + p_e \delta_{ij} \quad (5.10)$$

with

$$p_e = f_{cap} \cdot p \quad (5.10a)$$

where p_e is defined as the effective vapor pressure. The effective stress controls the elastic volume change and the failure behavior of the porous medium.

5.4 Example of vapor pressure determination

To illustrate how the vapor pressure develops in a porous medium, a sealed/undrained cube with a porosity of 8% exposed to elevated temperatures is investigated. Three moisture contents, i.e., 10%, 50%, and 90% are considered. The highest heating temperature is 600 °C. Under the assumption that the highest value that the vapor pressure can reach is 35 MPa and by the use of steam tables, the development of the vapor pressure can be predicted as shown in Fig. 5.6, together with the calculated effective vapor pressure. It can be seen that, at the stage of vaporization, in the three cases, the vapor pressure developments are identical. In the case of 10% moisture content, at around 344 °C, the moisture turns into superheated steam. In the other two cases, however, the moisture is not superheated until the temperature reaches the critical point (374.15 °C). The prediction of vapor pressure with the effects of the moisture transport and the thermal decomposition of hardened cement paste is shown in Chapter 8.

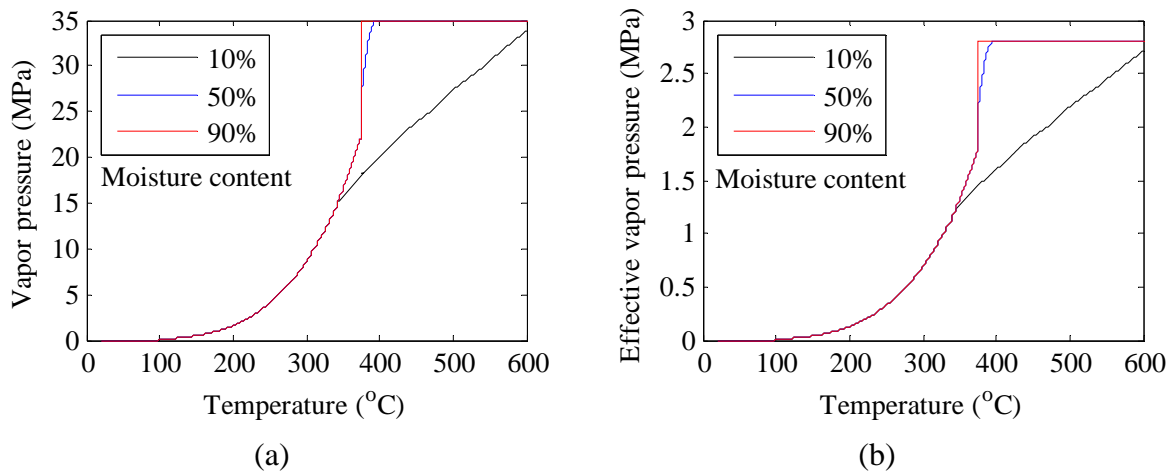


Fig. 5.6 Development of vapor pressure (a) and effective vapor pressure (b) versus temperature in a sealed cube with a porosity of 8% with different moisture contents.

5.5 Summary

In this chapter, for the fire spalling study of heated concrete, the vapor pressure is analyzed. Two aspects has been considered, i.e., the determination of vapor pressure and the mechanical effect analysis of vapor pressure. Steam tables have been used for the vapor pressure determination and the poromechanics has been applied for the mechanical effect analysis. In the mechanical analysis, the Biot modulus has been determined by an equivalent expansion method proposed in this chapter. The mechanical coupling between fluid and solid has also been discussed and the one-way coupling of the fluid-to-solid has been applied.

Chapter 6

Moisture transport analysis

6.1 Introduction

The moisture content of concrete determines the magnitude of the build-up vapor pressure and the moisture transport determines the moisture content. Therefore, the modeling part of the moisture transport analysis is of great importance in the fire spalling analysis. This modeling part is proposed and presented in this chapter and the application is shown in Chapter 8 (Fig. 6.1).

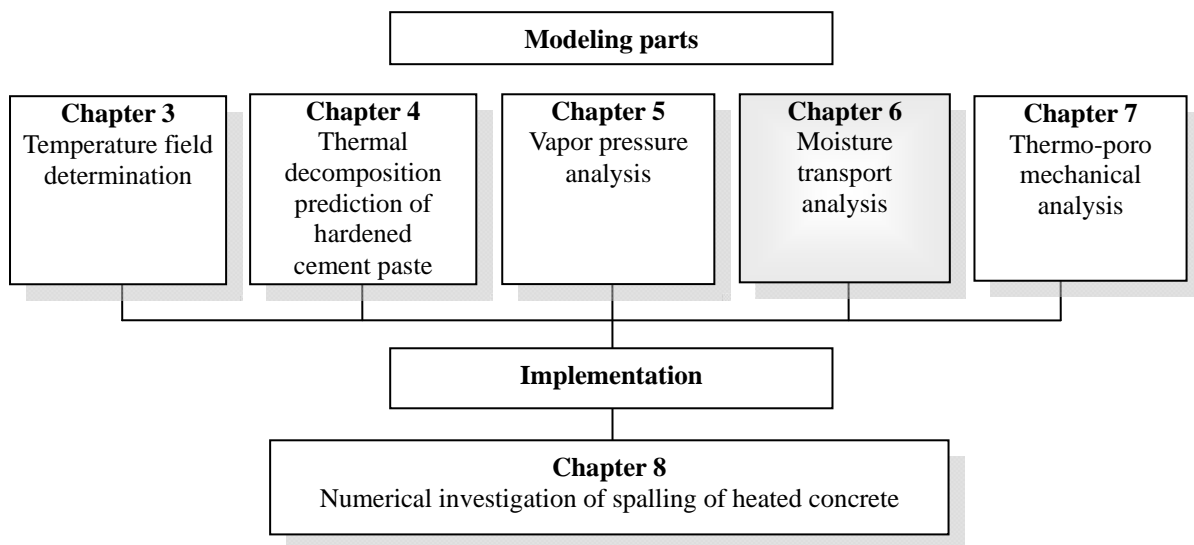


Fig. 6.1 Modeling parts of fire spalling analysis.

It has been concluded after the literature review in Chapter 2 that, in most existing moisture transport models, the permeability is usually taken as temperature dependent; the moisture released from the decomposition of the hydration products is either expressed as a function of temperature or not considered. The effect of the heating history as such is neglected.

In the moisture transport modeling of this thesis, the permeability, the moisture content, and the vapor pressure (Chapter 5) are determined based on the thermal decomposition of the hydration products (Chapter 4). The general effective medium theory [Mclachlan, 1988] is applied for the permeability prediction. For the transport of the vapor phase, the effects of slip-flow [Klinkenberg, 1941] and the water saturation degree on the permeability are considered. The governing equation of the moisture transport is derived based on the mass conservation principle and solved numerically.

6.2 Governing equation of moisture transport

When concrete is exposed to elevated temperatures, a moisture transport driven by the build-up vapor pressure gradient occurs. In view of the low permeability of concrete, which results in the low velocity of the vapor flow, Darcy's law is used for the description.

$$q' = -k\nabla p \quad (6.1)$$

where q' is the moisture flux, k is the permeability, and p is the pressure. In this thesis, only the moisture transport in vapor phase driven by the gradient of build-up vapor pressure is studied, since the moisture transport in liquid phase is negligibly small compared with that transport in vapor phase [Bažant and Kaplan, 1996; Gawin et al., 2002, 2003; Chung and Consolazio, 2005]. The diffusion of moisture driven by the gradient of moisture concentration is also assumed negligible in view of the fact that the diffusion takes time [Bažant and Kaplan, 1996] and fire spalling occurs in the first several minutes of heating.

Based on the mass conservation principle, the governing equation of moisture transport can be derived. Taking a rectangular prism with sides dx , dy , and dz in x , y , and z directions, respectively, as an investigated volume (Fig. 6.2), the net mass inflow in unit time in x direction, m_x , is equal to

$$m_x = -(q'_x|_{x+dx} - q'_x|_x)dydz = -\frac{\partial q'_x}{\partial x} dx dy dz \quad (6.2)$$

where q'_x is the mass flux in x direction, which can be determined using Darcy's law

$$q'_x = -k \frac{\partial p}{\partial x} \quad (6.3)$$

By substituting Eq. 6.3 in Eq. 6.2, the net inflow in x direction can be written as

$$m_x = \frac{\partial}{\partial x} \left(k \frac{\partial p}{\partial x} \right) dx dy dz \quad (6.4a)$$

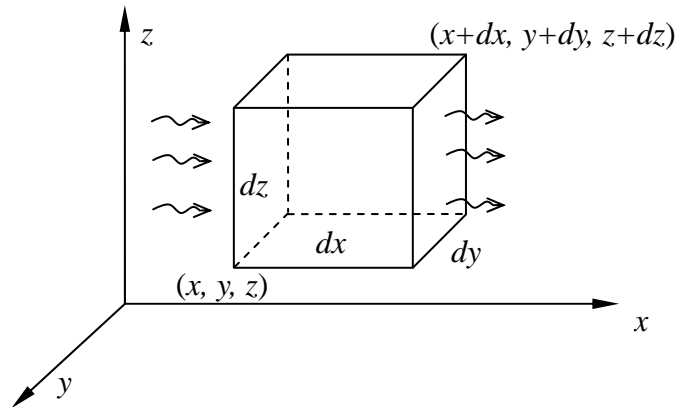


Fig. 6.2 Moisture transport in an investigated volume.

Similarly, the net mass inflow in unit time in y and z directions is equal to, respectively,

$$m_y = \frac{\partial}{\partial y} \left(k \frac{\partial p}{\partial y} \right) dx dy dz \quad (6.4b)$$

$$m_z = \frac{\partial}{\partial z} \left(k \frac{\partial p}{\partial z} \right) dx dy dz \quad (6.4c)$$

Therefore, the total net inflow in unit time is

$$m_{xyz} = \left[\frac{\partial}{\partial x} \left(k \frac{\partial p}{\partial x} \right) + \frac{\partial}{\partial y} \left(k \frac{\partial p}{\partial y} \right) + \frac{\partial}{\partial z} \left(k \frac{\partial p}{\partial z} \right) \right] dx dy dz \quad (6.5)$$

Also, the change in mass caused by inflow in the investigated volume can be expressed as

$$m_{xyz} = \left(\frac{\partial \rho}{\partial t} - \dot{m}_{dh} \right) dx dy dz \quad (6.6)$$

where ρ is the mass density of vapor, t is time, and \dot{m}_{dh} is the moisture source from the thermal decomposition of hardened cement paste (Chapter 4). Equating Eq. 6.5 and Eq. 6.6 gives the governing equation of moisture transport

$$\left[\frac{\partial}{\partial x} \left(k \frac{\partial p}{\partial x} \right) + \frac{\partial}{\partial y} \left(k \frac{\partial p}{\partial y} \right) + \frac{\partial}{\partial z} \left(k \frac{\partial p}{\partial z} \right) \right] - \frac{\partial \rho}{\partial t} + \dot{m}_{dh} = 0 \quad (6.7)$$

The permeability, k , is given by

$$k = \rho \frac{k_e'}{\eta} \quad (6.8)$$

where η is the dynamic viscosity of vapor, which is determined using steam tables, and k_e' is the effective intrinsic permeability in m^2 , in which the effects of the slip-flow of vapor phase and the presence of the liquid phase on the intrinsic permeability are accounted for. The effective intrinsic permeability is determined in the following section.

6.3 Permeability determination

Under high temperature conditions, hardened cement paste will undergo thermal decomposition (Chapter 4), resulting in a pore structure change and thus a variation in the permeability. It has been pointed out after the literature survey in Chapter 2 that, in most existing models, the permeability is taken as temperature dependent. The heating history effect on pore structure evolution as such couldn't be reflected (Chapter 4). In this thesis, the general effective medium theory is applied for the prediction of the intrinsic permeability. The coarsening effect of thermal decomposition as a function of heating history is considered. The effects of the gas phase slip-flow and the water saturation degree on the permeability are also taken into account.

6.3.1 Intrinsic permeability determination

The general effective medium theory was developed originally for the calculation of the effective electric conductivity of two-phase composite solid conductor [Mclachlan, 1998]. As the moisture transport in porous media is mathematically the same as the electron transport in

a conductor, the general effective medium theory can be applied for the prediction of the permeability of cementitious material [Cui and Cahyadi, 2001; Zheng and Zhou, 2008]. The equation for the prediction is as follows [Mclachlan, 1988; Cui and Cahyadi, 2001]:

$$\frac{(1-f_h)(k_l^{1/2}-k')}{k_l^{1/2}+A'k'^{1/2}}+\frac{f_h(k_h^{1/2}-k'^{1/2})}{k_h^{1/2}+A'k'^{1/2}}=0 \quad (6.9a)$$

with

$$A'=\frac{1-f_{hc}}{f_{hc}} \quad (6.9b)$$

where f_h and k_h are respectively the volume fraction and the permeability of the high-permeable phase, k_l is the permeability of the low-permeable phase, k' is the intrinsic permeability of the two-phase composite material, and f_{hc} is the critical percolation volume fraction of the high permeable phase. When its volume fraction is lower than f_{hc} , the high-permeable phase is isolated by the other phase,

For silica fume blended hardened cement paste, as the pore system consists of three types of pores, i.e., capillary pores, gel pores in conventional C-S-H, and gel pores in pozzolanic C-S-H, a three-step permeability prediction is conducted (Fig. 6.3 and Fig. 6.4):

- Step 1 The permeable phase is pozzolanic C-S-H gel and the impermeable phase consists of CH, hydrated aluminates, and unhydrated cement and SF, if any. The critical volume fraction for percolation of pozzolanic C-S-H is taken as 0.17 according to the simulation results of Bentz and Garboczi [1991]. The permeability of pozzolanic C-S-H gel is taken as $7 \times 10^{-25} \text{ m}^2$ [Song et al., 2010] and the permeability of the impermeable phase is zero. The volume fraction of pozzolanic C-S-H can be obtained from the thermal decomposition analysis (Chapter 4). Substitution of these parameters into Eq. 6.9 yields the permeability of the first step.

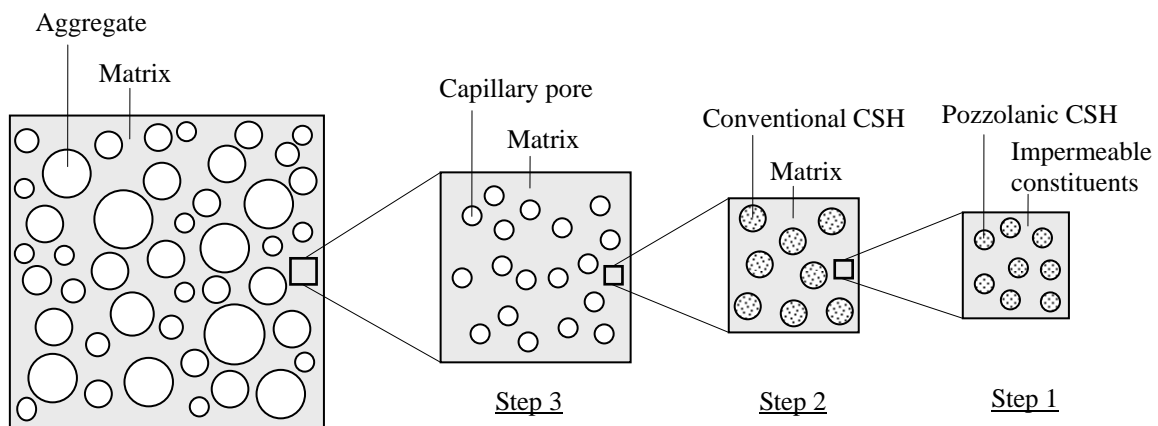


Fig. 6.3 Three-step permeability prediction.

- Step 2 The high permeable phase is conventional C-S-H and the low permeable phase is the composite of step one, whose permeability is already obtained. The critical percolation volume fraction of conventional C-S-H is equal to 0.17 [Bentz and Garboczi, 1991] and the permeability of conventional C-S-H is equal to $7 \times 10^{-23} \text{ m}^2$ [Powers, 1958]. Solving Eq. 6.9 with these parameters yields the permeability of the step two.

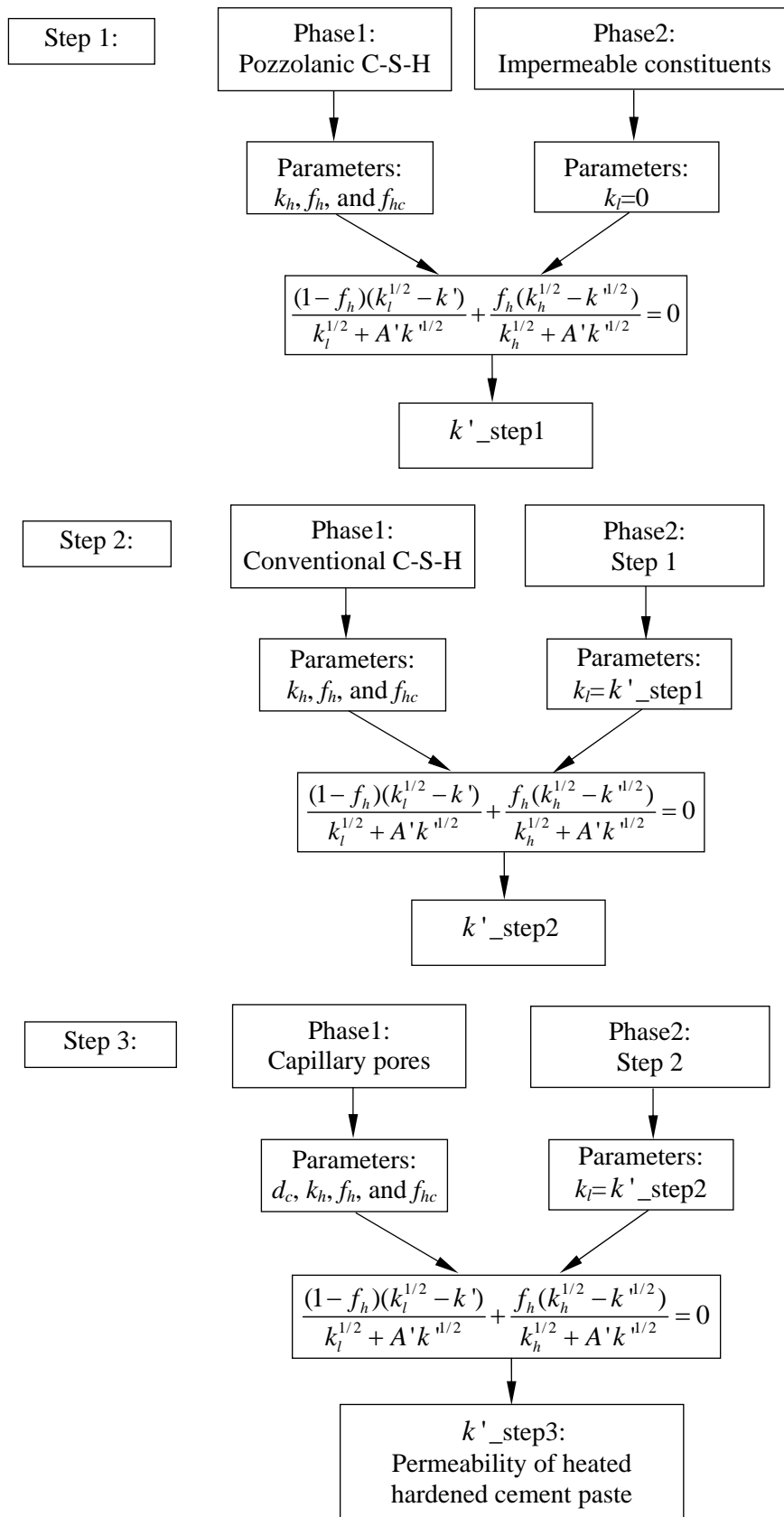


Fig. 6.4 Three-step prediction of intrinsic permeability of heated hardened cement paste.

- **Step 3** The high permeable phase is the capillary pores and the low permeable phase is the composite of step two, whose permeability is already known. According to Cui and Cahyadi [2001], the permeability of capillary pores is equal to

$$k_h = \frac{1.8d_c^2}{226}(1 - f_{hc})^2 \quad (6.10)$$

where f_{hc} is the critical percolation volume fraction of capillary pores, which is found to be 0.18 [Bentz and Garboczi, 1991], and d_c is the critical pore diameter. The critical pore diameter is defined as follows: if the pores are added to the network of the pore system one by one from largest to smallest, the diameter of the pore which connects the first pore path throughout the sample is the critical pore diameter [Katz and Thompson, 1986; Cui and Cahyadi, 2001; Zheng and Zhou, 2008]. Experimentally, the critical pore diameter can be determined by mercury intrusion porosimetry (MIP). In the MIP test, mercury, which is an ideal nonwetting fluid, is forced into the evacuated pore system of a sample. The data on the cumulative intrusion volume of mercury and the corresponding equivalent diameter of the pores where mercury is penetrating can be obtained. The critical pore diameter is that corresponding to the inflection point in the cumulative intrusion volume versus the equivalent pore diameter plot [Katz and Thompson, 1986; Cui and Cahyadi, 2001].

The coarsening evolution of the critical pore diameter as a function of the decomposition degree, β (Eq. 4.30), is determined according to the sensitivity analysis of three different evolution patterns, i.e., linear, quadratic-1, and quadratic-2, as shown in Fig. 6.5. The study of the sensitivity of the intrinsic permeability to the evolution pattern of the critical pore diameter is conducted in Chapter 8 (Section 8.6.1) based on the experimental results of Peng [2000]. The results (Fig. 6.6/Fig. 8.14) show that, for HPC, when the capillary porosity is less than the critical percolation value (18%), the evolution pattern of the critical pore diameter as a function of decomposition degree has no effect on the intrinsic permeability, while for NSC, whose initial capillary porosity before heating already exceeds the critical percolation value, the intrinsic permeability is much more sensitive to the evolution pattern. In view of the sensitivity, since it gives the median value, the linear evolution pattern is applied in the permeability analysis. The prediction of the intrinsic permeability is verified in Chapter 8 and also shown in the next section.

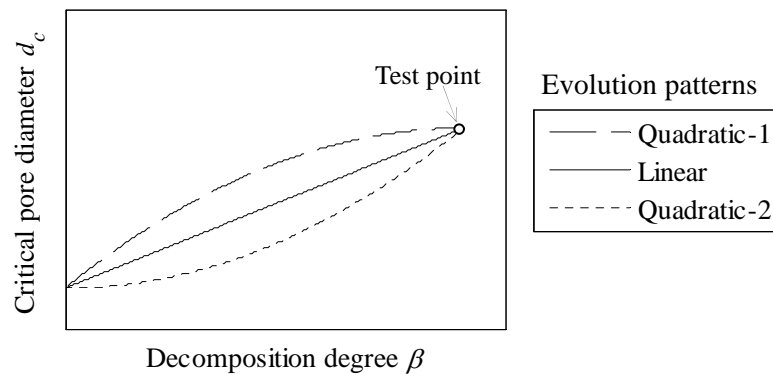


Fig. 6.5 There evolution patterns of critical pore diameter d_c as a function of decomposition degree β .

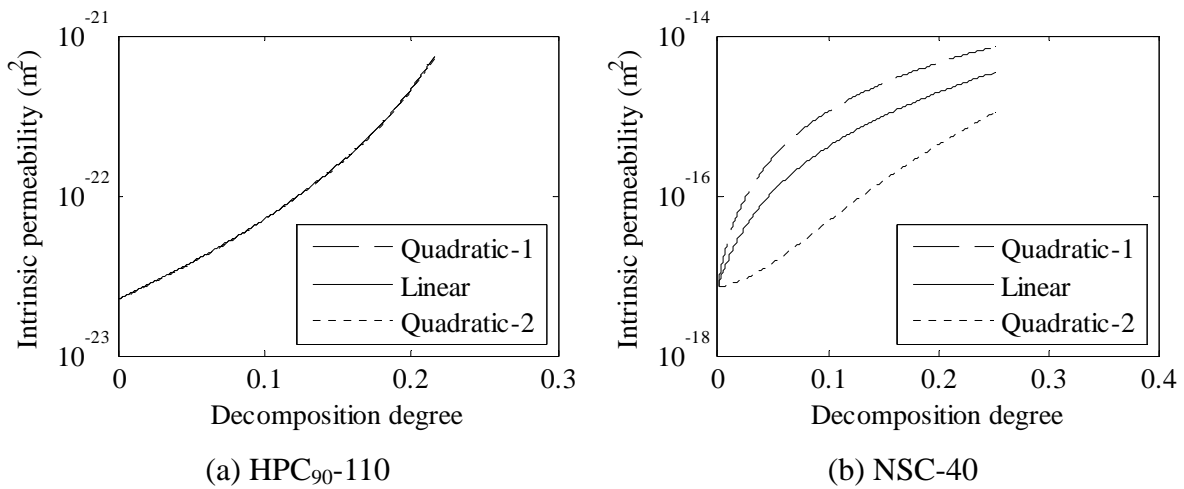


Fig. 6.6 Predicted intrinsic permeability based on different evolution patterns of critical pore diameter.

6.3.2 Verification of prediction of intrinsic permeability

Under the high temperature condition, by using the method proposed in this chapter, the evolution of intrinsic permeability of the matrix of HPC₉₀₋₁₁₀ and NSC-40 in the test of Peng [2000] is predicted (Chapter 8). Owing to the lack of the experimental data on heated hardened cement paste, the predicted evolution of intrinsic permeability as a function of capillary porosity is compared with the experimental data of hardened cement paste at room temperature of Powers et al. [1955] (Young [1988]), Cui and Cahyadi [2001], and Nyame and Illston [1981] (Zheng and Zhou [2008]) in Fig. 6.7/ Fig. 8.15. The comparison shows that the predicted results correlate reasonably well with the experimental data.

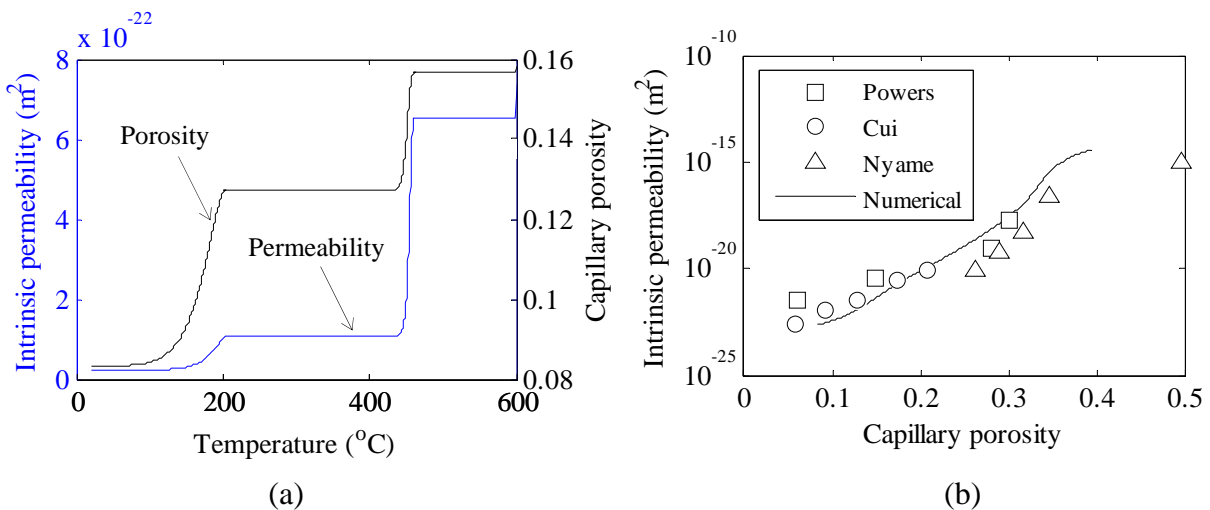


Fig. 6.7 (a) Intrinsic permeability and capillary porosity evolution of heated HPC₉₀₋₁₁₀ matrix as a function of temperature (5 °C/min); (b) Comparison of predicted intrinsic permeability of heated matrix of HPC₉₀₋₁₁₀ and NSC-40 [Peng, 2000] as a function of capillary porosity with experimental data of hardened cement paste at room temperature collected from literature.

6.3.3 Gas phase slip-flow and effective permeability

As a material property, the intrinsic permeability of concrete ought to be independent of the fluid involved. However, it has been found that the measured value by using gas is higher than that by using liquid [Bamforth, 1987; Chung and Consolazio, 2005]. The difference can be explained by the theory of slip-flow of gas proposed by Klinkenberg [1941]. When a liquid flow passes a surface, the liquid immediately in contact with the surface has a zero velocity and, due to the dynamic viscosity induced shear stress, the velocity of the liquid in the successive layers away from the surface will increase. Compared to liquid flow, gas has a certain velocity at the interface between the gas and the solid surface (Fig. 6.8), resulting in the quantity of gas flow is higher than that of liquid. This phenomenon is called slippage. For high permeable media, the difference in the intrinsic permeabilities for liquids and gases is small, while for low permeable media, such as concrete, the difference is considerable [Klinkenberg, 1941; Bamforth, 1987]. The following equation was developed by Klinkenberg [1941] for relating the gas intrinsic permeability, k'_g , to the liquid intrinsic permeability, k'_l

$$k'_g = k'_l \left(1 + \frac{b}{p}\right) \quad (6.11)$$

where b is the Klinkenberg constant and p is the gas pressure. In this thesis, for the Klinkenberg constant, the following expression proposed by Chung and Consolazio [2005] for cement-based materials is adopted

$$b = \exp(-0.5818 \ln(k'_l) - 19.1213) \quad (6.12)$$

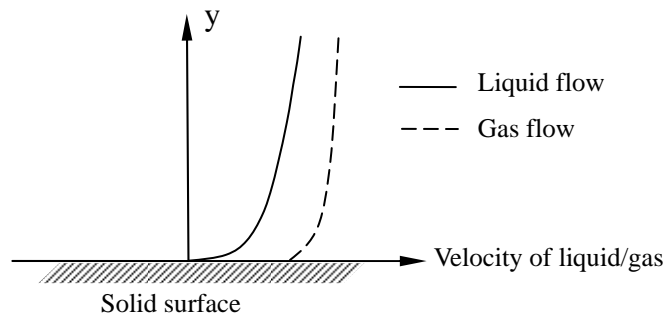


Fig. 6.8 Schematic illustration of gas slip-flow.

For the vapor phase transport, the presence of liquid phase decreases the permeability as shown in Fig. 6.9. This effect is accounted for by introducing an effective coefficient, k_{rg} , to the intrinsic permeability for gas as follows [Chung and Consolazio, 2005]

$$k_{rg} = 10^{S_w \gamma} - 10^\gamma S_w \quad (6.13a)$$

with

$$\gamma = 0.05 - 22.5 f_{cap} \quad (6.13b)$$

where f_{cap} is the capillary porosity of cement paste and S_w is the water saturation degree (Eq. 5.2). Those parameters can be determined in the thermal decomposition analysis (Chapter 4) and the vapor pressure analysis (Chapter 5). The effective permeability coefficient versus the water saturation degree is plotted in Fig. 6.10. The interface-react between vapor and liquid, which can be described by the Kelvin equation, is not considered explicitly.

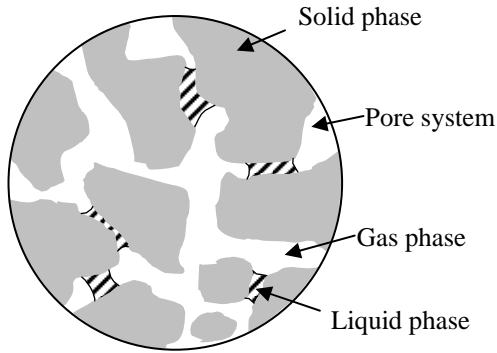


Fig. 6.9 Liquid phase in hardened cement paste.

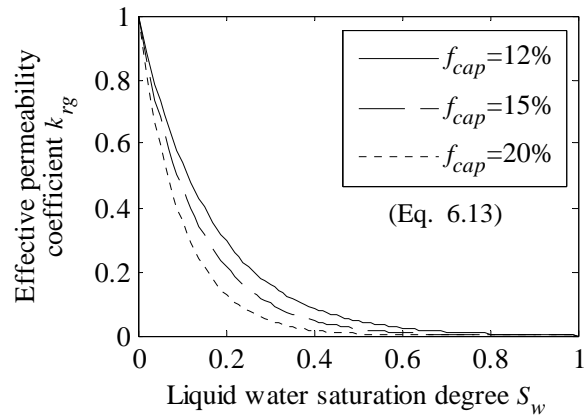


Fig. 6.10 Effective permeability coefficient as a function of water saturation degree.

6.4 Numerical solution of moisture transport

For the moisture transport analysis, the FEM is used and the Galerkin weighted-residual scheme is applied [Zienkiewicz and Taylor, 2000]. By discretizing the spatial domain of interest into a number of finite elements, the approximate value of the unknown field in each element can be expressed in terms of nodal unknowns using the interpolation polynomial shape functions, N_i ,

$$p = \sum_{i=1}^n N_i p_i^e \quad (6.14)$$

where p_i^e are the element nodal unknowns, n is the number of nodes of the element. Substitution of the approximate solution, p , into Eq. 6.7 yields the residual, R_Ω

$$R_\Omega = \frac{\partial}{\partial x_i} \left(k \frac{\partial p}{\partial x_i} \right) - \frac{\partial \rho}{\partial t} + \dot{m}_{dh} \quad (6.15)$$

Three-node triangular elements are used for the 2D discretization. By applying the Galerkin method, in which the weight function ω_j is equal to

$$\omega_j = N_j \quad (j=1, 2, 3) \quad (6.16)$$

the following equation is obtained

$$\int_{\Omega} \omega_j R_\Omega d\Omega = 0 \quad (6.17)$$

where Ω is the 2D domain of each element. By integrating Eq. 6.17 by parts and by summing up all the elements, the weighted residual integral can be expressed in matrix form as

$$[K']\{\dot{p}\} + [K'']\{p\} = \{F'\} \quad (6.18)$$

where $[K']$, $[K'']$, and $\{F'\}$ are as follows

$$[K'] = \sum_e \int_{\Omega_e} \frac{\rho}{P} N_i N_j d\Omega \quad (6.19a)$$

$$[K''] = \sum_e \int_{\Omega_e} k \frac{\partial N_i}{\partial x_l} \frac{\partial N_j}{\partial x_l} d\Omega \quad (6.19b)$$

$$\{F'\} = \sum_e \int_{\Omega_e} \dot{m}_{dh} N_i d\Omega \quad (6.19c)$$

with $i, j=1, 2, 3$ and $l=1, 2$. In Eq. 6.18, the time derivative term exists. By applying the backward difference method, Eq. 6.18 can be transformed into

$$\left([K''] + \frac{[K']}{\Delta t} \right) \{p_t\} = \{F'_t\} + \frac{[K']}{\Delta t} \{p_{t-\Delta t}\} \quad (6.20)$$

where Δt is the given time interval.

6.5 Application

The moisture transport of heated concrete cubes is investigated in the spalling analysis in Chapter 8 based on the experiments of Peng [2000]. As an example, the moisture transport of the HPC₂₈₋₁₁₀ cube with 90% initial moisture content under the slow heating condition (0.5 °C/min) is shown in Fig. 6.11/ Fig. 8.27. The detailed description is shown in Chapter 8.

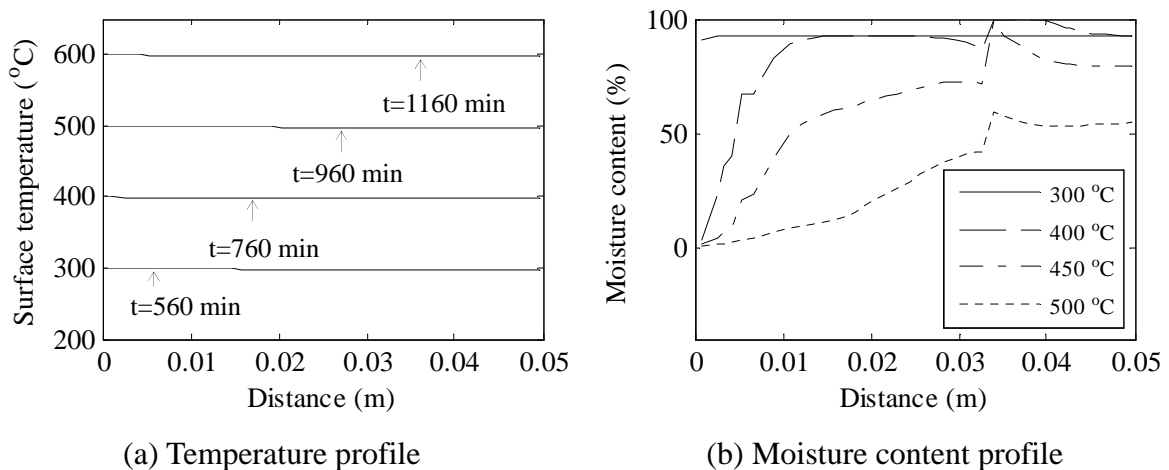


Fig. 6.11 Profile of predicted moisture content of HPC cube with 90% initial moisture content under slow heating (0.5 °C/min).

6.6 Summary

The modeling part of moisture transport for fire spalling analysis has been proposed and described in this chapter. First, the governing equation of moisture transport has been derived according to the mass conservation principle. Based on the thermal decomposition analysis discussed in Chapter 4, the permeability of hardened cement paste has been predicted by applying the general effective medium theory. The effects of gas slip-flow and the water saturation degree on the permeability have been taken into account. The finite element method has been applied in solving the governing equation. As the moisture transport involves the temperature field, the vapor pressure, and the thermal decomposition analyses, the modeling result of the moisture transport of heated concrete cubes of the experiments of Peng [2000] is systematically shown in Chapter 8.

Chapter 7

Thermo-poro mechanical analysis

7.1 Introduction and literature review

For the fire spalling analysis, the modeling part of thermo-poro mechanical analysis is discussed in this chapter (Fig. 7.1). The existing mechanical models and the model used in the fire spalling analysis in the literature are reviewed first. Then the model proposed in this thesis is presented in the following sections. The application of the mechanical analysis is shown in Chapter 8.

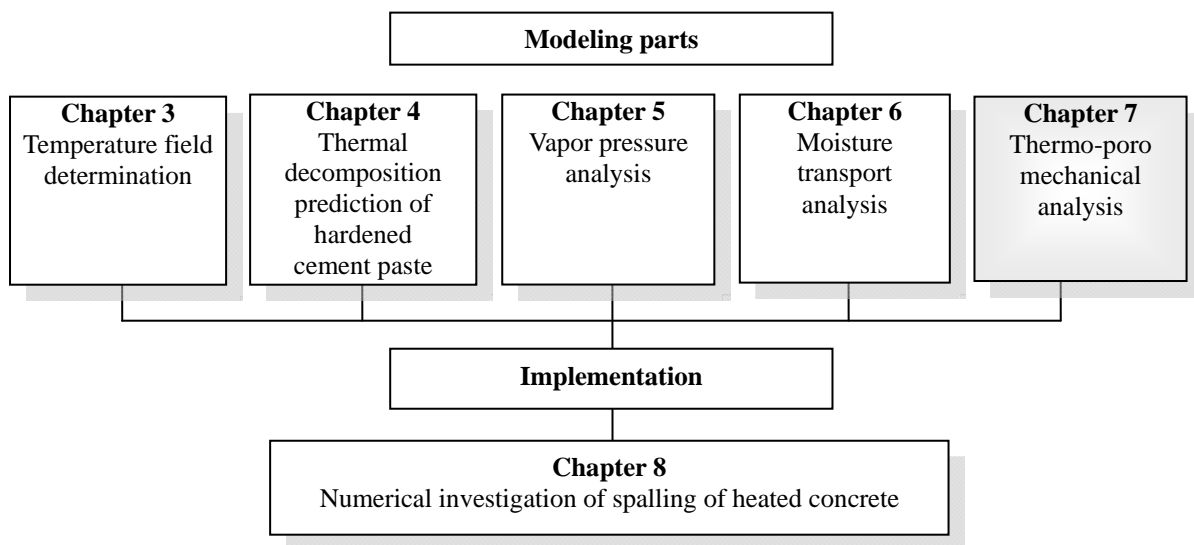


Fig. 7.1 Modeling parts of fire spalling analysis.

When concrete is exposed to elevated temperatures, mechanical damage, such as cracking or even explosive spalling, may occur (Chapters 1 and 2). For modeling cracking in a solid, three main numerical approaches exist, i.e., the discrete crack model [Ngo and Scordelis, 1967], the smeared crack model [Rashid, 1968; Mazars, 1989], and the lattice model [Schlangen and van Mier, 1992]:

- In the lattice model, the continuous solid is represented by a lattice of truss or beam elements. The cracking is modeled by breaking of elements during the loading process.
- In the discrete crack model, cracks are usually modeled to propagate along the FE mesh lines. When the nodal force, which is normal to the element boundaries, exceeds the tensile strength of the solid, cracking is assumed to occur and the two elements are separated. This

approach has two drawbacks. First, the crack is constrained to follow a predefined path along the element edges. Second, it gives rise to a continuous change of topology of the geometrical discretization. Two techniques of improvement are the automatic remeshing and the use of interface element [Rots, 1991].

- In the smeared crack model, the cracked solid is assumed to be still a continuum and the crack damage is represented by degrading the mechanical properties. The geometrical topology of the initial FE mesh can be preserved and the orientation of the crack is not restricted. Those two advantages, together with the computational efficiency, make this method to be widely used. A distinction can be made between fixed and rotating crack models within the smeared crack approach [Rots, 1988]. In a fixed smeared crack model, the direction of the crack is fixed upon the initiation of cracking. The rotating crack model allows the crack to rotate according to the principal direction of stress or strain. If the solid is assumed to behave isotropically after cracking, the isotropic smeared crack model [Mazars, 1989] is derived. This model works well for monotonic loading [Rots, 1991] and its simplicity is also attractive.

For the thermal mechanical analysis of concrete exposed to high temperatures, the isotropic smeared crack model was used by Majorana et al. [1998], Schrefler et al. [2002], Houry et al. [2002], Tenchev and Purnell [2005], Pont et al. [2005a, 2005b], Grondin et al. [2007], and Gawin et al. [2002, 2003, 2004, 2006] (Chapter 2). However, when both the value and the direction of stress/strain are changing with the temperature development, difficulties may be encountered. The mechanical behavior of heated concrete might be better modeled if the anisotropic description is employed.

In this thesis, to analyze the thermo-poro mechanical behavior of heated concrete, the fixed anisotropic smeared crack theory is applied. The effect of vapor pressure (Chapter 5) on the mechanical damage is incorporated. Both cracking and spalling are analyzed (Chapter 8). The thermal decomposition induced decrease of the elastic modulus of hardened cement paste is predicted and verified with the experimental data collected from the literature.

7.2 Basic equations of elastic thermo-poro mechanical analysis

For isotropic material, the generalized linear elastic constitutive relation incorporating the one-way coupling of the fluid-to-solid in index notation is as follows [Biot, 1941; Coussy, 2004]

$$\varepsilon_{ij} = \frac{1}{2G} \left[\sigma_{ij} - \frac{\nu}{1+\nu} \sigma_{kk} \delta_{ij} \right] + \frac{1}{3H} p \delta_{ij} + \varepsilon_{th} \delta_{ij} + \varepsilon_{cp} \delta_{ij} \quad (7.1)$$

where ν is the drained Poisson's ratio, G is the drained shear modulus, p is the pore pressure (Chapter 5), $1/H$ is the Biot modulus (Chapter 5), δ_{ij} is the Kronecker delta (if i equals j , $\delta_{ij}=1$, else $\delta_{ij}=0$), σ_{ij} is the stress tensor, and ε_{ij} is the total strain tensor, which can be obtained from the geometric equations

$$\varepsilon_{ij} = \frac{1}{2} \left(\frac{\partial u_i}{\partial x_j} + \frac{\partial u_j}{\partial x_i} \right) \quad (7.2)$$

where u is the displacement. ε_{th} is the free thermal strain, ε_{cp} is the total creep strain, which consists of the transient creep, ε_{tr} , and the basic creep, ε_{bcp} (Chapter 2), as

$$\varepsilon_{cp} = \varepsilon_{tr} + \varepsilon_{bcp} \quad (7.3)$$

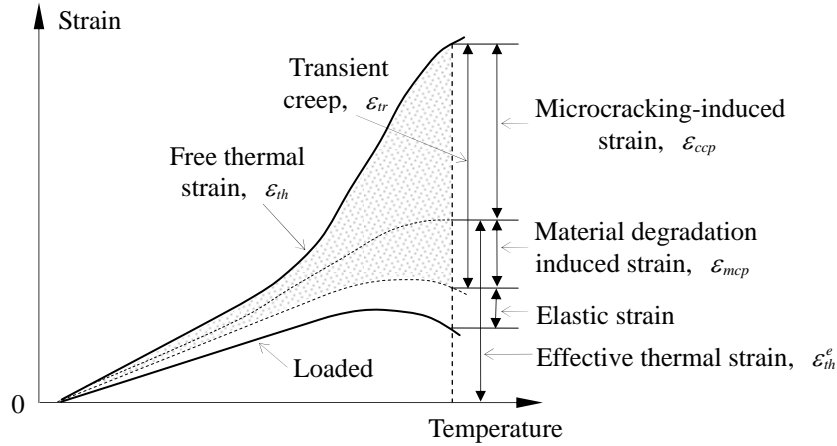


Fig. 7.2 Decomposition of transient creep into microcracking-induced strain of free expansion and material degradation-induced strain

In this thesis, the basic creep (Chapter 2) is assumed negligibly small since the heating duration before fire spalling is only several minutes. The transient creep is divided into two parts, i.e., the microcracking-induced strain of free expansion, ε_{ccp} [Wan et al., 2008], and the material degradation-induced strain, ε_{mcp} , as shown in Fig. 7.2. Thus, the total creep strain is equal to

$$\varepsilon_{cp} = \varepsilon_{ccp} + \varepsilon_{mcp} \quad (7.4)$$

The material degradation-induced creep strain, ε_{mcp} , is accounted for in the decrease of the elastic modulus (Section 7.5) in this study. For the microcracking-induced strain of free expansion, ε_{ccp} , a parameter called the effective thermal strain, ε_{th}^e , is introduced, which is defined as the free thermal strain minus the absolute value of the microcracking-induced strain as (Fig. 7.2)

$$\varepsilon_{th}^e = \varepsilon_{th} + \varepsilon_{ccp} \quad (7.5)$$

Although, under the load condition, the confining extent of the microcracking of expansion depends on the magnitude of the applied load, this dependency is assumed negligible. Thus, the constitutive relation in Eq. 7.1 can be expressed as

$$\varepsilon_{ij} = \frac{1}{2G} \left[\sigma_{ij} - \frac{\nu}{1+\nu} \sigma_{kk} \delta_{ij} \right] + \frac{1}{3H} p \delta_{ij} + \varepsilon_{th}^e \delta_{ij} \quad (7.6)$$

with

$$\varepsilon_{th}^e = \alpha_t^e \cdot T \quad (7.6a)$$

where α_t^e is the coefficient of effective thermal expansion and T is the temperature change, (Chapter 3). For the mechanical analysis, the equation of static equilibrium is as follows

$$\frac{\partial \sigma_{ji}}{\partial x_j} + f_i = 0 \quad (7.7)$$

where f_i is the body force. As only the state change is investigated, the body force is not considered. The effective stress tensor is given by (Chapter 5)

$$\sigma_{ij}^e = \sigma_{ij} + \alpha_b \cdot p \delta_{ij} \quad (7.8)$$

where α_b is the Biot-Willis coefficient (Chapter 5).

Eq. 7.1 through Eq. 7.8 describe the elastic thermo-poro mechanical behavior of a solid. For two-dimensional analysis, such as the plane stress problem, where $\sigma_z = \tau_{xz} = \tau_{yz} = 0$, the above equations can be transformed accordingly and those equations can be transformed further to describe the plane strain problem by replacing the material properties, E , ν , and α_i^e , with $E/(1-\nu^2)$, $\nu/(1-\nu)$, and $(1+\nu)\alpha_i^e$, respectively. In this thesis, the quasi-static state is assumed for each instant of time, that is, the mechanical equilibrium is assumed to be obtained instantaneously under certain temperature field and vapor pressure field. The finite amount of time needed for accommodating the stress change is ignored.

7.3 Non-linear mechanical analysis

When the material couldn't sustain the load, failure, such as cracking, will occur. In this thesis, the anisotropic fixed smeared crack theory is applied for the non-linear mechanical analysis.

7.3.1 Derivation of constitutive relation

In the anisotropic fixed smeared crack theory, the direction-dependent evolution of the cracking damage is considered by degrading the elastic modulus in the cracking direction. For a two-dimensional plane-stress situation, the anisotropic constitutive relation in principal space can be expressed as

$$\sigma_1 = \frac{E_1}{1-\nu_{12}\nu_{21}} [\varepsilon_1 + \nu_{21}\varepsilon_2 - (1+\nu_{21})\varepsilon_0] \quad (7.9a)$$

$$\sigma_2 = \frac{E_2}{1-\nu_{12}\nu_{21}} [\varepsilon_2 + \nu_{12}\varepsilon_1 - (1+\nu_{12})\varepsilon_0] \quad (7.9b)$$

where E_i and ν_{ij} ($i, j = 1, 2$) are the elastic moduli and Poisson's ratios in the two principal directions, respectively, and ε_0 is the initial strain induced by effective thermal expansion and vapor pressure. The elastic moduli are expressed as

$$E_1 = \alpha_1 E_c \quad (7.10a)$$

$$E_2 = \alpha_2 E_c \quad (7.10b)$$

where α_i ($0 \leq \alpha_i \leq 1$, $i = 1, 2$) are the damage variables, which reflect the degrading degrees of E_i , and E_c is the elastic modulus of the undamaged material. It is assumed that the Poisson's ratio of damaged material is related with that of the undamaged material, ν_c , as

$$v_c = \sqrt{v_{12} \cdot v_{21}} \quad (7.10c)$$

By applying the reciprocal theorem of work and substituting Eq. 7.10 into Eq. 7.9, the constitutive relation in the cracking n - s space (Fig. 7.6) can be expressed in matrix form as

$$\sigma_{ns} = D_{ns}^s \varepsilon_{ns} - B' \varepsilon_0 \quad (7.11)$$

with

$$D_{ns}^s = \begin{bmatrix} \frac{\alpha_1 E_c}{1-v_c^2} & \frac{\sqrt{\alpha_1 \alpha_2} v_c E_c}{1-v_c^2} & 0 \\ \frac{\sqrt{\alpha_1 \alpha_2} v_c E_c}{1-v_c^2} & \frac{\alpha_2 E_c}{1-v_c^2} & 0 \\ 0 & 0 & \gamma G \end{bmatrix} \quad (7.11a)$$

$$B' = \begin{Bmatrix} \frac{(\alpha_1 + \sqrt{\alpha_1 \alpha_2} v_c) E_c}{1-v_c^2} \\ \frac{(\alpha_2 + \sqrt{\alpha_1 \alpha_2} v_c) E_c}{1-v_c^2} \\ 0 \end{Bmatrix} \quad (7.11b)$$

where γ ($0 \leq \gamma \leq 1$) is the shear retention factor. For a two-dimensional plane-strain situation, the matrices D_{ns}^s and B' are written as

$$D_{ns}^s = \begin{bmatrix} \frac{\alpha_1 (1-v_c) E_c}{(1-2v_c)(1+v_c)} & \frac{\sqrt{\alpha_1 \alpha_2} v_c E_c}{(1-2v_c)(1+v_c)} & 0 \\ \frac{\sqrt{\alpha_1 \alpha_2} v_c E_c}{(1-2v_c)(1+v_c)} & \frac{\alpha_2 (1-v_c) E_c}{(1-2v_c)(1+v_c)} & 0 \\ 0 & 0 & \gamma G \end{bmatrix} \quad (7.11c)$$

$$B' = \begin{Bmatrix} \frac{(\alpha_1 (1-v_c) + \sqrt{\alpha_1 \alpha_2} v_c) E_c}{1-2v_c} \\ \frac{(\alpha_2 (1-v_c) + \sqrt{\alpha_1 \alpha_2} v_c) E_c}{1-2v_c} \\ 0 \end{Bmatrix} \quad (7.11d)$$

The local constitutive relation (Eq. 7.11) can be transformed into the global coordinate system through the standard transformation matrix, R_0 ,

$$\sigma_{xy} = R_0^T D_{ns}^s R_0 \varepsilon_{xy} - R_0^T B^t \varepsilon_0 \quad (7.12)$$

7.3.2 Damage evolution

In the local n - s coordinate system (Fig. 7.6), the loading function for damage evolution is [Rots, 1988]

$$f(\varepsilon'_{mn}, \kappa) = \varepsilon'_{mn} - \kappa \quad (7.13)$$

where κ is a history-dependent damage parameter, which memorizes the highest value of ε'_{mn} , and ε'_{mn} is defined as

$$\varepsilon'_{mn} = \varepsilon_{mn} - \varepsilon_{th}^e \quad (7.14)$$

The loading function (Eq. 7.13) is subjected to the standard Kuhn-Tucker loading-unloading conditions [Simo et al, 1988]

$$f \leq 0, \quad \dot{\kappa} \geq 0, \quad f \cdot \dot{\kappa} = 0 \quad (7.15)$$

where $\dot{\kappa}$ is the rate of κ . The value of κ is monotonically increasing during the whole loading process. If the loading function, f , is negative, unloading occurs and $\dot{\kappa} = 0$. If the loading function, f , vanishes, further loading takes place and $\dot{\kappa} \geq 0$.

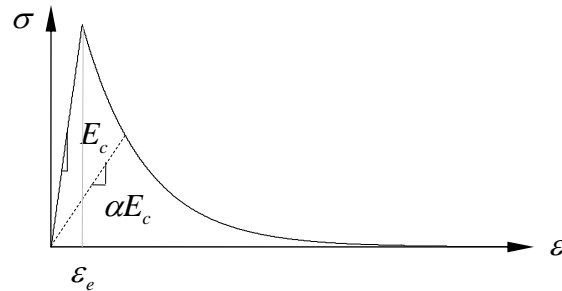


Fig. 7.3 Stress-strain relation under uniaxial tension.

The damage variable α is defined as a function of the history parameter, κ . Its evolution is inferred from the one-dimensional tensile stress-strain relation (Fig. 7.3), which is expressed as

$$\alpha = \alpha(\kappa) = \begin{cases} 1 & \text{if } \kappa \leq \varepsilon_e \\ \frac{\varepsilon_e}{\kappa} \exp[-\mu(\kappa - \varepsilon_e)] & \text{if } \kappa \geq \varepsilon_e \end{cases} \quad (7.16)$$

where ε_e is the strain at the peak stress under uniaxial tension and μ is a parameter that controls the slope of the exponential strain softening curve and can be determined according to the fracture energy of the material.

7.3.3 Failure criterion

Prior to cracking, both aggregates and matrix are modeled as isotropic, linear-elastic materials. When the combination of principal stresses reaches the tension cut-off criterion [Kupfer et al., 1969] as shown in Fig. 7.4, a crack perpendicular to the direction of principal stress is initiated and the orientation of the crack is fixed thereafter. At this stage, the initial isotropic constitutive relation is replaced by the orthotropic one with fixed axes of orthotropy (Fig. 7.6).

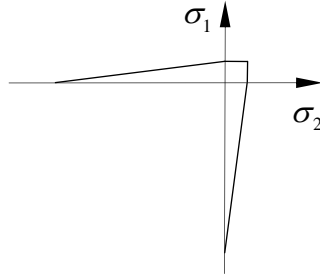


Fig. 7.4 Tension cut-off criterion.

7.3.4 Determination of shear retention factor

The shear retention factor is used to reflect the interlock of the material after cracking. It represents the capability of a crack to transfer shear stresses in mode-II[†]. In this thesis, the shear retention factor, γ , in Eq. 7.11 is taken as inversely proportional to the crack strain, ε_{cr} , as shown in Fig. 7.5 [Kolmar and Mehlhorn, 1984].

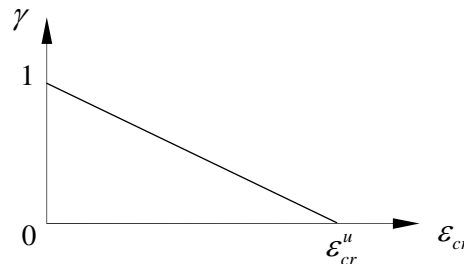


Fig. 7.5 Shear retention factor.

The crack strain is determined as

$$\varepsilon_{cr} = \varepsilon'_{mn} - \varepsilon_{con} \quad (7.17)$$

where ε_{con} is the elastic strain of concrete. As concrete and crack behave like springs connected in series, the following relation holds

$$\frac{1}{E_c} + \frac{1}{E_{cr}} = \frac{1}{\alpha E_c} \quad (7.18)$$

where E_{cr} is the elastic modulus of crack. Thus, ε_{cr} can be further expressed as

$$\varepsilon_{cr} = (1 - \alpha)\varepsilon'_{mn} \quad (7.19)$$

[†] Mode I crack – Opening mode; Mode II crack – Sliding mode; Mode III crack – Tearing mode

7.3.5 Stiffness recovery

As the stress and strain, both magnitudes and directions, in a solid may change with the temperature development, a stiffness recovery caused by crack closure may occur (Fig. 7.6), that is, the degraded elastic modulus caused by cracking will regain its original value. This recovery is considered in the analysis.

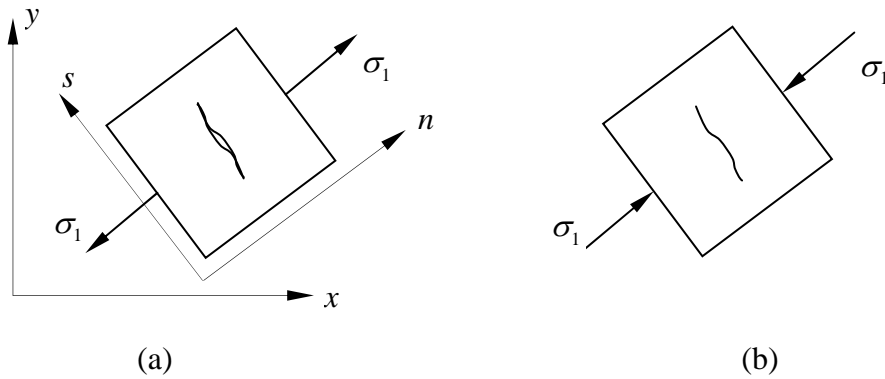


Fig. 7.6 Schematic illustration of stiffness recovery: (a) crack formation; (b) crack closure.

7.4 Numerical solution of two-dimensional problem

As illustrated in the previous sections, the stress and strain fields in a solid subjected to elevated temperatures are described by differential equations. The principle of minimum potential energy and the FEM are applied in solving the equations [Zienkiewicz and Taylor, 2000]. The principle of minimum potential energy is that, out of all the possible displacement fields, the one that satisfies both the static equilibrium equations and the geometric boundary conditions, results in the minimum total potential energy of a body. The total potential energy is defined as the sum of the internal potential energy (strain energy) and the external potential energy. Based on this principle, the following finite element analysis is conducted.

When three-node triangular elements are used to discretize the two-dimensional domain of interest, the displacement in each element, u , can be expressed as a function of nodal-unknowns, u^e ,

$$u = Nu^e \quad (7.20)$$

where N is the shape function matrix. The strain energy of each element, U_{te} , is equal to

$$U_{te} = \frac{1}{2} \iint_e \{\sigma\}^T (\{\varepsilon\} - \{\varepsilon_0\}) dx dy \quad (7.21)$$

Substitution of the constitutive equation and the geometric equation into Eq. 7.21 yields

$$U_{te} = \frac{1}{2} (\{u\}^e)^T [K_1]^e \{u\}^e - (\{u\}^e)^T \{F_1\}^e + C_e \quad (7.22)$$

with

$$[K_1]^e = \iint_e [B]^T [D][B] dxdy = [B]^T [D][B] \Delta \quad (7.23)$$

$$\{F_1\}^e = \iint_e [B]^T [D]\{\varepsilon_0\} dxdy = [B]^T [D]\{\varepsilon_0\} \Delta \quad (7.24)$$

$$C_e = \frac{1}{2} \iint_e \{\varepsilon_0\}^T [D]\{\varepsilon_0\} dxdy = \frac{1}{2} \{\varepsilon_0\}^T [D]\{\varepsilon_0\} \Delta \quad (7.25)$$

where [D] is the elastic matrix, [B] is the geometric matrix, and Δ is the area of the 2D element. As no external load is applied in addition to the thermal load, the work done by the external forces is equal to zero. Thus, the total potential energy, U_e , can be written as

$$U_e = U_{te} = \frac{1}{2} (\{u\}^e)^T [K_1]^e \{u\}^e - (\{u\}^e)^T \{F_1\}^e + C_e \quad (7.26)$$

According to the principle of minimum potential energy, the nodal displacements of each element satisfies the following expression

$$\frac{\partial U_e}{\partial \{u\}^e} = 0 \quad (7.27)$$

which yields

$$[K_1]^e \{u\}^e = \{F_1\}^e \quad (7.28)$$

Assembling Eq. 7.28 of all the elements gives

$$[K_1]\{u\} = \{F_1\} \quad (7.29)$$

where $[K_1]$ is the global stiffness matrix

$$[K_1] = \sum_e [K_1]^e \quad (7.30)$$

In the nonlinear analysis, as the stiffness matrix, $[K_1]$, is a function of the displacement, $\{u\}$, the Newton-Raphson iteration method is used for solving Eq. 7.29. Differentiation of Eq. 7.12 with respect to virtual time yields the tangential constitutive relation needed in the iterative procedure

$$\dot{\sigma}_{xy} = R_0^T (D_{ns}^s + \Delta D_{ns} - \Delta D_t) R_0 \dot{\varepsilon}_{xy} \quad (7.31)$$

with ΔD_{ns} given by

$$\Delta D_{ns} = \begin{bmatrix} d_{11} & d_{12} & 0 \\ d_{21} & d_{22} & 0 \\ d_{31} & 0 & 0 \end{bmatrix} \quad (7.32)$$

with

$$d_{11} = \frac{E_c}{(1+v_c)(1-2v_c)} \left[\dot{\alpha}_1(1-v_c)\varepsilon_{11} + \frac{1}{2}(\alpha_1\alpha_2)^{-\frac{1}{2}}v_c\dot{\alpha}_1\alpha_2\varepsilon_{22} \right] \quad (7.32a)$$

$$d_{12} = \frac{E_c}{2(1+v_c)(1-2v_c)} (\alpha_1\alpha_2)^{-\frac{1}{2}}v_c\dot{\alpha}_2\alpha_1\varepsilon_{22} \quad (7.32b)$$

$$d_{21} = \frac{E_c}{2(1+v_c)(1-2v_c)} (\alpha_1\alpha_2)^{-\frac{1}{2}}v_c\dot{\alpha}_1\alpha_2\varepsilon_{11} \quad (7.32c)$$

$$d_{22} = \frac{E_c}{(1+v_c)(1-2v_c)} \left[\dot{\alpha}_2(1-v_c)\varepsilon_{22} + \frac{1}{2}(\alpha_1\alpha_2)^{-\frac{1}{2}}v_c\dot{\alpha}_2\alpha_1\varepsilon_{11} \right] \quad (7.32d)$$

$$d_{31} = \frac{E_c}{2(1+v_c)} \dot{\alpha}_1\varepsilon_{12} \quad (7.32e)$$

$$\dot{\alpha}_1 = \frac{\partial k}{\partial \varepsilon'_{11}} \frac{\varepsilon_0(-\mu\varepsilon'_{11}-1)}{\varepsilon_{11}^2} \exp[-\mu(\varepsilon'_{11}-\varepsilon_0)] \quad (7.32f)$$

$$\dot{\alpha}_2 = \frac{\partial k}{\partial \varepsilon'_{22}} \frac{\varepsilon_0(-\mu\varepsilon'_{22}-1)}{\varepsilon_{22}^2} \exp[-\mu(\varepsilon'_{22}-\varepsilon_0)] \quad (7.32g)$$

and with ΔD_t given by

$$\Delta D_t = \begin{bmatrix} t_{11} & t_{12} & 0 \\ t_{21} & t_{22} & 0 \\ 0 & 0 & 0 \end{bmatrix} \quad (7.33)$$

with

$$t_{11} = \frac{v_c E_c \varepsilon_{th}^e}{1-2v_c} \left[\dot{\alpha}_1(1-v_c) + \frac{1}{2}(\alpha_1\alpha_2)^{-\frac{1}{2}}\dot{\alpha}_1\alpha_2v_c \right] \quad (7.33a)$$

$$t_{12} = \frac{v_c E_c \varepsilon_{th}^e}{2(1-2v_c)} (\alpha_1\alpha_2)^{-\frac{1}{2}}\dot{\alpha}_2\alpha_1v_c \quad (7.33b)$$

$$t_{21} = \frac{v_c E_c \varepsilon_{th}^e}{2(1-2v_c)} (\alpha_1 \alpha_2)^{-\frac{1}{2}} \dot{\alpha}_1 \alpha_2 v_c \quad (7.33c)$$

$$t_{22} = \frac{v_c E_c \varepsilon_{th}^e}{1-2v_c} \left[\dot{\alpha}_2 (1-v_c) + \frac{1}{2} (\alpha_1 \alpha_2)^{-\frac{1}{2}} \dot{\alpha}_2 \alpha_1 v_c \right] \quad (7.33d)$$

7.5 Thermal variation of elastic modulus

In the aforementioned mechanical analysis, the elastic modulus, E_c , is changing with the heating process. For aggregate, the elastic modulus is taken as temperature dependent according to the experimental data collected from the literature (Chapter 8). For the matrix, based on the thermal decomposition process (Chapter 4), the elastic modulus is predicted using a two-phase composite sphere model (Fig. 7.7) [Christensen, 1979; Zheng et al., 2010]. In the two-phase composite sphere model, the effective bulk modulus of a two-phase composite, K_e , is given by

$$K_e = K_m + \frac{(K_{in} - K_m) f_{in}}{1 + \left[(1 - f_{in})(K_{in} - K_m) / (K_m + 4G_m/3) \right]} \quad (7.34)$$

where K and G with subscript are the bulk and shear modulus, the subscripts in and m denote the inclusion phase and the matrix phase, and f_{in} is the volume fraction of the inclusion phase. In this thesis, the residual undecomposed phase is treated as matrix and the products of thermal decomposition are treated as inclusion. In the equation, the bulk and shear modulus is equal to

$$G = \frac{E}{2(1+\nu)} \quad (7.35)$$

$$K = \frac{E}{3(1-2\nu)} \quad (7.36)$$

where E and ν are Young's modulus and Poisson's ratio, respectively. Poisson's ratio is taken as 0.2 in this study. When the elastic modulus and the volume fraction of the inclusion phase are known, the effective elastic modulus of decomposed hardened cement paste can be obtained using Eq. 7.34.

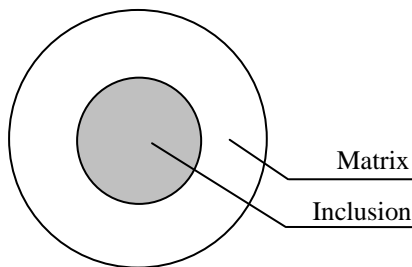


Fig. 7.7 Two-phase composite sphere model.

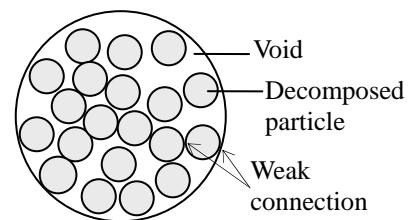


Fig. 7.8 Schematic illustration of geometry of decomposition product.

The volume fraction and the porosity of the decomposition products can be obtained by the thermal decomposition analysis (Chapter 4). Since the decomposition products are poorly connected to each other and to the other constituents, their contribution to the stiffness of the material is little (Fig.7.8) [Lin et al., 1996; Shimada and Young, 2001; Pourchez et al., 2006]. According to the decomposition analysis in Chapter 4, the porosity of all the decomposition products is around 50% (52%, 54%, 58%, and 40% for the decomposition products of AFt, CH, conventional C-S-H, and pozzolanic C-S-H, respectively). It is, therefore, assumed that their contributions to the stiffness are the same. As schematically illustrated in Fig.7.8, the drained elastic modulus of void product of decomposition is zero. If the weak connection of the decomposition particles is taken into account, a low value of 0.02 GPa is assumed for the elastic modulus of the decomposition product owing to the lack of the experimental data. This assumption and the proposed model will be verified in Section 7.6.

It should be pointed out that, first, in the elastic modulus prediction model, the effect of the drying shrinkage-induced crack on the elastic modulus is not considered in view of the fact that fire spalling occurs in the first several minutes of heating [Peng, 2000]. Second, the proposed model can only be used for the heating temperature up to 600 °C. When the temperature is higher than 600 °C and most of C-S-H is decomposed, a more complicated model will be needed for the elastic modulus prediction.

7.6 Verification of elastic modulus prediction

The proposed method for the prediction of the elastic modulus of heated hardened cement paste is verified with the experimental data of Masse et al. [2002]. In their experiment, a Portland cement CEM I 52.5 was used. After 28-day curing at room temperature, three specimens of hardened cement paste with water-to-cement ratios of 0.25, 0.35, and 0.5, respectively, were exposed to elevated temperatures. The elastic moduli were measured by non-destructive ultrasonic technique after the specimens were naturally cooled to room temperature. The target temperatures were 80, 120, 150, 200, 250, 300, 400, 500, 600, 700, and 800 °C and the heating rate was 0.2 °C/min. The exposure duration at each target temperature was 10 hours. The size of the cylindrical specimens was 15 mm in diameter and 15-19 mm in height.

To predict the elastic modulus, according to the test condition, first, the hydration degrees of cement of the three specimens are predicted to be 52.66%, 62.86%, and 75.36%, respectively [Parrot and Killoh, 1984]. Based on the thermal decomposition analysis (Chapter 4), the elastic moduli are then predicted using the proposed method in Section 7.5. The predicted relative value of the elastic modulus of the three specimens is shown in Fig. 7.10, together with the experimental results.

It can be seen from Fig. 7.10 that the predicted result is reasonably in good agreement with the experimental result. The discrepancy in the temperature range of 250 °C to 400 °C is caused by the drying shrinkage-induced cracking since on decomposition occurs in this temperature range (Fig. 7.9). In the test, the exposure duration at each target temperature was long (10 hours), the heating rate was low (0.2 °C/min), and the size of the sample was small. All those factors might result in significant drying shrinkage, leading to shrinkage-induced cracks and thus the additional reduction of the elastic modulus of hardened cement paste [Lin et al., 1996; Fu et al., 2004c].

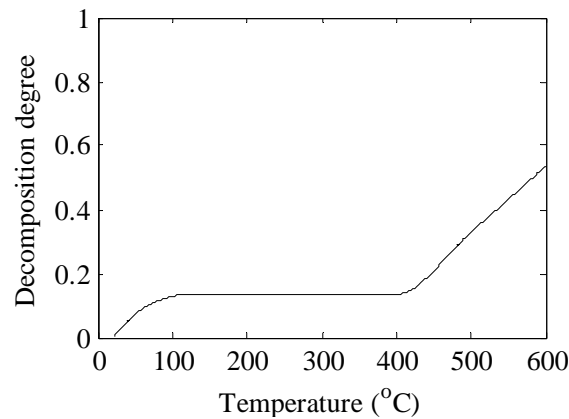


Fig. 7.9 Predicted decomposition degree of heated hardened cement paste of Masse et al. [2002].

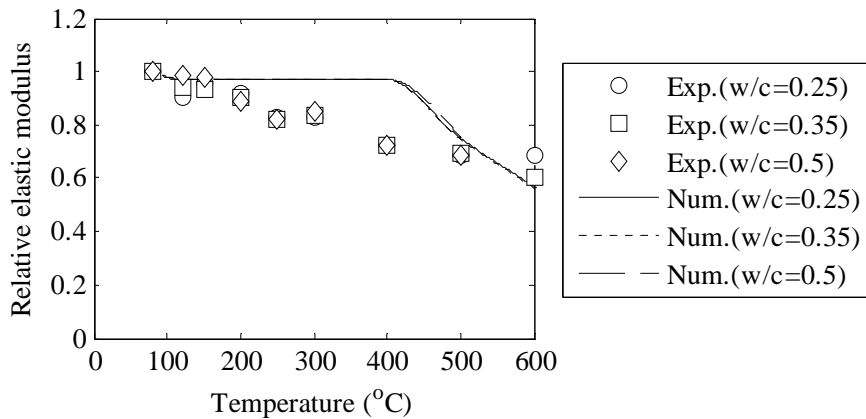


Fig. 7.10 Comparison between numerical results and experimental results of elastic modulus of heated hardened cement paste of Masse et al. [2002].

7.7 Summary

In this chapter, the anisotropic fixed smeared crack theory has been discussed for the nonlinear mechanical analysis of heated concrete. Both the thermal load and the load of vapor pressure have been incorporated. The constitutive relation with two directional damage parameters has been derived and the tension cut-off criterion has been used to evaluate the initiation of cracking. The crack closure-induced stiffness recovery has also been accounted for. The stress and strain fields have been solved numerically by FEM. The Newton-Raphson method has been employed for the non-linear analysis. The tangential constitutive relation needed in the iteration has been formulated. Finally, according to the thermal decomposition process, an analytical method for the prediction of the elastic modulus of heated hardened cement paste has been proposed and verified with experimental data collected from the literature. The thermo-hydro mechanical analysis of heated concrete cubes of Peng [2000] is shown in Chapter 8.

Chapter 8

Numerical investigation of spalling of heated concrete

8.1 Introduction

As has been mentioned in Chapters 1 and 2, two hypotheses have been proposed to interpret spalling of heated concrete: the vapor pressure mechanism [Anderberg, 1997; Peng, 2000] and the temperature gradient induced thermal stress mechanism [Bažant, 1997; Ulm et al., 1999a, 1999b]. In the former, a theory of moisture-clog spalling has also been proposed [Bažant, 1997; Consolazio et al., 1998; Kalifa et al., 2000]. However, quantitative analysis of the spalling mechanism is seldom reported in the literature. It has been decided, after the literature survey in Chapter 2, that a meso-level spalling study will be conducted. In this chapter, by synthesizing and implementing the afore-mentioned modeling parts in Chapters 3 through 7, the spalling mechanism is qualitatively analyzed (Fig. 8.1).

In the numerical investigation of the spalling mechanism, the spalling behaviour of 100 mm cube specimens of both HPC and NSC with 0% and 90% initial moisture content is analyzed and the heating rate effect is also studied. The concrete cube is modeled as a 2D two-phase (aggregate and matrix) composite in view of the fact that, for HPC, the ITZ effect is negligible [Peng, 2000]. In the analysis, spalling is assumed to occur when the non-linear mechanical analysis fails to converge and the damage pattern before spalling is investigated. It can be inferred from the numerical analysis that, under the fast heating condition, the temperature gradient induced thermal stress plays a dominate role in explosive spalling, while under the slow heating condition, the damage is mainly caused by vapor pressure induced stress.

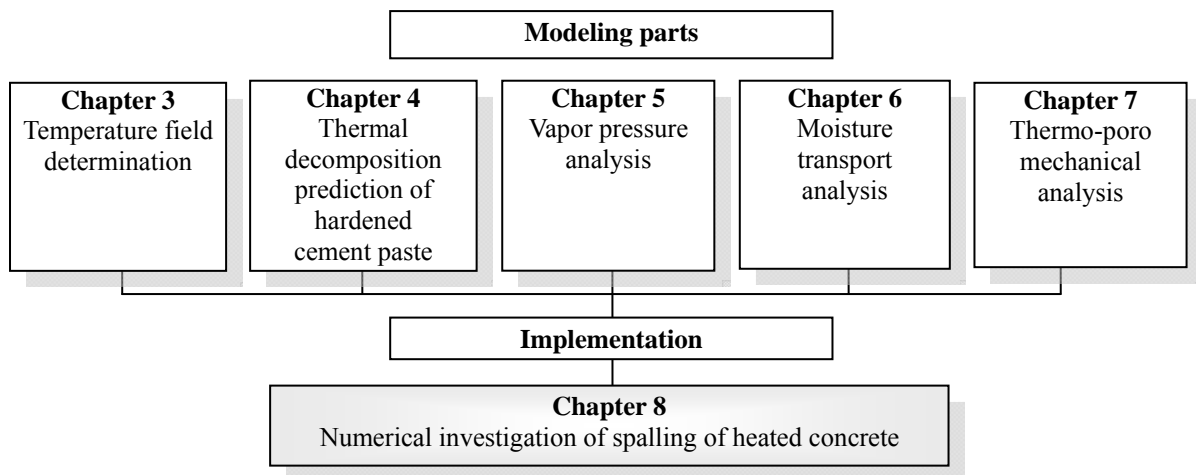


Fig. 8.1 Flowchart of implementation of spalling analysis.

8.2 Numerical model description

To investigate fire spalling, the experiments conducted by Peng [2000] are numerically analyzed. The experiments and the numerical model are described as follows:

- Experiments In Peng's experiments, 100 mm concrete cubes of different strengths (NSC-40, HPC-60, HPC-70, HPC-110, and HPC-120) were cast. An ordinary Portland cement (OPC 52.5) with chemical composition of C_3S -55.8%, C_2S -15.8%, C_3A -9.2%, and C_4AF -9.1% by mass was used and 10% cement by mass was replaced by silica fume with a density of 2.2 g/cm^3 . The water-to-binder ratio ranged from 0.21 to 0.6 for making different concretes. A crushed granite with a density of 2.62 g/cm^3 was used as coarse aggregate and a river sand with a density of 2.61 g/cm^3 was used as fine aggregate. The volume fraction of aggregate is 64.8% for all the specimens. After 90-day curing at room temperature, the fire spalling test was conducted by exposing the specimens with different moisture contents to ISO 834 fire until $600 \text{ }^\circ\text{C}$ (Fig. 8.2). The temperature evolution in the specimens was recorded. The probability of spalling was studied. The experimental results showed that explosive spalling occurred in the temperature range of $480 \text{ }^\circ\text{C}$ to $510 \text{ }^\circ\text{C}$. The higher the strength and moisture content of concrete, the higher the probability of spalling. The cracking pattern of un-spalled concrete specimens was observed by sawing the specimens in half and it was found that the internal cracks reside in the central region of the specimens [Peng, 2000].

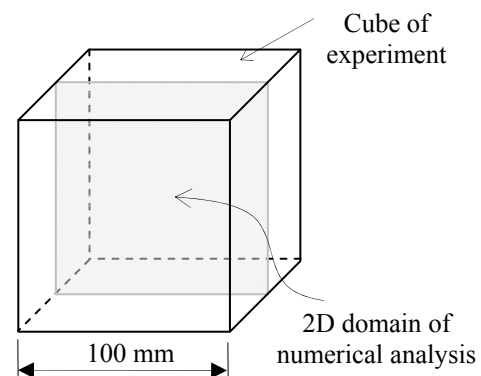
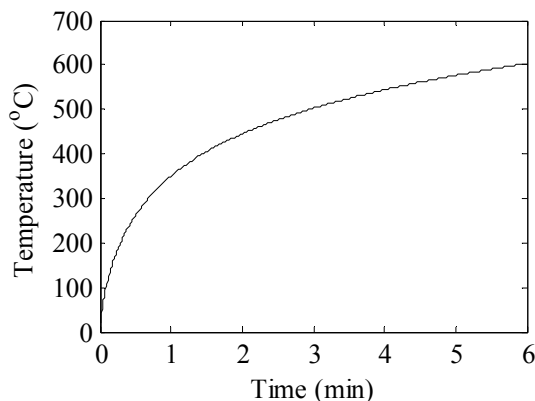


Fig. 8.2 Heating curve of ISO 834 fire until $600 \text{ }^\circ\text{C}$.

Fig. 8.3 2D domain of numerical analysis.

- Numerical model For the numerical analysis, the concrete cube is modeled as a 2D plane strain two-phase (aggregate and matrix) composite (Fig. 8.3). The aggregates, both coarse and fine, are modeled as spheres and randomly distributed according to the aggregate gradation of the experiments. Three distributions are modeled (Fig. 8.4 (a to c)). Three-node triangle elements are used for the discretization as shown in Fig. 8.4 (d) corresponding to the distribution in Fig. 8.4 (c). The aggregate particles with diameter less than 2 mm are ignored. The thermo-chemo-hydro-mechanical behavior of HPC-110 and NSC-40 specimens with 90% and 0% moisture content at the curing age of 90 days is numerically investigated. The moisture in the matrix is assumed uniformly distributed and the isothermal adsorption is not considered. For moisture transport comparison, a specimen of HPC-110 at the curing age of 28 days is also studied. For the display of numerical results, such as the saturation degree, the permeability, and the vapor pressure, 40 points in the matrix are selected along the x-axis in the middle of the specimen (Fig. 8.4 (d)). As similar numerical results are obtained for the three distributions of aggregate in the following analysis, only the results of the distribution in Fig. 8.4 (c) are shown in the following sections.

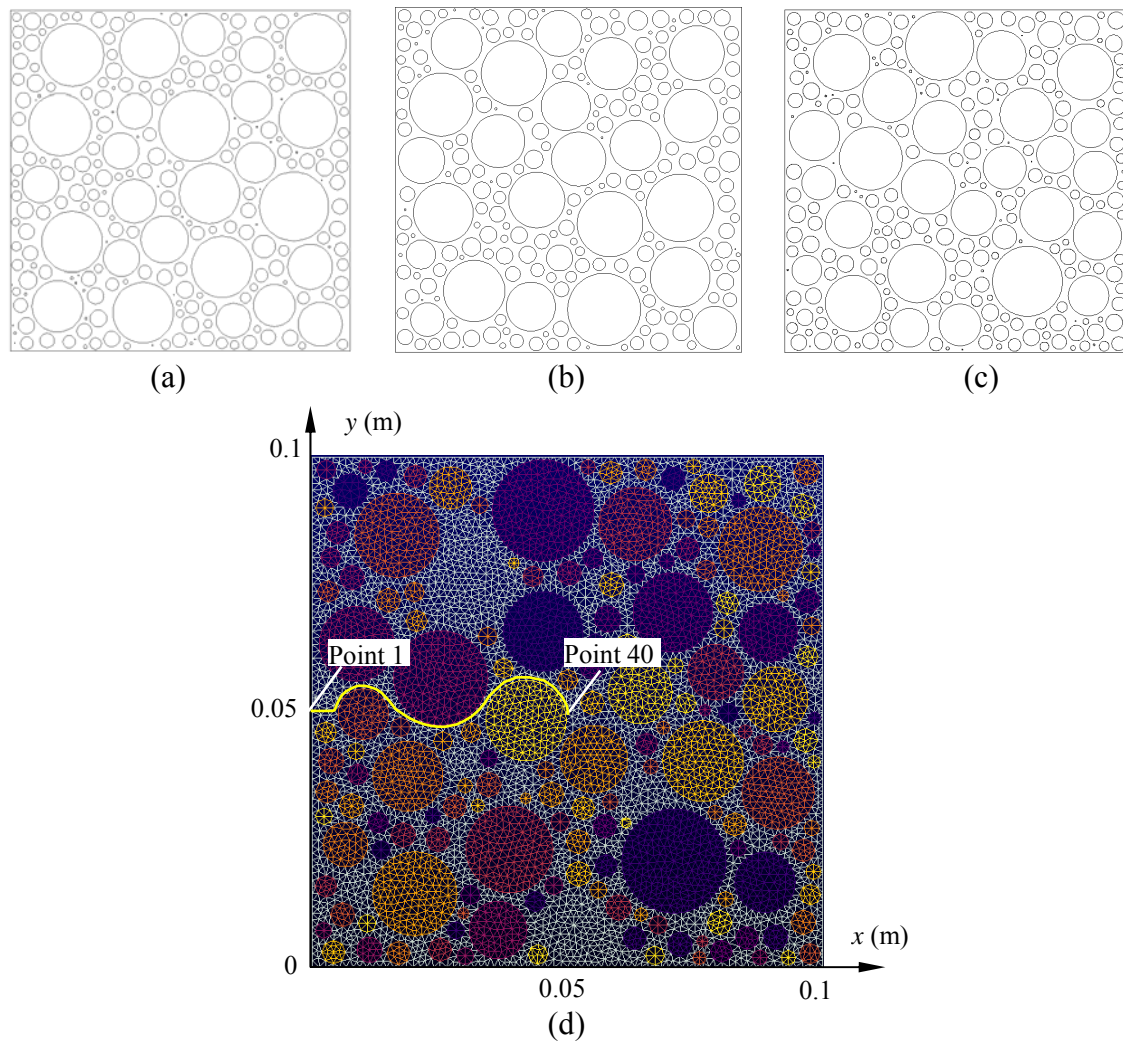


Fig. 8.4 Particle distribution (a to c) and discretization (d) of 2D domain, together with forty points in matrix for results display (d).

8.3 Determination of material parameters

8.3.1 Thermal material properties

As the measured temperature evolution of the specimen of HPC was almost identical to that of the specimen of NSC [Peng, 2000], the constant thermal parameters listed in Table 8.1 are used for both HPC and NSC. The heat sink induced by the thermal decomposition of the matrix and the vaporization of free water in concrete is assumed negligibly small (This assumption is verified later in the temperature prediction). As in the experiments, the concrete specimens were put in fire directly, the boundary condition for the calculation is of the first type (Chapter 3), i.e., the surface temperature of the specimen equals the imposed heating temperature, which follows the heating curve of ISO 834 fire (The imposed temperature is the result of the direct thermal conduction between the specimen and the flame of fire, the convection, and the radiation of fire). By using the model for the temperature prediction discussed in Chapter 3 (The time interval is 5 second), the predicted temperature evolution under the ISO 834 fire condition is compared in Fig. 8.5 (a) with the measured temperature at the four points in the concrete specimen (Fig. 8.5 (b)). It can be seen that the predicted

temperature is in good agreement with the measured temperature. Thus, it can be concluded that the thermal parameters, the time interval, the boundary condition, the assumption of ignoring the heat sink, and the prediction approach presented in Chapter 3 satisfy the spalling analysis.

Table 8.1 Thermal material properties

| | Thermal conductivity (W/m · °C) | Specific heat (J/kg · °C) | Mass density (kg/m ³) |
|-----------|------------------------------------|------------------------------|--------------------------------------|
| Aggregate | 5.0 | 710.0 | 2620.0 |
| Matrix | 4.0 | 1175.0 | 2078.0 |

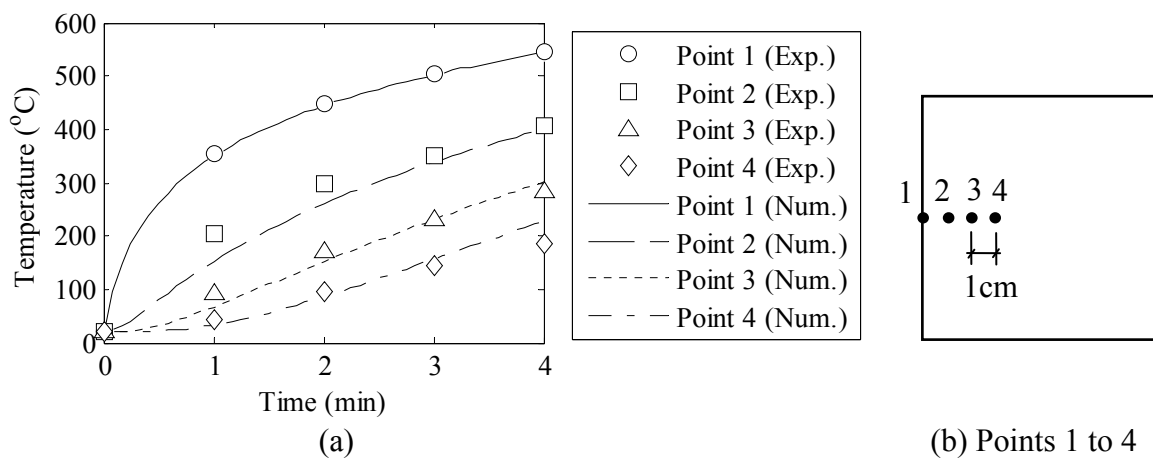


Fig. 8.5 Comparison of measured and predicted temperature evolution in a concrete specimen.

8.3.2 Material parameters of thermal decomposition and moisture transport

According to the water-to-binder ratio (0.26 for HPC-110 and 0.6 for NSC-40) and the curing age, the hydration degrees of both cement and silica fume are predicted to be 55% and 50% for HPC-110 (at 90 days), 85% and 50% for NSC-40 (at 90 days), and 50% and 40% for HPC-110 (at 28 days), respectively [Parrot and Killoh, 1984; Lu et al., 1993]. By using the prediction method proposed in Chapter 4, the following parameters can be obtained. From the chemical composition of the used cement, the calculated volume fractions of C-S-H, CH, and hydrated aluminates in cement gel are 66.41%, 18.59%, and 15.00%, respectively. The predicted initial volume fractions of hydrated aluminates (f_{AL}^0), CH (f_{CH}^0), conventional C-S-H (f_{CSH}^0), pozzolanic C-S-H (f_{pCSH}^0), unhydrated silica fume (f_{unhySF}), unhydrated cement (f_{unhyC}), and capillary pores (f_{cap}^0) in the matrix of HPC-110 and NSC-40 are shown in Table 8.2, together with the volume fraction of capillary pores at the stages of complete decomposition of hydrated aluminates (f_{cap}^{AL}), CH (f_{cap}^{CH}), and C-S-H (f_{cap}^{CSH}). The volume fractions of water released from the complete decomposition of hydrated aluminates (f_{AL}^w), CH (f_{CH}^w), and C-S-H (f_{CSH}^w) are also listed.

For the moisture transport analysis (Chapter 6), the critical pore diameter, d_c , of heated hardened cement paste at 20 °C and 600 °C is obtained from the MIP test results [Peng, 2000] and shown in Table 8.2. The decomposition degree, β , at 600 °C is also calculated according to the heating condition of the test (Chapter 4). For HPC-110, at the curing age of 28 days, the critical pore diameter has the same value as that of HPC-110 at 90-day curing age.

Table 8.2 Parameters of decomposition and moisture transport of hardened cement paste

| Volume fraction in matrix | HPC ₉₀₋₁₁₀ (at 90 days) w/b=0.26 | HPC ₂₈₋₁₁₀ (at 28 days) w/b=0.26 | NSC-40 (at 90 days) w/b=0.6 |
|---|---|---|-----------------------------------|
| f_{AL}^0 | 8.50% | 7.73% | 8.35% |
| f_{CH}^0 | 5.37% | 5.45% | 7.07% |
| f_{CSH}^0 | 37.66% | 34.24% | 37.01% |
| f_{pCSH}^0 | 14.43% | 11.55% | 9.18% |
| f_{unhySF} | 3.82% | 4.60% | 2.43% |
| f_{unhyC} | 21.83% | 24.26% | 4.62% |
| f_{cap}^0 | 8.34% | 12.16% | 31.32% |
| f_{cap}^{AL} | 12.74% | 16.16% | 35.63% |
| f_{cap}^{CH} | 15.67% | 19.13% | 39.48% |
| f_{cap}^{CSH} | 42.93% | 43.28% | 64.28% |
| f_{AL}^w | 4.39% | 3.99% | 4.32% |
| f_{CH}^w | 2.93% | 2.96% | 3.85% |
| f_{CSH}^w | 27.26% | 24.16% | 24.79% |
| $d_c_{20\text{ }^\circ\text{C}}$ (μm) | 0.04 | 0.04 | 0.22 |
| $d_c_{600\text{ }^\circ\text{C}}$ (μm) | 2.51 | 2.51 | 5.62 |
| $\beta_{600\text{ }^\circ\text{C}}$ | 45.37% | 46.20% | 47.88% |

8.3.3 Mechanical material properties

The meso-level mechanical material properties of concrete at room temperature are shown in Table 8.3 [Peng, 2000]. The elastic modulus of used aggregates (granite) is equal to 45 GPa [Neville, 1995]. The elastic modulus of the matrix is predicted by the two-phase composite sphere model presented in Chapter 7 (Eq. 7.34). In Fig. 8.6, the predicted values as a function of the water to-cement/binder-ratio are compared with the experimental data collected from the literature [Haecker et al., 2005; Helmuth and Turk, 1966; Zheng et al., 2010; Masse et al., 2002] (The curing age of hardened cement paste in the experiments was 56 days, 6 months, 28 days, and 28 days, respectively). It can be seen from Fig. 8.6 that the predicted value correlates well with the experimental results. Thus, the prediction is reasonable. According to the test results of the fracture energy, the strain softening parameter, μ (Chapter 7), is determined using the crack band model proposed by Bažant [1986]. The fracture energies of HPC-110 and NSC-40 are 165 N/m and 100 N/m, respectively [Peng, 2000; Rao and Prasad, 2002].

Table 8.3 Mechanical material properties at room temperature

| | Compressive strength f_c (MPa) | Tensile strength f_t (MPa) | Elastic modulus E (GPa) | Strain softening parameter μ |
|----------------|-------------------------------------|---------------------------------|----------------------------|--|
| HPC-110 | 115.0 | 7.2 | 42.0 | - |
| NSC-40 | 47.0 | 3.6 | 26.4 | - |
| Matrix_HPC-110 | 115.0 | 7.2 | 37.0 | 2686 |
| Matrix_NSC-40 | 47.0 | 3.6 | 12.0 | 1106 |
| Aggregate | 115.0 | 7.2 | 45.0 | 2686 |

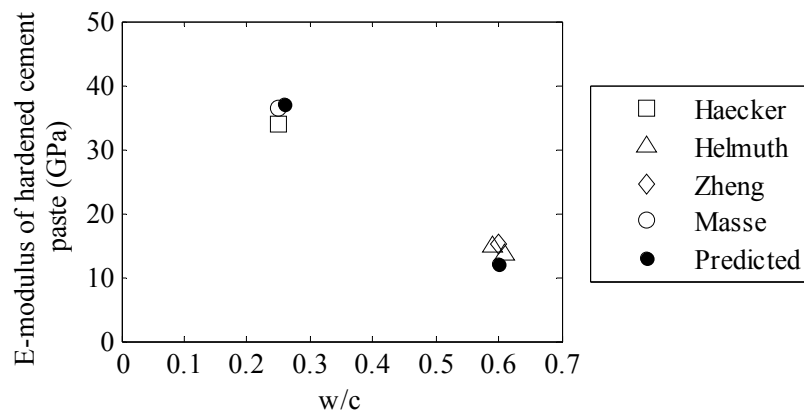


Fig. 8.6 Comparison of predicted initial elastic modulus of matrix of HPC-110 ($w/b=0.26$) and NSC-40 ($w/b=0.60$) with experimental data collected from literature (at room temperature).

Under high temperatures, based on the thermal decomposition analysis (Chapter 4), the elastic modulus of the matrix is predicted using the numerical method proposed in Chapter 7. The predicted values under different heating conditions, i.e., $5\text{ }^\circ\text{C}/\text{min}$ and ISO 834 fire (Fig. 8.2), are shown in Fig. 8.7 as an example. For the matrix in the concrete specimen, the elastic modulus will be predicted according to the corresponding heating history of each element. The elastic modulus of aggregate (granite) is taken as temperature dependent and also shown in Fig. 8.7 [Wan et al., 2008].

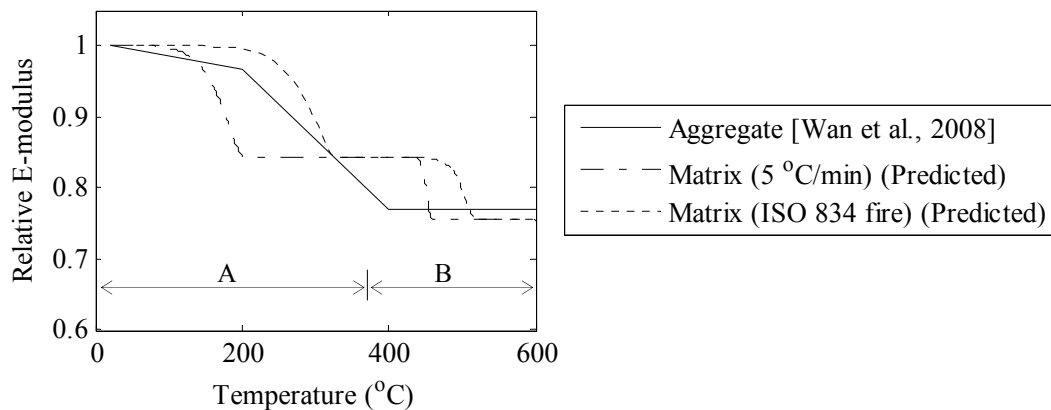


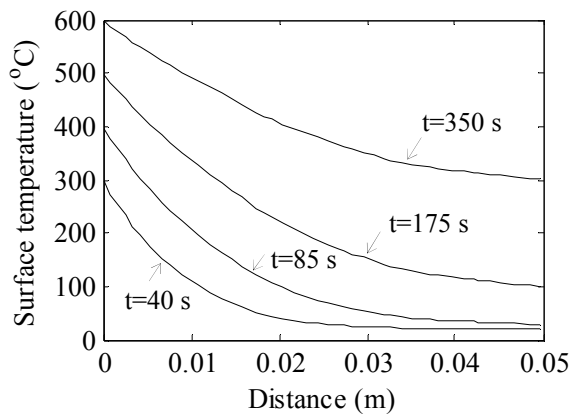
Fig. 8.7 Relative elastic modulus of aggregate and matrix of HPC₉₀₋₁₁₀ under high temperature conditions (A-effect of decomposition of hydrated aluminates on E-modulus of matrix; B-effect of decomposition of CH on E-modulus of matrix).

8.4 Temperature field analysis

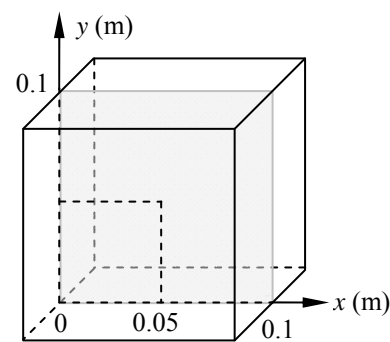
For the thermal damage analysis, both fast heating (ISO 834 fire) and slow heating at the heating rates of 0.5 °C/min and 5 °C/min are studied. The time interval for the transient temperature field analysis is listed in Table 8.4. The thermal material parameters in Table 8.1 are used. Using the model of temperature prediction in Chapter 3 (The boundary condition is of the first type). The temperature profile along the x or y-axis in the middle of the specimen is shown in Fig. 8.8. As can be seen from Fig. 8.8, the temperature gradient of slow heating is much lower than that of ISO 834 fire. The predicted temperature field at the surface temperature is around 300 °C and 400 °C under ISO 834 fire is shown in Fig. 8.9.

Table 8.4 Time interval for transient temperature field analysis

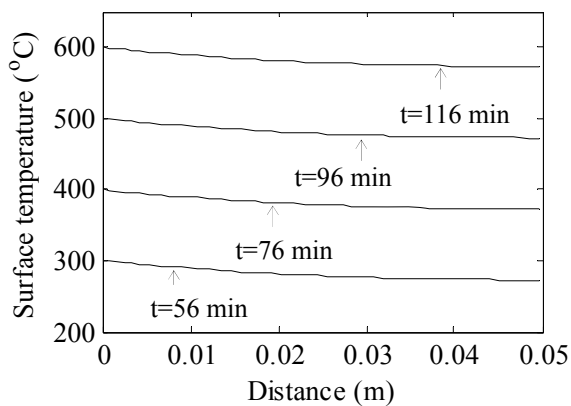
| | Time interval |
|--------------|---------------|
| ISO 834 fire | 5 seconds |
| 5 °C/min | 2 minutes |
| 0.5 °C/min | 10 minutes |



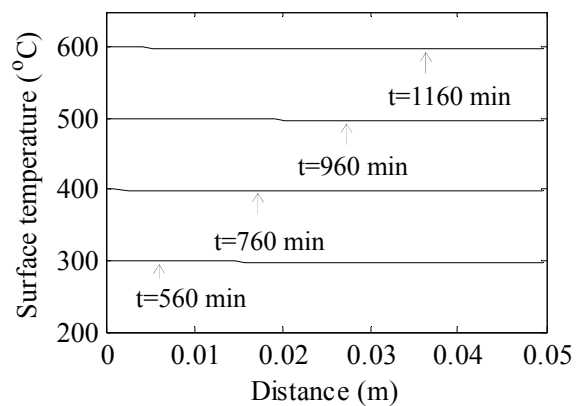
(a) ISO 834 fire (Fig. 8.2)



(b)



(c) 5 °C/min



(d) 0.5 °C/min

Fig. 8.8 Predicted temperature profile in middle of specimen (b) under different heating conditions: ISO 834 fire (a), 5 °C/min (c), and 0.5 °C/min (d).

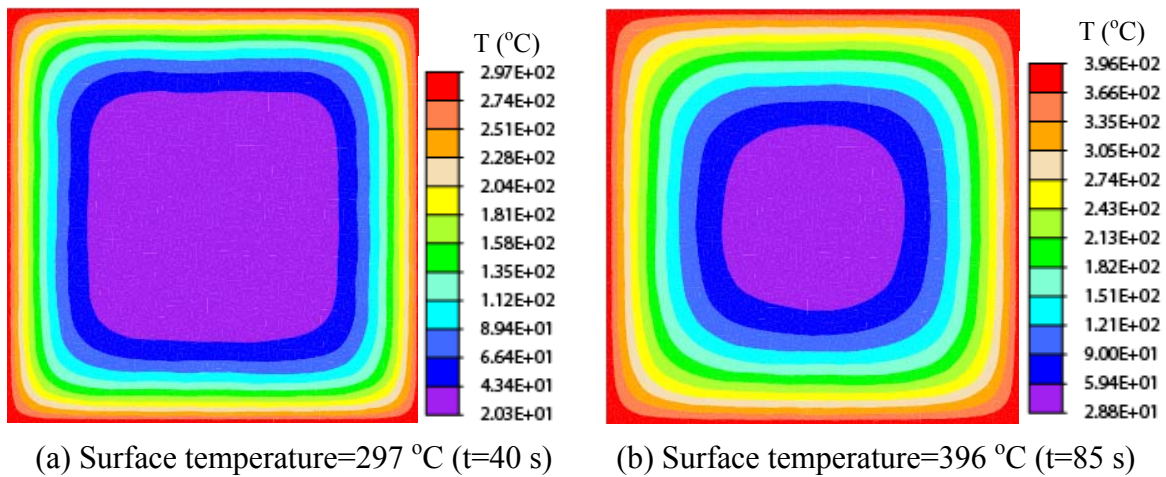


Fig. 8.9 Temperature field under ISO 834 fire.

8.5 Thermal decomposition analysis

By using the prediction method of thermal decomposition proposed in Chapter 4, the predicted profile of capillary porosity of the matrix of HPC₉₀₋₁₁₀ and NSC-40 at different surface temperatures under ISO 834 fire is shown in Fig. 8.10. The 2D contour of the decomposition degree, β (Eq. 4.30), of HPC₉₀₋₁₁₀ at the surface temperatures of 300 °C and 400 °C under ISO 834 fire are shown in Fig. 8.11. The values represented by different colors in the contour in Fig. 8.11 and hereafter are listed in Table 8.5, where 1.0 represents the maximum value and 0.0 represents the minimum value of the parameter investigated. It can be seen from Fig. 8.10 that a high gradient of decomposition exists. The upper horizontal portion of the curves in Fig. 8.10 indicates the effect of the complete decomposition of hydrated aluminates on the capillary porosity and the upper portion of the curve of 500 °C beyond this line indicates the effect of the decomposition of CH. It can be inferred from the numerical analysis that when the surface temperature reaches 500 °C under ISO 834 fire, only little CH decomposed and the depth of decomposition in concrete specimens is around 3 mm.

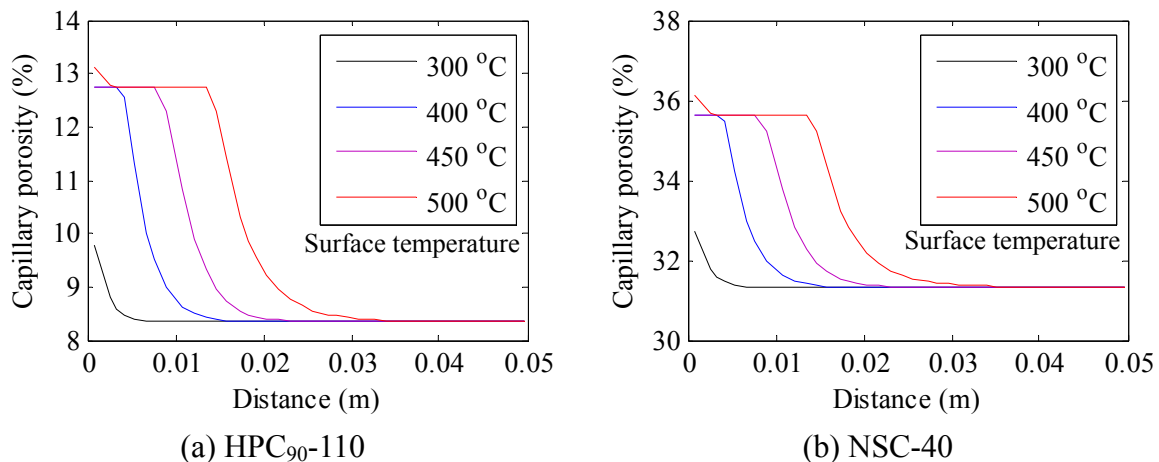


Fig. 8.10 Profile of predicted capillary porosity of matrix under ISO 834 fire when surface temperature reaches different values.

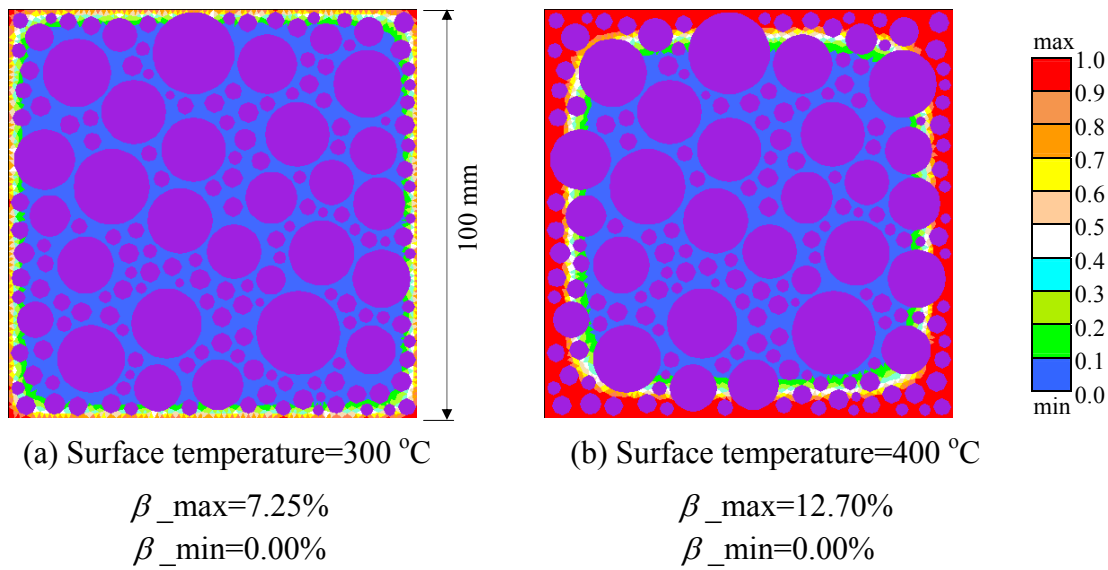


Fig. 8.11 Example of predicted decomposition degree β of matrix of HPC₉₀₋₁₁₀ under ISO 834 fire.

Table 8.5 Values represented by different colors

| Color | Value range | Color | Value range |
|-------|-------------|-------|-------------|
| | 0.9-1.0 | | 0.4-0.5 |
| | 0.8-0.9 | | 0.3-0.4 |
| | 0.7-0.8 | | 0.2-0.3 |
| | 0.6-0.7 | | 0.1-0.2 |
| | 0.5-0.6 | | 0.0-0.1 |
| | zero | | aggregate |

As the temperature gradients are low under slow heating conditions (Fig. 8.8c and d), the evolution of capillary porosity is almost uniform in the specimen at any surface temperature. The evolution of the porosity as a function of surface temperature is shown in Fig. 8.12, where the lower horizontal line of each curve represents the capillary porosity at room temperature, the middle horizontal line indicates the effect of complete decomposition of hydrated aluminates on the porosity, and the upper horizontal line indicates the effect of complete decomposition of CH on the porosity.

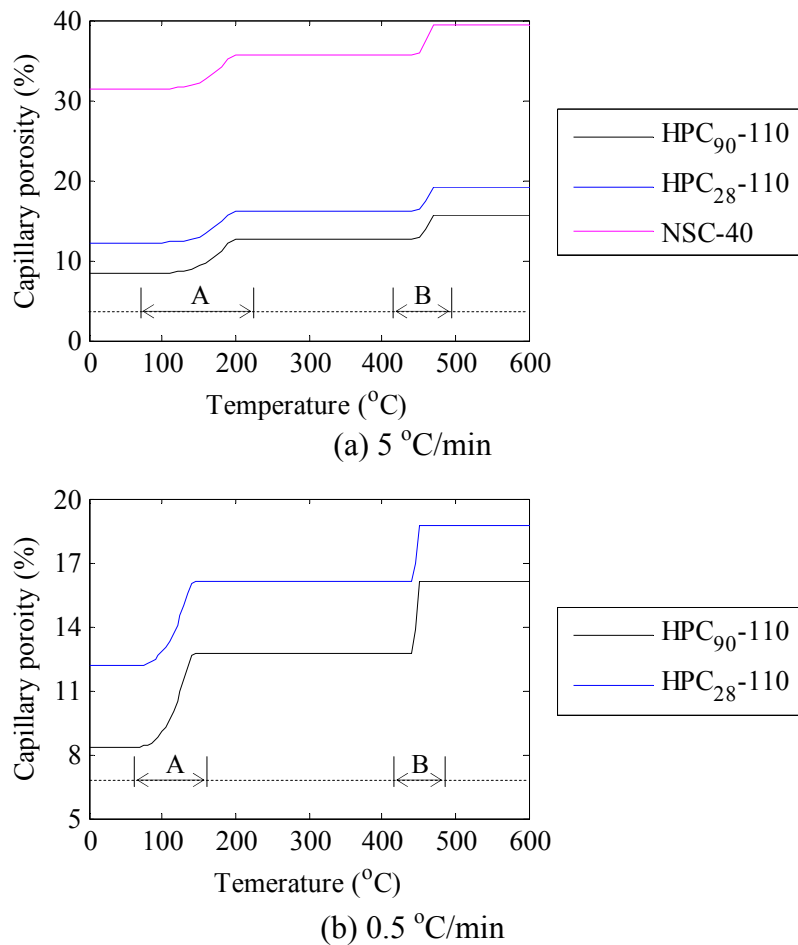


Fig. 8.12 Evolution of capillary porosity of matrix versus surface temperature under slow heating (A-effect of decomposition of hydrated aluminates on porosity; B-effect of decomposition of CH on porosity).

8.6 Moisture transport and vapor pressure analysis

As the moisture transport and the vapor pressure are coupled with each other, that is, the moisture transport is driven by the vapor pressure gradient and, in return, the magnitude of vapor pressure is influenced by the amount of moisture transported, a “staggered way” of calculation [Zienkiewicz and Taylor, 2000] is applied for the moisture transport and the vapor pressure analyses. In each time interval, as the temperature increases gradually from the value of last time step to the value of this time step, the moisture transport analysis is conducted based on the mean temperature of the two adjacent time steps. After the moisture is transported, the vapor pressure is recalculated for the mechanical analysis under the temperature of current time step.

In this section, the modeling parts in Chapters 5 and 6 are used for the moisture transport and vapor pressure analyses. The boundary condition of the moisture transport driven by the vapor pressure gradient is atmospheric pressure. Based on the decomposition analysis, the intrinsic permeability of heated matrix is predicted. After the water saturation degree is determined, the effective permeability is calculated. The predicted variation of the local concentration of moisture is then presented. The vapor pressure for both moisture transport and the mechanical analysis is predicted using the method proposed in Chapter 5.

8.6.1 Prediction of intrinsic permeability

The intrinsic permeability of heated matrix is predicted using the method proposed in Chapter 6. First, the evolution pattern of the critical pore diameter as a function of decomposition degree (Eq. 4.30) is determined by sensitivity analysis. Then, the predicted intrinsic permeability is verified by comparison with the experimental data collected from the literature. Finally, the evolution of the intrinsic permeability of the heated matrix in concrete specimens as a result of the heating and decomposition process is predicted.

8.6.1.1 Sensitivity of intrinsic permeability to evolution of critical pore diameter

In the three-step intrinsic permeability prediction method proposed in Chapter 6, the critical capillary pore diameter, which is coarsened by decomposition, needs to be determined. The coarsening evolution of the critical pore diameter as a function of the decomposition degree, β (Eq. 4.30), is determined based on the sensitivity analysis of the intrinsic permeability to the evolution patterns as shown in Fig. 8.13.

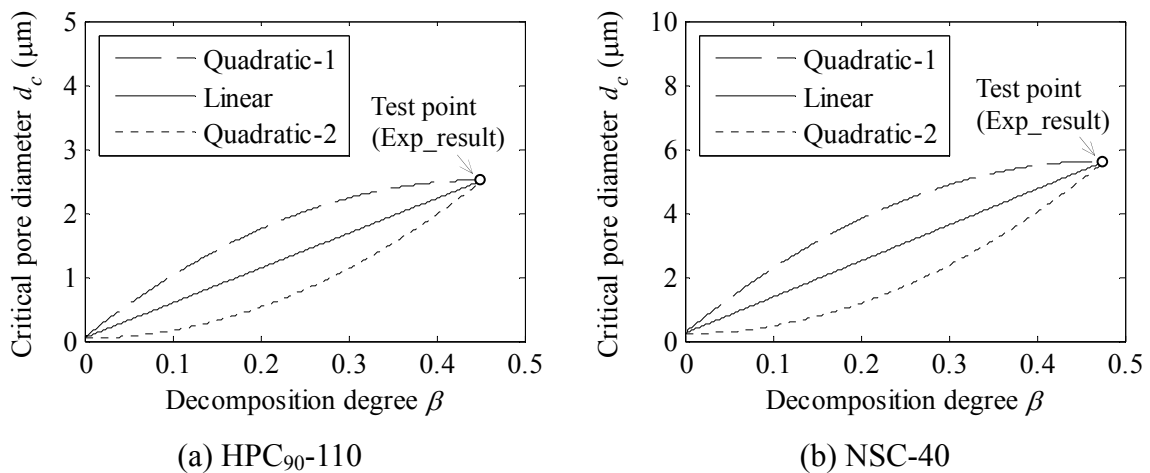


Fig. 8.13 Evolution pattern of critical pore diameter d_c versus decomposition degree β .

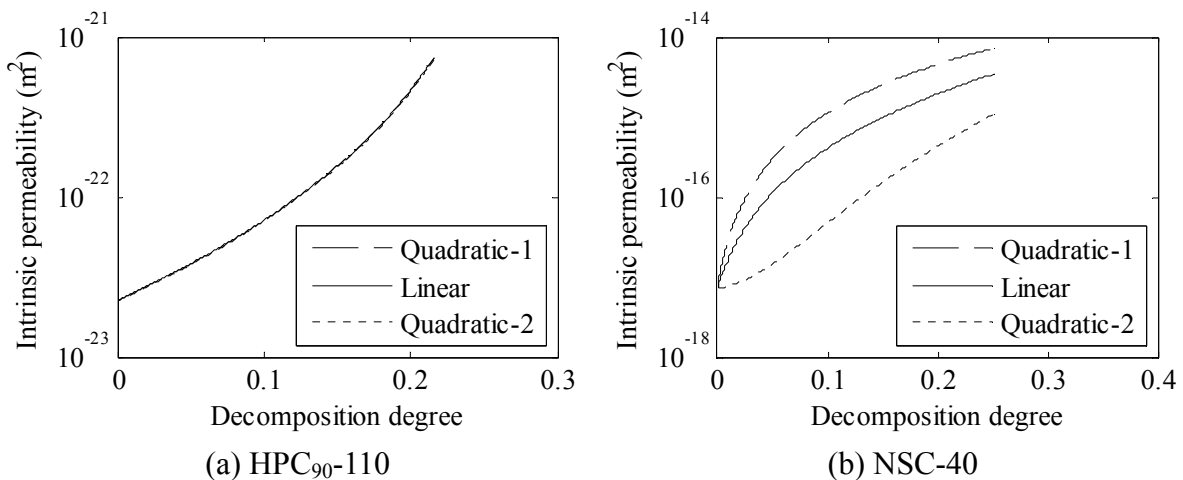


Fig. 8.14 Predicted intrinsic permeability of different evolution patterns of critical pore diameter.

For HPC₉₀₋₁₁₀ and NSC-40, between the initial point at 20 °C and the test point at 600 °C (Table 8.2), three evolution patterns are investigated, i.e., linear, quadratic-1, and quadratic-2. The predicted intrinsic permeability corresponding to the evolution patterns until the heating temperature reaches 600 °C are shown in Fig. 8.14. It can be seen that for HPC₉₀₋₁₁₀, the evolution pattern has no effect on the predicted results, i.e., the intrinsic permeability is not sensitive at all to the evolution pattern (Fig. 8.14 (a)), while for NSC-40, the evolution pattern exerts some effect on the predicted value (Fig. 8.14 (b)). The reason for this is that, for HPC₉₀₋₁₁₀, when the temperature reaches 600 °C, the capillary porosity (Table 8.2) is still less than the percolation value of 18% [Bentz and Garboczi, 1991] (Chapter 6). Thus, the permeability is not controlled by the capillary pores. However, for NSC-40, since the initial capillary porosity before heating already exceeds the percolation value, the permeability is mainly controlled by the capillary pores and the critical pore diameter influences the permeability a lot. The linear evolution pattern is applied for the intrinsic permeability prediction and the results are verified in the following section.

8.6.1.2 Verification of the prediction

The values of the predicted intrinsic permeability at different decomposition stages are listed in Table 8.6. To verify the predicted intrinsic permeability, in view of the lack of the experimental data of heated hardened cement paste, in Fig. 8.15, the predicted results as a function of porosity are compared with the experimental data of unheated hardened cement paste of Powers et al. [1955] (Young [1988]), Cui and Cahyadi [2001], and Nyame and Illston [1981] (Zheng and Zhou [2008]) (The experimental data are digested in the reference in the brackets). From the comparison, it can be seen that the predicted results of the heated matrix correlate well with the test results. Thus, the prediction is reasonable.

Table 8.6 Predicted intrinsic permeability (m^2) of the matrix at different decomposition stages

| | at 20 °C | at AFt fully decomposed | at CH fully decomposed |
|-----------------------|------------------------|-------------------------|------------------------|
| HPC ₉₀₋₁₁₀ | 2.22×10^{-23} | 1.05×10^{-22} | 6.54×10^{-22} |
| HPC ₂₈₋₁₁₀ | 4.70×10^{-23} | 6.62×10^{-22} | 1.67×10^{-18} |
| NSC-40 | 7.12×10^{-18} | 7.16×10^{-16} | 3.35×10^{-15} |

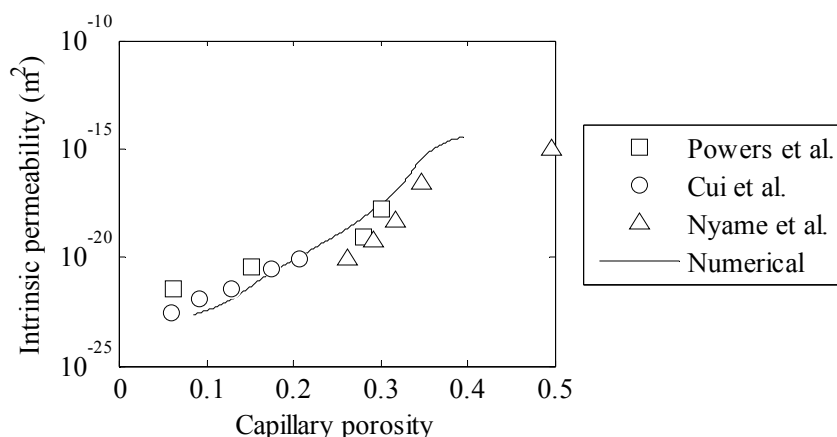


Fig. 8.15 Comparison between predicted intrinsic permeability of heated matrix of HPC₉₀₋₁₁₀ and NSC-40 as a function of capillary porosity with experimental data of unheated hardened cement paste collected from literature.

8.6.1.3 Evolution of intrinsic permeability

Under the ISO 834 fire condition, the profile of the predicted intrinsic permeability of the matrix of HPC₉₀₋₁₁₀ and NSC-40 is shown in Fig. 8.16. Under slow heating, the predicted intrinsic permeability is almost uniform in the specimen due to the low temperature gradient. The predicted value at different decomposition stages has been shown in Table 8.6.

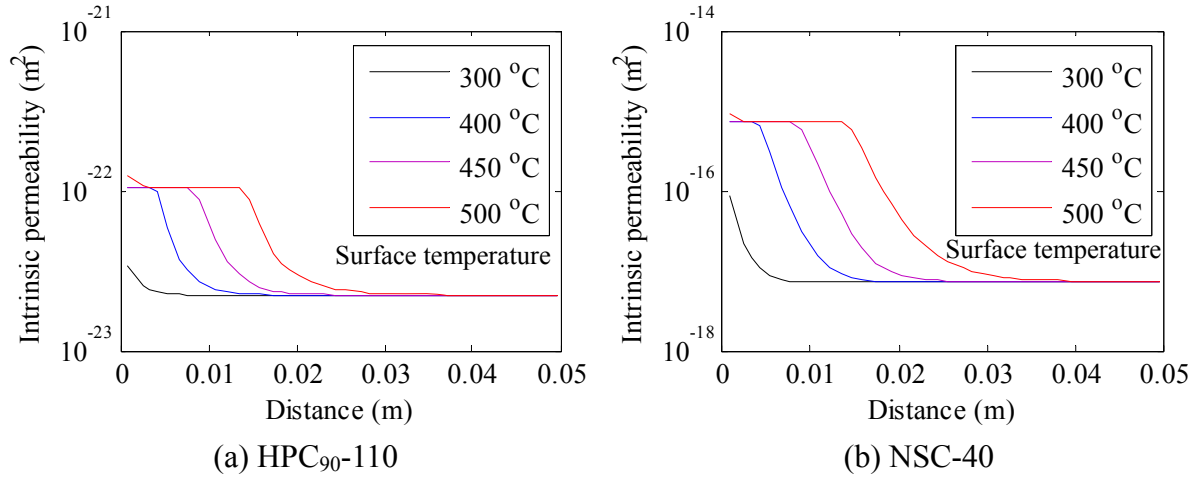


Fig. 8.16 Profile of predicted intrinsic permeability of matrix of concretes when surface temperature reaches different values under ISO 834 fire (The temperature profile is shown in Fig. 8.8 (a)).

8.6.2 Prediction of water saturation degree

The degree of water saturation significantly affects the effective permeability to gas (Fig. 6.9). In Chapter 6, an effective coefficient as a function of water saturation degree is introduced to the intrinsic permeability to obtain the effective permeability (Eq. 6.13). Thus, the evolution of the water saturation degree needs to be predicted (Chapter 5). Under the ISO 834 fire condition, the profile of the predicted saturation degree of HPC₉₀₋₁₁₀ and NSC-40 with 90% and 0% initial moisture content is shown in Fig. 8.17. The field of the saturation degree of HPC₉₀₋₁₁₀ with 90% initial moisture content when the surface temperature of the specimen reaches 300 °C, 400 °C, and 500 °C is shown in Fig. 8.18. Under the slow heating condition (5 °C/min), the profile is plotted in Fig. 8.19. When the temperature reaches the critical point (374.15 °C), no liquid water exists any more. Thus, the saturation degree is zero as can be seen in Fig. 8.17 and Fig. 8.19 (The vertical portion of the curves of the surface temperature of 450 °C and 500 °C goes to zero in Fig. 8.17 (a) and (b)).

It can be seen from Fig. 8.17 that, although with the same initial moisture content, the water saturation degree of HPC₉₀₋₁₁₀ is higher than that of NSC-40. It can be explained as follows: First, from the moisture content perspective, as the moisture content (or the moisture saturation degree) is defined as the volume fraction in the capillary pores occupied by the equivalent water of the moisture (the vapor phase is also converted into liquid water) (Chapter 5), the moisture content, S_d , at the stage of the thermal decomposition of hardened cement paste is equal to

$$S_d = (S_d^0 \times f_{cap}^0 + f_{dehy}^w) / f_{cap} \quad (8.1)$$

where S_d^0 is the initial moisture content, f_{cap}^0 is the initial capillary porosity, f_{dehy}^w is the volume fraction in matrix occupied by water released from decomposition, and f_{cap} is the capillary porosity at the stage of decomposition (Chapter 4). Since the decomposition degree is mainly attributed to the decomposition of hydrated aluminates when the surface temperature of the specimen reaches 500 °C (Fig. 8.10), by substituting the parameters in Table 8.2 into Eq. 8.1, the moisture content at the stage of complete decomposition of hydrated aluminates is calculated and listed in Table 8.7. The calculated results show that the saturation degree correlates with the corresponding calculated moisture content. Second, as NSC-40 is much more permeable than HPC-110, water vapor can be transported relatively easily, resulting in the decrease of the moisture content and thus the saturation degree. It can be clearly seen in Fig. 8.17(d) that the effect of moisture transport also makes the saturation peak move slightly inwardly compared with the decomposition profile shown in Fig. 8.10. After the water saturation degree is predicted, by taking the slip-flow effect of gas into account (Chapter 6), the effective permeability can be calculated.

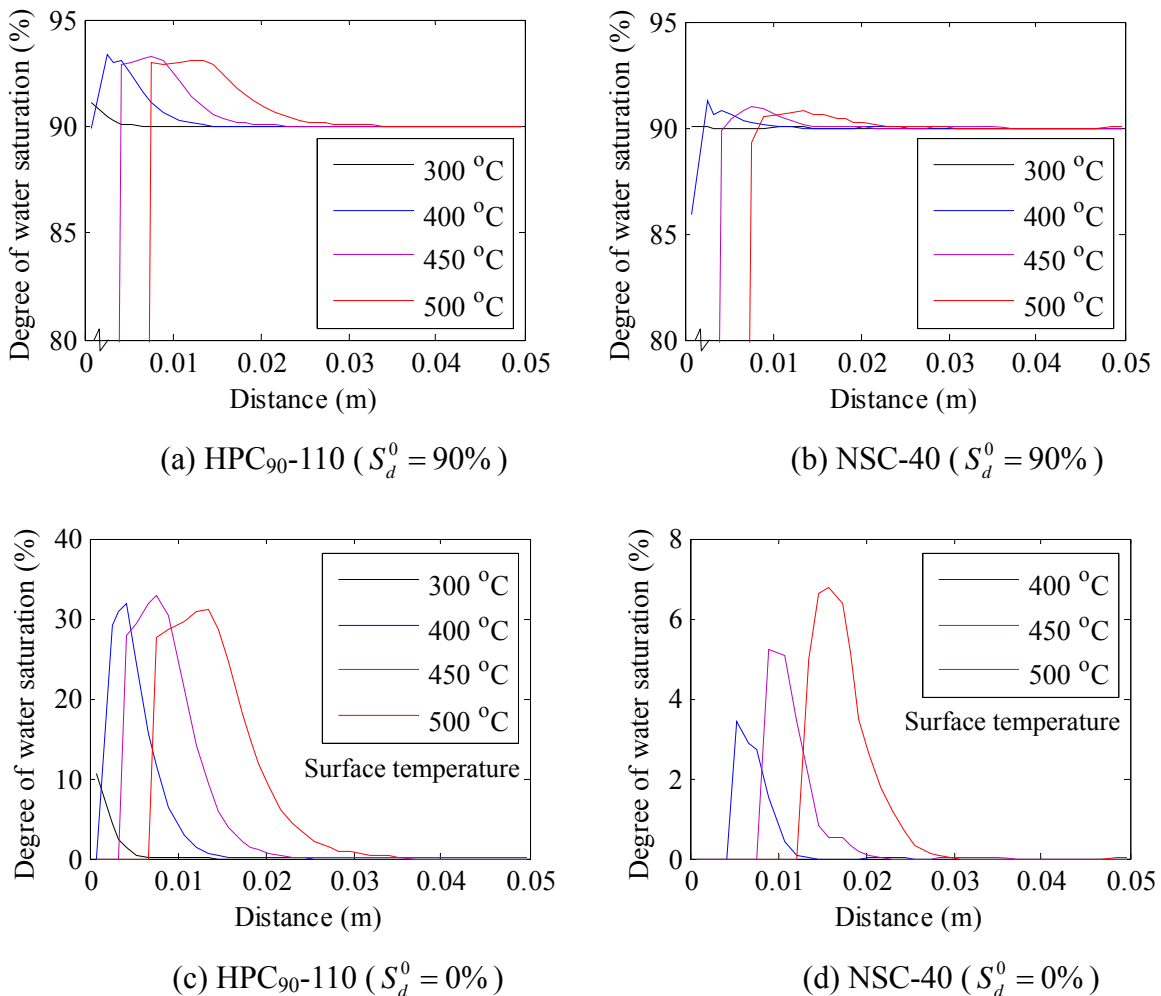


Fig. 8.17 Profile of predicted water saturation degree of matrix of concretes with 90% (a) (b) and 0% (c) (d) initial moisture content when surface temperature reaches different values under ISO 834 fire (The temperature profile is shown in Fig. 8.8 (a)).

Table 8.7 Moisture content at stage of complete decomposition of hydrated aluminates

| | Initial capillary porosity | Volume fraction of water released from decomposition | Capillary porosity after complete decomposition | Moisture content at complete decomposition | |
|-----------------------|----------------------------|--|---|--|----------------|
| | | | | $S_d^0 = 0\%$ | $S_d^0 = 90\%$ |
| | f_{cap}^0 | f_{AL}^w | f_{cap}^{AL} | S_d | S_d |
| HPC ₉₀₋₁₁₀ | 8.34% | 4.39% | 12.74% | 34.65% | 93.37% |
| NSC-40 | 31.32% | 4.32% | 35.63% | 12.08% | 91.24% |

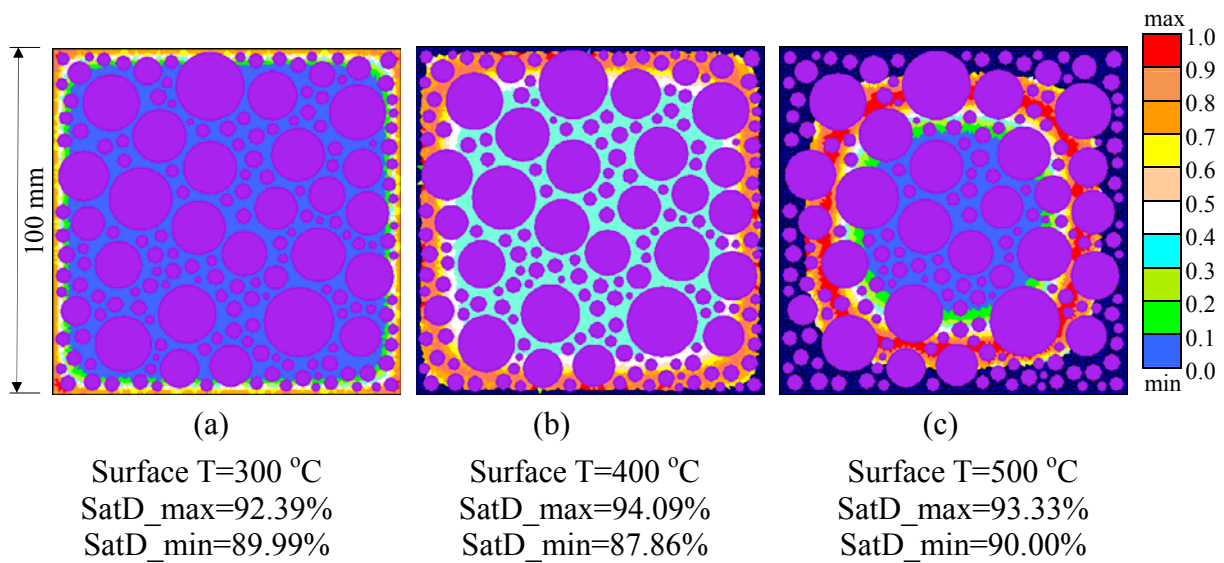


Fig. 8.18 Example of predicted water saturation degree in specimen of HPC₉₀₋₁₁₀ with 90% initial moisture content under ISO 834 fire (The temperature profile is shown in Fig. 8.8a and the corresponding saturation profile is shown in Fig. 8.17(a)).

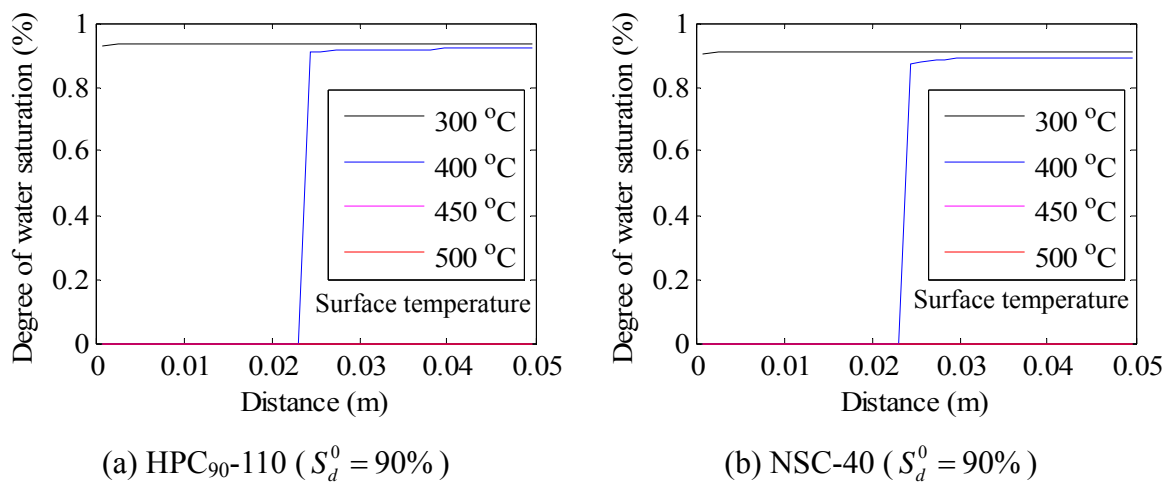


Fig. 8.19 Profile of predicted water saturation degree of matrix of concretes with 90 % initial moisture content when surface temperature reaches different values under slow heating (5 °C/min) (The temperature profile is shown in Fig. 8.8 (c)).

8.6.3 Prediction of effective permeability to gas

Under ISO 834 fire, the predicted effective permeability to gas of the matrix of HPC₉₀₋₁₁₀ and NSC-40 with 90% initial moisture content is shown in Fig. 8.20 and Fig. 8.21, respectively. Since the permeability to gas is influenced by the water saturation degree and the slip-flow of gas (Chapter 6), it can be seen from these figures that the effective permeability varies with the distance from the surface of the specimens. For slow heating, the effective permeability to gas is shown in Fig. 8.22.

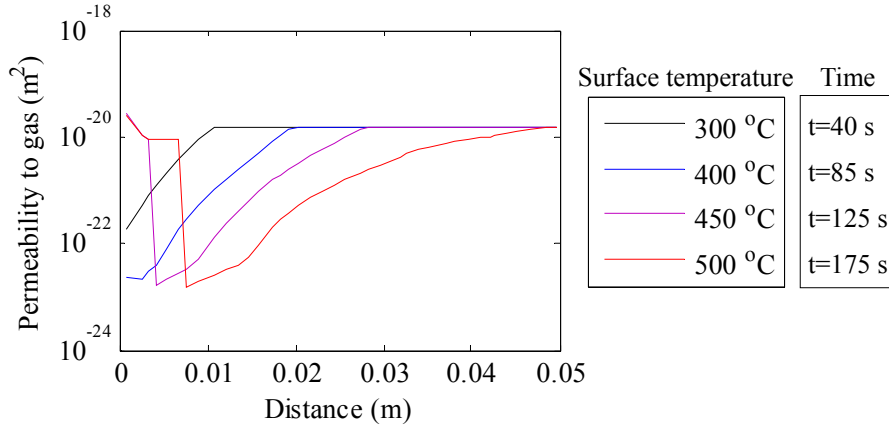


Fig. 8.20 Profile of predicted effective permeability to gas of matrix of HPC₉₀₋₁₁₀ with 90% initial moisture content when surface temperature reaches different values under ISO 834 fire (The temperature profile is shown in Fig. 8.8 (a)).

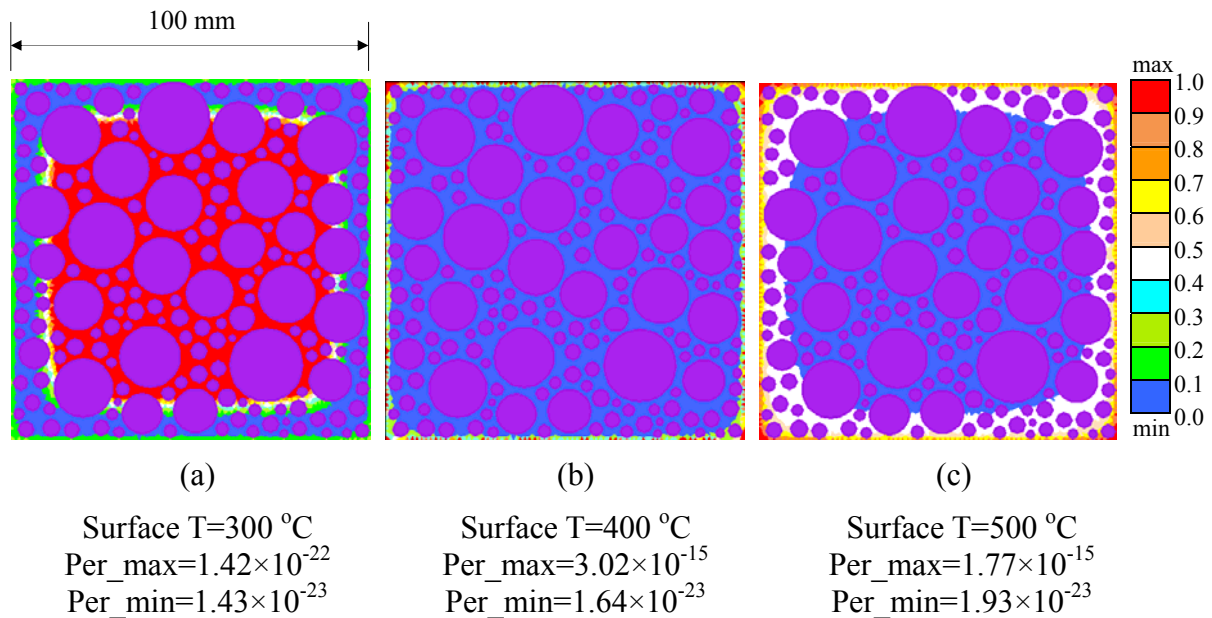


Fig. 8.21 Example of predicted effective permeability to gas of matrix of NSC-40 with 90% initial moisture content under ISO 834 fire (The temperature profile is shown in Fig. 8.8(a)).

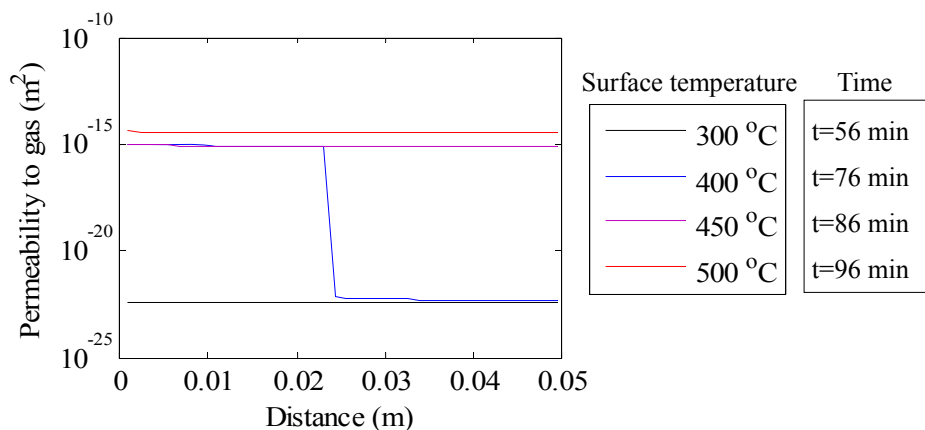


Fig. 8.22 Profile of predicted effective permeability to gas of matrix of NSC-40 with 90% initial moisture content under slow heating (5 °C/min) (The temperature profile is shown in Fig. 8.8 (c)).

8.6.4 Moisture content

Under ISO 834 fire, the predicted moisture content profile of HPC₉₀₋₁₁₀ and NSC-40 with 90% and 0% initial moisture content is shown in Fig. 8.23. The fields of the predicted moisture content at the surface temperatures of 400 °C and 500 °C are shown in Fig. 8.25. The enlarged peak portions of the curves of the profile of the surface temperature of 400 °C and 500 °C in Fig. 8.23 (a) and (b) are shown in Fig. 8.24. It can be seen from Fig. 8.24 that, in accordance with the decomposition profile (Fig. 8.10), the moisture contents are correspondingly increased due to the water released from the decomposition. To identify the amount of moisture accumulated due to the moisture transport, the calculated moisture contents at the stage of complete decomposition of hydrated aluminates are also plotted in Fig. 8.24 (the green line) for comparison. As can be seen, compared with the amount of moisture released from decomposition, the accumulated amount of moisture due to moisture transport is relatively low for both HPC₉₀₋₁₁₀ and NSC-40 with 90% initial moisture content. The reason for this is that, when a water phase is present, the effective permeability of the matrix decreases, resulting in little amount of moisture transported both inwardly and outwardly. However, after the water turns into vapor, the gas phase escapes outwardly more easily (Fig. 8.20 and Fig. 8.21), resulting in the decrease of moisture content in that zone as shown in Fig. 8.23 (a) and (b). The similar trend of the moisture distribution evolution in heated concrete was observed experimentally by nuclear magnetic resonance (NMR) measurements [van der Heijden et al., 2011].

For concretes with zero initial moisture content, Fig. 8.23 shows that, for HPC₉₀₋₁₁₀, the moisture transport doesn't affect too much the moisture content compared with the moisture released from the decomposition. This can be explained by the low permeability of the matrix of HPC₉₀₋₁₁₀. For NSC-40 (Fig. 8.23(b)), the moisture content at any heating stage is lower than the calculated value at the stage of complete decomposition of hydrated aluminates, i.e., 12.8%. This is due to the fact that the permeability of the matrix of NSC-40 is high and the moisture can move relatively easily both inwardly and outwardly compared with HPC-110. This also results in the peak of the moisture content shifting inwardly.

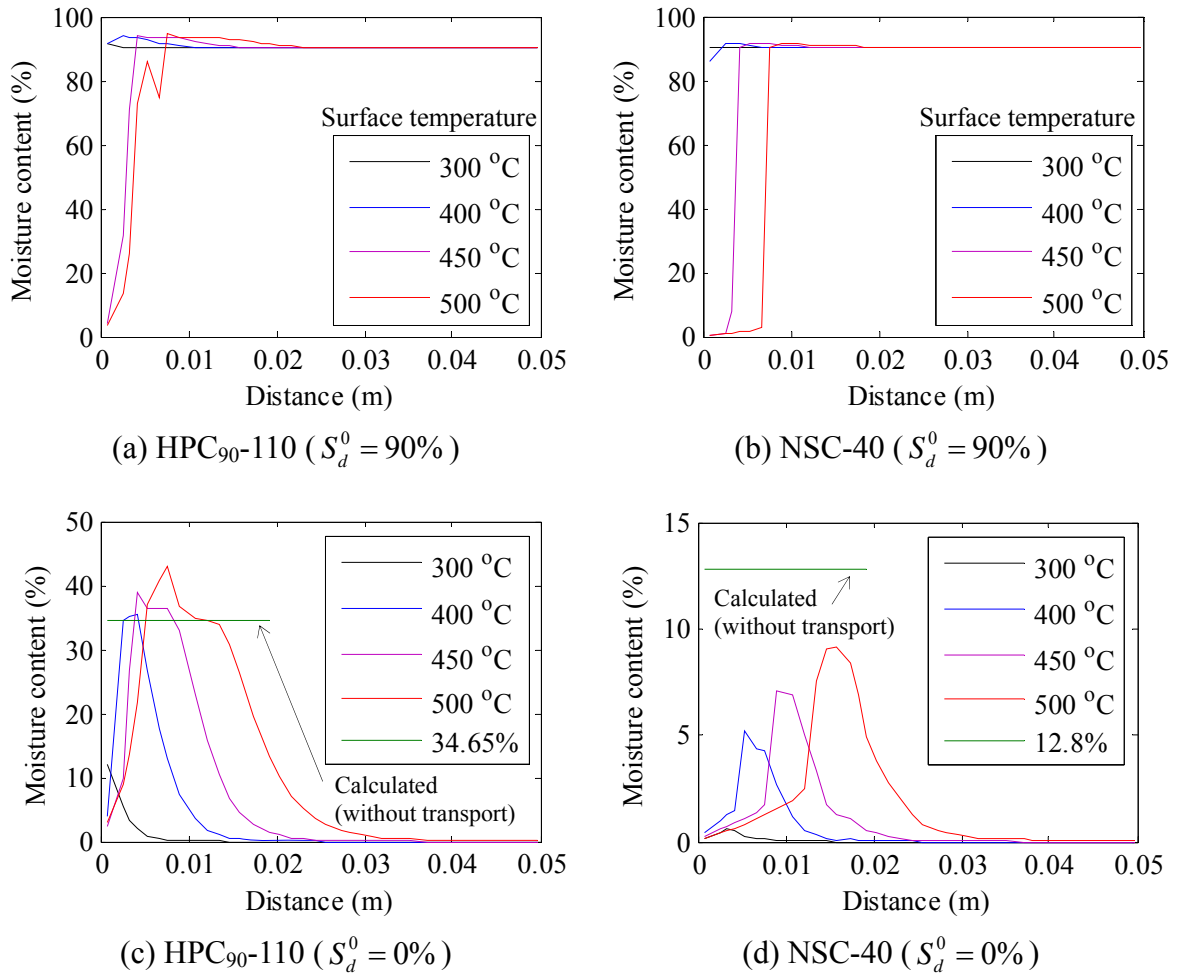


Fig. 8.23 Profile of predicted moisture content of concretes with 90% (a) (b) and 0% (c) (d) initial moisture content when surface temperature reaches different values under ISO 834 fire (The temperature profile is shown in Fig. 8.8(a)).

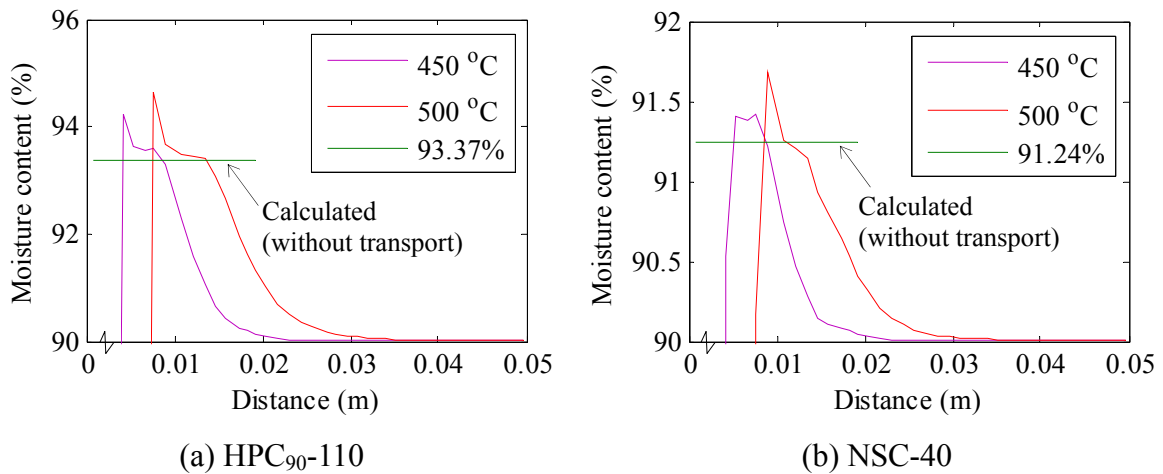


Fig. 8.24 Comparison between predicted moisture content and calculated moisture content without moisture transport of matrix of concretes with 90% initial moisture content when surface temperature reaches 450 °C and 500 °C under ISO 834 fire.

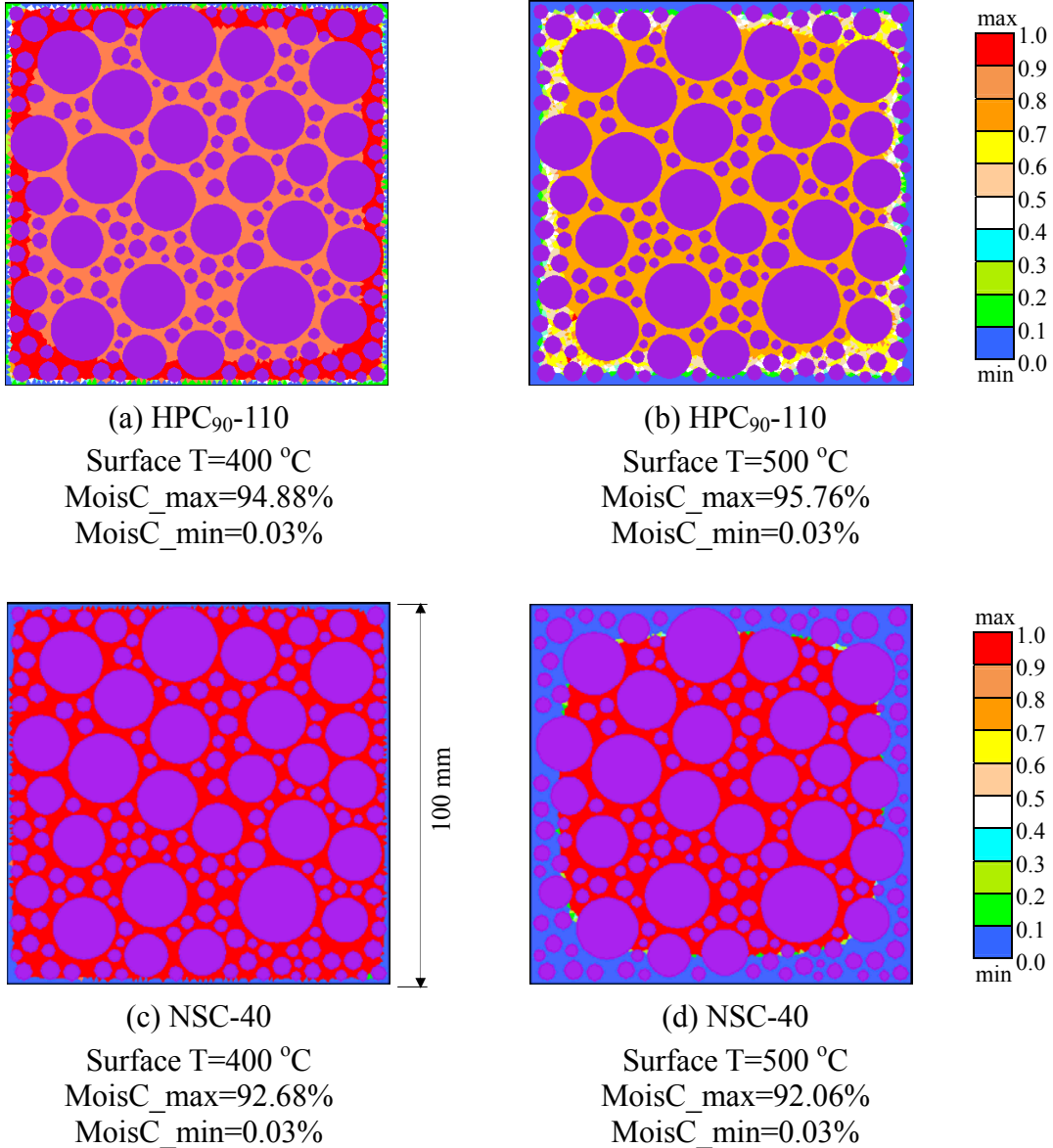


Fig. 8.25 Predicted moisture content distribution in concretes with 90% initial moisture content under ISO 834 fire (The temperature profile is shown in Fig. 8.8 (a)).

Under slow heating conditions, the profiles of the moisture content of concretes with 90% initial moisture content are shown in Fig. 8.26 and Fig. 8.27. It can be seen that, under the heating rates of 5 °C/min and 0.5 °C/min, the profiles of moisture content of HPC₉₀₋₁₁₀ are similar. It implies that the heating rate doesn't affect the moisture transport of HPC₉₀₋₁₁₀ very much. Similar profiles can also be found under ISO 834 fire condition when the surface temperature reaches 450 °C and 500 °C in Fig. 8.23 (a). The reason for this is that the permeability of the matrix of HPC₉₀₋₁₁₀ is low and doesn't change much at any decomposition stage at temperatures below 600 °C (Table 8.6). For HPC₂₈₋₁₁₀, it can be seen that the moisture content decreases markedly when the surface temperature reaches 500 °C at the heating rate of 5 °C/min, and 450 °C and 500 °C at the heating rate of 0.5 °C/min. This is due to the orders of magnitude increase in the permeability of the matrix of HPC₂₈₋₁₁₀ after the decomposition of CH (Table 8.6). For comparison, the 2D images of the fields of the

moisture content of HPC₉₀₋₁₁₀ and HPC₂₈₋₁₁₀ at 500 °C under slow heating are shown in Fig. 8.28.

For NSC-40, it can be seen from Fig. 8.26 (c) that the moisture escapes very fast after the temperature reaches the critical point (374.15 °C). When the surface temperature reaches 450 °C and 500 °C, the values are almost zero. This can be explained by the high permeability of NSC-40 (Table 8.6).

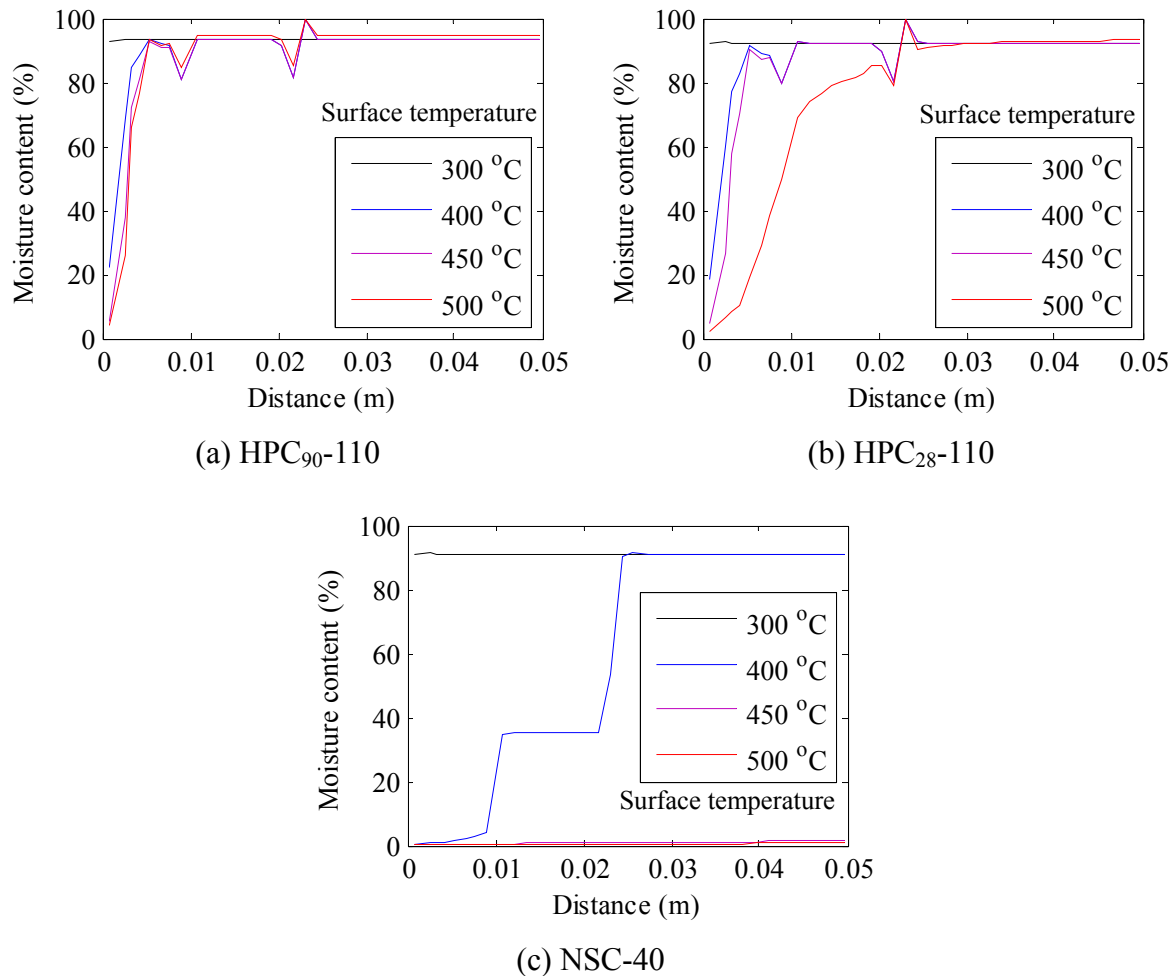
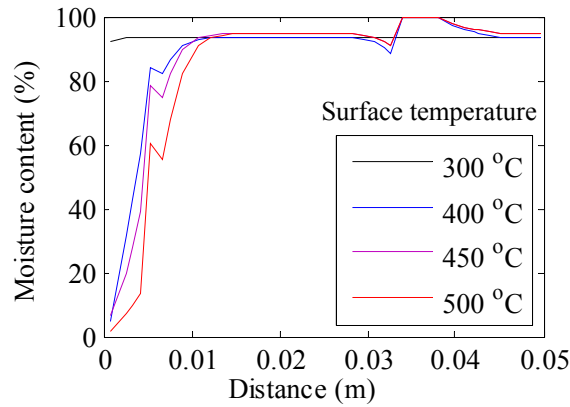
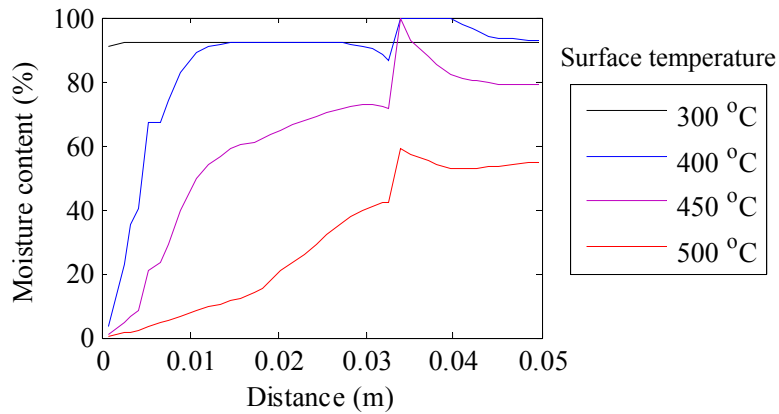


Fig. 8.26 Profile of predicted moisture content of concretes with 90% initial moisture content when surface temperature reaches different values under slow heating (5 °C/min) (The temperature profile is shown in Fig. 8.8 (c)).



(a) HPC₉₀₋₁₁₀



(b) HPC₂₈₋₁₁₀

Fig. 8.27 Profile of predicted moisture content of concretes with 90% initial moisture content when surface temperature reaches different values under slow heating (0.5 °C/min) (The temperature profile is shown in Fig. 8.8 (d)).

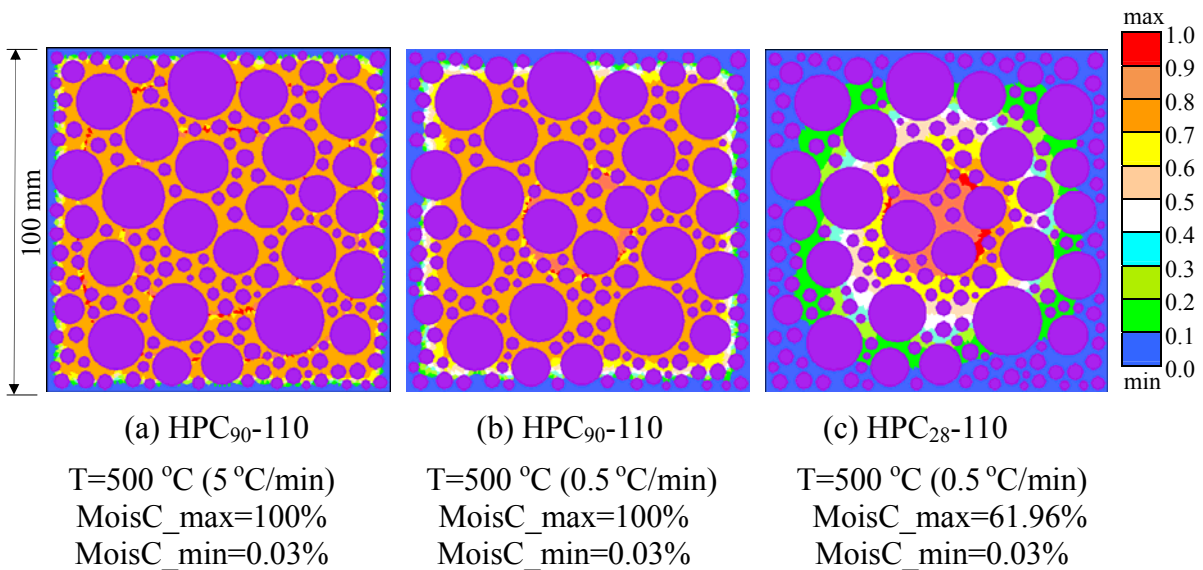


Fig. 8.28 Distribution of moisture content of concretes with 90% initial moisture content when surface temperature reaches 500 °C under slow heating.

It can be noted that for HPC-110 specimens, in Fig. 8.26 and Fig. 8.27, the moisture content profiles for surface temperatures of 400 °C, 450 °C, and 500 °C are not smooth, i.e., valleys and peaks are present. This is due to the fact that, with the temperature development, vapor pressure develops from the outer layer to the inner region of the specimen. When the temperature is around or beyond the critical point (374.15 °C), the magnitude of vapor pressure is very sensitive to the temperature. A small difference in temperature will lead to a big difference in vapor pressure [Meyer et al., 1967]. Although the temperature gradient is very low under slow heating (Fig. 8.8 (c and d)), the big difference of vapor pressure between adjacent elements can still occur as shown in Fig. 8.30, the sudden drop in vapor pressure in the curve for the surface temperature of 400 °C. On the other hand, due to the assumption that the highest value the vapor pressure can reach is 35 MPa (Chapter 5), pressure plateaus are present in the pressure profiles in Fig. 8.30 (In the figure, the vapor pressure is converted into the effective vapor pressure by multiplying the capillary porosity (Eq. 5.10a)). Due to the sudden drop of vapor pressure and together with the pressure plateau, the moisture in the fringe of the plateau moves to the low pressure region and accumulates there forming a moisture peak and the fringe region of the plateau forms the valley of moisture content. The same phenomenon is also present in Fig. 8.23 (a). In the NMR test of van der Heijden et al. [2011], the fluctuation of the moisture content in heated concrete was also observed, although it is not clear that whether it is due to the error of measurement or the mechanism stated here. The horizontal line in the middle of the curve of 400 °C in Fig. 8.26 (c) is also caused by the pressure plateau as shown in Fig. 8.30 (c).

8.6.5 Prediction of effective vapor pressure

Under the assumption that the highest value that the vapor pressure in heated concrete can reach is 35 MPa, the predicted profiles of effective vapor pressure in concrete specimens with 90% moisture content under different heating conditions are shown in Fig. 8.29 through Fig. 8.31 (Chapter 5). It can be seen from these figures that, under the ISO 834 fire condition, the vapor pressure resides only in the outer layer of the concrete specimens and the peak moves inwardly with the evolution of the temperature. The 2D image of the effective vapor pressure for the surface temperature of 500 °C under the fire condition is shown in Fig. 8.32.

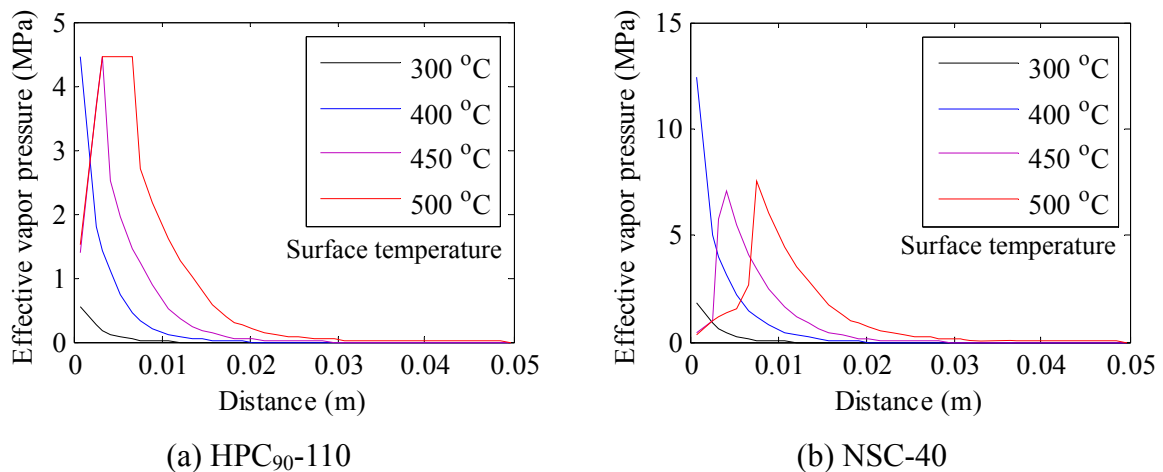
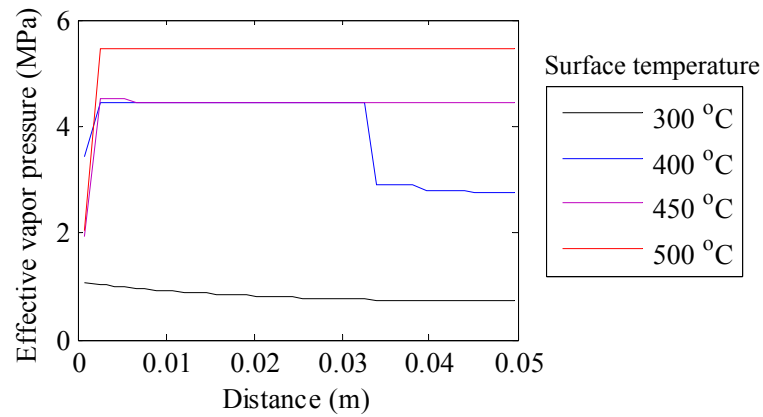
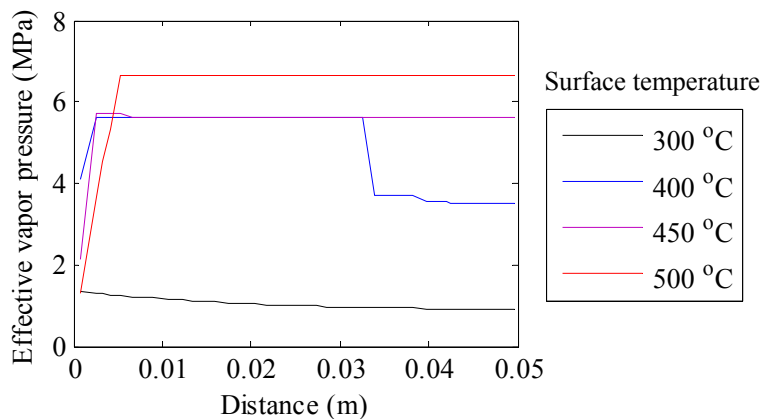


Fig. 8.29 Profile of predicted effective vapor pressure in concretes with 90% initial moisture content for different surface temperatures under ISO 834 fire (The temperature profile is shown in Fig. 8.8 (a)).

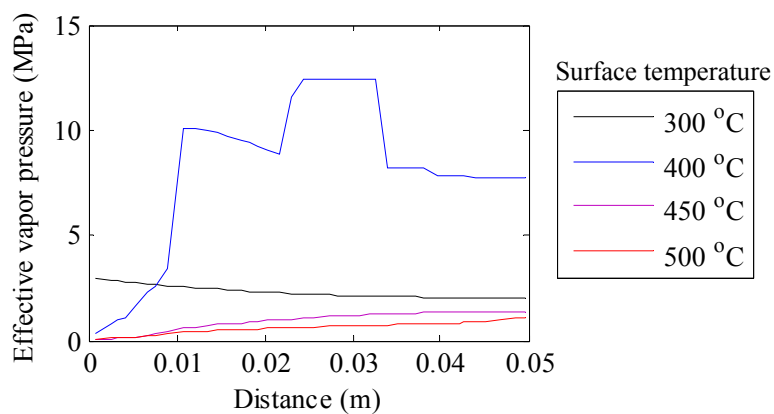
Under slow heating conditions, owing to the low temperature gradient (Fig. 8.8 (c) and (d)) and the high moisture content in the central region of the specimen (Fig. 8.26 and Fig. 8.27), high vapor pressure resides in the central region (The effective vapor pressure shown in these figures is calculated after the moisture transport at the time step corresponding to the surface temperatures shown in the figures).



(a) HPC₉₀₋₁₁₀

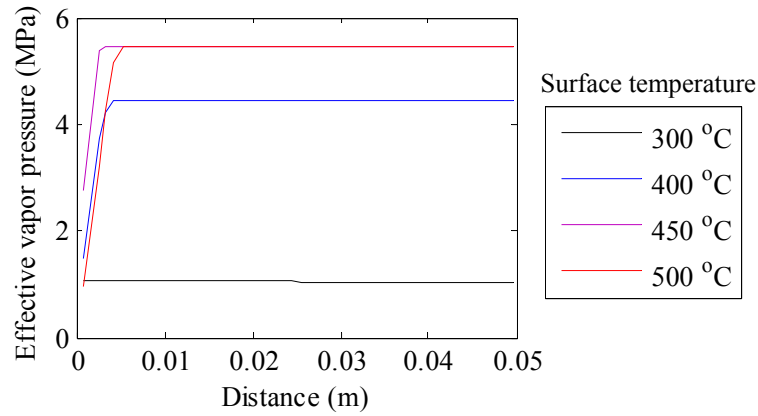


(b) HPC₂₈₋₁₁₀

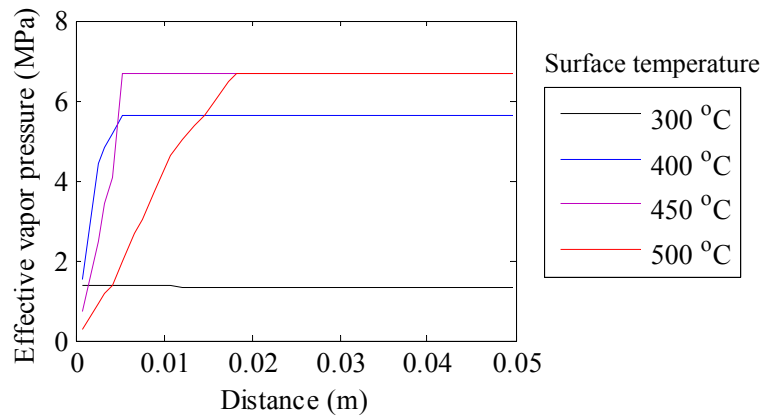


(c) NSC-40

Fig. 8.30 Profile of predicted effective vapor pressure in concretes with 90% initial moisture content for different surface temperatures under slow heating (5 °C/min) (The temperature profile is shown in Fig. 8.8 (c)).



(a) HPC₉₀₋₁₁₀



(b) HPC₂₈₋₁₁₀

Fig. 8.31 Profile of predicted effective vapor pressure in concretes with 90% initial moisture content for different surface temperatures under slow heating (0.5 °C/min) (The temperature profile is shown in Fig. 8.8 (d)).

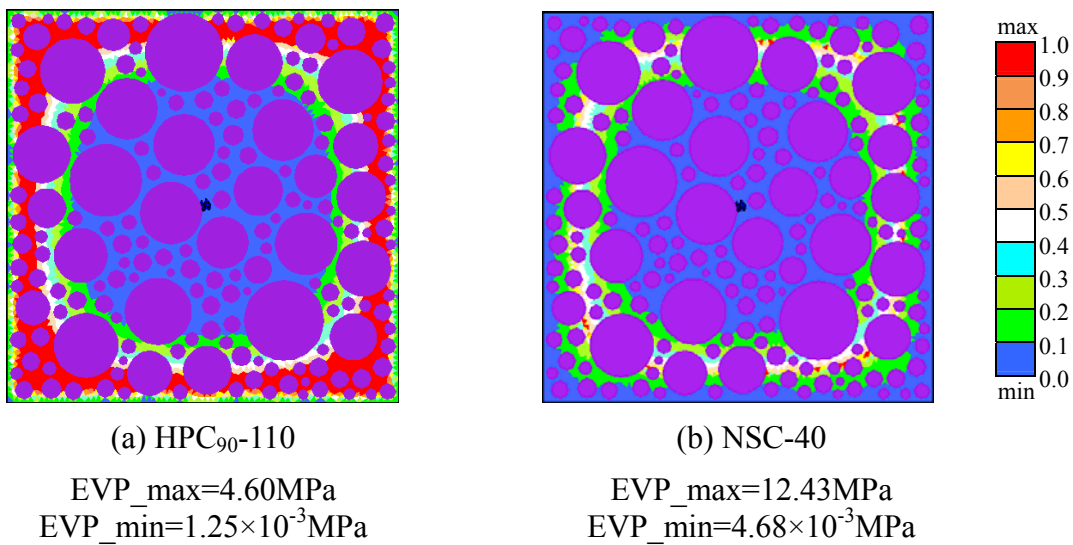


Fig. 8.32 Distribution of predicted effective vapor pressure in concretes with 90% initial moisture content for surface temperature of 500 °C under ISO 834 fire.

8.7 Analysis of thermal reduction of elastic modulus

In the mechanical analysis, under thermal load, the evolution of the elastic modulus with heating has to be known. Using the method proposed in Section 7.5 of Chapter 7, the variation of the elastic modulus of heated matrix is predicted based on the thermal decomposition analysis. Under the ISO 834 fire condition, the predicted reduction of the elastic modulus of the matrix of HPC₉₀₋₁₁₀ and NSC-40 is shown in Fig. 8.33. The lower horizontal line in the figure indicates the effect of the complete decomposition of hydrated aluminates on the elastic modulus. The distribution of the predicted reduction of relative elastic modulus of the matrix of HPC₉₀₋₁₁₀ for the surface temperatures of 300 °C, 400 °C, and 500 °C are shown in Fig. 8.34. Under slow heating, the reduction is almost uniform in the concrete specimens due to the low temperature gradient (Fig. 8.8 (c and d)). The relative elastic modulus of the matrix of different concretes at different decomposition stages is shown in Table 8.8. The proposed prediction method has been verified in Section 7.6 of Chapter 7.

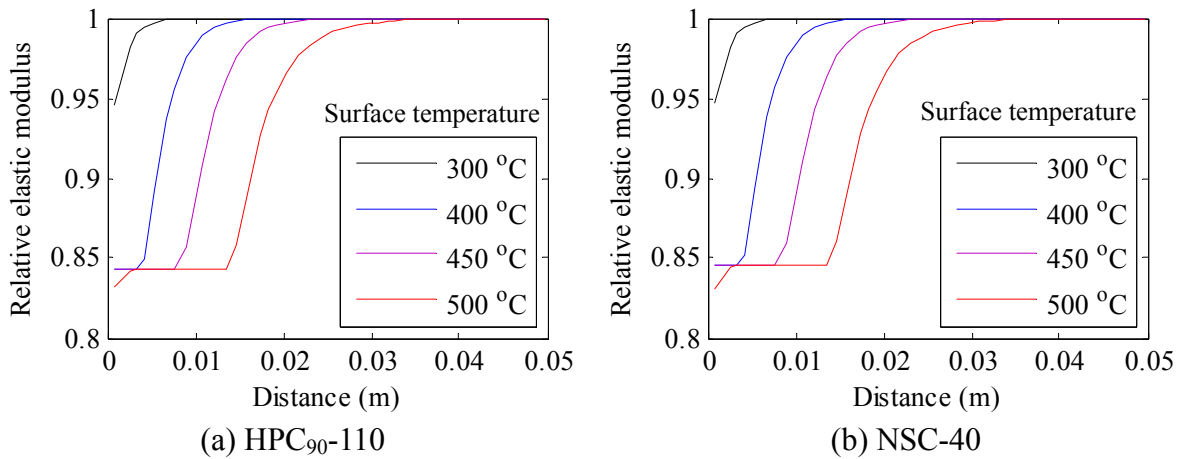


Fig. 8.33 Profile of predicted relative elastic modulus of matrix of concretes for different surface temperatures under ISO 834 fire (The temperature profile is shown in Fig. 8.8 (a)).

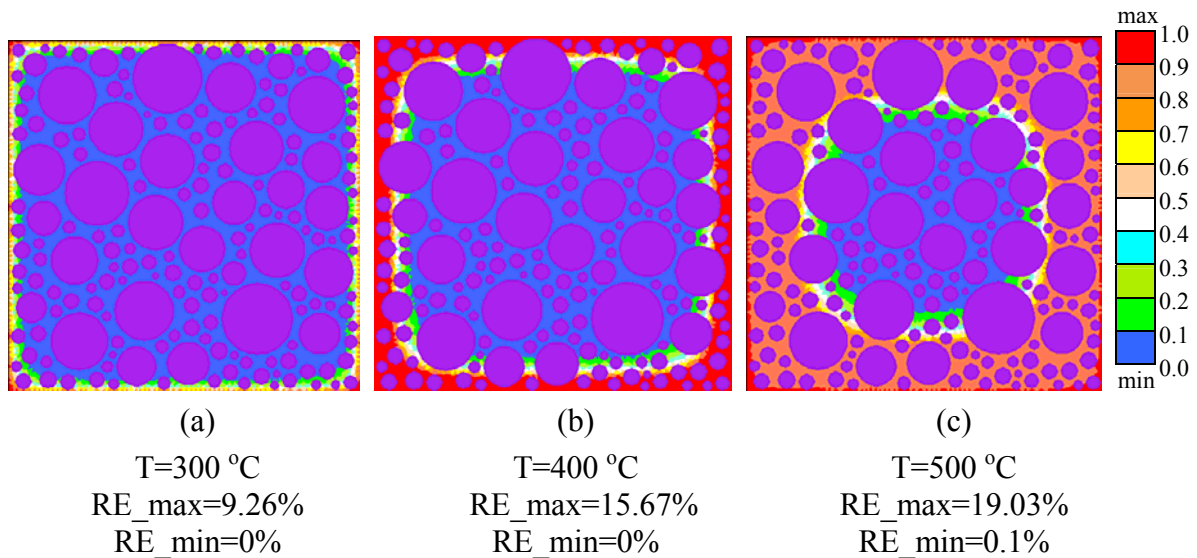


Fig. 8.34 Reduction of relative elastic modulus of matrix of HPC₉₀₋₁₁₀ for different surface temperatures under ISO 834 fire.

Table 8.8 Relative elastic modulus of matrix at different decomposition stages

| | at AFt fully decomposed | at CH fully decomposed |
|------------------------|-------------------------|------------------------|
| HPC ₉₀ -110 | 84.3% | 75.6% |
| HPC ₂₈ -110 | 85.6% | 76.7% |
| NSC-40 | 84.6% | 73.3% |

8.8 Thermo-poro mechanical damage analysis of heated concretes

In this section, the thermo-poro mechanical damage of heated concretes are numerically investigated using the method proposed in Chapter 7. The afore-mentioned predictions of the temperature field, the vapor pressure, and the variation of the elastic modulus of the matrix are incorporated in the analysis. The damage mechanisms of HPC₉₀-110 and NSC-40 under both fast heating (IOS 843 fire) and slow heating (5 °C/min) until the heating temperature reaches 600 °C are numerically studied, respectively. Two types of spalling, i.e., explosive spalling and surface spalling (scaling) are numerically encountered and interpreted.

It should be pointed out that, for the thermo-poro mechanical analysis of heated concrete, although the vapor pressure and the elastic modulus can be predicted as shown in the previous sections, the effective thermal expansion coefficient (Eq. 7.6a) is still an unknown parameter. For free expansion, large scattering of the experimental data on the expansion coefficient can be found in the literature: It was found by Browne [1967] that the expansion coefficient of granite is in the rang of 1.8-11.9 ($10^{-6} \text{ }^{\circ}\text{C}^{-1}$) and that of concrete made with granite is in the range of 8.1-10.3 ($10^{-6} \text{ }^{\circ}\text{C}^{-1}$); It was reported by Komarovskii [1965] that the expansion coefficient of concrete made with granite is in the range of 0.71-15.9 ($10^{-6} \text{ }^{\circ}\text{C}^{-1}$); For the matrix, it was found that the expansion coefficient changes from positive to negative during heating [Bažant and Kaplan, 1996]. In this thesis, the effective expansion coefficient is used for the mechanical analysis. The effective expansion is defined as the free expansion strain minus the microcracking-induced strain of free expansion (Section 7.2 in Chapter 7). However, experimental data on effective expansion coefficient can hardly be found in the literature. Owing to the lack of the experimental data on the effective expansion coefficient of the used material in Peng's test and the scattering of the reported experimental results of the free expansion coefficient, different values of the effective expansion coefficient are used in the mechanism analysis of fire spalling. From the results of the analysis it can be seen that this method is feasible for the investigation of the mechanism of fire spalling.

This section consists of three sub-sections: In Sec. 8.8.1, the fire spalling mechanism of HPC is investigated; In Sec. 8.8.2, the fire damage of NSC is studied; In Sec. 8.8.3, the mechanical damage of slow heating of both HPC and NSC is discussed.

8.8.1 Fire spalling mechanism investigation of high-performance concrete

To investigate the fire spalling mechanism of HPC, the patterns of mechanical damage caused only by thermal expansion (using different effective expansion coefficients) and only by vapor pressure are studied first, respectively. By comparing the numerically predicted damage pattern with the experimentally observed results, it can be concluded that the temperature gradient induced thermal stress plays a dominant role in fire spalling. This conclusion is then confirmed by the energy analysis in the fire spalling study.

8.8.1.1 Mechanical damage caused only by thermal expansion

To study the mechanical damage to HPC₉₀₋₁₁₀ caused only by thermal expansion (0% initial moisture content), different values (constant) of the effective expansion coefficient are used as shown in Table 8.9 (The value of $5.0 \times 10^{-6} \text{ } ^\circ\text{C}^{-1}$ is used for concrete by Bažant [1996]). For HPC₉₀₋₁₁₀, no crack induced by volume mismatch between aggregates and the matrix was observed in the experiments [Peng, 2000], which implies the aggregate and the matrix have the same extent of expansion under the same heating condition. Thus, the effective expansion coefficients of the aggregate and the matrix are assumed to have the same value. The numerical results (Table 8.9) show that, when the effective expansion coefficient exceeds $1.5 \times 10^{-6} \text{ } ^\circ\text{C}^{-1}$, the non-linear mechanical analysis fails to converge when the surface temperature reaches a certain value (Column 5 in Table 8.9), which means that the concrete specimen couldn't sustain the thermal load [Rots, 1988], i.e., mechanical failure occurs. The damage pattern of the time step before failure is shown in Fig. 8.35 (the time step is 5 s). It can be seen from this figure that the failure can be corner spalling (Fig. 8.35 (a, b)) and explosive spalling (Fig. 8.35 (c, d)). With the decrease of the effective expansion coefficient, the time and the surface temperature at spalling are increasing and the damage moves towards the central region of the specimen as shown in Fig. 8.35. When the effective expansion coefficient of concrete is equal to 1.5×10^{-6} (Case 5_HPC), no spalling but little damage in the deep central region occurs (Fig. 8.35 (e)).

The fields of the principal stress before spalling in Case 1_HPC and at the first element damaged in Case 6_HPC are shown in Fig. 8.36 and Fig. 8.37, respectively. It can be seen from these figures that the damaged elements lie in the tensile region of the first principal stress field. In comparison with the second principal stress, the first principal stress plays a dominant role in the resulting damage.

Table 8.9 Mechanical damage caused only by thermal expansion at different effective thermal expansion coefficients (0% initial moisture content)

| | Effective thermal expansion coefficient ($^\circ\text{C}^{-1}$) α_i^e | Spalling | Spalling time (Second) | Spalling surface temperature ($^\circ\text{C}$) | Damage pattern before spalling/until $600 \text{ } ^\circ\text{C}$ |
|------------|---|----------|------------------------|---|--|
| Case 1_HPC | 5.0×10^{-6} | Yes | 15 | 184.6 | Fig. 8.35 (a) |
| Case 2_HPC | 4.0×10^{-6} | Yes | 20 | 214.7 | Fig. 8.35 (b) |
| Case 3_HPC | 3.0×10^{-6} | Yes | 25 | 239.7 | - |
| Case 4_HPC | 2.0×10^{-6} | Yes | 55 | 337.6 | Fig. 8.35 (c) |
| Case 5_HPC | 1.6×10^{-6} | Yes | 135 | 461.2 | Fig. 8.35 (d) |
| Case 6_HPC | 1.5×10^{-6} | No | - | - | Fig. 8.35 (e) |

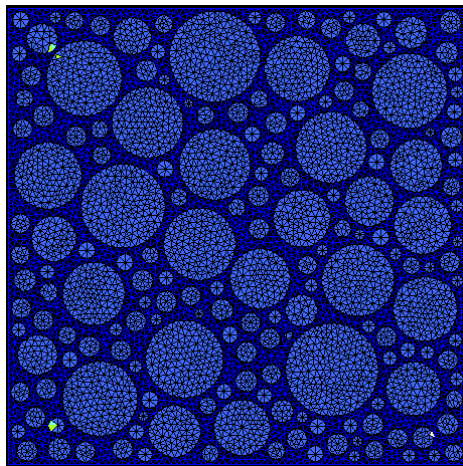
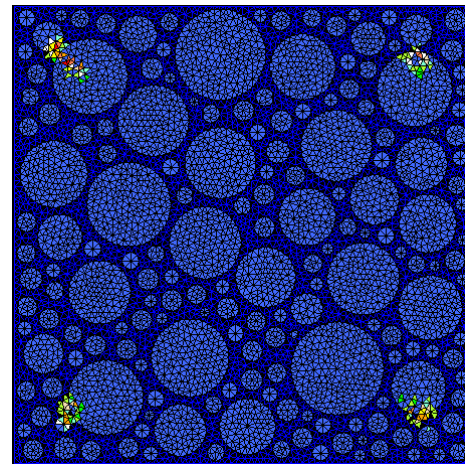
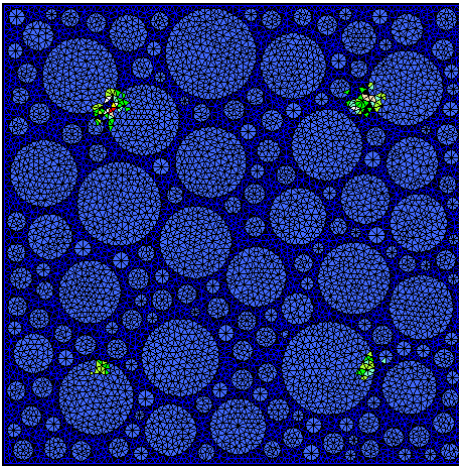
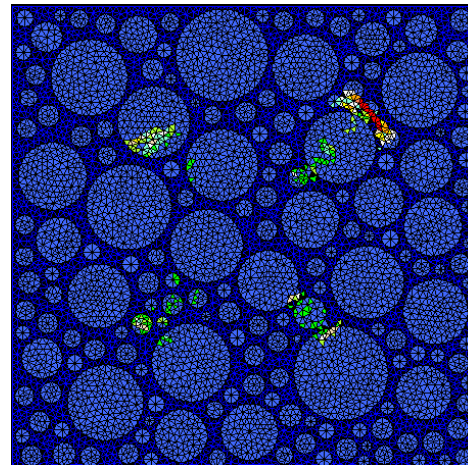
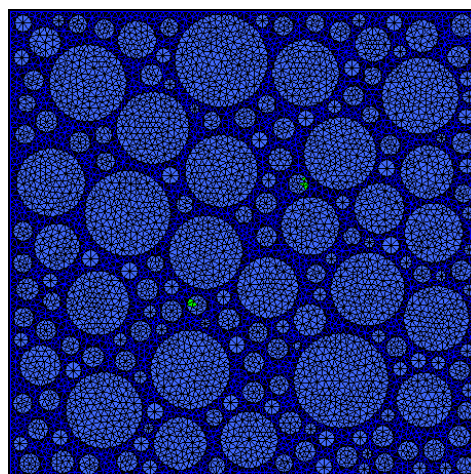
(a) $\alpha_t^e = 5.0 \times 10^{-6}$ (t=10 s)(b) $\alpha_t^e = 4.0 \times 10^{-6}$ (t=15 s)(c) $\alpha_t^e = 2.0 \times 10^{-6}$ (t=20 s)(d) $\alpha_t^e = 1.6 \times 10^{-6}$ (t=50 s)(e) $\alpha_t^e = 1.5 \times 10^{-6}$ (t=130 s)

Fig. 8.35 Mechanical damage pattern in specimen of HPC₉₀₋₁₁₀ caused only by thermal expansion at different effective thermal expansion coefficients before spalling (a to d)/until 600 °C (e) under ISO 834 fire condition.

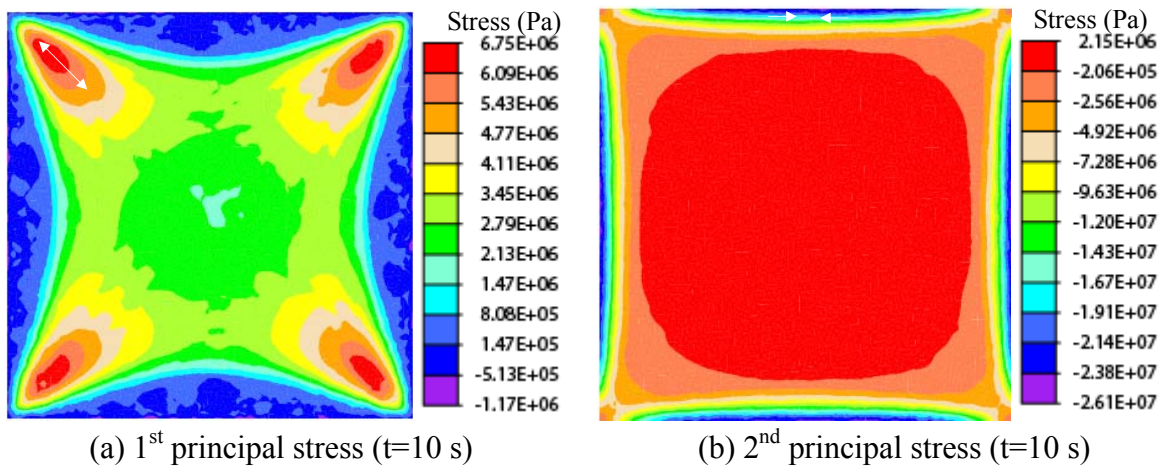


Fig. 8.36 Stress field at effective thermal expansion coefficient of $5.0 \times 10^{-6} \text{ } ^\circ\text{C}^{-1}$ before spalling (Case 1-HPC in Table 8.9) (The direction of the stress is marked in arrow).

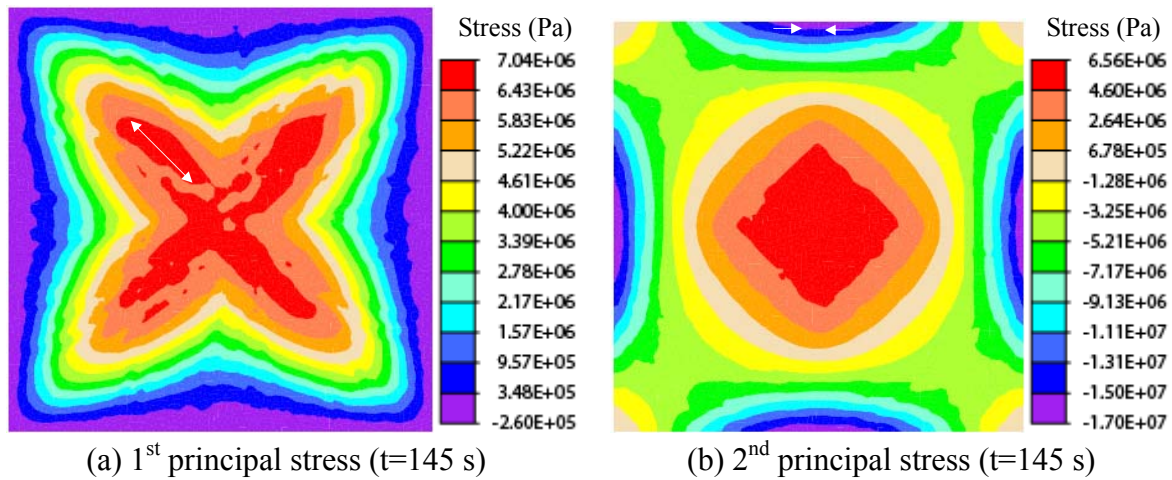
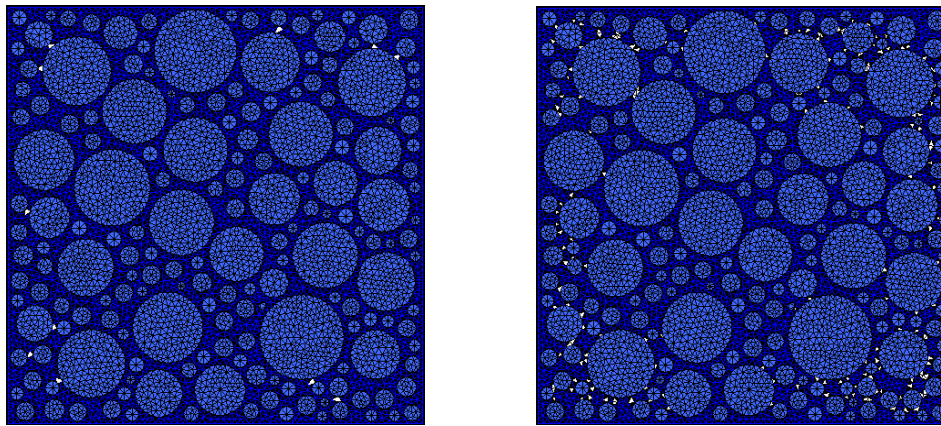


Fig. 8.37 Stress field at effective thermal expansion coefficient of $1.5 \times 10^{-6} \text{ } ^\circ\text{C}^{-1}$ when first element failed at surface temperature of $471 \text{ } ^\circ\text{C}$ (Case 6-HPC in Table 8.9) (The direction of the stress is marked in arrow).

8.8.1.2 Mechanical damage caused only by vapor pressure

The mechanical damage to HPC₉₀₋₁₁₀ and HPC₂₈₋₁₁₀ with 90% initial moisture content caused only by vapor pressure (no thermal expansion) under ISO 834 fire is also numerically investigated. No spalling occurs before the temperature reaches $600 \text{ } ^\circ\text{C}$ (Table 8.10). The damage patterns in the specimens are shown in Fig. 8.38. The effective vapor pressure and the effective first principal stress are show in Fig. 8.39 and Fig. 8.40 for the two concretes.

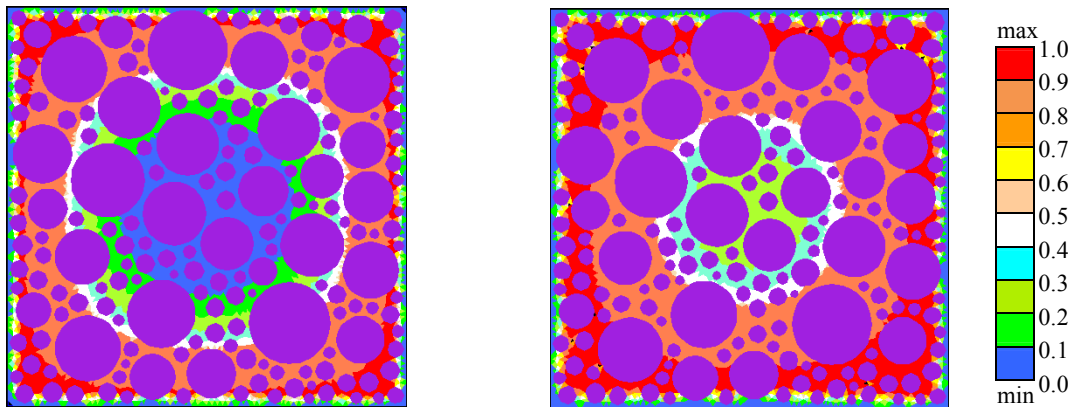
The comparison between Fig. 8.35 and Fig. 8.38 shows that the damage caused only by vapor pressure is more local than that caused only by thermal expansion, i.e., the mechanically damaged elements lie in the region where the vapor pressure is high (Fig. 8.39 and Fig. 8.40) and the core region of the specimen remains intact. This can be explained as follows: From the constitutive equation (Eq. 7.6) it can be seen that the effect of the vapor pressure on the stress and strain field is similar to that of the thermal expansion. If the vapor pressure effect is converted into equivalent expansion, it can be calculated that the magnitude



(a) HPC₉₀-110

(b) HPC₂₈-110

Fig. 8.38 Damage caused only by vapor pressure to HPC-110 with 90% initial moisture content under ISO834 fire.

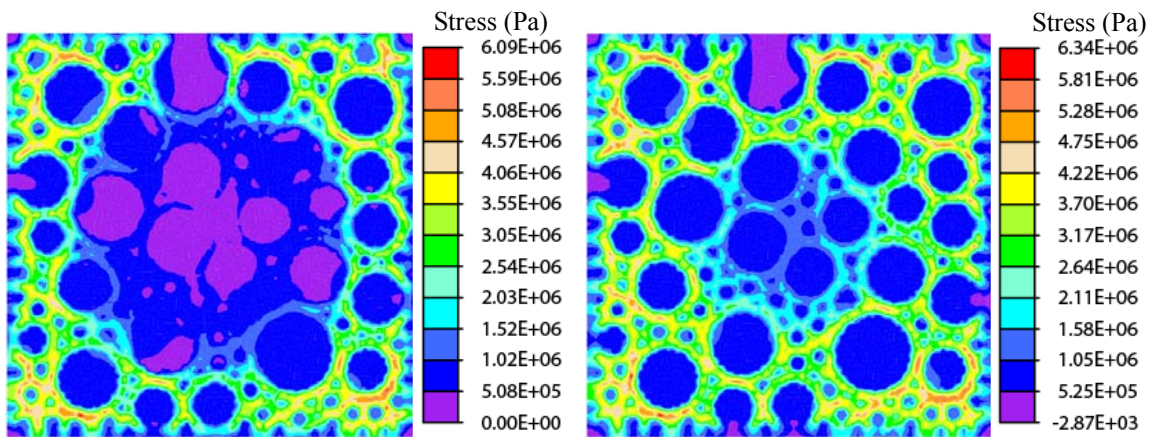


(a) Effective vapor pressure at 555 °C

(b) Effective vapor pressure at 600 °C

Evp_max=5.47 (MPa)
Evp_min= 5.80×10^{-3} (MPa)

Evp_max=5.47 (MPa)
Evp_min= 4.37×10^{-4} (MPa)



(c) Effective 1st principal stress at 555 °C

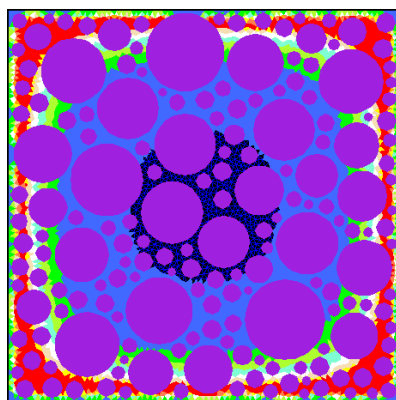
(d) Effective 1st principal stress at 600 °C

Fig. 8.39 Effective vapor pressure (a, b) and effective 1st principal stress induced only by vapor pressure (c, d) of HPC₉₀-110 with 90% initial moisture content when surface temperature reaches 555 °C and 600 °C under ISO 834 fire.

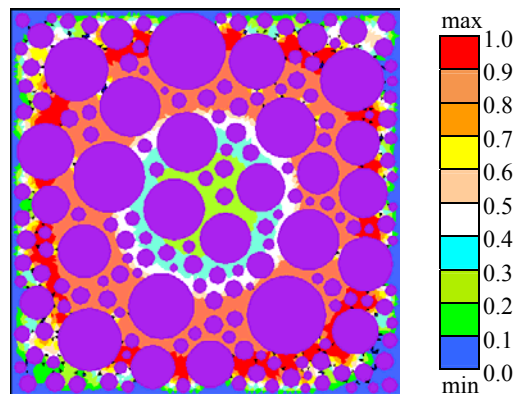
of the coefficient of equivalent expansion, α_p ($\alpha_p = p/(3H \cdot T)$), induced by vapor pressure is 10^{-7} (Fig. 8.41). It is one order of magnitude lower than the effective thermal expansion coefficient used for HPC₉₀₋₁₁₀ (Table 8.9). Moreover, since vapor pressure only exists in the matrix and not in the aggregates, the equivalent expansion effect of the vapor pressure is even less. Therefore, the thermal stress induced only by vapor pressure in the core region is much lower than that caused only by thermal expansion. This can clearly be seen by comparing the stress fields in Fig. 8.39 and Fig. 8.40 with those in Fig. 8.37.

Table 8.10 Mechanical damage caused only by vapor pressure to HPC-110 with 90% initial moisture content under ISO 834 fire

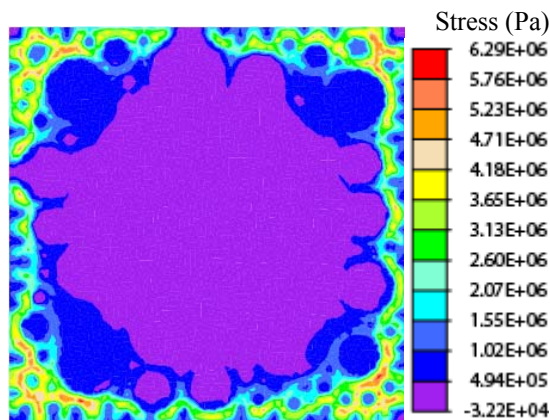
| | Spalling | Surface temperature when the first damaged element appears (°C) | Damage pattern at 600 °C |
|-----------------------|----------|---|--------------------------|
| HPC ₉₀₋₁₁₀ | No | 555.5 | Fig. 8.38 (a) |
| HPC ₂₈₋₁₁₀ | No | 461.1 | Fig. 8.38 (b) |



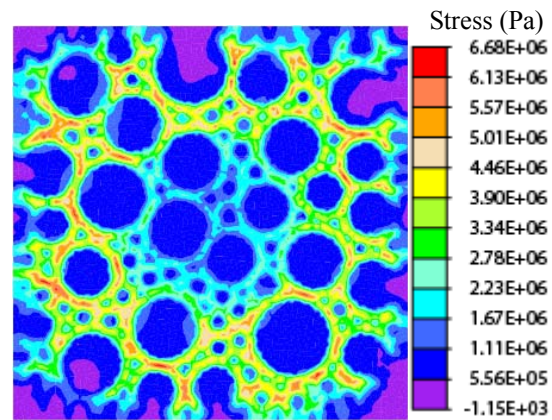
(a) Effective vapor pressure at 461 °C
 Evp_max=5.65 (MPa)
 Evp_min= 1.46×10^{-4} (MPa)



(b) Effective vapor pressure at 600 °C
 Evp_max=6.67 (MPa)
 Evp_min= 2.10×10^{-4} (MPa)



(c) Effective 1st principal stress at 461 °C



(d) Effective 1st principal stress at 600 °C

Fig. 8.40 Effective vapor pressure (a, b) and effective 1st principal stress induced only by vapor pressure (c, d) of HPC₂₈₋₁₁₀ with 90% initial moisture content when surface temperature reaches 461 °C and 600 °C under ISO 834 fire.

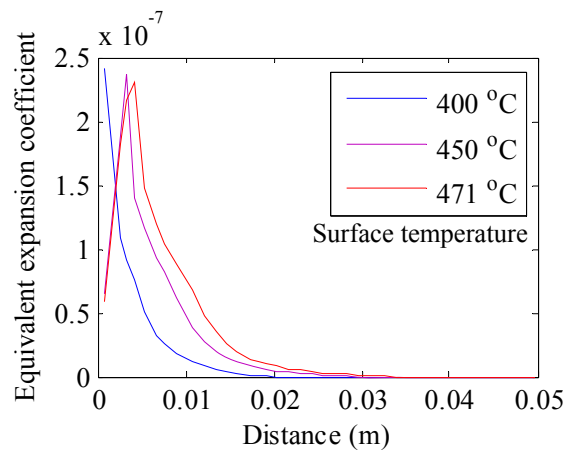
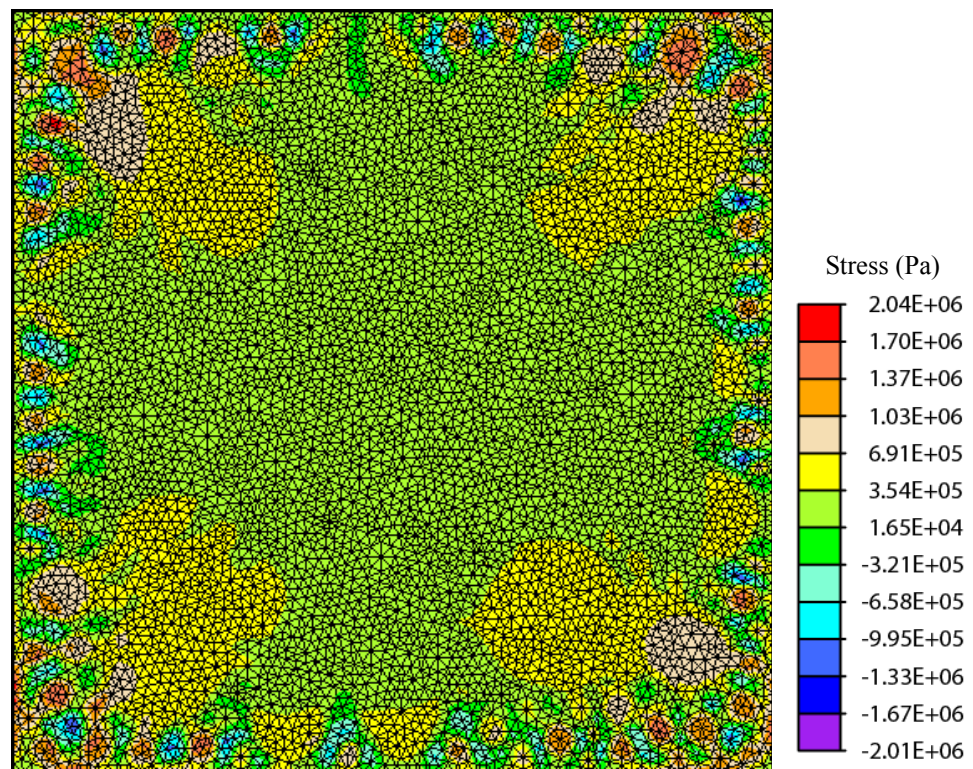


Fig. 8.41 Profile of coefficient of equivalent expansion induced by vapor pressure of matrix of HPC₉₀₋₁₁₀ with 90% initial moisture content for different surface temperatures under ISO 834 fire.

To further illustrate the stress field induced by vapor pressure, corresponding to the field of the effective first principal stress of HPC₂₈₋₁₁₀ shown in Fig. 8.40 (c), the field of the first principal stress is shown in Fig. 8.42 (a), where the value of the stress in the core region can be seen more clearly. To check the correctness of the calculation, the stress field in the y -direction (σ_y) is shown in Fig. 8.42 (b) and the corresponding profile of element stress along the x -axis in the middle of the 2D region is also shown (Fig. 8.42 (c)). It can be seen from Fig. 8.42 (c) that the equilibrium is satisfied.



(a) 1st principal stress

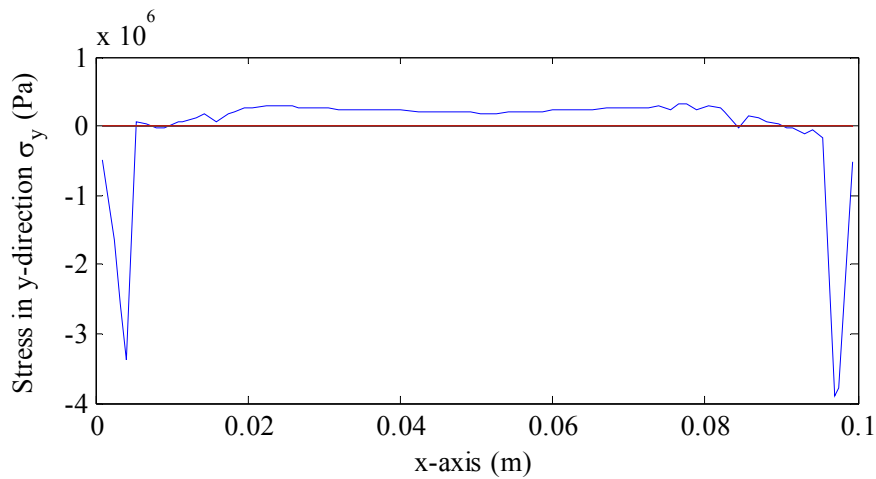
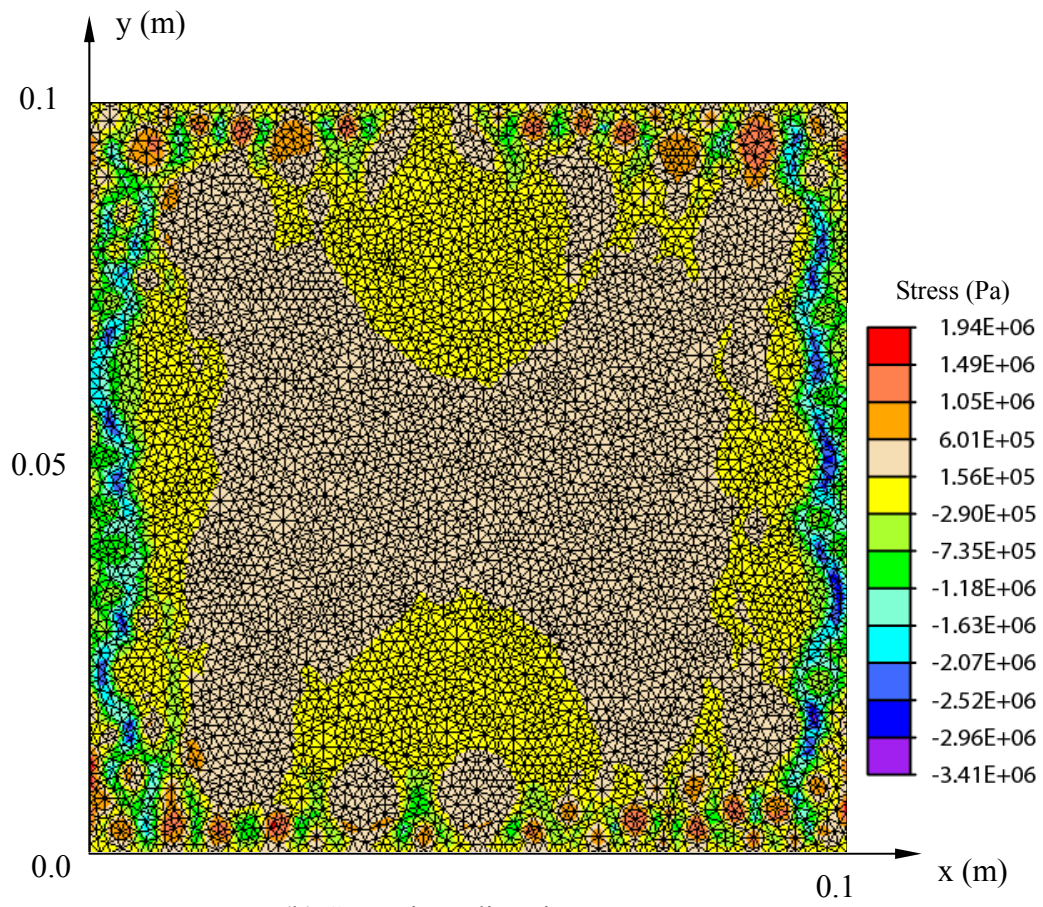


Fig. 8.42 First principal stress (a), stress in y-direction (b), and profile of stress in y-direction induced only by vapor pressure of HPC₂₈₋₁₁₀ with 90% initial moisture content when surface temperature of specimen reaches 461 °C under ISO 834 fire.

8.8.1.3 Analysis of mechanism of fire spalling by comparing damage patterns

In Sections 8.8.1.1 and 8.8.1.2, under the ISO 843 fire condition, the mechanical damage caused only by thermal expansion and only by vapor pressure is investigated respectively and the corresponding damage patterns are studied. To determine which one of the two factors plays the dominant role in fire spalling, the numerical damage patterns in Fig. 8.35 and Fig. 8.38 are compared with the observed results in the fire spalling experiments of specimens with different moisture contents shown in Fig. 8.43 [Peng, 2000]. In the experiments, as the probability of fire spalling is not 100% for the concrete specimens from the same batch, such as two samples out of three spalled, the un-spalled specimens with different moisture contents were sawn in half for the observation of internal cracks. Fig. 8.43 clearly shows internal cracks near/in the central region of the specimens. The spalled specimens (explosive spalling) are shown in Fig. 8.43 (d). Explosive spalling occurred when the surface temperature is in the range of 480 °C to 510 °C and the heating duration is around 3 minutes. It can be inferred from the comparison that under the ISO 834 fire condition, the internal cracks are mainly caused by the temperature gradient induced thermal stress since the pattern of damage caused only by thermal expansion correlates well with the experimentally observed results. Thus, it can be concluded that the explosive spalling of HPC is mainly attributed to the temperature gradient induced thermal stress.

8.8.1.4 Fire spalling analysis of high-performance concrete

The fire spalling of the specimen of HPC₉₀₋₁₁₀ with 90% initial moisture content is numerically studied. The effective thermal expansion coefficient of 1.5×10^{-6} in Case 6_HPC (Table 8.9) is used since the experimental result showed that the specimen of HPC₉₀₋₁₁₀ with 0% initial moisture content didn't spall [Peng, 2000]. The numerical analysis shows that, when the surface temperature reaches 476.1 °C, mechanical failure occurs, i.e., the nonlinear mechanical analysis fails to converge. The damage pattern of the time step before spalling is shown in Fig. 8.44. The corresponding effective principal stress and the effective vapor pressure before spalling are shown in Fig. 8.45. From these two figures it can be inferred that the spalling mode is explosive since, in the central region, the effective 1st principal stress is the highest and some cracks exist in the central region already. Comparing Fig. 8.44 with Fig. 8.43, it can be seen that the predicted damage in the up-right corner is similar to that of the major cracks in Fig. 8.43 (a) and the predicted cracks in the central region are similar to the small cracks in Fig. 8.43 (a to b). Therefore, the numerical result of spalling correlates well with the experimental results in terms of both the spalling time and the damage pattern.

The profile of effective vapor pressure together with the profile of temperature is plotted in Fig. 8.45 (d). It can be seen from Fig. 8.45 (c) and (d) that, although the effective vapor pressure profile correlates well with the pressure profile described in the moisture-clog spalling theory (Fig. 2.4 in Chapter 2) [Bažant, 1997; Consolazio et al., 1998; Kalifa et al., 2000], the high stress resides in the central region of the specimen (Fig. 8.45(a)). It suggests that explosive spalling is not caused by the moisture clog, but by the thermal stress in the central region of the 100 mm cubic specimen.

It should be pointed out that since the coefficient of effective expansion is used in the mechanical analysis, i.e., the microcracking induced strain of free expansion is already deducted from the thermal strain (Section 7.2 in Chapter 7), a relatively low value of the coefficient of effective expansion is resulted.

It has been shown by experiments that the probability of spalling of HPC can be lowered by adding polypropylene fibers to concrete and it was supposed that the vapor release-effect of the fiber upon melting plays a dominant role in avoiding spalling [Knack, 2009]. However, according to the numerical analysis of this thesis, for different heating conditions, the role that the fiber plays should be different. For fast heating, the concrete stiffness-lowering effect of the fiber should also be accounted for because the effect lowers the thermal stress in concrete. For slow heating, the vapor pressure release-effect of the fiber should be dominant since the mechanical damage is mainly caused by vapor pressure as shown in the following sections.

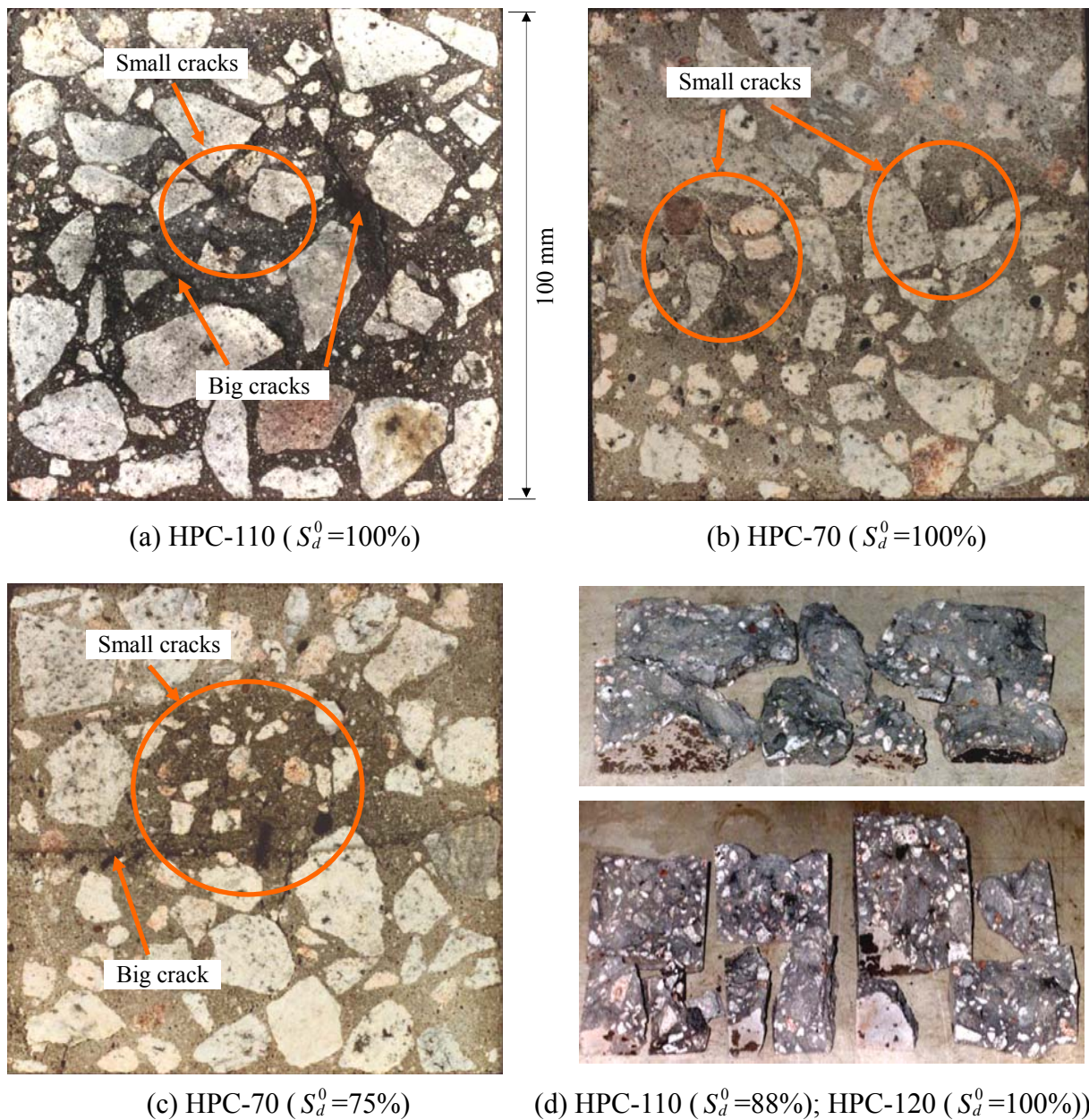


Fig. 8.43 Experimentally observed damage pattern of un-spalled concrete specimens (a to c) and spalled concrete specimens (d) with different initial moisture contents exposed to ISO 834 fire up to 600 °C [Peng, 2000] (Explosive spalling occurred when the surface temperature is in the range of 480 °C to 510 °C and the heating duration is around 3 minutes).

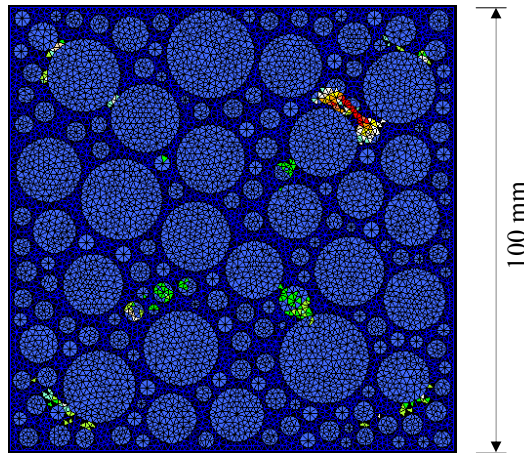


Fig. 8.44 Damage pattern before spalling in specimen of HPC₉₀₋₁₁₀ with 90% initial moisture content when surface temperature reaches 471 °C under ISO 834 fire.

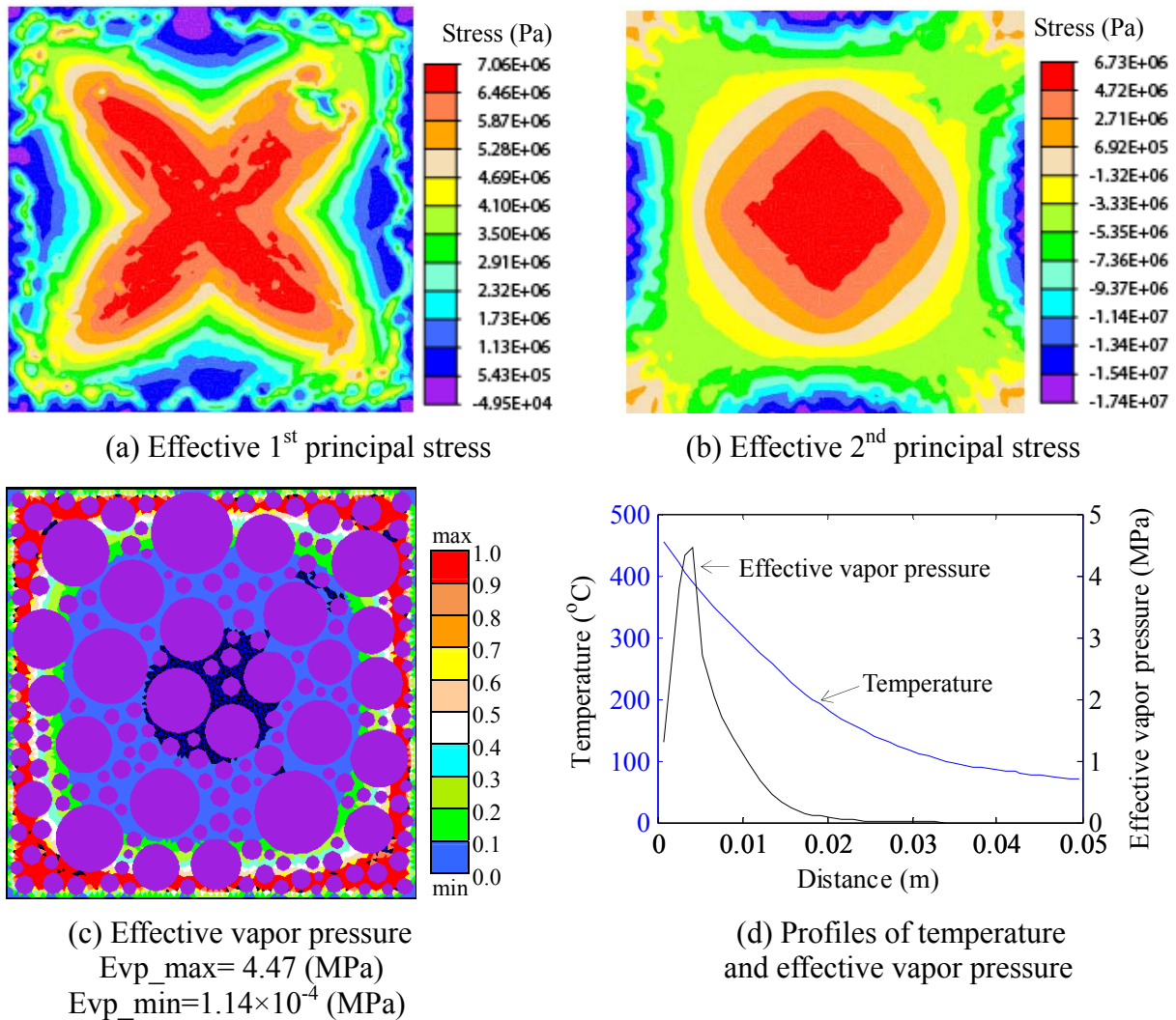


Fig. 8.45 Field of effective principal stress (a, b) and effective vapor pressure (c), and profiles of temperature and effective vapor pressure (d) in specimen of HPC₉₀₋₁₁₀ with 90% initial moisture content before spalling for surface temperature of 471 °C under ISO 834 fire.

8.8.1.5 Energy analysis of fire spalling

To further confirm the conclusion drawn in the previous sections, i.e., fire spalling is mainly caused by the temperature gradient induced thermal stress, the mechanism of fire spalling will be interpreted from an energy perspective in this section. The development of the elastic strain energy is investigated. In the 100×100 mm region (unit thickness), the elastic strain energy, I_c , can be calculated as follows

$$I_c = \sum_{k=1}^{ne} \frac{1}{2} \sigma_{ij}^e \varepsilon'_{ij} A_e \quad (8.2)$$

where σ_{ij}^e is the effective stress, ε'_{ij} is the elastic strain (Eq. 5.9 in Chapter 5 and Eq. 7.14 in Chapter 7), A_e is the surface area of each element, and ne is the number of elements. The development of the elastic strain energy in HPC₉₀₋₁₁₀ with 0% and 90% initial moisture content exposed to ISO 834 fire in the region is calculated and plotted in Fig. 8.46. It can be seen that, in the case of 90% initial moisture content, spalling occurs at the highest elastic strain energy, where the energy induced by thermal expansion reaches the highest value. It can also be noted as shown in the figure that the increase of energy induced by vapor pressure is very low, only 12.6% of the strain energy of thermal expansion at spalling. It implies that, from the energy perspective, the thermal expansion induced strain energy plays a dominant role in spalling, which confirms the conclusion drawn in Section 8.8.1.3. Fig. 8.46 also shows that the strain energy of thermal expansion decreases with the increase of temperature after the peak value at around 476 °C. This is due to the decrease of the heating rate (Fig. 4.11 (b)), which lowers the temperature gradient and thus decreases the thermal stress and the elastic strain energy in the region.

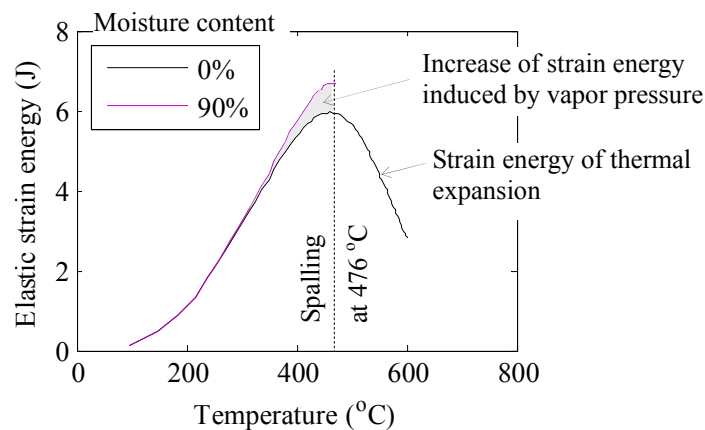


Fig. 8.46 Development of elastic strain energy in 100×100 mm region (unit thickness) of HPC₉₀₋₁₁₀ with 0% and 90% initial moisture content as a function of heating temperature under ISO 834 fire.

8.8.2 Fire damage investigation of normal strength concrete

Under the ISO 834 fire condition, to compare with the fire spalling analysis of HPC, the mechanical fire damage to NSC-40 with 90% and 0% initial moisture content is numerically studied. First, the mechanical damage caused only by thermal expansion (0% initial moisture content) and only by vapor pressure is investigated. Then, the behavior of NSC-40 with 90% initial moisture content under the fire condition is studied and the elastic strain energy is also analyzed.

8.8.2.1 Mechanical damage caused only by thermal expansion

For the analysis of the mechanical damage caused only by thermal expansion (0% initial moisture content), four cases of using different effective thermal expansion coefficients are studied (Table 8.11). The numerical results (Table 8.11 and Fig. 8.47) show that in Case 1_NSC, where the effective expansion coefficient of concrete is equal to that in Case 6_HPC (Table 8.9), spalling occurs when the surface temperature reaches 396.4 °C. As the matrix of NSC is much more porous than that of HPC, the coefficient of effective expansion of the two matrices should be different. It has been found that, under the free expansion condition, heated harden cement paste of normal strength contracts after the temperature reaches around 200 °C, namely, the coefficient of free expansion changes from positive to negative [Bažant, 1996]. It has also been found that, when the same aggregate was used, NSC expands less than HPC under both loaded and unloaded conditions [Hu and Dong, 2002]. In addition, it has been reported by Peng [2000] that NSC with zero moisture content didn't spall. Thus, it can be deduced that the coefficient of effective thermal expansion of the matrix of NSC-40 is lower than that of HPC₉₀₋₁₁₀ as the same aggregate was used for both NSC and HPC. Therefore, the effective expansion coefficient of the matrix of NSC-40 is decreased in Case 2_NSC through Case 4_NSC. Fig. 8.47 shows that the bigger the difference between the effective expansion coefficient of the aggregate and that of the matrix, the more severe the local damage induced by volume mismatch. In Case 2_NSC and Case 3_NSC, spalling occurs. In Case 4_NSC, no spalling occurs till the heating temperature reaches 600 °C and the damage pattern is shown in Fig. 8.47 (d).

Table 8.11 Mechanical damage at different coefficients of effective thermal expansion

| | Coefficient of effective thermal expansion (α_i^e) ($^{\circ}\text{C}^{-1}$) | | Spalling | Spalling time (Second) | Spalling surface temperature ($^{\circ}\text{C}$) | Damage pattern before spalling/until 600 $^{\circ}\text{C}$ |
|------------|---|-----------------------|----------|------------------------|---|---|
| | Aggregate | Matrix | | | | |
| Case 1_NSC | 1.5×10^{-6} | 1.5×10^{-6} | Yes | 85 | 396.4 | Fig. 8.47(a) |
| Case 2_NSC | 1.5×10^{-6} | 1.0×10^{-6} | Yes | 245 | 546.8 | Fig. 8.47(b) |
| Case 3_NSC | 1.5×10^{-6} | 0.8×10^{-6} | Yes | 305 | 578.8 | Fig. 8.47(c) |
| Case 4_NSC | 1.5×10^{-6} | 0.68×10^{-6} | No | - | - | Fig. 8.47(d) |

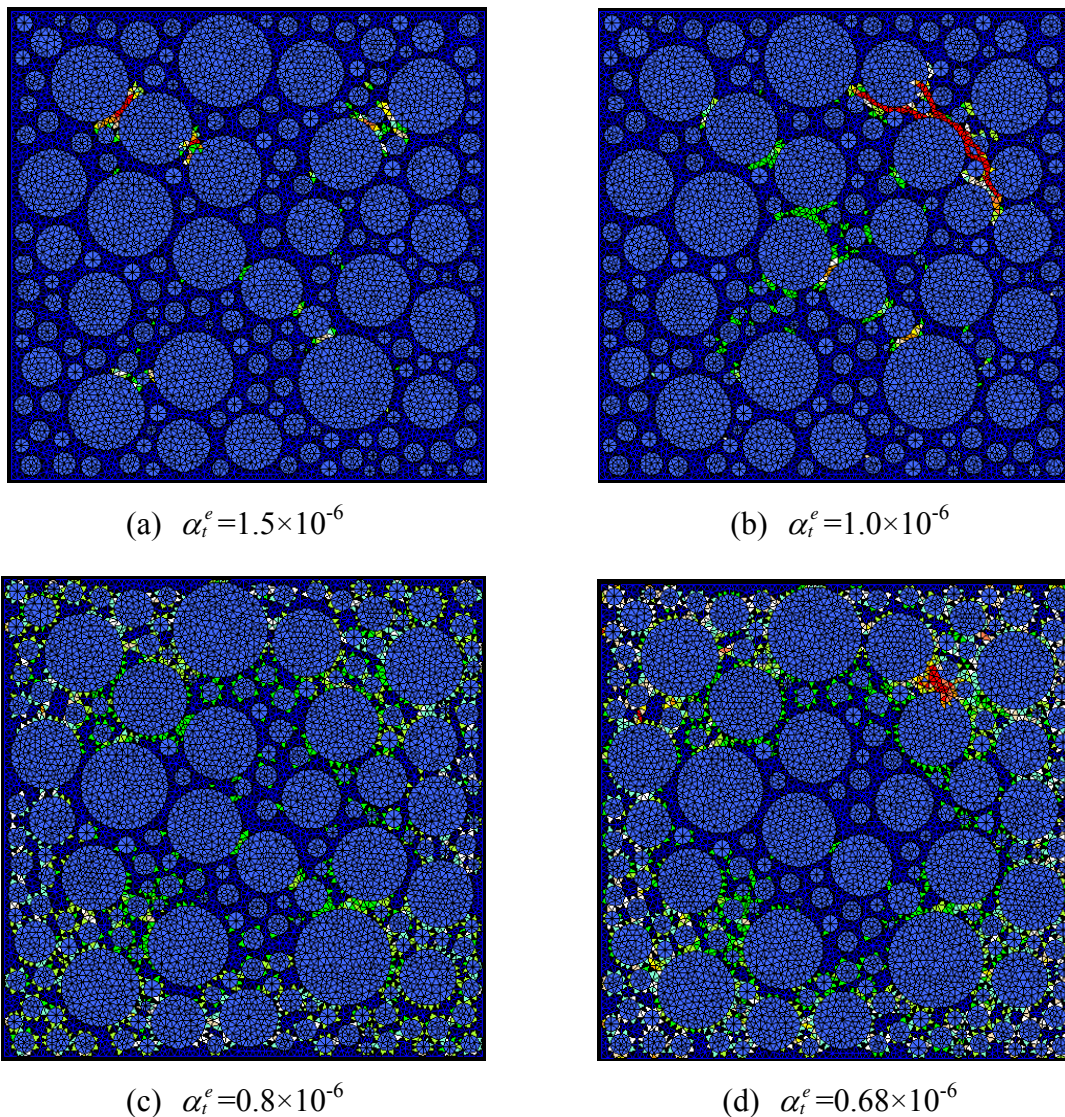


Fig. 8.47 Pattern of mechanical damage to NSC-40 caused only by thermal expansion at different coefficients of effective thermal expansion of matrix before spalling (a to c)/until 600 °C (d) under ISO 834 fire.

8.8.2.2 Mechanical damage caused only by vapor pressure

The mechanical damage to NSC-40 with 90% initial moisture content caused only by vapor pressure (no thermal expansion) under ISO 834 fire is numerically studied. The numerical result shows that, when the surface temperature reaches 369.9 °C, the non-linear mechanical analysis fails to converge. The effective first principal stress and the damage pattern of the time step before divergence (Fig. 8.48) suggest that the mechanical failure is caused by partial surface layer breaking off (surface spalling). The reason for this is that, although the permeability of NSC-40 is high, the effective vapor pressure can still reach a high value, as shown in Fig. 8.29 (b), and can cause local damage to the matrix.

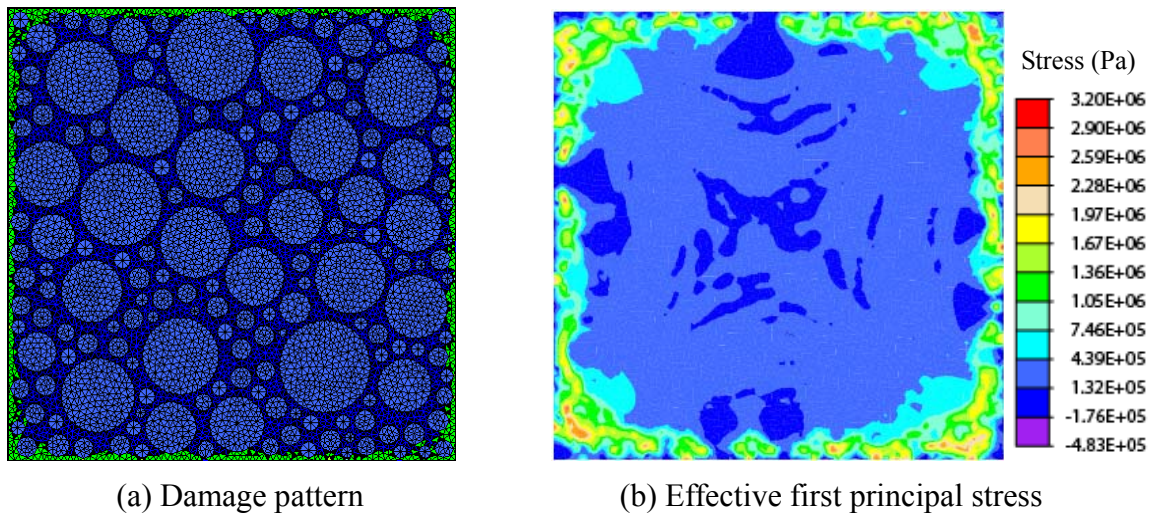


Fig. 8.48 Damage pattern (a) and effective first principal stress (b) of NSC-40 with 90% initial moisture content induced only by vapor pressure before surface spalling under ISO 843 fire condition.

8.8.2.3 Fire damage analysis of normal strength concrete

The behavior under fire of NSC-40 with 90% initial moisture content is numerically studied. The effective thermal expansion coefficient in Case 4_NSC, i.e., 1.5×10^{-6} for the aggregates and 0.68×10^{-6} for the matrix is used (Table 8.11) since the experimental results showed that the specimen of NSC-40 with 0% initial moisture content didn't spall [Peng, 2000]. The numerical result shows that, when the surface temperature reaches 396.4 °C, the non-linear mechanical analysis fails to converge. From the damage pattern of the time step before divergence shown in Fig. 8.49 (the time interval is 5 s), it can be inferred that the divergence is caused by the partial surface layer breaking off (surface spalling).

The development of the elastic strain energy in the 2D region (unit thickness) is plotted in Fig. 8.50, together with the elastic strain energy of NSC-40 with 0% initial moisture content (the case of expansion only) for comparison. It can be seen from Fig. 8.50 that the energy at mechanical failure is lower than the peak value of the energy induced only by thermal expansion and thus lower than the energy-storage capacity of the sample. It suggests, therefore, that local failure occurs. In the case of local failure, only part of the stored energy is released and the energy stored in the bulk specimen is not released. Thus, compared with the energy released by explosive spalling of HPC₉₀₋₁₁₀ shown in Fig. 8.46, the energy released by the local failure of NSC-40 is much lower, i.e., the surface spalling of NSC-40 is much less violent compared with the explosive spalling. It is conceivable that, when the heating proceeds, the energy will be released progressively by local failure. Hence, explosive spalling will not occur in NSC. This is in good agreement with the experimental results that explosive spalling usually occurs in HPC but not in NSC [Hertz, 1992; Sanjayan and Stocks, 1993; Peng, 2000].

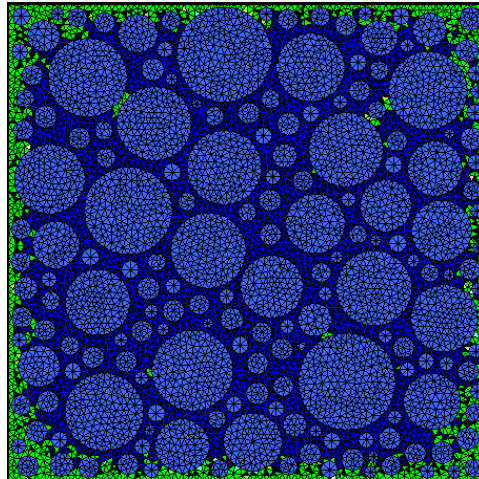


Fig. 8.49 Damage pattern of NSC-40 with 90% initial moisture content when surface temperature reaches 396.4 °C under ISO 834 fire.

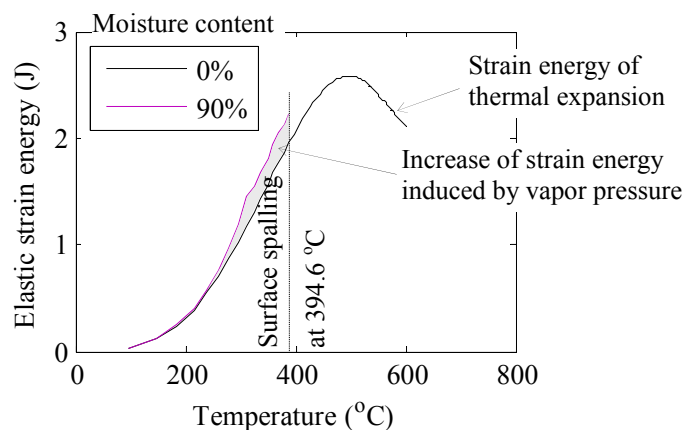


Fig. 8.50 Development of elastic strain energy in 2D domain of NSC-40 with 0% and 90% initial moisture content under ISO 834 fire condition.

8.8.3 Mechanical damage analysis under slow heating condition

To investigate the heating rate effect on the mechanical damage of heated concrete, the mechanical behaviour of HPC-110 and NSC-40 with 0% and 90% initial moisture content under slow heating (5 °C/min) until the heating temperature reaches 600 °C is numerically studied (the time interval for the calculation is 2 minutes). The effective expansion coefficients have the same values as those in the fire spalling analyses (Section 8.8.1.4 and Section 8.8.2.3), i.e. $1.5 \times 10^{-6} \text{ } ^\circ\text{C}^{-1}$ for HPC-110 and $1.5 \times 10^{-6} \text{ } ^\circ\text{C}^{-1}$ and $0.68 \times 10^{-6} \text{ } ^\circ\text{C}^{-1}$ for the aggregate and the matrix of NSC-40, respectively. The numerical results are summarized in Table 8.12.

- **High-performance concrete** For HPC-110 specimens with 0% and 90% initial moisture content, no divergence occurs in the non-linear mechanical analysis. It implies that no spalling occurs. Although no spalling occurs but many elements in the matrix are damaged in the case

of 90% initial moisture content (Fig. 8.51). The effective first principal stress of HPC-110 with 90% initial moisture content when the surface temperature reaches 600 °C is shown in Fig. 8.52. The development of the elastic strain energy in the 2D region (with unit thickness) is plotted in Fig. 8.53.

It can be seen by comparing Fig. 8.51 with Fig. 8.44 that the damage pattern of HPC-110 under the slow heating condition is different from that under the fire condition. In the latter case, the damage clusters in certain regions, while in the former case, the damage is more evenly distributed in the matrix over the cross section. By comparing the field of the effective first principal stress in Fig. 8.52 and Fig. 8.45 (a), it can be concluded that, for HPC-110 with 90% initial moisture content under slow heating, the local effect of vapor pressure plays a dominant role in the resulting damage. This conclusion can be further confirmed by the energy analysis as shown in Fig. 8.53. It can be seen from Fig. 8.53 that the strain energy in the 2D region of HPC₉₀-110 with 90% initial moisture content is almost completely induced by vapor pressure, which is different from the case under the fire condition (Fig. 8.46).

Table 8.12 Results of mechanical analysis of different concretes under slow heating condition (5 °C/min)

| | HPC ₉₀ -110 | | HPC ₂₈ -110 | | NSC-40 | |
|---|------------------------|---------------|------------------------|---------------|---------------|---------------|
| Initial moisture content | 0% | 90% | 0% | 90% | 0% | 90% |
| Explosive spalling | No | No | No | No | No | No |
| Surface spalling | No | No | No | No | No | Yes |
| Surface temperature when the first damaged element appears (°C) | - | 470 | - | 380 | 390 | 310 |
| Surface temperature at mechanical failure (°C) | - | - | - | - | - | 330 |
| Time at mechanical failure (min) | - | - | - | - | - | 66 |
| Damage pattern before mechanical failure/until - 600 °C | | Fig. 8.51 (a) | | Fig. 8.51 (b) | Fig. 8.54 (a) | Fig. 8.54 (b) |

- **Normal-strength concrete** For NSC-40 with 0% initial moisture content, before the surface temperature reaches 600 °C, no divergence occurs in the non-linear mechanical analysis. It implies that no spalling occurs. The elements in the matrix are, however, damaged after the surface temperature reaches 390 °C after heating for 78 minutes. The damage pattern and the first principal stress when the surface temperature reaches 600 °C are shown in Fig. 8.54 (a) and Fig. 8.55 (a), respectively. As the coefficient of effective thermal expansion of the matrix is lower than that of the aggregate, the volume mismatch induced thermal stress can be clearly seen in Fig. 8.55 (a) (the red color in the figure), which causes the damage to the matrix.

For NSC-40 with 90% initial moisture content, the non-linear mechanical analysis fails to converge when the surface temperature reaches 330 °C after heating for 66 minutes. The damage pattern, the first effective principal stress, and the effective vapor pressure of the time step before divergence are shown in Fig. 8.54 (b), Fig. 8.55 (b), and Fig. 8.56, respectively. As can be seen from the damage pattern (Fig. 8.54 (b)), the mechanical failure of the sample is caused by partial surface layer breaking off. From the energy development shown in Fig. 8.57, it can be seen that the elastic strain energy of NSC-40 with 0% initial moisture content increases gradually with the increase of the surface temperature due to the volume mismatch between aggregates and the matrix. In the case of 90% initial moisture content, the energy increases dramatically with the increase of vapor pressure. When some elements fail after heating for around one hour, the energy drops due to the release of vapor pressure.

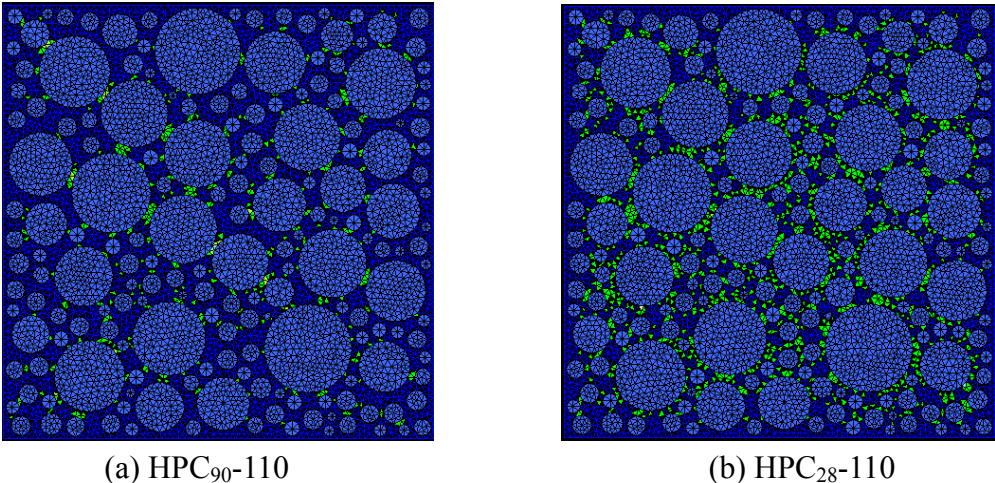


Fig. 8.51 Mechanical damage to HPC-110 with 90% initial moisture content when surface temperature reaches 600 °C under slow heating condition (5 °C/min) (No divergence occurs in the non-linear mechanical analysis, i.e., no spalling occurs).

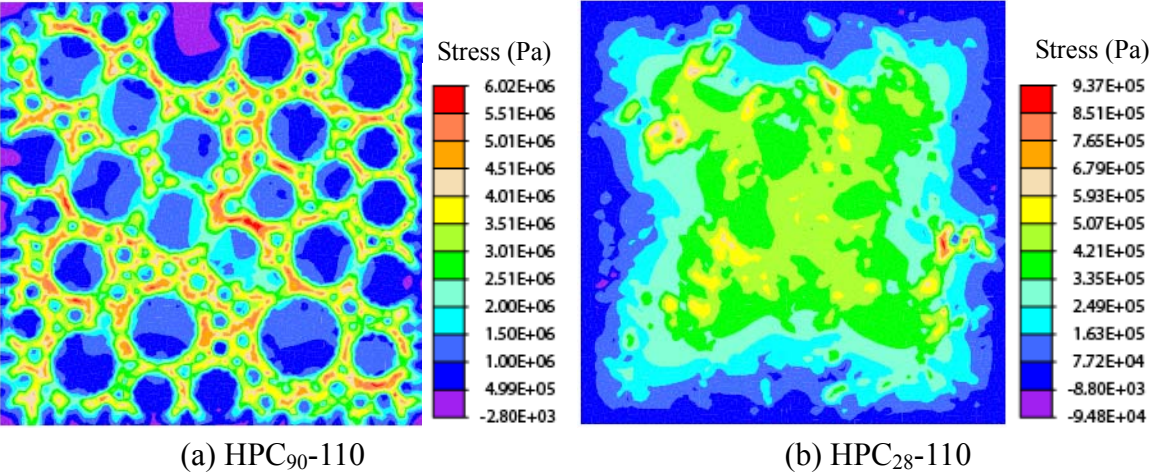


Fig. 8.52 Effective first principal stress of HPC-110 with 90% initial moisture content when surface temperature reaches 600 °C after heating for 116 minutes under slow heating condition (5 °C/min).

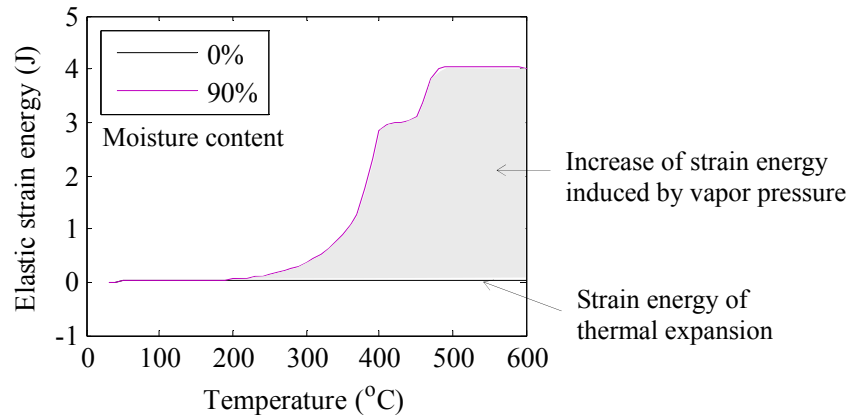
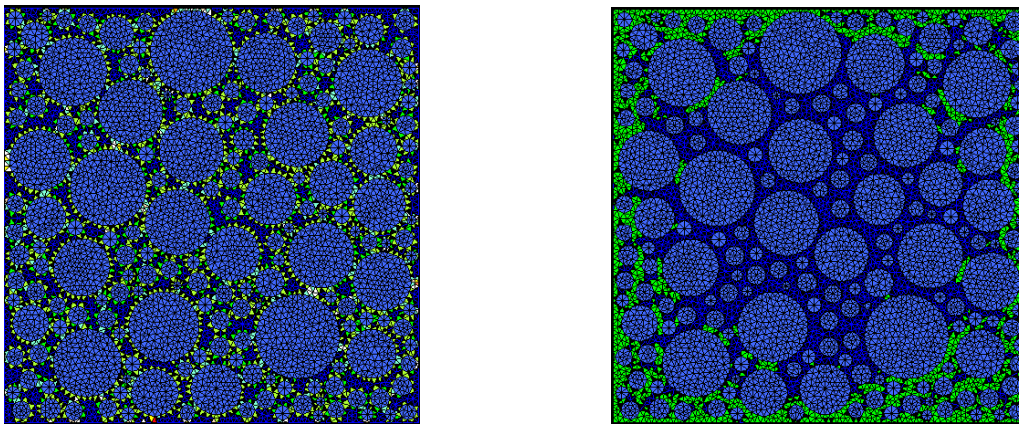
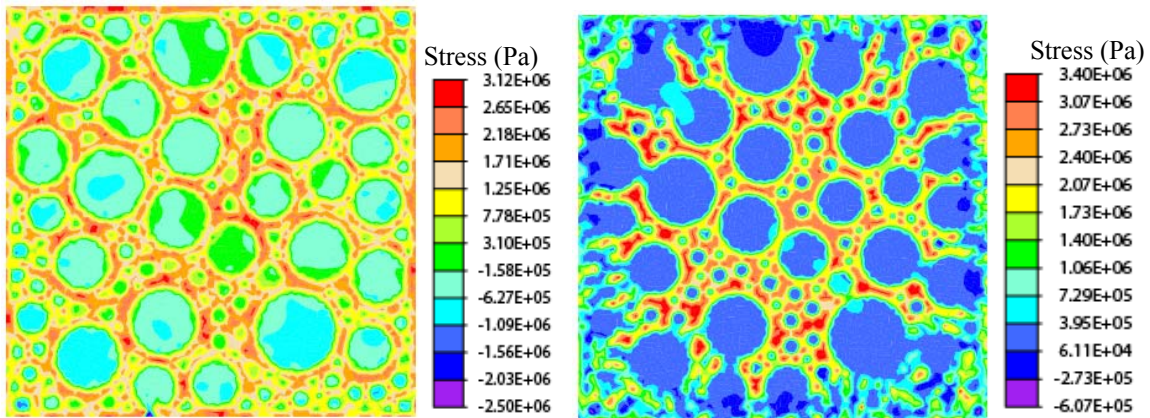


Fig. 8.53 Development of elastic strain energy in HPC₉₀₋₁₁₀ with 0% and 90% initial moisture content under slow heating condition (5 °C/min) (The strain energy induced only by thermal expansion is very low. This is attributed to the low thermal stress induced by the low temperature gradient of slow heating (Fig. 8.8 (c))).



(a) Surface T=600 °C, t=120 min (0%) (b) Surface T=330 °C, t=66 min (90%)

Fig. 8.54 Mechanical damage to NSC-40 with 0% (a) and 90% (b) initial moisture content under slow heating condition (5 °C/min).



(a) Surface T=600 °C, t=120 min (0%) (b) Surface T=330 °C, t=66 min (90%)

Fig. 8.55 Effective first principal stress of NSC-40 with 0% (a) and 90% (b) initial moisture content under slow heating condition (5 °C/min).

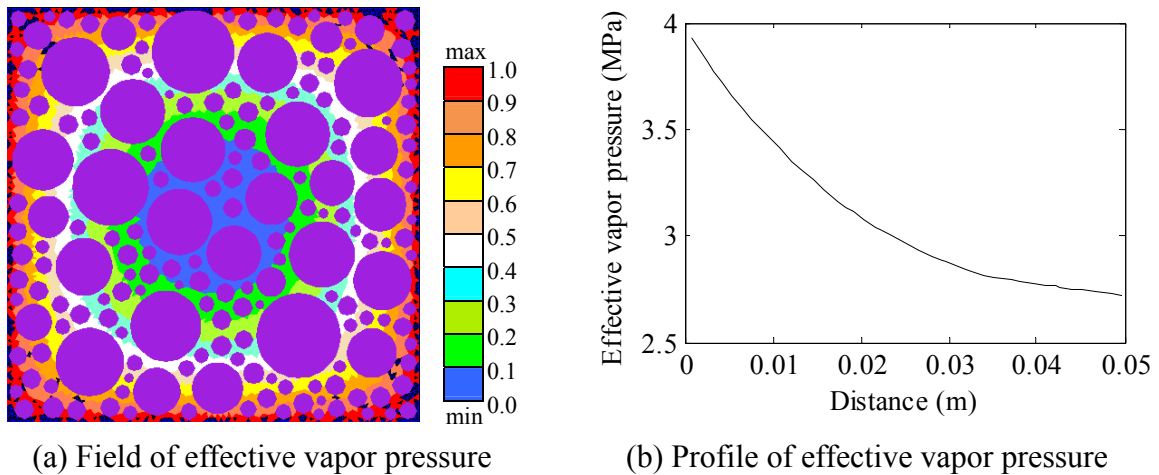


Fig. 8.56 Effective vapor pressure in NSC-40 with 90% initial moisture content when surface temperature reaches 330 °C after heating for 66 minutes under slow heating condition (5 °C/min).

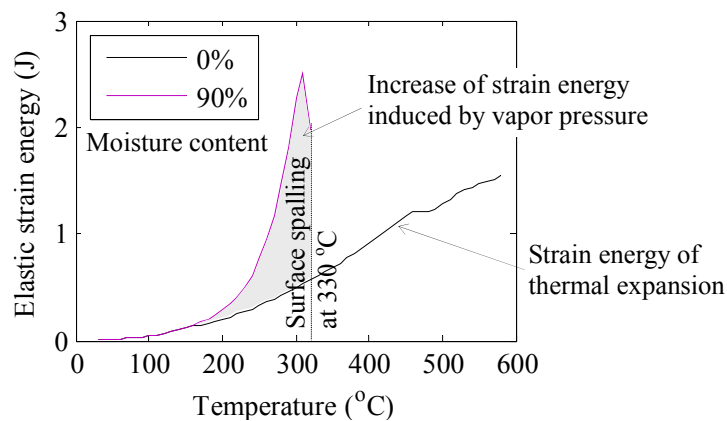


Fig. 8.57 Development of elastic strain energy in NSC-40 with 0% and 90% initial moisture content under slow heating condition (5 °C/min).

8.9 Summary and conclusions

In this chapter, the thermo-chemo-hydro-mechanical behaviour of the specimens of HPC and NSC with 0% and 90% initial moisture content in the experiments of Peng [2000] has been numerically studied at a meso-level. Different heating rates have been considered, i.e., fast heating (ISO 834 fire) and slow heating at the heating rates of 0.5 °C/min and 5 °C/min. The concrete specimens have been modeled as 2D plane strain two-phase composites. In the analysis, the predicted evolution of temperature field has been verified with the experimental results. The thermal variation of the material properties of the matrix, such as the permeability and the elastic modulus have been predicted according to the heating history. The vapor pressure in the matrix has been determined by the use of the steam tables and the moisture transport driven by the vapor pressure gradient has been analyzed. The mechanism of explosive fire spalling of HPC has been investigated. The role of the vapor pressure and the temperature gradient induced thermal stress in the mechanical damage has been quantitatively analyzed. The development of the elastic strain energy of the heated concrete has also been studied.

Owing to the lack of the experimental data on the effective expansion coefficient of the used material in Peng's test [Peng, 2000], different values of the effective expansion coefficient have been used in the mechanism study of fire spalling. It has been shown by the analysis results that this method is feasible for the investigation of the mechanism of fire spalling. According to the results of the numerical analysis, the following conclusions can be drawn:

- The temperature gradients generated in concrete under the ISO 834 fire condition are much higher than that under slow heating conditions (Fig. 8.8).
- Under the ISO 834 fire condition, before the surface temperature reaches 500 °C, only little CH decomposed and the depth of the decomposition in concrete specimens is around 3 mm (Section 8.5).
- The intrinsic permeability of the matrix can only be increased much after the capillary porosity exceeds the percolation threshold (Section 8.6.1).
- The water saturation degree of both HPC and NSC with 90% initial moisture content is high before the temperature reaches the critical point (374.15 °C) (Fig. 8.17 (a, b) and Fig. 8.18).
- For HPC, the moisture content doesn't change much before the capillary porosity exceeds the percolation threshold for both fast heating and slow heating. For NSC, the moisture escapes fast after the temperature reaches the critical point.
- The vapor pressure resides in the outer layer of the concrete specimens until the surface temperature reaches 600 °C under the ISO 834 fire condition, while it resides in the central region of the specimen under the slow heating condition.
- The mechanical damage caused only by vapor pressure and only by thermal expansion is different. The damage caused by the former lies in the region where the vapor pressure is present, however, the damage caused by the latter goes to deeper region in the specimen with the decrease of the effective thermal expansion coefficient under the ISO 834 fire condition.
- The temperature gradient induced thermal stress plays a dominate role in fire spalling of the HPC specimen.
- Fire spalling of the HPC specimen is not caused by the moisture-clog phenomenon.
- Under the ISO 834 fire condition, the thermal expansion induced elastic strain energy of specimens of both HPC and NSC increases to a peak value when the surface temperature reaches around 470 °C and then decreases with the increase of the heating temperature.
- From the energy perspective, the thermal expansion induced elastic strain energy plays a dominant role in the fire spalling of HPC specimens.
- Under the slow heating condition, the mechanical damage of NSC with 0% initial moisture content is caused by volume mismatch between the aggregate and the matrix.
- For both slow heating and fast heating, partial surface layer breaking off caused by vapor pressure occurs to NSC specimens with high initial moisture content.
- For HPC with 90% initial moisture content, the damage pattern under the slow heating condition is different from that under the fire condition. In the latter case, the damage

is clustered in certain regions, while, in the former case, the damage is distributed in the matrix.

- Under slow heating conditions, for HPC with high initial moisture content, the elastic strain energy is mainly induced by vapor pressure.
- Under slow heating conditions, as most of the moisture is still trapped in the matrix, the non-spalling behavior of HPC specimens with high initial moisture content is attributed to the low thermal stress/low elastic strain energy induced by low temperature gradient.

Chapter 9

Conclusions and prospects

Under high temperature conditions, such as fire, HPC is prone to spalling. Two types of spalling are often encountered in reality: surface spalling/scaling and explosive spalling. For HPC, explosive spalling has been frequently reported. Two hypotheses have been proposed to explain spalling of heated concrete: the vapor pressure mechanism and the temperature gradient induced thermal stress mechanism. However, the quantitative analysis of the spalling mechanism is still inadequate and the spalling mechanism is still not clear (Chapters 1 and 2). The first goal of this thesis is to investigate the spalling mechanism in a quantitative manner. In view of the fact that the heating history effect on the material properties hasn't been considered in the existing models, the second goal of this thesis is to propose a heating history-based material-property prediction model to investigate the spalling mechanism. The third goal of this thesis is to quantitatively study the influencing factors of spalling, such as the moisture content and the heating rate.

To achieve the aforementioned goals, the thermo-chemo-hydro-mechanical behavior of 100 mm cube specimens of both HPC and NSC with 0% and 90% moisture content has been numerically studied. In the study, the cube specimen has been modeled as a 2D plane strain two-phase (aggregate and matrix) composite. For the analysis of the heating rate effect on spalling, both fast heating (ISO 834 fire) and slow heating (0.5 °C/min and 5 °C/min) have been considered. The highest heating temperature is 600 °C. In the analysis, the temperature field has been numerically determined. The thermal decomposition of the matrix and the variation of material properties of the matrix, such as the permeability and the elastic modulus, have been predicted according to the heating history. The vapor pressure build-up and the moisture transport have been analyzed. The mechanical analysis incorporating the vapor pressure has been conducted. Although the cube concrete specimens have been modeled in two-dimension, the results show that the spalling mechanism has been reasonably explained. The specific features, the conclusions, and the prospects are shown in the following sections.

9.1 Specific features

In this thesis, the following contributions have been made to the existing techniques for the computational modeling of thermal damage of heated concrete:

- The heating history-based prediction of the thermal decomposition of hardened cement paste (Chapter 4). As the material properties are determined by the microstructure and the microstructure is closely related to the thermal decomposition process, it is of fundamental importance to appropriately evaluate the decomposition in the fire spalling

analysis of heated concrete. However, there is no such model available in the literature.

- The heating history-based prediction of material properties of hardened cement paste, such as the permeability and the elastic modulus (Chapters 6 and 7). In most existing models, material properties are taken as temperature dependent according to the experimental results. However, in experiments, usually the heating rate is low and the heating duration is long. A significant drying shrinkage of the matrix might be induced and the material properties could be affected markedly. As fire spalling occurs in the first several minutes of heating and the shrinkage effect is negligibly small, the actual material properties under the fire condition can be much different from the temperature-dependent ones. In this thesis, the material properties have been predicted based on the heating history-based decomposition analysis.
- The prediction of vapor pressure using steam tables with the consideration of the coarsening and moisture release effect of thermal decomposition of the matrix (Chapter 5). The ideal gas equation is usually adopted for the determination of vapor pressure in existing models. However, when the moisture saturation degree is high, water vapor behaves much differently from ideal gases, resulting in a large deviation. When the steam tables are used, better predictions can be expected.
- The meso-level quantitative analysis of spalling (Chapter 8). In most of the existing models, spalling is analyzed at the macro-level, where concrete is treated as a homogenous material. Some details are, therefore, missing for the spalling investigation, such as the aggregate influence on the moisture transport, the decomposition of the matrix, the damage induced by the volume mismatch between aggregates and the matrix, the vapor pressure effect on the stress/strain field, etc.
- The energy-based analysis of the spalling mechanism (Chapter 8). The interpretation of the mechanism of fire spalling from an energy perspective is seldom reported in the literature.

9.2 Conclusions

From the two-dimensional spalling analysis of the heated 100 mm cube specimens, several conclusions can be drawn. It is emphasized, however, that for validating the conclusions, only little experimental data were considered. Still, the conclusions are considered relevant and in line with other reported data.

- The temperature gradient induced thermal stress/elastic strain energy plays a dominant role in explosive fire spalling of HPC.
- The fire spalling of the HPC specimen is not caused by the moisture-clog phenomenon.
- The pattern of damage caused only by vapor pressure is different from that caused only by thermal expansion. For the former, the damage lies in the region where the vapor pressure exists, while for the latter, the damage goes to the deeper inner region in the specimen with the decrease of the thermal expansion coefficient under the fire condition.
- For the NSC specimen with 0% initial moisture content, the mechanical damage is caused by the volume mismatch between aggregates and the matrix under slow heating

conditions.

- For both slow heating and fast heating, partial surface layer breaking off caused by vapor pressure occurs to the NSC specimens with high initial moisture content.
- Under slow heating conditions, as most of the moisture is still trapped in the matrix, the non-spalling behavior of HPC specimens with high moisture content is attributed to the low thermal stress/elastic strain energy induced by low temperature gradient.

Under the ISO 834 fire condition, in the early stage of heating, the aforementioned conclusions can be generalized for HPC and NSC structural elements as follows:

For HPC structural elements:

- The temperature gradient induced thermal stress plays a dominant role in fire spalling.
- Vapor pressure exists in the outer layer of the elements.
- Vapor pressure can only cause local damage to the elements.
- Decreasing the expansion extent of heated concrete is more efficient than working out measures for releasing vapor pressure in preventing concrete from spalling.

For NSC structural elements:

- The non-spalling (explosive) behavior is attributed to the relatively low expansion extent of NSC compared with HPC.
- When the moisture content is high, local damage caused by vapor pressure will occur.

9.3 Prospects

Although in this thesis several aspects have been considered in the meso-level analysis of fire spalling, to get a better picture of the thermo-mechanical behavior of heated concrete, the following aspects need to be considered in the future work:

- The effect of water expansion on the mechanical damage to concrete. In this thesis, the expansion of water with increasing temperature has been assumed negligible (90% initial moisture content). However, when concrete is fully saturated (100% initial moisture content), the expansion might exert some effect on the mechanical damage.
- The upper bound of the build-up vapor pressure in heated concrete. Owing to the lack of the experimental data, an upper bound of the build-up vapor pressure in the pore system of heated concrete has been assumed in this thesis (35 MPa). This aspect needs to be investigated further.
- The effect of vapor pressure on the thermal decomposition kinetics of hardened cement paste. This effect has been considered negligible in this thesis. The effect need to be quantitatively evaluated and incorporated into the decomposition analysis.
- The drying shrinkage effect on material properties, such as the elastic modulus and the permeability. Drying shrinkage will cause additional microcracks to concrete and thus will cause further material degradation in addition to the thermal decomposition effect. In this thesis, since the heating duration before spalling is very short (several minutes), the shrinkage effect has been considered negligibly small.

- The moisture diffusion. For the fire spalling analysis, as the heating duration before spalling is very short, the effect of moisture diffusion on the moisture content has been assumed negligible. However, for prolonged heating, the effect should be considered.
- The initial moisture distribution. The initial moisture distribution might not be uniform in concrete, which depends on the environment where the concrete stored and the pretreatment of concrete.
- The 3D analysis. To precisely predict the behavior of heated concrete, 3D modeling is needed.
- The fully coupled model. In this thesis, the coupled thermo-chemo-hydro-mechanical reaction of concrete to high temperatures has been modeled in the staggered way. A fully coupled model will be considered in the future work.
- The heat sink effect of the vaporization of water and the thermal decomposition of concrete on the temperature field determination. In this thesis, this effect has been assumed negligible and the predicted evolution of temperature correlates well with the experimental results. However, in other cases, such as prolonged heating, the heat sink might exert some effect on the temperature distribution.
- The thermal creep modeling of heated concrete. Although thermal creep has been taken into account implicitly in the spalling analysis in this thesis, an explicit model will be helpful in better understanding the thermo-mechanical behavior of heated concrete, especially under longer heating conditions.
- The ITZ effect. In this thesis, the ITZ effect on the thermo-hydro-mechanical behavior of heated HPC has been assumed negligible. However, for NSC, the ITZ effect should be considered.
- Macro-level fire spalling investigation. The proposed method needs to be scaled up for the analysis of structural elements, where the effect of reinforcing steel bars and the external load need to be considered.

References

- Aitcin, P. C. (1998). *High Performance Concrete*. E & FN SPON Press, London.
- Ali, F., Nadjai, A., and Choi, S. (2010). Numerical and experimental investigation of the behavior of high strength concrete columns in fire, *Engineering Structures*, Vol. 32, p. 1236-1243.
- Anderberg, Y. (1997). Spalling phenomena of HPC and OC, *Proceedings of International Workshop on Fire Performance of High-Strength Concrete*, NIST, Gaithersburg, MD, p. 69-73.
- Anderberg, Y. and Thelandersson, S. (1976). *Stress and deformation characteristics of concrete, 2-experimental investigation and material behaviour model*, Bulletin 54, Lund institute of technology, Lund, Sweden.
- Bamforth, P. B. (1987). The relationship between permeability coefficients for concrete obtained using liquid and gas, *Magazine of Concrete Research*, Vol. 39(138), p. 3-11.
- Bažant, Z. P. (1986). Mechanics of distributed cracking, *Applied Mechanics Reviews*, Vol. 39(5), p. 675-705.
- Bažant, Z. P. (1997). Analysis of pore pressure, thermal stress and fracture in rapidly heated concrete, *Proceedings of International Workshop on Fire Performance of High-Strength Concrete*, NIST, Gaithersburg, MD, p. 155-164.
- Bažant, Z. P. and Kaplan, M. F. (1996). *Concrete at High Temperatures: Material Properties and Mathematical Models*, Longman Group Ltd, England.
- Bažant, Z. P. and Thonguthai, W. (1978). Pore pressure and drying of concrete at high temperature, *Journal of the Engineering Mechanics Division*, ASCE, Vol. 104(5), p. 1059-1079.
- Behnood, A. and Ziari, H. (2008). Effects of silica fume addition and water to cement ratio on the properties of high-strength concrete after exposure to high temperatures, *Cement & Concrete Composites*, Vol. 30, p. 106-112.
- Benes, M. and Mayer, P. (2008). Coupled model of hygro-thermal behavior of concrete during fire, *Journal of Computational and Applied Mathematics*, Vol. 218, p. 12-20.
- Bentz, D. P. (2000). Fibers, percolation, and spalling of high-performance concrete, *ACI Materials Journal*, Vol. 97(3), p. 351-359.
- Bentz, D. P. and Garboczi, E. J. (1991). Percolation of phases in a three-dimensional cement paste microstructural model, *Cement and Concrete Research*, Vol. 21(2-3), p. 325-344.
- Berryman, J. G. (1992). Effective stress for transport properties of inhomogeneous porous rock, *Journal of Geophysical Research*, Vol. 97(B12), p. 17409-17424.
- Biolzi, L., Cattaneo, S., and Rosati, G. (2008). Evaluating residual properties of thermally damaged concrete, *Cement & Concrete Composites*, Vol. 30(10), p. 907-916.

- Biot, M. A. (1941). General theory of three-dimensional consolidation, *Journal of Applied Physics*, Vol. 12, p.155-164.
- Bratina, S., Saje, M., and Planinc, I. (2007). The effects of different strain contributions on the response of RC beams in fire, *Engineering Structures*, Vol. 29, p. 418–430.
- Browne, R. D. (1967). Properties of concrete in reactor vessels, *Proceedings of Conference on Prestressed Concrete Pressure Vessels*, Institute of Civil Engineers, London, p. 13-31 (In Bažant and Kaplan (1996)).
- Caldas, R. B., Sousa Jr., J. B. M., and Fakury, R. H. (2010). Interaction diagrams for reinforced concrete sections subjected to fire, *Engineering Structures*, Vol. 32, p. 2832-2838.
- Caré, S. (2008). Effect of temperature on porosity and on chloride diffusion in cement pastes, *Construction and Building Materials*, Vol. 22, p. 1560-1573.
- Chan, S. Y. N., Peng, G. F., and Anson, M. (1999). Fire Behavior of high-performance concrete made with silica fume at various moisture contents, *ACI Materials Journal*, Vol. 96(3), p. 405-411.
- Chiang, C. H. and Yang, C. C. (2005). Artificial neural networks in prediction of concrete strength reduction due to high temperature, *ACI Materials Journal*, Vol. 102(2), p. 93-102.
- Christensen, R. M. (1979). *Mechanics of composite materials*, John Wiley & Sons, NewYork.
- Chung, J. H. and Consolazio, G. R. (2005). Numerical modeling of transport phenomena in reinforced concrete exposed to elevated temperatures, *Cement and Concrete Research*, Vol. 35, p. 597-608.
- Chung, J. H., Consolazio, G. R., and McVay, M. C. (2006). Finite element stress analysis of a reinforced high-strength concrete column in severe fires, *Computers and Structures*, Vol. 84, p. 1338-1352.
- Colombo, A. G. (2001). *Lessons Learnt from Tunnel Accidents*. EUR Report.
- Consolazio, G. R., McVay, M. C., and Rish, J. W. (1998). Measurement and prediction of pore pressures in saturated cement mortar subjected to radiant heating. *ACI Materials Journal*, Vol. 95(5), p. 525-536.
- Coussy, O. (2004). *Poromechanics*, John Wiley & Sons Ltd, England.
- Cui, L. and Cahyadi, J. H. (2001). Permeability and pore structure of OPC paste, *Cement and Concrete Research*, Vol. 31(2), p. 277-282.
- de Moraes, M. V. G., Pliya, P., Noumowé, A., Beaucour, A. L., and Ortola, S. (2010). Contribution to the explanation of the spalling of small specimen without any mechanical restraint exposed to high temperature, *Nuclear Engineering and Design*, Vol. 240(10), p. 2655-2663.
- Dwaikat, M. B. and Kodur, V. K. R. (2009). Hydrothermal model for predicting fire-induced spalling in concrete structural systems, *Fire Safety Journal*, Vol. 44, p. 425-434.
- Fares, H., Remond, S., Noumowe, A., and Cousture, A. (2010). High temperature behaviour of self-consolidating concrete microstructure and physicochemical properties, *Cement and Concrete Research*, Vol. 40, p. 488-496.
- Feldman, R. F. (1972). Factors affecting young's modulus-porosity relation of hydrated Portland cement compacts, *Cement and Concrete Research*. Vol. 2, p. 375-386.
- Feng, N. Q. (1992). *High-Strength Concrete Technology*. China Construction Materials Industry Press, Beijing, China.
- Fu, Y. F., Wong, Y. L., Tang, C. A., and Poon, C. S. (2004a). Thermal induced stress and associated cracking in cement-based composite at elevated temperatures-Part I: thermal cracking around single inclusions, *Cement & Concrete Composites*, Vol. 26, p. 99-111.

- Fu, Y. F., Wong, Y. L., Tang, C. A., and Poon, C. S. (2004b). Thermal induced stress and associated cracking in cement-based composite at elevated temperatures-Part II: thermal cracking around multiple inclusions, *Cement & Concrete Composites*, Vol. 26, p. 113-126.
- Fu, Y. F., Wong, Y. L., Poon, C. S., Tang, C. A., and Lin, P. (2004c). Experimental study of micro/macro crack development and stress-strain relations of cement-based composite materials at elevated temperatures, *Cement and Concrete Research*, Vol. 34, p. 789-797.
- Fu, Y. F., Wong, Y. L., Poon, C. S., and Tang, C. A. (2007). Numerical tests of thermal cracking induced by temperature gradient in cement-based composites under thermal loads, *Cement & Concrete Composites*, Vol. 29, p. 103-116.
- Galwey, A. K. and Brown, M. E. (1999). *Thermal decomposition of ionic solids*, Elsevier, Amsterdam.
- Gawin, D., Majorana, C. E., and Schrefler, B. A. (1999). Numerical analysis of hygro-thermic behaviour and damage of concrete at high temperature, *Mechanics of Cohesive-Frictional Materials*, Vol. 4(1), p. 37-74.
- Gawin, D., Pesavento, F., and Schrefler, B. A. (2002). Simulation of damage permeability coupling in hygro-thermo-mechanical analysis of concrete at high temperature, *Communications in Numerical Methods in Engineering*, Vol. 18, p. 113-119.
- Gawin, D., Pesavento, F., and Schrefler, B. A. (2003). Modelling of hygro-thermal behaviour of concrete at high temperature with thermo-chemical and mechanical material degradation, *Computer Methods in Applied Mechanics and Engineering*, Vol. 192, p. 1731-1771.
- Gawin, D., Pesavento, F., and Schrefler, B. A. (2004). Modelling of deformations of high strength concrete at elevated temperatures, *Materials and Structures*, Vol. 37, p. 218-236.
- Gawin, D., Pesavento, F., and Schrefler, B. A. (2006). Towards prediction of the thermal spalling risk through a multi-phase porous media model of concrete, *Computer Methods in Applied Mechanics and Engineering*, Vol. 195, p. 5707-5729.
- Ghabezloo, S., Sulem, J., and Saint-Marc, J. (2009). The effect of undrained heating on a fluid-saturated hardened cement paste, *Cement and Concrete Research*, Vol. 39(1), p. 54-64.
- Grondin, F., Dumontet, H., Hamida, A. B., Mounajed, G., and Boussa, H. (2007). Multi-scales modeling for the behavior of damaged concrete, *Cement and Concrete Research*, Vol. 37, p. 1453-1462.
- Haecker, C. J., Garboczi, E. J., Bullard, J. W., Bohn, R. B., Sun, Z., Shah, S. P., and Voigt, T. (2005). Modeling the linear elastic properties of Portland cement paste, *Cement and Concrete Research*, Vol. 35(10), p. 1948-1960.
- Hansen, T. C. (1986). Physical structure of hardened cement paste: a classical approach, *Materials and Structures*, Vol. 19(6), p. 423-436.
- Helmuth, R. A., and Turk, D. H. (1966). Elastic moduli of hardened Portland cement and tricalcium silicate pastes: effect of porosity, *Proceedings of Symposium on Structure of Portland Cement Paste and Concrete*, Highway Research Board, Washington, p. 135-144.
- Hertz, K. D. (1992). Danish investigations on silica fume concretes at elevated temperatures, *ACI Materials Journal*, Vol. 89(4), p. 345-347.
- Hsu, T. R. (1986). *The finite element method in thermomechanics*, Allen & Unwin, Ltd, Boston.
- Hu, H. T. and Dong, Y. L. (2002). Experimental research on the transient thermal strain of high strength concrete at elevated temperature, *Journal of Building Structures*, Vol. 23(4), p. 32-35 (in Chinese).
- Huang, Z. H., Burgess, I. W., and Plank, R. J. (1999). Nonlinear analysis of reinforced concrete slabs subjected to fire, *ACI Structural Journal*, Vol. 96(1), p. 127-135.

- Huang, Z. H., Burgess, I. W., and Plank, R. J. (2003a). Modeling membrane action of concrete slabs in composite buildings in fire. I: Theoretical development, *Journal of Structural Engineering*, Vol. 129(8), p. 1093-1102.
- Huang, Z. H., Burgess, I. W., and Plank, R. J. (2003b). Modeling membrane action of concrete slabs in composite buildings in fire. II: Validations, *Journal of Structural Engineering*, Vol. 129(8), p. 1103-1112.
- Huang, Z. H. (2010). The behaviour of reinforced concrete slabs in fire, *Fire Safety Journal*, Vol. 45, p. 271-282.
- Hurst, J. P. and Ahmed, G. N. (1998). Validation and application of a computer model for predicting the thermal response of concrete slabs subjected to fire, *ACI Structural Journal*, Vol. 95(5), p. 480-487.
- Husem, M. (2006). The effects of high temperature on compressive and flexural strengths of ordinary and high-performance concrete, *Fire Safety Journal*, Vol. 41(2), p. 155-163.
- Ichikawa, Y. and England, G. L. (2004). Prediction of moisture migration and pore pressure build-up in concrete at high temperatures, *Nuclear Engineering and Design*, Vol. 228, p. 245-259.
- Kalifa, P., Menneteau, F. D., and Quenard, D. (2000). Spalling and pore pressure in HPC at high temperatures, *Cement and Concrete Research*, Vol. 30, p. 1915-1927.
- Katz, A. J. and Thompson, A. H. (1986). Quantitative prediction of permeability in porous rock, *Physical Review B*, Vol. 34(11), p. 8179-8181.
- Khoury, G. A., Grainger, B. N., and Sullivan, P. J. E. (1985). Strain of concrete during first heating to 600 °C under load, *Magazine of Concrete Research*, Vol. 37(133), p. 195-215.
- Khoury, G. A., Majorana, C. E., Pesavento, F., and Schrefler, B. A. (2002). Modelling of heated concrete, *Magazine of concrete research*, Vol. 54(2), p. 77-101.
- Klinkenberg, L. J. (1941). The permeability of porous media to liquids and gases, *Drilling and Production Practice*, American Petroleum Institute, Washington DC, USA, p. 200-213.
- Knaack, A. M., Kurama, Y. C., and Kirkner, D. J. (2010). Compressive strength relationships for concrete under elevated temperatures, *ACI Materials Journal*, Vol. 107(2), p. 164-175.
- Knack, I. (2009). New PP-fiber with exceptional melting characteristics for improved fire protection in concrete building, *Proceedings of 1st International Workshop on Concrete Spalling due to Fire Exposure*, RILEM, Leipzig, Germany, p. 238-247.
- Kodur, V. K. R. and Dwaikat, M. (2008a). A numerical model for predicting the fire resistance of reinforced concrete beam, *Cement & Concrete Composites*, Vol. 30, p. 431-443.
- Kodur, V. K. R., Dwaikat, M., and Dwaikat, M. B. (2008b). High-temperature properties of concrete for fire resistance modeling of structures, *ACI Materials Journal*, Vol. 105(5), p.517-527.
- Kodur, V. K. R., Dwaikat, M., and Raut, N. (2009). Macroscopic FE model for tracing the fire response of reinforced concrete structures. *Engineering Structures*, Vol. 31, p. 2368-2379.
- Kolmar, W. and Mehlhorn, G. (1984). Comparison of shear stiffness formulations for cracked reinforced concrete elements, *Proceedings of the International Conference on Computer Aided Analysis and Design of Concrete Structures*, p. 133-147.
- Komarovskii, A. N. (1965). *Design of Nuclear Plants*, 2nd edition, Atomizdat, Moscow, Chapter 7 (In Bažant and Kaplan (1996)).
- Komonen, J. and Penttala, V. (2003). Effects of high temperature on the pore structure and strength of plain and polypropylene fiber reinforced cement pastes, *Fire Technology*, Vol. 39(1), p. 23-34.
- Kupfer, H. B., Hildorf, H. K., and Rusch, H. (1969). Behavior of concrete under biaxial stresses, *ACI*

- Materials Journal*, Vol. 66(8), p. 656-666.
- Lee, J., Xi, Y., Willam, K., and Jung, Y. (2009). A multiscale model for modulus of elasticity of concrete at high temperatures, *Cement and Concrete Research*, Vol. 39(9), p. 754-762.
- Li, X. K., Li, R. T., and Schrefler, B. A. (2006). A coupled chemo-thermo-hygro-mechanical model of concrete at high temperature and failure analysis, *International Journal for Numerical and Analytical Methods in Geomechanics*, Vol. 30, p. 635-681.
- Lim, L., Buchanan, A., Moss, P., and Franssen, J. M. (2004). Numerical modelling of two-way reinforced concrete slabs in fire, *Engineering Structures*, Vol. 26, p. 1081-1091.
- Lin, W. M., Lin, T. D., and Powers-Couche, L. J. (1996). Microstructures of fire-damaged concrete, *ACI Materials Journal*, Vol. 93(3), p. 199-205.
- Liu, X. (2006). *Microstructural Investigation of Self-Compacting Concrete and High-Performance Concrete during Hydration and after Exposure to High Temperatures*. Ph.D. Thesis, Ghent University.
- Lu, P., Sun, G., and Young, J. F. (1993). Phase composition of hydrated DSP cement pastes, *Journal of the American Ceramic Society*, Vol. 76(4), p. 1003-1007.
- Luo, X., Sun, W., and Chan, S. Y. N. (2000). Effect of heating and cooling regimes on residual strength and microstructure of normal and high-performance concrete, *Cement and Concrete Research*, Vol. 30, p. 379-383.
- Majorana, C. E., Salomoni, V., and Schrefler, B. A. (1998). Hygrothermal and mechanical model of concrete at high temperature, *Materials and Structures*, Vol. 31, p. 378-386.
- Majumdar, P., Gupta, A., and Marchertas, A. (1995). Moisture propagation and resulting stress in heated concrete walls, *Nuclear Engineering and Design*, Vol. 156, p. 147-158.
- Majumdar, P. and Marchertas, A. (1997). Heat, moisture transport, and induced stresses in porous materials under rapid heating, *Numerical Heat Transfer, Part A: Applications*, Vol. 32(2), p. 111-130.
- Masse, S., Vetter, G., Boch, P., and Haehnel, C. (2002). Elastic modulus changes in cementitious materials submitted to thermal treatments up to 1000 °C, *Advances in Cement Research*, Vol. 14(4), p. 169-177.
- Mazars, J. and Pyaudier-Cabot, G. (1989). Continuum damage theory-application to concrete, *Journal of Engineering Mechanics*, ASCE, Vol. 115(2), p. 345-365.
- McLachlan, D. S. (1988). Measurement and analysis of a model dual-conductivity medium using a generalized effective-medium theory, *Journal of Physics C: Solid State Physics*, Vol. 21(8), p. 1521-1532.
- Meyer, C. A., McClintock, R. B., Silvestri, G. J., and Spencer, R.C. (1967). *ASME Steam Tables*, The American society of mechanical engineers, New York.
- Mindeguia, J. C., Pimienta, P., Noumowé, A., and Kanema, M. (2010). Temperature, pore pressure and mass variation of concrete subjected to high temperature-experimental and numerical discussion on spalling risk, *Cement and Concrete Research*, Vol. 40, p. 477-487.
- Moran, M. J. and Shapiro, H. N. (2008). *Fundamentals of Engineering Thermodynamics*, John Wiley & Sons, Ltd, England.
- Mounajed, G. and Obeid, W. (2004). A new coupling F.E. model for the simulation of thermally-mechanical behaviour of concretes at high temperatures, *Materials and Structures*, Vol. 37, p. 422-432.
- Neville, A. M. (1995). *Properties of Concrete*, Fourth edition, Longman Group Ltd, England.

- Ngo, D. and Scordelis, A. C. (1967). Finite element analysis of reinforced concrete beams, *ACI Structural Journal*, Vol. 64, p. 152-163.
- Noumowe, A. N., Siddique, R., and Debicki, G. (2009). Permeability of high-performance concrete subjected to elevated temperature (600 °C), *Construction and Building Materials*, Vol. 23, p. 1855-1861.
- Nyame, B. K. and Illston, J. M. (1981). Relationships between permeability and pore structure of hardened cement paste, *Magazine of Concrete Research*, Vol. 33(116), p. 139-146.
- Parrot, L. J. and Killoh, D. C. (1984). Prediction of cement hydration, *British Ceramic Proceedings*, Vol. 35, p. 41-53.
- Peng, G. F. (2000). *Evaluation of fire damage to high performance concrete*. Ph.D. Thesis, Hong Kong Polytechnic University.
- Peng, G. F. and Huang, Z. S. (2008). Change in microstructure of hardened cement paste subjected to elevated temperatures, *Construction and Building Materials*, Vol. 22, p. 593-599.
- Pereira, F., Pistol, K., Korzen, M., Weise, F., Pimienta, P., Carré, H., and Huismann, S. (2011). Monitoring of fire damage processes in concrete by pore pressure and acoustic emission measurements, *Proceedings of 2nd International Workshop on Concrete Spalling due to Fire Exposure*, RILEM, Delft, The Netherlands, p. 69-77.
- Phan, L. T. and Carino, N. J. (1998). Review of mechanical properties of HSC at elevated temperature, *Journal of Materials in Civil Engineering*, ASCE, Vol. 10(1), p. 58-64.
- Phan, L. T. and Carino, N. J. (2002). Effects of test conditions and mixture proportions on behavior of high-strength concrete exposed to high temperatures, *ACI Materials Journal*, Vol. 99(1), p. 54-66.
- Piasta, J., Sawicz, Z., and Rudzinski, L. (1984). Changes in the structure of hardened cement paste due to high temperature, *Materials and constructions*, Vol. 17(100), p. 291-296.
- Pont, S. D., Schrefler, B. A., and Ehrlacher, A. (2005a). Experimental and finite element analysis of a hollow cylinder submitted to high temperatures, *Materials and Structures*, Vol. 38, p. 681-690.
- Pont, S. D., Schrefler, B. A., and Ehrlacher, A. (2005b). Intrinsic permeability evolution in high temperature concrete: an experimental and numerical analysis, *Transport in Porous Media*, Vol. 60, p. 43-74.
- Pont, S. D., Meftah, F., and Schrefler, B. A. (2011). Modeling concrete under severe conditions as a multiphase material, *Nuclear engineering and design*, Vol. 241(3), p. 562-572.
- Pourchez, J., Valdivieso, F., Grosseau, P., Guyonnet, R., and Guilhot, B. (2006). Kinetic modelling of the thermal decomposition of Ettringite into metaettringite, *Cement and Concrete Research*, Vol. 36, p. 2054-2060.
- Powers, T. C. (1958). Structure and physical properties of hardened Portland cement paste, *Journal of the American Ceramic Society*, Vol. 41(1), p. 1-6.
- Powers, T. C., Copeland, L. E., and Mann, H. M. (1955). Permeability of Portland cement paste, *Journal of the American Concrete Institute*, Vol. 51(3), p. 285-298.
- Rao, G. A. and Prasad, B. K. R. (2002). Fracture energy and softening behaviour of high-strength concrete, *Cement and Concrete Research*, Vol. 32, p. 247-252.
- Rashid, Y. R. (1968). Ultimate strength analysis prestressed concrete pressure vessels, *Nuclear Engineering and Design*, Vol. 7, p. 334-344.
- Rots, J. G. (1988). *Computational modeling of concrete fracture*. Ph.D. Thesis, Delft University of Technology.
- Rots, J. G. (1991). Smearred and discrete representations of localized fracture, *International Journal of*

- Fracture*, Vol. 51, p. 45-59.
- Sadaoui, A. and Khennane, A. (2009). Effect of transient creep on the behaviour of reinforced concrete columns in fire, *Engineering Structures*, Vol. 31, p. 2203-2208.
- Sanjayan, G. and Stocks, L. J. (1993). Spalling of high-strength silica fume concrete in fire, *ACI Materials Journal*, Vol. 90(2), p. 170-173.
- Schlengen, E. and van Mier, J. G. M. (1992). Micromechanical Analysis of Fracture of Concrete, *International Journal of Damage Mechanics*, Vol. 1, p. 435-454.
- Schneider, U. (1998). Concrete at high temperatures-a general review, *Fire Safety Journal*, Vol. 13, p. 55-68.
- Schrefler, B. A., Brunello, P., Gawin, D., Majorana, C. E., and Pesavento, F. (2002). Concrete at high temperature with application to tunnel fire, *Computational Mechanics*, Vol. 29, p. 43-51.
- Schrefler, B. A., Khoury, G. A., Gawin, D., and Majorana, C. E. (2002). Thermo-hydro-mechanical modelling of high performance concrete at high temperatures, *Engineering Computations*, Vol. 19(7), p. 787-819.
- Shimada, Y. and Young, J. F. (2001). Structural changes during thermal dehydration of Ettringite, *Advances in Cement Research*, Vol. 13(2), p. 77-81.
- Simo, J. C., Ju, J. W., Pister, K. S., and Taylor, R. L. (1988). Assessment of cap model: consistent return algorithms and rate-dependent extension, *Journal of Engineering Mechanics*, Vol. 114(2), p. 191-218.
- Song, H. W., Pack, S. W., Nam, S. H., Jang, J. C., and Saraswathy, V. (2010). Estimation of the permeability of silica fume cement concrete, *Construction and Building Materials*, Vol. 24, p. 315-321.
- Tanyildizi, H. and Çevik, A. (2010). Modeling mechanical performance of lightweight concrete containing silica fume exposed to high temperature using genetic programming, *Construction and Building Materials*, Vol. 24(12), p. 2612-2618.
- Tenchev, R. T., Li, L. Y., Purkiss, J. A., and Khalafallah, B. H. (2001a). Finite element analysis of coupled heat and mass transfer in concrete when it is in a fire, *Magazine of Concrete Research*, Vol. 53(2), p.117-125.
- Tenchev, R. T., Li, L. Y., and Purkiss, J. A. (2001b). Finite element analysis of coupled heat and moisture transfer in concrete subjected to fire, *Numerical Heat Transfer, Part A: Applications*, Vol. 39(7), p. 685-710.
- Tenchev, R. T. and Purnell, P. (2005). An application of a damage constitutive model to concrete at high temperature and prediction of spalling, *International Journal of Solids and Structures*, Vol. 42, p. 6550-6565.
- Tennis, P. D. and Jennings, H. M. (2000). A model for two types of calcium silicate hydrate in the microstructure of Portland cement pastes, *Cement and Concrete Research*, Vol. 30, p. 855-863.
- Terro, M. J. (1998). Numerical modeling of the behavior of concrete structures in fire, *ACI Structural Journal*, Vol. 95(2), p. 183-193.
- Tsai, C. L., Chiang, C. H., Yang, C. C., and Chen, C. M. (2005). Tracking concrete strength under variable high temperature, *ACI Materials Journal*, Vol. 102(5), p. 322-329.
- Ulm, F. J., Coussy, O., and Bazant, Z. P. (1999a). The 'Chunnel' fire. I: chemoplastic softening in rapidly heated concrete, *Journal of Engineering Mechanics*, Vol. 125(3), p. 272-282.
- Ulm, F. J., Acker, P., and Levy, M. (1999b). The 'chunnel' fire. II: analysis of concrete damage, *Journal of Engineering Mechanics*, Vol. 125(3), p. 283-289.

- Ulm, F. J., Constantinides, G., and Heukamp, F. H. (2004). Is concrete a poromechanics material? - A multiscale investigation of poroelastic properties, *Materials and Structures*, Vol. 37, p. 43-58.
- Usmani, A. S. and Cameron, N. J. (2004). Limit capacity of laterally restrained reinforced concrete floor slabs in fire, *Cement and Concrete Composites Fire Resistance*, Vol. 26, p. 127-140.
- van der Heijden, G. H. A., Pel, L., and Adan, O. C. G. (2011). Fire spalling of concrete, as studied by NMR, *Proceedings of the 2nd International RILEM Workshop on Concrete Spalling due to Fire Exposure*, Delft, the Netherlands, p. 353-359.
- Velez, K., Maximilien, S., Damidot, D., Fantozzi, G., and Sorrentino, F. (2001). Determination by nanoindentation of elastic modulus and hardness of pure constituents of Portland cement clinker, *Cement and Concrete Research*, Vol. 31, p. 555-561.
- Wan, Z., Zhao, Y., Dong, F., Feng, Z., Zhang, N., and Wu, J. (2008). Experimental study on mechanical characteristics of granite under high temperatures and triaxial stresses, *Chinese Journal of Rock Mechanics and Engineering*, Vol. 27(1), p. 72-77 (in Chinese).
- Yang, D., Sun, W., and Liu, Z. (2007). Thermal decomposition kinetics of ettringite crystal, *Journal of the Chinese Ceramic Society*, Vol. 35(12), p. 1641-1646 (in Chinese).
- Young, J. F. (1988). A review of the pore structure of cement paste and concrete and its influence on permeability, *Proceedings of Permeability of Concrete*, American Concrete Institute, Detroit, p. 1-19.
- Youssef, M. A. and Mofteh, M. (2007). General stress-strain relationship for concrete at elevated temperatures, *Engineering Structures*, Vol. 29, p. 2618-2634.
- Zelić, J., Rušić, D., and Krstulović, R. (2002). Kinetic analysis of thermal decomposition of $\text{Ca}(\text{OH})_2$ formed during hydration of commercial Portland cement by DSC, *Journal of Thermal Analysis and Calorimetry*, Vol. 67, p. 613-622.
- Zha, X. X. (2003). Three-dimensional non-linear analysis of reinforced concrete members in fire, *Building and Environment*, Vol. 38, p. 297-307.
- Zheng, J. J. and Zhou X. Z. (2008). Analytical method for prediction of water permeability of cement paste, *ACI Materials Journal*, Vol. 105(2), p. 200-206.
- Zheng, J. J., Zhou, X. Z., Shao, L., and Jin, X. Y. (2010). Simple three-step analytical scheme for prediction of elastic moduli of hardened cement paste, *Journal of Materials in Civil Engineering*, Vol. 22(11), p. 1191-1194.
- Zienkiewicz, O. C. and Taylor, R. L. (2000). *The Finite Element Method*, Butterworth-Heinemann, Oxford.
- International Organization for Standardization (ISO). (1999). *Fire-resistance tests-Elements of building construction-Part 1: General requirements*. ISO 834-1:1999, International Standards for Business, Government and Society, Geneva, Switzerland.

Summary

Nowadays, high-performance concrete (HPC) is increasingly applied in various structures as it can satisfy the expectations for excellent mechanical properties and a long service life. However, from the evidence of fire accidents that have happened in reality, it has been found that HPC is prone to explosive spalling under fire conditions. The explosive spalling can cause direct exposure of steel reinforcement to high temperatures, resulting in a lower fire resistance capacity of HPC structures compared with NSC structures.

To investigate the fire spalling of HPC, considerable experimental and modeling work have been conducted by researchers. It has been found that explosive spalling is closely related to the heating rate, the moisture content, and the strength of concrete. The higher the heating rate, the moisture content, and the strength, the higher the probability of explosive spalling. Two hypotheses have been proposed to explain spalling: the vapor pressure mechanism and the temperature gradient induced thermal stress mechanism. However, the quantitative analysis of fire spalling is still inadequate and the spalling mechanism is still not clear.

In this thesis, the mechanism of fire spalling has been quantitatively studied. In view of the fact that the heating history effect on the material properties hasn't been considered in the existing models, a heating history-based material-property prediction model has been proposed. The influencing factors of spalling, such as the moisture content and the heating rate, have also been investigated. The following aspects has been considered in the analysis: the evolution of temperature field, the thermal decomposition of hardened cement paste, the vapor pressure, the moisture transport, and the non-linear mechanical behavior of heated concrete.

In Chapter 3, the modeling part of the prediction of the temperature field has been presented. The finite element method has been used. The predicted evolution of temperature field has been verified with the test results for spalling mechanism investigation. In Chapter 4, the thermal decomposition of heated hardened cement paste has been analyzed based on the kinetic and stoichiometric analysis according to the heating history. The volume variation of various constituents in hardened cement paste has been calculated. The modeling part of the build-up vapor pressure has been shown in Chapter 5. The vapor pressure has been determined on the application of steam tables. The thermal decomposition effect on the build-up vapor pressure, such as the release of moisture and the change of porosity, has also been considered. The transport effect on the vapor pressure has been taken into account. The mechanical effect of vapor pressure on fire spalling has also been modeled based on the theory of poro-mechanics. The moisture transport driven by vapor pressure has been modeled

and shown in Chapter 6. The evolution of the permeability of matrix with the heating process has been predicted. The effects of the slip-flow of the gas phase and the water saturation degree on the permeability have been taken into account. The non-linear mechanical analysis has been presented in Chapter 7. The fixed anisotropic smeared crack concept has been employed to analyze the non-linear thermo-poro mechanical response of heated concrete. Both the thermal load and the load of vapor pressure have been considered. A heating history-based numerical method for the prediction of the variation of the elastic modulus of the matrix has been proposed. In Chapter 8, all the modeling parts presented in the previous chapters have been integrated to investigate the spalling mechanism of 100 mm cubic specimens of concrete on a meso level. The thermo-chemo-hydro-mechanical behavior of both HPC and NSC are modeled. The effect of the moisture contents and the heating rate on spalling has been studied. The spalling mechanism has also been interpreted from an energy perspective.

It can be inferred from the numerical analysis that the temperature gradient induced thermal stress plays a dominant role in the explosive fire spalling of 100 mm cubic specimens of HPC; Under slow heating conditions, the non-spalling behavior of HPC specimens with high moisture content is attributed to the low thermal stress induced by low temperature gradient; Vapor pressure can only cause local damage to heated concrete; Decreasing the expansion extent of heated concrete can be helpful in preventing concrete from fire spalling; Under slow heating conditions, however, the vapor pressure becomes dominant in the thermo-mechanical damage of concrete. The results of this study can provide a guidance and reference to engineers and researchers for working out measures to prevent HPC from spalling and to designers for designing HPC structures with high fire-resistance capacity.

Samenvatting

Tegenwoordig wordt high-performance beton (HPC) meer en meer toegepast in verschillende constructies omdat het voldoet aan de hoge verwachtingen van excellente mechanische eigenschappen en een lange levensduur. Echter, uit de resultaten van diverse branden in de praktijk is gebleken dat HPC gevoelig is voor explosief afspatten tijdens brand. De explosief afspatten kan directe blootstelling van de wapening aan hoge temperaturen veroorzaken, wat kan leiden tot een lagere brandbestendigheid van HPC vergeleken met normale sterkte beton (NSC) constructies.

Om afspatten van HPC te onderzoeken is een aanzienlijke hoeveelheid werk verricht door onderzoekers, zowel experimenteel als numeriek. Men heeft gevonden dat explosief afspatten nauw verbonden is met zowel de snelheid van temperatuursverandering, het vochtgehalte als de sterkte van het beton. Hoe sneller de temperatuursverandering, en hoe hoger het vochtgehalte en de sterkte zijn, des te hoger is de kans op explosief afspatten. Twee hypothesen zijn voorgesteld om explosief afspatten te verklaren: het stoomdruk mechanisme en het door temperatuurgradiënten geïntroduceerd temperatuurspanning mechanisme. Echter, de kwantitatieve analyse van afspatten is nog onvoldoende en het mechanisme van afspatten is nog onduidelijk.

In dit promotiewerk is het mechanisme van afspatten bij brandbelasting op kwantitatieve wijze onderzocht. In het licht van het gegeven dat het effect van de warmtegeschiedenis op de materiaaleigenschappen niet wordt beschouwd in de bestaande modellen, wordt een model gebaseerd op de warmtegeschiedenis voorgesteld voor de voorspelling van de materiaaleigenschappen. De factoren die beïnvloeden, zoals vochtgehalte en de snelheid van temperatuursverandering, zijn ook onderzocht. De volgende aspecten zijn in de analyse beschouwd: de ontwikkeling van het temperatuursveld, de decompositie van de uitgeharde cementpasta ten gevolge van temperatuur, de stoomdruk, het vochtransport en het niet-lineaire mechanische gedrag van verhit beton.

In hoofdstuk 3 wordt de modellering van de voorspelling van het temperatuursveld gepresenteerd, waarvoor de eindige elementen methode is gebruikt. De voorspelde ontwikkeling van het temperatuursveld is getoetst aan testresultaten van afspatonderzoek. In hoofdstuk 4 wordt de decompositie van de verhitte uitgeharde cementpasta geanalyseerd, gebaseerd op kinetische en stoichiometrische analyse volgens de temperatuursgeschiedenis. De variatie in volume van de diverse componenten in uitgeharde cementpasta is berekend. Het model voor de opgebouwde stoomdruk wordt getoond in hoofdstuk 5. De stoomdruk is berekend door toepassing van stoomtabellen. Het decompositie-effect op de opgebouwde

stoomdruk, zoals de afgifte van vocht en de verandering van porositeit, is eveneens beschouwd. Het mechanische effect van stoomdruk op afspatten is gemodelleerd op basis van de poro-mechanische theorie. Het vochttransport dat wordt aangedreven door de stoomdruk is gemodelleerd en getoond in hoofdstuk 6. De ontwikkeling van de doorlatendheid van de matrix tijdens verhitting is voorspeld. De effecten van slip-flow van de gasfase en verzadigingsgraad van het water op de doorlatendheid zijn in rekening gebracht. De niet-lineaire mechanische analyse wordt gepresenteerd in hoofdstuk 7. Het concept van gefixeerde anisotrope uitgesmeerde scheuren is toegepast voor het niet-lineaire thermo-poreuze mechanische gedrag van verhit beton. Zowel de thermische belasting als de belasting van de stoomdruk zijn in rekening gebracht. Een numerieke methode gebaseerd op de temperatuursgeschiedenis voor de voorspelling van de variatie in elasticiteitsmodulus van de matrix wordt voorgesteld. In hoofdstuk 8 worden alle delen van het model uit de voorgaande hoofdstukken geïntegreerd om het mechanisme van afspatten van een 100 mm^3 betonmonster op meso-niveau te onderzoeken. Het gecombineerde thermo-chemo-hydronechanische gedrag van zowel HPC en NSC zijn gemodelleerd. Het effect van vochtgehalte en snelheid van temperatuursverandering zijn bestudeerd. Het mechanisme van afspatten is ook geïnterpreteerd middels een energiebeschouwing.

Uit de numerieke analyse kan worden afgeleid dat de temperatuurspanning die wordt veroorzaakt door de temperatuursgradient een belangrijke rol speelt in het explosief afspatten van een 100 mm^3 monster HPC. Het feit dat HPC monsters met een hoog vochtgehalte niet afspatten onder langzame verhitting, wordt toegewezen aan de lage temperatuursspanning ten gevolge van de langzame temperatuursverandering; de stoomdruk veroorzaakt slechts lokaal schade aan het verhitte beton. Verlaging van de expansie van het verhitte beton kan helpen om afspatten van het beton te voorkomen. Echter, onder langzame temperatuursverandering wordt de stoomdruk dominant voor de thermo-mechanische schade van het beton. De resultaten van deze studie kunnen een leidraad en referentie vormen voor ingenieurs en onderzoekers om maatregelen uit te werken om afspatten van HPC te voorkomen tijdens het ontwerp van HPC constructies met hoge brandweerstand.

Publications

- Jie Zhao, Jian-Jun Zheng, Gai-Fei Peng, and Klaas van Breugel. Prediction of Thermal Decomposition of Hardened Cement Paste, *Journal of Materials in Civil Engineering (ASCE)*, 2012, Vol.24 (5).
- Jie Zhao, Jian-Jun Zheng, and Gai-Fei Peng. Fire Spalling Modeling of High Performance Concrete, *Applied Mechanics and Materials*, 2011, Vol. 52-54, p. 378-383.
- Jie Zhao, Jian-Jun Zheng, Gai-Fei Peng, and Klaas van Breugel. Mesoscopic Thermal-Mechanical Fire Damage Modeling of High Performance Concrete, *Advanced Materials Research*, 2011, Vol. 194-196, p. 1095-1098.
- Jie Zhao, Gai-Fei Peng, and Klaas van Breugel. Fire Damage Modeling of High Performance Concrete, *Proceedings of Symposium on Concrete Modeling (CONMOD2010)*, 22-25 June, 2010, Lausanne, Switzerland.
- Jie Zhao, Zhan-Qi Guo, and Gai-Fei Peng. Vapor Pressure Modeling for Fire Damage Assessment of HPC. *Key Engineering Materials*, 2010, Vol. 417-418, p.509-512.
- Jie Zhao, Gai-Fei Peng, Zhan-Qi Guo, and Zhi-Wei Qian. Spalling Driving Force Analysis of HPC under High Temperatures based on Vapor Pressure Modeling Combined with Finite Element Analysis. *Proceedings of the First International Conference on Computational Technologies in Concrete Structures (CTCS'09)*, p. 904-914, 24-27 May, 2009, Jeju, South Korea.
- Jie Zhao, Gai-Fei Peng, Zhan-Qi Guo, and Xian-Wei Chen. Simulation Analysis Procedures on Damage by Fire to High-Performance Concrete. *Key Engineering Materials*, 2009, Vol. 405-406, p. 322-328.

Curriculum Vitae



Name: Jie Zhao

Nov. 20th, 1972: Born in Harbin, Heilongjiang province, P. R. China

Sept. 1992 - July 1996: Undergraduate, Department of Civil Engineering, Harbin Institute of technology, P. R. China, Bachelor's Degree.

Sept. 1996 - July 1999: Postgraduate, School of Civil Engineering, Beijing University of Technology, P. R. China, Master's Degree.

Sept. 1999 - Oct. 2007: Teaching assistant, Lecturer, School of Civil Engineering, Beijing Jiaotong University, P. R. China.

Oct. 2007 - Feb. 2012: Ph.D. candidate, Faculty of Civil Engineering and Geosciences, Delft University of Technology, the Netherlands.

